CEA / Irfu - Service de Physique des Particules

THÈSE de DOCTORAT
de l'Université Pierre et Marie Curie
École Doctorale 560
Discipline : Physique de l'Univers

présentée
par

Vincent FISCHER

Beta-decay emitted electronic antineutrinos as a tool for unsolved problems in neutrino oscillation physics

Soutenue le 23 Septembre 2015 devant le jury composé de :

M.	Jacques	Dumarchez	Président du Jury
Mme	Asmaa	Abada	Rapporteur
M.	Leslie	Camilleri	Rapporteur
Mme	Cristina	Volpe	Examinateur
M.	Jacques	Chauveau	Examinateur
M.	Thierry	Lasserre	Directeur de thèse
M.	Stavros	Katsanevas	Invité
M.	Hervé	De Kerret	Invité

Dedication

À ma famille et mes amis.

Aknowledgements

Malgré le fait que mon manuscrit soit rédigé en anglais, mes remerciements le seront en français afin d'être le plus accessible possible à tous leurs destinataires. Il me faudrait tout un chapitre supplémentaire pour pleinement remercier la totalité des personnes m'ayant supporté et encouragé donc je m'excuse par avance si j'omets des noms ou des qualités. Sachez qu'il n'en est rien et que je n'oublie pas vos contributions au bon déroulement de cette thèse.

Je souhaite tout d'abord remercier Philippe Chomaz, directeur de l'Institut de Recherche sur les lois Fondamentales de l'Univers du CEA Saclay, ainsi que Ursula Bassler et Anne-Isabelle Etienvre, chefs consécutives du Service de Physique des Particules, pour m'avoir permis d'effecteur ma thèse au sein de l'IRFU dans des conditions optimales. Je tiens également remercier Anne-Isabelle pour avoir accepter d'être ma marraine de thèse.

Je remercie Asmaa Abada et Leslie Camilleri d'avoir accepté d'être rapporteurs de mon manuscrit malgré son imposante épaisseur. De la même façon, je tiens à remercier Cristina Volpe, Jacques Chauveau, Stavros Katsanevas et Hervé De Kerret pour leur participation à mon jury de thèse et Jacques Dumarchez pour avoir accepté de le présider.

J'aimerai pleinement remercier Thierry Lasserre pour m'avoir permis d'effectuer cette thèse. Ce fut un réel plaisir de travailler sous ta supervision et nos échanges professionnels ou personnels ont été très enrichissants et me seront très précieux pour la suite de ma carrière.

Merci à Guillaume Mention pour ses conseils et explications, en particulier dans le domaine des statistiques, ainsi qu'à Matthieu Vivier, qui est arrivé dans le groupe en même temps que moi, et avec qui j'ai partagé de nombreux séjours à Chooz. Merci également pour ses conseils concernant ma recherche de postdocs.

Je tiens à remercier Jonathan Gaffiot pour son aide et ses explications, que ce soit en physique des neutrinos, des réacteurs et parfois pas en physique du tout.

Merci à Michel Cribier pour ses conseils, son expérience et pour nous montrer que la passion de la recherche ne s'atténue pas avec le temps.

Je remercie également les collègues du SPhN, David Lhuillier et Alain Letourneau ainsi que Maxime Pequignot et Valérian Sibille avec lesquels j'ai monté des murs de plomb, fait des shifts ou simplement échangé à propos de Nucifer et Double Chooz.

Je remercie Mathieu Durero et Thibaut Houdy et leur souhaite bonne chance pour la

suite de leur doctorat qui se déroulera, j'en suis sûr, sans soucis. Je leur souhaite également bon courage pour les futures séances de remplissage du détecteur germanium auxquelles je ne pourrai plus participer, à mon grand dam.

J'aimerai maintenant remercier toutes les personnes du laboratoire qui ont contribué à rendre ces trois années plus agréables et en particulier Martine Oger pour son efficacité et ses conseils, Béatrice Guyot pour m'avoir patiemment aidé lors de mes préparations de missions. Je tiens également à remercier chaleureusement Fouzia Ben Mesbah grâce à qui chacune de mes journées commençaient dans la bonne humeur.

Je tiens à remercier Inoue-san et Suekane-san de m'avoir invité à travailler quelques mois au RCNS de Tohoku ainsi que tous les membres des groupes KamLAND et Double Chooz pour leur accueil. Merci donc à Takemoto-san, Sayuri, Azusa, Benda, Ayumu, Hiroko-san, Shimizu-san, Tamae-san, Thiago et Furuta-san.

Merci à tous les membres de Double Chooz avec lesquels j'ai passé du temps à Chooz lors de l'intégration du détecteur proche ou lors de shifts. Merci à Christian Veyssiere, Loris Scola, Olivier Corpace, Michel Fontaine, Antoine Collin, Emmanuel Chauveau, Guillaume Pronost, Romain Roncin et Erica Caden.

Je remercie également Annette pour son accueil qui rendait les séjours au château de Double Chooz plus agréables.

Merci à tous les doctorants et stagiaires dont j'ai croisé la route durant ces 3 ans: Théophile Chirac avec qui j'ai beaucoup apprécié travailler et à qui je souhaite une bonne continuation en Norvège, Yo Kato, Marie Vidal, Simon Appel et Birgit Neumair.

Finalement, merci aux autres doctorants du SPP et en particulier à Thibaut Hennequin, avec lequel j'ai partagé mes pauses café et quelques séances de farming sur Diablo III, et Anais Moller pour son amitié depuis les bancs du Master NPAC et à qui je souhaite un formidable séjour en Australie.

J'en profite maintenant pour remercier tous mes proches, amis et famille, qui m'ont supporté et soutenu durant de nombreuses années.
Merci à Florian, Claudio, Arnaud, Guillaume, Guillaume, Alexandre, Céline, Hélène, Vincent, Christophe et j'en oublie sûrement beaucoup d'autres. Merci pour ces bons moments passés ensemble autour d'une table ou d'un écran. J'espère de tout coeur que, malgré les distances géographiques, nous resterons toujours aussi soudés que maintenant.

Et enfin, je remercie mes parents, ma soeur, mon beau-frère et tous les membres de ma famille qui ont toujours été présents pour moi et qui sont ou seraient fiers que je sois devenu docteur.

Contents

Introduction **1**

1 Theory of neutrino physics **3**
1.1 History . . . 3
1.2 Standard Model of particle physics . . . 6
1.2.1 Electroweak interaction . . . 6
1.2.2 Higgs mechanism . . . 7
1.3 Neutrinos and their masses . . . 9
1.3.1 Neutrino masses in the SM . . . 9
1.3.2 Neutrino Majorana mass . . . 9
1.3.3 See-saw mechanism . . . 10
1.4 Neutrino oscillations . . . 11
1.4.1 Neutrino mixing . . . 11
1.4.2 Oscillation probability . . . 13
1.4.3 The 2-neutrino practical case . . . 15
1.4.4 Oscillations in matter . . . 16

2 Experimental status of neutrino physics **19**
2.1 Neutrino masses . . . 19
2.1.1 Absolute mass measurements . . . 19
2.1.2 Mass hierarchy . . . 22
2.1.3 Double beta decay . . . 23
2.2 Neutrino oscillations . . . 24
2.2.1 Oscillation framework . . . 26
2.2.2 Anomalies . . . 36
2.3 Sterile neutrinos . . . 38
2.3.1 Theoretical motivations . . . 39
2.3.2 Neutral Leptons: Light, keV, MeV or more . . . 41
2.3.3 Light sterile neutrino oscillation phenomenology . . . 46

3 MeV (Anti)Neutrino generators **49**
3.1 Nuclear reactors . . . 49
3.1.1 Basic fission principles . . . 49
3.1.2 Reactor mechanisms . . . 51
3.1.3 Antineutrino production . . . 51
3.1.4 Antineutrino energy spectrum . . . 53

3.2 Radioactive sources . . . 55
3.2.1 History . . . 56
3.2.2 Neutrino sources . . . 57
3.2.3 Antineutrino sources . . . 58
3.3 Supernovae . . . 60
3.3.1 Core-collapse supernova . . . 61
3.3.2 SN1987A - An observed supernova . . . 69
3.3.3 The SNEWS network . . . 71

4 Inverse Beta Decay process: Theory and Simulation 73
4.1 Inverse Beta Decay reaction . . . 73
4.1.1 Theoretical basis . . . 73
4.1.2 Observables . . . 74
4.2 Detailed IBD kinematics . . . 75
4.2.1 Total cross section: Interaction rate . . . 75
4.2.2 Differential cross section: Angular distributions . . . 76
4.3 IBD simulation codes . . . 80
4.3.1 NuMC for GEANT4 . . . 80
4.3.2 SuperNustradamus for MATLAB . . . 84

5 Exploiting the directionality of the IBD Process 95
5.1 Motivations . . . 95
5.2 Methods . . . 96
5.3 Application: Double Chooz . . . 97
5.3.1 Results of past experiments . . . 97
5.3.2 The Double Chooz layout . . . 98
5.3.3 Double CHOOZ results . . . 100
5.4 Application: Supernovae detection . . . 109
5.4.1 Toy Monte Carlo for supernova position reconstruction . . . 110
5.4.2 Detectors of interest . . . 112
5.4.3 Combined multi-detectors fit . . . 115
5.4.4 Discussion . . . 118
5.4.5 Retrieving astrophysical information from supernova neutrinos . . . 120
5.5 Application: Geoneutrinos detection . . . 123
5.5.1 Geoneutrinos . . . 123
5.5.2 Results and limitations . . . 128

6 Measurement of θ_{13} with Double Chooz 133
6.1 The Double Chooz experiment . . . 133
6.1.1 The experimental design . . . 133
6.1.2 Chooz power plant . . . 135
6.1.3 The Double Chooz detector . . . 137
6.2 Data acquisition and calibration . . . 140
6.2.1 Data acquisition . . . 140
6.2.2 Calibration system . . . 141
6.3 Event reconstruction . . . 144
6.3.1 Pulse reconstruction . . . 144

6.3.2 Vertex reconstruction . . . 145
6.3.3 Energy reconstruction . . . 146
6.3.4 Muon tracks reconstruction . . . 150
6.4 The Double Chooz simulation package . . . 150
6.4.1 $\bar{\nu}_e$ generation . . . 150
6.4.2 Detector response simulation . . . 151
6.4.3 Readout simulation . . . 152
6.5 Data analysis . . . 153
6.5.1 Backgrounds . . . 153
6.5.2 Data samples . . . 155
6.5.3 Neutrino selection . . . 156
6.6 Oscillation parameters determination . . . 169
6.6.1 Reactor Rate Modulation Analysis . . . 171
6.6.2 Rate+Shape Analysis . . . 172
6.6.3 Near detector sensitivity . . . 174

7 Study of a 4^{th} neutrino state with KamLAND/Borexino 177
7.1 The CeSOX/CeLAND project . . . 177
7.1.1 Physics case . . . 177
7.1.2 The KamLAND/Borexino detectors . . . 178
7.1.3 The ^{144}Ce -^{144}Pr AntiNeutrino Generator . . . 180
7.1.4 Transportation and deployment . . . 188
7.2 Simulations . . . 195
7.2.1 Simulation softwares . . . 196
7.2.2 Signals . . . 197
7.2.3 Backgrounds . . . 200
7.3 Expected sensitivity . . . 208

Conclusion 212

A Study of accidental background in the Nucifer experiment 213
A.1 Nuclear non-proliferation . . . 213
A.2 The Nucifer experiment . . . 214
A.3 Accidental background reduction . . . 215

B Characterization of ^{144}Ce samples 219
B.1 Gamma spectroscopy . . . 219
B.2 Beta spectroscopy . . . 222

Bibliography 242

Introduction

From its early years as a tool to solve an old energy conservation issue, the neutrino has come a long way. Postulated by Wolfgang Pauli in 1930 as he was pointing out the radioactive activity, mostly from ^{40}K decays, of his colleagues [1], the neutrino, by its light and neutral nature, was supposed to definitely solve the puzzle of the β-decay missing energy as well as the apparent non-conservation of momentum. After its classification as weakly interacting by Enrico Fermi in 1933 [2] and the first calculations of its interacting cross section, it became obvious that the detection of the neutrino was an unprecedent challenge that would require prodigeous sources and/or detectors. It is only in 1956 that Frederick Reines and Clyde Cowan finally succeeded this challenge by detecting electronic antineutrinos from the Savannah River nuclear reactor using a tank filled with 400 kg of cadmium-loaded water [3]. Since then, the improvement of the detection techniques has allowed the discovery of many properties of neutrinos.

However, while constituting the most abundant matter particle in our Universe, it is nowadays still one of the most mysterious particle of our Standard Model. Answering the questions it raises may open the way to reveal physics beyond the Standard Model.

Amongst these questions, one of the most crucial is "Why do neutrinos oscillate ?". Indeed, recent observations proved that one of the puzzling properties of the neutrino was its ability to change its flavor among the three different available. This is the so-called "neutrino oscillation" phenomenon that will be explored in details in this thesis.

The first chapter is dedicated to the theory of neutrino physics. After an historical introduction, we will take a deeper look into the Standard Model, supposed to account for all our knowledge in particle physics. After reviewing the basics of neutrino physics, we will see how recent non-zero neutrino masses discoveries can be considered as limitations of this Model, opening an appealing window to BSM (Beyond Standard Model) physics. Finally, we will introduce in details the phenomenon of neutrino oscillations, a conclusive evidence of the existence of non-zero neutrino masses.

In the second chapter, we will review the experimental status of neutrino physics. The current status of neutrino mass determination experiments will be studied. In the second part of this chapter, we will fully explore the current status of neutrino oscillations experiments in the current 3-neutrino oscillation framework. Finally, after introducing the concept of neutral heavy lepton, its implementation as a sterile neutrino in our current understanding of flavor oscillations will be described.

The third chapter is entirely dedicated to the emitters of (anti-)neutrinos at the MeV energy scale. After exploring nuclear reactors physics, from the fission process to the properties

of consequently generated antineutrinos, we will discuss the possibility of using radioactive sources as neutrino generators. Finally, we will review an astrophysical process, the supernova, releasing a tremendous amount of neutrinos and antineutrinos at the MeV scale. Starting from the basic principles and stages of the process, we will then look at the properties of its neutrino emission to finally study the SN1987A case, the only supernova ever observed through neutrino.

After the latter chapter dedicated to the generation of MeV neutrinos, the fourth chapter will be focusing on the detection of neutrinos through the Inverse Beta Decay reaction. This reaction, considered as the "golden channel" for MeV electronic antineutrino detection, will here be presented from a theoretical to a technical point a view. Finally, we will explore the domain of interaction simulation with two different computer codes dedicated to simulate IBD processes, NuMC in a GEANT4 framework and SuperNustradamus in a MATLAB framework.

In the fifth chapter, we will connect the last two chapters and study how IBD kinematics can be used to retrieve the direction of an incoming neutrino flux. This idea called neutrino directionality hereafter will, in this chapter, be applied to the Double Chooz experiment, to localization of supernovae and the detection of geoneutrinos. This first application proves the possibility of directionality with the Double Chooz detector and opens the possibility of using directionality as a tool for background rejection and other purposes, as supernovae localization. The second application could be of interest for the astronomical community looking forward to the observation of a supernova process, since the direction information carried by neutrinos arrives prior to the observable photons. The third application could help determine the origin of geoneutrinos within the Earth's geological layers as well as reject backgrounds originating from other neutrino sources.

The sixth chapter will be fully dedicated to the Double Chooz experiment and its purpose of measuring the θ_{13} mixing angle. After presenting the experiment and the detector, we will look into the full chain starting from data acquisition through the event reconstruction, the Monte-Carlo simulation and finally the data analysis with both near and far detectors that gives the results taken as inputs of the final oscillation fit. This fit, comparing the actual data to non-oscillated simulated data, is the last step leading to the precise determination of the θ_{13} mixing angle.

Finally, the seventh chapter of this thesis will be dedicated to the CeLAND/CeSOX experiments and their goal for testing the hypothetical existence of a new neutrino state. After describing the project from its physics case to its technical challenges, we will move on to the simulations of the neutrino signals, mandatory in order to fully caracterize the expected signal in case of the discovery of a new neutrino state. Backgrounds will be studied in order to accurately determine the sensitivity of the various experimental setups.

Chapter 1

Theory of neutrino physics

In this chapter, the basic theory of neutrino physics will be reviewed. After an historical introduction in Section 1.1, we will quickly describe the Standard Model of particle physics and its components needed for a good understanding of neutrino physics in Section 1.2. Then, we will describe the status of neutrinos and their masses in the Standard Model in Section 1.3 in order to finally study the theory of neutrino oscillations in Section 1.4.

1.1 History

In 1896, after several experiments on phosphorescence, Henri Becquerel began to illuminate uranium salts with sunlight with the hope of observing the emission of X-ray radiation, recently discovered [4]. Quite soon, he noticed that the patterns he wanted to observe on his photographic plates were as bright whether the uranium salts had been exposed to sunlight or not. This phenomenon, which we call now radioactivity, was thus discovered by pure serendipity and opened a new chapter of physics that led to the discovery of the three α, β and γ radiations.

In 1914, James Chadwick showed the β spectrum was continuous [5] which was not compatible with the previous observations of discrete spectra in the α and γ decays.

It is only in 1930, more than a decade later, that Wolfgang Pauli in his famous letter "Dear radioactive ladies and gentlemen" [1] proposed his approach to solve this issue of missing energy by adding a new particle in the β decay. This particle, originally called "neutron", was supposed to carry away the additional spin 1/2 and missing energy. It was also supposed to be a neutral light particle to explain its lack of interaction and the apparent conservation of the mass during a decay. The new neutral particle discovered by Chadwick in 1932 [6] was too heavy to satisfy these conditions and was named "neutron" but in 1934, Enrico Fermi introduced his theory of β decay [2] and incorporated the particle postulated by Pauli in his model that he baptized "neutrino", meaning "small neutral one". This theory of β-decay became the theory of weak interaction.

It is finally in 1956, more than twenty years after the claim of its existence, that the neutrino was experimentally detected [3, 7]. This discovery was the fruitful result of an experiment conducted by Frederick Reines and Clyde Cowan using the Savanah River nuclear

reactor (USA) as an intense electron antineutrino source[1]. Their detector, as illustrated in Figure 1.1, consisted of two tanks filled with $CdCl_2$-doped water and placed between three tanks of liquid scintillator. They were both surrounded by photomultipliers in order to observe the positron annihilation and the neutron capture on ^{113}Cd from the

$$\bar{\nu_e} + p \rightarrow e^+ + n \tag{1.1}$$

detection reaction, also called Inverse Beta Decay (IBD).

This experiment took the credit for the discovery of the neutrino though a preliminary one led by the same team took place at the Hanford reactor (USA) in 1953 using a similar setup. Unfortunately, due to the high rate of cosmic background, the faint signal observed was not significant enough and the experiment was moved to the Savanah River reactor, better shielded against cosmic background.

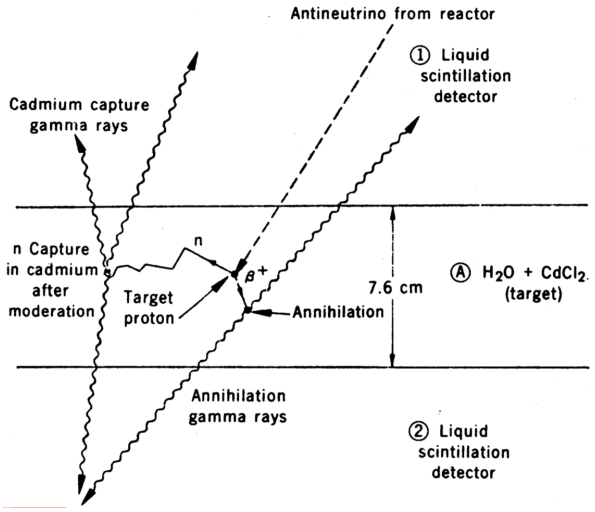

Figure 1.1: Sketch of the Savanah River experimental setup. The IBD positrons and neutrons are generated and captured in the target (A) and the secondary gammas they create deposit their energy in the surrounding liquid scintillator tanks (1) and (2).

This experiment gave the first experimental average cross section for the IBD reaction

$$\langle \sigma_{\text{IBD}} \rangle = (11 \pm 2.6) \times 10^{-44} \text{cm}^2 \tag{1.2}$$

which is in rather good agreement with the current measurement [8].

In 1956 as well, T. D. Lee and C. N. Yang noticed that, although it was supposed to be conserved in all interactions, evidences for parity conservation in weak interaction were lacking [9]. This symmetry violation was a possible solution to the so-called $\tau - \theta$ puzzle observed in kaon decays where a K^+ decay could lead to two final states of respectively two and three pions, thus violating parity conservation.

To test this hypothesis, C. S. Wu carried out an experiment monitoring the angular distributions of gammas and electrons emitted from ^{60}Co decays in a magnetic field [10]. The

[1]Note that the distinction between neutrino and antineutrino has been made by Davis at the Brookhaven reactor in 1955.

observation of a difference between the direction of emission of the gammas and the electrons led to the discovery of P-violation in weak interaction. A year later, Goldhaber carried out an experiment to measure the polarization of a neutrino in the process:

$$e^- + {}^{152}\text{Eu} \rightarrow {}^{152}\text{Sm}^* + \nu_e \tag{1.3}$$

He found that the polarization of the ν_e was in the opposite direction with respect to its momentum [11].

Combining the results of these two experiments leads to the following conclusion: being massless, antineutrinos can only have a right helicity while neutrinos can only have a left helicity[2].

The discovery of the W and Z gauge bosons of the weak interaction in 1983 at CERN brought confirmation of the Glashow-Weinberg-Salam model [12, 13, 14] which defines neutrinos and antineutrinos as massless, given their respective left and right chirality. Further results from the LEP experiments showed that only 3 families of light neutrinos could couple with the Z boson [15]. The ν_μ neutrino from the second family had already been discovered at Brookhaven in 1963 [16] while the ν_τ neutrino was finally discovered in 2000 with the DONUT experiment [17] confirming the LEP results.

In the meantime, several experiments tried to detect neutrinos from sources other than nuclear reactors. The fusion reactions powering the Sun lead to the creation of several neutrinos with different energy lines and spectra. The Homestake mine experiment, carried out by R. Davis Jr. and dedicated to detect electronic neutrinos from the Sun, was the first experiment to observe solar neutrinos and subsequently their deficit with respect to the current astrophysical models [18].

Similar deficits have been observed with atmospheric neutrinos, created by the decays of the secondary particles, such as muons, pions and kaons, produced by interactions between cosmic rays, mostly high energy protons, and the molecules of the high atmosphere. The Kamiokande experiment, originally dedicated to study proton decay, thus having atmospheric neutrinos as background, was the first to detect a deficit of ν_μ with respect to the incident angle of the event while the number of ν_e was in agreement with the Monte Carlo prediction [19].

While several explanations, such as neutrino decay or decoherence [20], were proposed to solve these anomalies, the answer actually came from an effect, postulated long ago: the oscillation of neutrinos. In 1957, Bruno Pontecorvo first postulated the existence of an oscillation between neutrinos and antineutrinos, in analogy of the $K^0 - \overline{K^0}$ meson oscillations [21, 22]. This idea was later fully developed by three Japanese physicists, Ziro Maki, Masami Nakagawa and Shoichi Sakata [23]. According to their theory, the neutrino flavor and mass eigenstates, respectively (ν_e, ν_μ, ν_τ) and (ν_1, ν_2, ν_3), are different. The matrix transforming one base into the other, named the PMNS (Pontecorvo-Maki-Nakagawa-Sakata) matrix U_{PMNS} takes as parameters three mixing angles θ_{ij}, two differences of squared masses Δm^2_{ij}, a CP violation phase parameter δ_{CP} and additional phases depending on the Majorana nature of the neutrino. A more detailed presentation of the neutrino oscillations phenomenon will be in Section 1.4.

[2]The helicity is the projection of the spin $\vec{s}$ onto the momentum $\vec{p}$ such as $h = \vec{s}.\vec{p}$

This oscillation was finally found responsible for the deficit and distortion observed in the atmospheric sector in 1998 by the Super-Kamiokande experiment [24] and for the deficit observed in the solar sector by many experiments including the SNO experiment in 2000 [25]. Since then, several experiments refined the observation of these oscillations in the solar and atmospheric sector thus measuring the two mixing angles θ_{12} (solar) and θ_{23} (atmospheric) and the two squared masses differences Δm^2_{12} and Δm^2_{23}. The last mixing angle θ_{13} is significantly smaller than the other two, it was thus the last one to be measured in 2012 by the Double Chooz [26], RENO [27] and Daya Bay [28] experiments, the latter providing the highest precision.

The existence of a non-zero θ_{13} mixing angles opened the way for a measurement of the CP violation phase δ, impossible otherwise. The hierarchy between mass states, the value of the absolute neutrino mass and the nature of the neutrino, whether it is a Dirac particle, as the other fermions in the Standard Model or a Majorana particle, are still undetermined at this point. Besides, several anomalies observed in the last decades point towards the existence of one or more additional neutrinos and leave the neutrino oscillation framework with some hypothetical unknown parameters.

1.2 Standard Model of particle physics

The Standard Model (SM) is the full description of the elementary particles and their interactions. It is a gauge theory based on the local symmetry group $SU(3)_C \times SU(2)_L \times U(1)_Y$ where C represents the color, L the weak isospin and Y the hypercharge. It consists of twelve gauge bosons, responsible for three interactions, the Higgs boson, providing masses to the W and Z bosons, and twelve fermions (with their twelve associated antiparticles) as seen on Figure 1.2. Its success and strength account for its ability to have accurately predicted all particle physics measurements with no significant deviation. In this section, we will not enter in the details of the Standard Model of particle physics but discuss its components that ought to be introduced for an understanding of neutrino physics.

1.2.1 Electroweak interaction

The Standard Model incorporates three of the fundamental interactions: electromagnetism, the weak interaction and the strong interaction. Gravitation cannot be incorporated since it has yet to been quantized.

While strong interaction is described by quantum chromodynamics (QCD) based on the $SU(3)_C$ symmetry group, electromagnetism and the weak interaction are unified in a single interaction based on the $SU(2)_L \times U(1)_Y$ symmetry group. This interaction, called electroweak interaction and based on the Glashow-Weinberg-Salam model unifies Fermi's theory of weak interaction and electromagnetism at high energies ($\sim$ 100 GeV). However, at low energies, a spontaneous symmetry breaking occurs separating the two interactions and generating the massive W^+, W^- and Z^0, gauge bosons of the weak interaction and the massless photon, vector of the electromagnetic force. This spontaneous symmetry breaking is caused by the Higgs mechanism and will be discussed in Section 1.2.2.

Unlike its chirality, the helicity of a particle is not relativisticaly invariant. For a massive particle, it can be reversed by observing the particle in a reference frame which speed is larger than the particle's motion. However, in the case of massless particles such as photons,

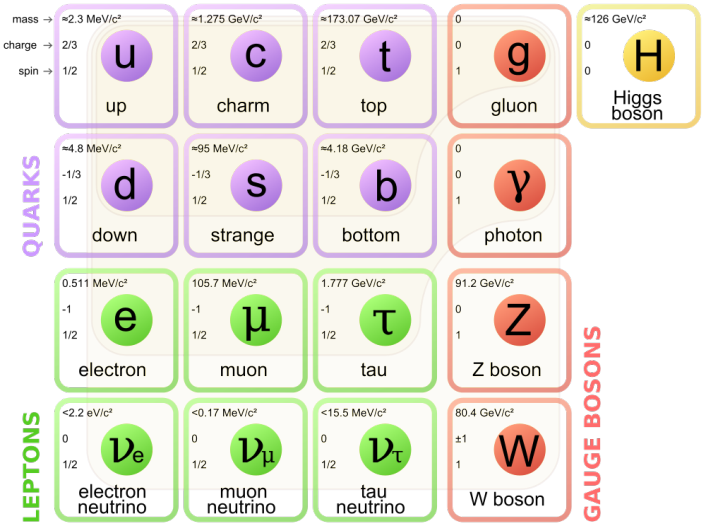

Figure 1.2: The constituents of the Standard Model. 12 fermions: 6 quarks and 6 leptons, each separated in 3 different families, and 13 bosons: 8 gluons, a photon, the $W^{\pm}$ and Z^0 bosons and the recently discovered scalar Higgs boson [15].

there are no reference frame where the particle appears to move backwards and the helicity, in this case equal to the chirality, is invariant. In the SM, Fermions of a same family are doublets if their chirality is left or singlets if their chirality is right. The opposite happens for antifermions. This way, only left-handed fermions or right-handed antifermions interact with gauge bosons. The discovery of neutrino oscillations and its consequence on the massive nature of neutrinos implies that right-handed neutrinos and left-handed antineutrinos exist but do not interact with gauge bosons.

The lack of mass terms in the electroweak Lagrangian is mandatory to conserve $SU(2)_L$ gauge invariance. However, experimental evidences showed the existence of massive fermions and bosons which led to the development of an apparatus to confer mass to these particles, the Higgs mechanism.

1.2.2 Higgs mechanism

While it is commonly called Higgs mechanism, it was mostly developed in 1964 by R. Brout, F. Englert and P. Higgs thus the name BEH mechanism should be more appropriate.

This BEH mechanism is responsible for the spontaneous symmetry breaking of $SU(2)_L \times U(1)_Y$ at low scales since it introduces a non-zero minimum of potential in the Lagrangian, by the addition of a new scalar field of $SU(2)_L$ of spin 0 and hypercharge 1, called the Higgs doublet:

$$\Phi(x) = \begin{pmatrix} \Phi^+(x) \\ \Phi^0(x) \end{pmatrix}, \tag{1.4}$$

where $\Phi^+(x)$ and $\Phi^0(x)$ are charged and neutral scalar fields.

Taking this new Higgs field into account implies to add a new term $\mathcal{L}_{\text{Higgs}}$ to the elec-

troweak Lagrangian $\mathcal{L}_{\text{EW}}$:

$$\mathcal{L}_{\text{Higgs}} = (D^{\mu}\Phi)^{\dagger}(D_{\mu}\Phi) - V(\Phi), \tag{1.5}$$

where $V(\Phi)$ is the symmetry breaking potential expressed as:

$$V(\Phi) = -\mu^2\Phi^{\dagger}\Phi + \lambda(\Phi^{\dagger}\Phi)^2, \tag{1.6}$$

with λ the Higgs self-coupling and μ^2 the Higgs quadratic coupling, negative in the case of a spontaneous symmetry breaking and related to the Higgs boson mass through $m_{\text{Higgs}} = \sqrt{-2\mu^2}$.

The minimum of this potential is the vacuum expectation value (v.e.v) $v/\sqrt{2}$ with $v = \sqrt{-\mu^2/\lambda} \approx 246.22$ GeV, which is nonzero due to the neutral scalar Higgs field Φ^0.

By representing the physical Higgs boson by the $H(x)$ field, one can express the Higgs doublet as:

$$\Phi(x) = \frac{1}{\sqrt{2}}\begin{pmatrix} 0 \\ v + H(x) \end{pmatrix}, \tag{1.7}$$

Integrating this field in the Lagrangian $\mathcal{L}_{\text{EW}}$ and using covariant derivatives in order to introduce gauge fields implies the gauge bosons to acquire masses such as:

$$M_H = \lambda v, M_W = \frac{ev}{2\sin\theta_W}, M_Z = \frac{M_W}{\cos\theta_W}, M_{\gamma} = 0. \tag{1.8}$$

with θ_W the weak mixing angle, $e = g\sin\theta_W$ the positron electric charge ang g the weak coupling constant.

In order for fermions to acquire masses, they need to be coupled to the v.e.v. of the Higgs field. To conserve isospin, the Higgs doublet needs to be combined with a fermion doublet and singlet thus forming a Yukawa coupling of the form (here for an electron):

$$\mathcal{L}_{\text{Yukawa}} = -c_e\overline{e_R}\phi^{\dagger}\begin{pmatrix} \nu_{eL} \\ e_L \end{pmatrix} + h.c. \tag{1.9}$$

with c_e an arbitrary electron coupling constant. After a few calculations, this equation gives $\mathcal{L}_{\text{Yukawa}} = -c_e\frac{v}{\sqrt{2}}\bar{e}e$ highlighting the mass of the electron $m_e = c_e\frac{v}{\sqrt{2}}$. These methods and equations are valid for the other charged leptons and quarks with their respective coupling constants c_i.

Without evidence for a right-handed neutrino state, one cannot write Yukawa couplings such as Eq. 1.9 for neutrinos. Neutrinos thus remain massless in the current understanding of the Standard Model. In order to give neutrinos their masses, proven since the observation of oscillations, one has either to introduce a new mechanism of mass generation for neutrinos or to keep the same mechanism but introduce a right-handed neutrino (ν_{R}) in the SM. Some of these mechanisms, considered physics beyond the Standard Model as we speak, will be dealt with in Section 1.3.

1.3 Neutrinos and their masses

As seen in Section 1.2, the Standard Model shows its limitations when it comes to neutrino masses since, despite experimental proofs of their existences, they cannot be generated by the Higgs mechanism due to the absence of ν_{R} in the SM. In this section, we will review the different ways of generating neutrino masses in "Beyond Standard Model" (BSM) physics.

1.3.1 Neutrino masses in the SM

This limitation that forbids neutrino to acquire masses in the Standard Model is the non-existence of right-handed neutrinos. However, by including ν_R singlets in the model, one can write Yukawa couplings such as in Eq. 1.9 of the form:

$$\mathcal{L}_{\text{Yukawa}} = -c_\nu \overline{\nu_R} \phi^\dagger \begin{pmatrix} \nu_{eL} \\ e_L \end{pmatrix} + h.c. \tag{1.10}$$

resulting in terms such as $\mathcal{L}_{\text{Yukawa}} = -c_\nu v \bar{\nu}\nu$ with c_ν, the Yukawa coupling for neutrinos, to be much smaller than the other charged leptons' couplings in order to account for the neutrinos tiny masses, given by $m_\nu = c_\nu \frac{v}{\sqrt{2}}$.

The introduction of the ν_R singlet leads to Dirac neutrino mass terms, similar to the ones already existing for charged leptons, which gives a Dirac mass Lagrangian of the form:

$$-\mathcal{L}^D_{\text{mass}} = m^D_\nu (\overline{\nu_R}\nu_L + \overline{\nu_L}\nu_R) \tag{1.11}$$

where m^D_ν is the Dirac mass of the neutrino, result of the introduction of right-handed neutrinos in the Standard Model.

There is another way for neutrinos to acquire masses with the Higgs mechanism that does not require the existence of right-handed neutrinos: the introduction of a new Higgs boson triplet and its gauge-invariant Yukawa couplings. Several models such as Grand Unified Theory (GUT) and Supersymmetry (SUSY) also offer possibilities to explain the existence of neutrino masses but they will not be discussed in this thesis. More details about these mass generation methods can be found in [29].

1.3.2 Neutrino Majorana mass

For all the Standard Model fermions, the only difference between particles and antiparticles lies in their opposed electric charge. Since they are neutral particles, the situation is not that trivial with neutrinos and antineutrinos. While the Dirac formalism postulates particles and antiparticles are different, neutrinos might be considered identical to antineutrinos thus leading to a possible violation of the lepton number.

This theoretical possibility would make the neutrino a Majorana particle, a particle state identical to its antiparticle, as postulated in 1937 by Ettore Majorana [30].

In the Majorana formalism, the charge conjugate of a field is equal to the initial field up to a phase:

$$\Psi^C = \eta\Psi \tag{1.12}$$

with η an arbitrary phase.

This field can be expressed with its left and right handed components such as $\Psi = \Psi_L + \Psi_R$.

If we consider neutrinos as Dirac particles, Ψ_L and Ψ_R are independent Dirac fields we can express in the Dirac mass term of the Lagragian as:

$$-\mathcal{L}_D = m_D(\overline{\Psi_R}\Psi_L + \overline{\Psi_L}\Psi_R) \tag{1.13}$$

with m_D the Dirac mass of the neutrino, as seen earlier.

However, if neutrinos are considered Majorana particles, the left and right handed components Ψ_L and Ψ_R are no longer independent and the Ψ field can be expressed as:

$$\Psi = \Psi_{M_L} + \Psi_{M_R} \tag{1.14}$$

with Ψ_{M_L} and Ψ_{M_R} the two Majorana components of the field defined as:

$$\Psi_{M_L} = \Psi_R + \eta_1 \Psi_R^C \tag{1.15}$$
$$\Psi_{M_R} = \Psi_L + \eta_2 \Psi_L^C \tag{1.16}$$

with $\eta_{1,2}$ arbitrary phases.

This gives a Majorana mass term in the Lagrangian of the form:

$$-\mathcal{L}_M = \frac{m_{M_L}}{2}(\overline{\Psi_R^C}\Psi_R + \overline{\Psi_R}\Psi_R^C) + \frac{m_{M_R}}{2}(\overline{\Psi_L^C}\Psi_L + \overline{\Psi_L}\Psi_L^C) \tag{1.17}$$

with $m_{M_{L,R}}$ two Majorana mass terms.

The neutrino being a Majorana particle is not incompatible with the existence of a right-handed neutrino. In this case, the neutrino Lagrangian contains both Majorana and Dirac mass terms such that:

$$\mathcal{L}_{D+M} = \mathcal{L}_D + \mathcal{L}_{M_L} + \mathcal{L}_{M_R}. \tag{1.18}$$

1.3.3 See-saw mechanism

In the previous case where Majorana neutrinos and right-handed field singlets coexist, one needs to consider both Dirac and Majorana mass terms in the Lagrangian such as:

$$-\mathcal{L}_{D+M} = m_D(\overline{\Psi_R}\Psi_L + \overline{\Psi_L}\Psi_R) + \frac{m_{M_L}}{2}(\overline{\Psi_R^C}\Psi_R + \overline{\Psi_R}\Psi_R^C) + \frac{m_{M_R}}{2}(\overline{\Psi_L^C}\Psi_L + \overline{\Psi_L}\Psi_L^C) \tag{1.19}$$

which, using matrix formalism, can be expressed as:

$$-\mathcal{L}_{D+M} = \frac{1}{2}\begin{pmatrix}\overline{\Psi_L} & \overline{\Psi^C{}_L}\end{pmatrix}\begin{pmatrix}m_{M_L} & m_D \\ m_D & m_{M_R}\end{pmatrix}\begin{pmatrix}\Psi^C{}_R \\ \Psi_R\end{pmatrix} + h.c. \tag{1.20}$$

using $\Psi^C{}_L = \Psi_R^C$ and $\Psi^C{}_R = \Psi_L^C$.

After diagonalisation of the mass matrix, the following mass eigenvalues can be extracted:

$$m_{1,2} = \frac{1}{2}\left(m_{M_L} + m_{M_R} \pm \sqrt{(m_{M_L} - m_{M_R})^2 + 4m_D^2}\right) \tag{1.21}$$

Since none of these masses are actually known, several cases with different values for m_D, m_{M_L} and m_{M_R} have to be studied. However, in the following, we will focus on a simple

scenario extracted from the see-saw model of neutrino masses.

In this case, $m_{M_L} = 0$ and $m_{M_R} \gg m_D$ leading to the two mass eigenvalues:

$$m_\nu = m_1 = \frac{m_D^2}{m_{M_R}} \qquad m_N = m_2 = m_{M_R}(1 + \frac{m_D^2}{m_{M_R^2}}) \approx m_{M_R} \tag{1.22}$$

Providing a natural explanation for the smallness of neutrino masses, the see-saw mechanism is one of the most appealing neutrino mass generation model. The smallness of the ν neutrino mass m_ν is compensated by the heaviness of the ν_M Majorana neutrino. This introduces a new energy scale in the neutrino sector that could be associated with the energy scale predicted by GUT theories where the electroweak and strong force happen to unify, around 10^{16} GeV. The existence of these heavy Majorana neutrinos could also be the key of the understanding of the baryon asymmetry in the Universe. Indeed, the lepton number violation associated to the Majorana neutrino is a source of lepton asymmetry that can be converted into a baryon asymmetry through radiative corrections to the electroweak Lagrangian [31].

Probing the existence of these Majorana neutrinos is the goal of the neutrinoless double beta-decay experiments, as discussed in Chapter 2.

1.4 Neutrino oscillations

As seen in Section 1.3, they are several ways to generate neutrinos masses. The development of many of these mechanisms had been triggered and supported by the observation of a phenomenon only possible in case of massive neutrinos: neutrino oscillation. In this section, we start by reviewing the theory of neutrino mixing, we then compute the oscillation probability, observable of the oscillation and finally study a useful simplification with a practical case: the 2-neutrino approximation. The last part will be devoted to the case of oscillations in matter, relevant for both solar and supernova neutrinos.

1.4.1 Neutrino mixing

The phenomenon of neutrino oscillations can, to first order, be explained with quantum mechanics only, without looking into the details of the Standard Model. One has to keep in mind that, while being very efficient and precise, this approximation relies on considering planar waves instead of wavepackets thus neglecting coherence issues. A more detailed derivation of the oscillation formalism from the Standard Model interaction Lagrangians with the use of wavepackets can be found in [32].

Since neutrinos are massive particles, the weak eigenstates ν_α with $\alpha = e, \mu, \tau$ the neutrino flavor are not identical to the mass eigenstates ν_k with $k = 1, 2, 3$. Similarly to the quarks connected by the CKM matrix, these eigenstates are connected by a 3×3 complex unitary matrix called the Pontecorvo-Maki-Nakagawa-Sakata (PMNS) matrix such that:

$$|\nu_\alpha\rangle = \sum_k U^*_{\alpha,k} |\nu_k\rangle \quad \text{or} \quad \begin{pmatrix} \nu_e \\ \nu_\mu \\ \nu_\tau \end{pmatrix} = U_{\text{PMNS}} \begin{pmatrix} \nu_1 \\ \nu_2 \\ \nu_3 \end{pmatrix} \tag{1.23}$$

Similarly to the CKM matrix in the quark sector, one can parametrize the PMNS matrix using 3 mixing angles θ_{ij} and a CP-violation phase δ. Using this parametrization, one can

factorize the PMNS matrix into 3 independent matrices, each one corresponding to a θ_{ij} angle such as:

$$U_{\text{PMNS}} = \begin{pmatrix} 1 & 0 & 0 \\ 0 & c_{23} & s_{23} \\ 0 & -s_{23} & c_{23} \end{pmatrix} \begin{pmatrix} c_{13} & 0 & s_{13}e^{-i\delta} \\ 0 & 1 & 0 \\ -s_{13}e^{i\delta} & 0 & c_{13} \end{pmatrix} \begin{pmatrix} c_{12} & s_{12} & 0 \\ -s_{12} & c_{12} & 0 \\ 0 & 0 & 1 \end{pmatrix} \tag{1.24}$$

using $c_{ij} = \cos\theta_{ij}$ and $s_{ij} = \sin\theta_{ij}$.

A more general expression would be:

$$U_{\text{PMNS}} = \begin{pmatrix} c_{12}c_{13} & s_{12}c_{13} & s_{13}e^{-i\delta} \\ -s_{12}c_{23} - c_{12}s_{23}s_{13}e^{i\delta} & c_{12}c_{23} - s_{12}s_{23}s_{13}e^{i\delta} & s_{23}c_{13} \\ s_{12}s_{23} - c_{12}s_{23}s_{13}e^{i\delta} & -c_{12}s_{23} - s_{12}c_{23}s_{13}e^{i\delta} & c_{23}c_{13} \end{pmatrix} \tag{1.25}$$

A graphical illustration of the θ_{ij} elements of the PMNS matrix is shown in Figure 1.3.

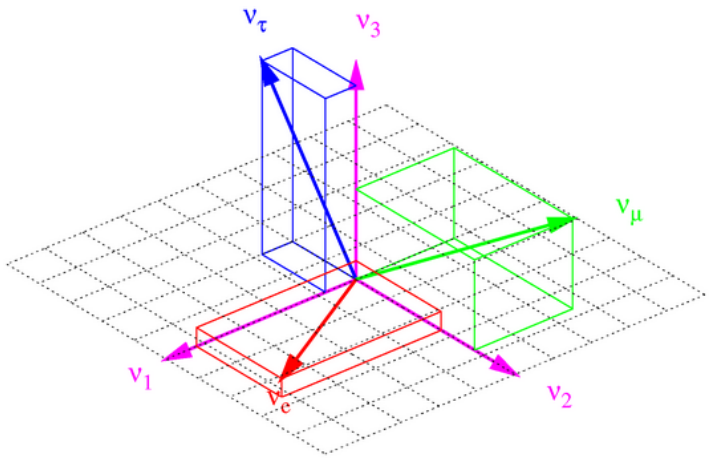

Figure 1.3: Representation of the U_{PMNS} elements linking the mass and flavor eigenstates. The values of the angles are realistic but not at the exact scale and the CP-violation phase is ignored [33].

As stated in Section 1.1, each one of these three matrices corresponds to an oscillation domain. The first one, driven by the θ_{23} angle, is the "atmospheric" term since it was first observed with atmospheric experiments. Similarly, the second and third matrices, respectively driven by θ_{13} and θ_{12} are the "reactor" and "solar" terms of the PMNS matrix.

Notice that the CP-violation phase δ appears in the reactor term. It is merely a convention and not only θ_{13} but all the mixing angles ought to have non-zero values in order to be able to test the CP violation in the neutrino sector and understand possible neutrino-antineutrino asymmetries.

As stated in Section 1.3, one might consider the Majorana nature of neutrinos. In this case, the identicalness of neutrino and antineutrino leads to the appearance of two additional CP-violation phases α and β (only one in the 2-neutrino oscillation case). The introduction of these phases is done through adding a diagonal matrix to the already existing PMNS matrix

thus giving a mixing matrix of the form:

$$U = U_{\text{PMNS}} \begin{pmatrix} 1 & 0 & 0 \\ 0 & e^{i\alpha} & 0 \\ 0 & 0 & e^{i\beta} \end{pmatrix} \tag{1.26}$$

Flavor oscillations experiments are not sensitive to these phases thus for simplicity reasons, they will not appear in the following calculations.

1.4.2 Oscillation probability

The only way to experimentally observe the mixing of neutrino flavors is to witness the appearance or the disappearance of a flavor while comparing actual data to expectations without oscillations. To do so, one needs to know the probability that one flavor has changed into another. In the following, we will compute this oscillation probability in the general case of a 3-neutrino mixing, using the formalism explained in [34].

This development lies on the fact that neutrinos can be considered as planes waves which, while being an approximation of the computation considering them as wavepackets, leads to the same expression of oscillation probability. Two hypotheses have to be postulated as well:

- Neutrinos are considered ultrarelativistic particles, well justified for light MeV neutrinos[3]. Therefore, the propagation time t is approximated to the distance traveled L, which is a very good approximation for relativistic neutrinos
- All mass eigenstates have similar momenta

The first hypothesis seems fairly reasonable since the supposed neutrino mass ($\lesssim$ 1 eV) is much smaller than the typical energy of the detected neutrino ($\gtrsim$ 100 keV) and since ultrarelativistic neutrinos travel nearly at the speed of light.

Within the plane waves approximation, the mass states $|\nu_k\rangle$ are eigenstates of the Hamiltonian $\widehat{H}$ extracted from the time-dependent Schrödinger's equation. Each of these mass eigenstate has an associated energy eigenvalue E_k such as:

$$\widehat{H}|\nu_k\rangle = E_k|\nu_k\rangle, \tag{1.27}$$

with $E_k = \sqrt{\overrightarrow{p_k}^2 + m_k^2}$.

The time and space evolution of the ν_k neutrino mass states is described by the Dirac equation which has for solution:

$$|\nu_k(x,t)\rangle = e^{-i(E_k t - p_k x)}|\nu_k(x,t)\rangle \tag{1.28}$$

Let us consider a neutrino in a flavor state $|\nu_\alpha(x,t)\rangle$ created at the initial condition, $t = 0$ and $x = 0$. After injecting the expression of the mass state $\widehat{H}|\nu_k(x,t)\rangle$ found in Eq. 1.28 into the expression of the flavor state with respect to the mass states found in Eq. 1.23, the time and space evolution of the flavor state appears as:

$$|\nu_\alpha(x,t)\rangle = \sum_k U^*_{\alpha,k} e^{-i(E_k t - p_k x)}|\nu_k(x,t)\rangle \tag{1.29}$$

[3]Very low energy neutrinos, such as relic neutrinos from the cosmic neutrino background [35], are expected to be non relativistic.

Using the unitarity of the mixing matrix:

$$\sum_k U^*_{\alpha,k} U_{\alpha,j} = \delta_{j,k}, \tag{1.30}$$

one can invert Eq. 1.23 and express the mass states as a function of the flavor states:

$$|\nu_k\rangle = \sum_k U_{\alpha,k} |\nu_\alpha\rangle \tag{1.31}$$

After substituting this last equation into the flavor state expression in Eq. 1.29, the evolution of the flavor state becomes:

$$|\nu_\alpha(x,t)\rangle = \sum_\beta \left(\sum_k U^*_{\alpha,k} e^{-i(E_k t - p_k x)} U_{\beta,k} \right) |\nu_\beta\rangle, \tag{1.32}$$

with $\beta = e, \mu, \tau$.

Consequently, while it was a pure flavor state $|\nu_\alpha\rangle$ at $t = 0$, the $|\nu_\alpha(x,t)\rangle$ neutrino state becomes a superposition of different flavor states a $t > 0$. It is worth noting that, since we approximated the travel time with the distance, the neutrino state and its flavor composition now depends on the distance traveled by the neutrino.

From this equation, one can compute the probability of detecting a neutrino, originally producing in a ν_α flavor state, in a ν_β flavor state after traveling a time t and a distance x. This probability is given by the squared amplitude of the $\nu_\alpha \to \nu_\beta$ transition as a function of time:

$$P_{\nu_\alpha \to \nu_\beta}(x,t) = |\langle \nu_\beta | \nu_\alpha \rangle|^2 = |\sum_k U^*_{\alpha,k} e^{-i(E_k t - p_k x)} U_{\beta,k}|^2 \tag{1.33}$$

Considering $t = x = L$ and $E = p$ for ultrarelativistic neutrinos, one can express the phase term as:

$$E_k t - p_k x = (E_k - p_k) L = \frac{E_k^2 - p_k^2}{E_k + p_k} L = \frac{m_k^2}{E_k + p_k} L, \tag{1.34}$$

and by approximating the energy-momentum relation such as:

$$E_k = \sqrt{\overrightarrow{p}^2 + m_k^2} \simeq E + \frac{m_k^2}{2E}, \tag{1.35}$$

one can express the phase as a function of the neutrino mass, the propagation distance and the energy of the neutrino:

$$\frac{m_k^2}{2E} L \tag{1.36}$$

Inserting this expression for the phase in Eq. 1.33 gives the general expression of the oscillation probability between the α and β flavors:

$$P_{\nu_\alpha \to \nu_\beta}(L,E) = \sum_{k,j} U^*_{\alpha,k} U_{\beta,k} U_{\alpha,j} U^*_{\beta,j} e^{-i \frac{\Delta m^2_{kj} L}{2E}} \tag{1.37}$$

The oscillatory behavior shown in Eq. 1.37 leads to define an oscillation length:

$$L^{osc}_{kj} = \frac{4\pi E}{\Delta m^2_{kj}} \frac{\hbar}{c^3}, \tag{1.38}$$

which is the distance at which the phase becomes equal to 2π. Note that, for simplicity reasons, in the following the equality $\hbar = c = 1$ will be assumed. In order to achieve a maximum of oscillation, L_{kj}^{osc} has to be carefully tuned.

Note that Eq. 1.37 satisfies the conservation of probabilities which means that:

- The sum of the probabilities of oscillation from a flavor ν_α to all the flavors ν_β is equal to 1:

$$\sum_{\beta} P_{\nu_\alpha \to \nu_\beta}(L, E) = 1 \tag{1.39}$$

- The sum of the probabilities of oscillation of all flavors ν_α to a flavor ν_β is equal to 1:

$$\sum_{\alpha} P_{\nu_\alpha \to \nu_\beta}(L, E) = 1 \tag{1.40}$$

The combination of U_{PMNS} terms in Eq. 1.37 represents the amplitude of the oscillation between the α and β flavors. This amplitude, which is the fraction of ν_α neutrinos that oscillated into ν_β neutrinos, depends on the PMNS matrix elements associated to each flavor and is therefore a function of the mixing angles θ_{12}, θ_{23} and θ_{13}.

1.4.3 The 2-neutrino practical case

In order to understand the previous derivation of the oscillation probability, we will now use a 2-neutrino framework to simplify the calculations. Note that this approximation, however simplistic, remains valid to a level satisfactory enough for most of the experiments looking for neutrino oscillations.

This framework consists of only two neutrino flavors ν_e and ν_μ, two neutrino mass states ν_1 and ν_2 and a 2×2 PMNS matrix parametrized by a single mixing angle θ such that:

$$\begin{pmatrix} \nu_e \\ \nu_\mu \end{pmatrix} = \begin{pmatrix} \cos\theta & \sin\theta \\ -\sin\theta & \cos\theta \end{pmatrix} \begin{pmatrix} \nu_1 \\ \nu_2 \end{pmatrix} \tag{1.41}$$

From Eq. 1.37, we can derive the oscillation probability in a 2-neutrino case:

$$P_{\nu_e \to \nu_\mu}(L, E) = \sin^2 2\theta \sin^2 \left(\frac{\Delta m^2 L}{2E} \right) \tag{1.42}$$

where $\Delta m^2 = m_2^2 - m_1^2$ is the squared mass difference between the ν_1 and ν_2 mass state, E is the energy of the neutrino and L is the distance it traveled from its generation point to its detection point.

Note that these parameters are responsible for the oscillatory behavior of the probability while the amplitude depends only on the mixing angle θ. The notation commonly used to express this mixing angle is thus $\sin^2 2\theta$ instead of only θ. This notation will then be used in the following thesis.

Eq. 1.42 is expressed by default in SI units, with $\hbar = c = 1$. However, for the following studies, one might appreciate to see it expressed in units more suited for nuclear and particle physics. It thus becomes:

$$P_{\nu_e \to \nu_\mu}(L, E) = \sin^2 2\theta \sin^2 \left(1.27 \frac{\Delta m^2[\text{eV}^2] \times L[\text{m}]}{E[\text{MeV}]} \right) \tag{1.43}$$

As stated earlier in the general case, the 2-neutrino oscillation must satisfy the conservation of probability as well: $P_{\nu_e \to \nu_\mu} + P_{\nu_e \to \nu_e} = 1$

From this equality, one can extract $P_{\nu_e \to \nu_e}$, the survival probability of a ν_e expressed as:

$$P_{\nu_e \to \nu_e}(L, E) = 1 - \sin^2 2\theta \sin^2 \left(1.27 \frac{\Delta m^2[\text{eV}^2] \times L[\text{m}]}{E[\text{MeV}]} \right) \tag{1.44}$$

For low energy neutrinos an oscillation can only be observed through a disappearance experiment, as in Double CHooz, as the creation of leptons heavier than the electron is not kinematically possible.

The 2-flavor approximation, as well as the plane waves approximation, can be used in most cases. However, some experiments are sensitive to another effect that was previously inexistent since we only worked in vacuum: the effect of matter on oscillations.

1.4.4 Oscillations in matter

Given their extremely low interaction cross section, neutrinos are often thought as impervious to matter. Thus, most of the calculations of neutrino oscillations are done in vacuum. However, neutrinos are weakly interacting particles and can interact coherently or incoherently and the rate of these interactions directly depends on the density of electrons in the medium. In high-density matter such as a stellar medium, neutrinos can undergo interactions that alter their propagation.

In 1978, L. Wolfenstein [36] discovered that when propagating through matter neutrinos were subject to a potential due to their coherent forward scattering interactions off electrons and nucleons of the medium. This potential, equivalent to an index of refraction and dependent on the density of the medium, has an effect on neutrinos oscillations and can induce a large effective mixing angle in matter even if the mixing angle in vacuum is small.

In 1985, S.P Mikheev and A. Yu. Smirnov [37, 38] discovered the existence of resonant flavor transitions along the propagation of neutrinos in non-constant density medium. This resonant transition affects the mixing of neutrinos through the so-called Mikheev-Smirnov-Wolfenstein (MSW) mechanism.

In the following we will not attempt to give a full description of the flavor conversion and the MSW mechanism but we will highlight the points that are relevant for the rest of this thesis. For simplicity reasons, the oscillation computations will be done in a 2-neutrino framework unless specified otherwise.

When propagating through matter, neutrinos can interact with the nucleons and electrons via the exchange of $W^{\pm}$ and Z^0 bosons. Since all three flavors are sensitive to neutral currents (NC), these interactions do not lead to the apparition of a specific flavor with respect to another one. On the other hand, only electronic neutrinos can interact coherently via charged currents (CC) since ordinary matter does not consist of muons and taus.

From the effective CC Hamiltonian $\mathcal{H}^{(CC)}$:

$$\mathcal{H}^{(CC)}(x) = \frac{G_F}{\sqrt{2}} \left[\overline{\nu_e}(x)\gamma_\mu \left(1-\gamma_5\right) e(x)\right] \left[\bar{e}(x)\gamma^\mu \left(1-\gamma_5\right) \nu_e(x)\right], \tag{1.45}$$

one can extract the charged current potential V_{CC}:

$$V_{CC} = \sqrt{2} G_F N_e, \tag{1.46}$$

with G_F the Fermi constant and N_e the electron density of the medium.

Similarly, one can compute the neutral current potential V_{NC}:

$$V_{NC} = -\frac{G_F}{\sqrt{2}} N_n, \tag{1.47}$$

with N_n the neutron density of the medium, since the neutral current potentials of protons and electrons cancel each other.

Combining these two potentials gives the total effective potential of a ν_α neutrino through matter:

$$V_\alpha = V_{CC}\delta_{\alpha e} + V_{NC} = \sqrt{2} G_F \left(N_e \delta_{\alpha e} - \frac{1}{2} N_n\right). \tag{1.48}$$

Note that these potentials are extremely small since:

$$\sqrt{2} G_F \simeq 7.63 \times 10^{-14} \ \frac{\text{eV.cm}^3}{N_A}, \tag{1.49}$$

where $N_A = 6.022 \times 10^{23}$ mol^{-1} is the Avogadro number.

The total Hamiltonian in matter is now expressed as:

$$\mathcal{H} = \mathcal{H}_0 + \mathcal{H}_I \quad \text{with} \quad \mathcal{H}_I|\nu_\alpha\rangle = V_\alpha|\nu_\alpha\rangle, \tag{1.50}$$

a combination of the vacuum and interaction Hamiltonians.

One might introduce a matter basis transforming the matter states into flavor states such as:

$$\begin{pmatrix} \widetilde{\nu}_A \\ \widetilde{\nu}_B \end{pmatrix} = \begin{pmatrix} \cos\widetilde{\theta} & \sin\widetilde{\theta} \\ -\sin\widetilde{\theta} & \cos\widetilde{\theta} \end{pmatrix} \begin{pmatrix} \nu_e \\ \nu_\mu \end{pmatrix}, \tag{1.51}$$

with $\widetilde{\theta}$ the mixing angle in matter, satisfying $\mathcal{H}_I|\widetilde{\nu}_{A,B}\rangle = E_{A,B}|\widetilde{\nu}_{A,B}\rangle$.

By doing so and after tedious computations, Mikheev and Smirnov discovered the existence of a resonance occurring at $\widetilde{\theta} = \pi/4$ where:

$$\frac{\Delta m^2}{2E} \cos 2\theta = \sqrt{2} G_F N_e \tag{1.52}$$

This is the MSW resonance condition where the mixing is maximal and the possibility of total transitions between two flavors is likely to occur. Note that the evolution of the mixing angle θ is dependent on the behavior of the density N_e.

A slow variation of the electron density $N_e(r)$ along the neutrino propagation, in a way that the density seems constant over several oscillation lengths, leads to an adiabatic evolution of the matter eigenstates and a high probability of flavor conversion. On the other hand, a fast density variation leads to a non-adiabatic evolution and a lower conversion probability.

This non-adiabaticity mainly occurs at transitions between two media of different densities such as the Sun structure shells [25] or a supernova shockwave and leads to a conversion of ν_e into other flavors.

Chapter 2

Experimental status of neutrino physics

Now that we've established the basics of neutrino physics phenomenology, we will review its experimental status. This manuscript is mainly focused on neutrino oscillations thus it deals with the current status of the searches for neutrino masses, leptonic CP violation, the current 3-neutrino oscillation framework and sterile light neutrinos. Other topics, such as neutrino magnetic moment [32] or neutrino decay [39], although very interesting will not be covered in the following.

2.1 Neutrino masses

In his letter in which he postulated the existence of the neutrino, Pauli mentioned that its mass should be of the same order of magnitude as the electron mass. Until recently most of the experiments had a sensitivity too low to observe the existence of a non-zero neutrino mass and were thus in agreement with the Standard Model massless neutrinos. This idea was globally accepted before the discovery of flavor oscillations indirectly proved the existence of massive neutrinos. We've established earlier that oscillations were a function of the mass squared differences Δm^2 (but not of the masses themselves). Therefore, absolute neutrino masses will have to be measured otherwise.

2.1.1 Absolute mass measurements

To date, the most sensitive direct method to infer electron neutrino mass is the study of the β^- decay:

$$ {}^{A}_{Z}\mathrm{N} \rightarrow {}^{A}_{Z+1}\mathrm{N} + e^- + \bar{\nu}_e, \tag{2.1} $$

and the detailed observation of the tail of the electron energy spectrum. This method only allows the measurement of the $\bar{\nu}_e$ mass. Experiments based on electron capture (EC) and β^+ decay allow to access the ν_e mass.

In a β^- decay process, the emitted electron and antineutrino share the total energy $\mathcal{Q}_\beta$ released in the reaction. If the $\bar{\nu}_e$ is considered as massless, the electron energy spectrum is maximum at $\mathcal{Q}_\beta$, total energy released in the decay. However, if the $\bar{\nu}_e$ is considered massive

with a mass $m_{\bar{\nu}_e}$, the energy conservation principle lowers the maximum of energy available to the electron to $\mathcal{Q}_\beta - m_{\bar{\nu}_e}$ as seen in Figure 2.1.

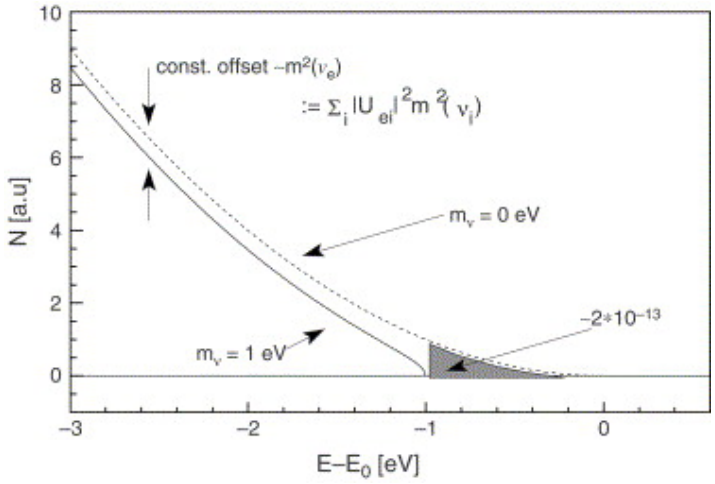

Figure 2.1: Close-up of the β decay spectrum around its endpoint at E_0. The dashed line corresponds to a case with a massless neutrino while the solid line corresponds to a massive neutrino with $m_{\bar{\nu}_e} = 1$ eV [40].

The neutrino mass is postulated to be very small compared to the $\mathcal{Q}_\beta$ of most nuclei and so, the energy shift it induces is seldom detectable with respect to $\mathcal{Q}_\beta$, especially since the latter is not known at the sub-eV scale. One has to study the β decay of a light nucleus, with a small $\mathcal{Q}_\beta$, in order to minimize this difference. In addition, the number of electrons in the spectrum's tail (the gray shaded area of Figure 2.1) directly depends on the smallness of $\mathcal{Q}_\beta$ through $N_{\text{tail}} \propto 1/\mathcal{Q}_\beta^3$. Another key aspect is that, as the spectrum approaches its endpoint, the number of decay electrons tends to decrease drastically. A high β activity is thus necessary to obtain a satisfactory signal over background.

The most used isotope that satisfies these requirements is tritium: ^{3}H. Its β decay:

$$^3\text{H} \rightarrow ^3\text{He} + e^- + \bar{\nu}_e, \tag{2.2}$$

has a low $\mathcal{Q}_\beta$ of 18.6 keV and its short half-life of 12.3 years delivers a sufficient specific activity. Besides, it has a simple electronic structure, simplifying the atomic effect treatment and its β decay is a super-allowed $1/2 \rightarrow 1/2$ transition. For these reasons, tritium is the most widely used isotope in experiments looking for absolute neutrino masses.

Two past experiments, Mainz and Troitsk, performed measurements of the $\bar{\nu}_e$ mass. Their setup were very similar to the one shown in Figure 2.2.

Their results:

$$\begin{aligned} m_{\bar{\nu}_e} &< 2.3 \text{ eV (95 \% CL)} \qquad \text{for Mainz [42]} \\ m_{\bar{\nu}_e} &< 2.05 \text{ eV (95 \% CL)} \qquad \text{for Troisk [43]} \end{aligned} \tag{2.3}$$

are the best direct upper limits obtained on the mass of the electronic antineutrino.

The upcoming KATRIN detector [44], whose structure is shown in Figure 2.2, will provide a better energy resolution and a lower background rate. Its goal is to reach a sensitivity as

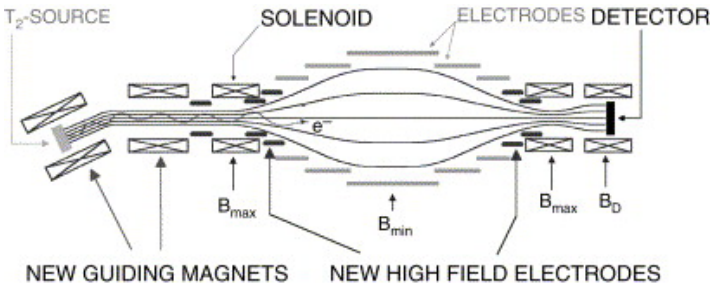

Figure 2.2: Sketch of the KATRIN detector. Electrons are generated from a molecular tritium gas (on the left), they travel through a filter and the spectrometer in order to only detect the most energetic ones with the detector on the far right [41].

low as 0.2 eV (90% CL) after 3 years of data taking, started in 2016.

Note that the mass $m_{\bar{\nu}_e}$ determined in these experiments is an effective mass since, as seen in Section 1.4.1, each neutrino flavor state is a combination of the mass states. This effective mass can be expressed as:

$$m_{\bar{\nu}_e} = \sum_k |U_{ek}|^2 m_k^2 = c_{12}^2 c_{13}^2 m_1^2 + s_{12}^2 c_{13}^2 m_2^2 + s_{13}^2 m_3^2, \tag{2.4}$$

using the mixing angles and masses of the PMNS formalism. Using the upper limits on $m_{\bar{\nu}_e}$ of Eq. 2.3, we obtain:

$$m_{\nu_k} < 2.05 \text{ eV (95 \% CL)}, \tag{2.5}$$

the upper limit on the mass eigenstates $m_k,\ k = 1, 2, 3$.

Tritium β decay experiments are only sensitive to the $\bar{\nu}_e$ mass but what of the ν_μ and ν_τ masses ? In laboratories, muon and tau neutrinos are usually man-made using accelerators. The decay of heavy particles, such as pions, kaons and taus, is carefully analyzed and the momenta and energy of the secondary neutrinos, invisible in the detectors, is obtained from the detection of the other secondary particles.

The kinematic analysis of the pion decay:

$$\pi^+ \rightarrow \mu^+ + \nu_\mu \tag{2.6}$$

and the tau decays:

$$\tau^- \rightarrow 2\pi^- + \pi^+ + \nu_\tau, \tag{2.7}$$
$$\tau^- \rightarrow 3\pi^- + 2\pi^+ + \nu_\tau(+\pi^0), \tag{2.8}$$

gave the following upper limits [45, 46]:

$$\begin{aligned} m_{\nu_\mu} &< 170 \text{ keV (90 \% CL)} \\ m_{\nu_\tau} &< 18.2 \text{ MeV (95 \% CL)} \end{aligned} \tag{2.9}$$

One might measure the neutrino mass by measuring its time of flight and energy. Given their ultrarelativistic nature, it is only possible to measure it through space using powerful neutrino generators also acting as triggers. By emitting light as well as neutrinos, supernovae

seem the ideal candidates. Observations from SN1987A [40] gave an upper limit of 5.7 eV on the neutrino mass without being able to distinguish between flavors. This method is rather disfavored since galactic supernovae are too rare and not enough understood to reach the limits set by β decay experiments.

Last but not least, recent results from cosmology have been setting very stringent limits on the total neutrino mass (summed over all three flavors). The measurement of the Lyα forest power spectrum combined with Baryonic Acoustic Oscillations (BAO) results and Cosmic Microwave Background (CMB) data set an upper limit [47]:

$$\sum m_\nu \ < \ 0.14 \text{ eV (95\% C.L.).} \tag{2.10}$$

2.1.2 Mass hierarchy

The limit of 2.05 eV set on the effective $\bar{\nu}_e$ mass by the Mainz experiment is insufficient to order the mass eigenstates by increasing order. Their sensitivity to the squared masses differences Δm^2_{ij} gives flavor oscillations experiments the possibility to place these masses on a relative scale. However due to the sign uncertainty, the absolute scale of the mass ordering is still unknown and two orderings are currently possible. By convention, these orderings are called "normal" and "inverted" mass hierarchies. The normal hierarchy states that the neutrino masses m_k are increasing with k so that $m_1 < m_2 < m_3$ while the inverted hierarchy postulates m_3 is the smallest mass thus leading to $m_3 < m_1 < m_2$. Considering $m_1 < m_2$ as the "solar" pair of neutrino mass states and m_3 as the "isolated" neutrino mass state, one can understand the determination of the mass hierarchy as the ordering between m_3 and m_1, m_2 A more comprehensive sketch of those hierarchies is displayed on Figure 2.3.

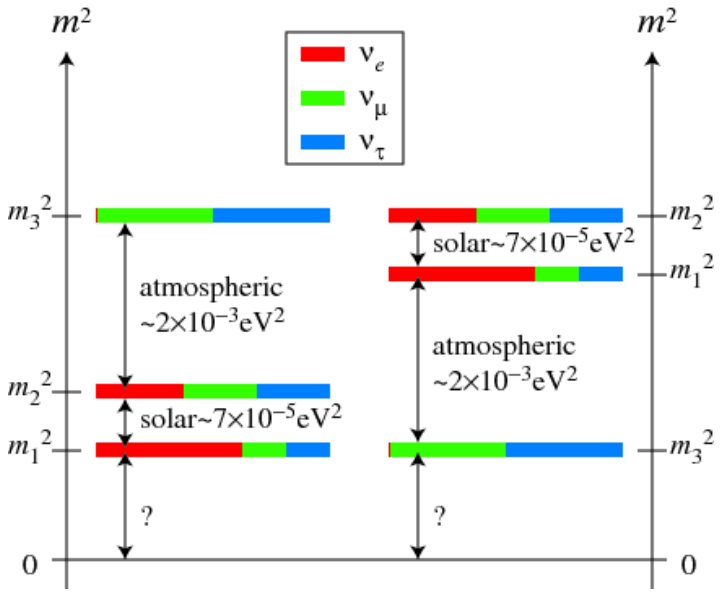

Figure 2.3: Ordering of the neutrino masses in the case of a normal (left) or an inverted (right) hierarchy. The flavor content of each mass state is up to scale and depends on the parameters of the PMNS matrix [48].

The current status of the search for mass hierarchy is such that we know the absolute

value of the squared masses differences Δm^2_{12} and Δm^2_{23} . However the sign of Δm^2_{23} is still unknown therefore it is impossible to distinguish the normal ($m_2 < m_3$) from the inverted ($m_2 > m_3$) hierarchies. The sign of Δm^2_{23} can only be obtained through matter effects as it has been done for Δm^2_{12} in the solar sector. More details about the experimental determination of these parameters will be given in Section 2.2.

2.1.3 Double beta decay

The double β decay is a known process proposed in 1935 by M. Goeppert-Mayer [49] and characterized by the decay of a ${}^A_Z$X nucleus with A nucleons and Z protons into a ${}^A_{Z+2}$X nucleus still with A nucleons but Z+2 protons such as:

$$ {}^A_Z\mathrm{X} \rightarrow {}^A_{Z+2}\,\mathrm{X} + 2e^- + 2\bar{\nu}_e \qquad (2\nu2\beta) \tag{2.11}$$

Unlike two consecutive β decays, this process leads to the simultaneous emission of two electrons and two antineutrinos. It has been successfully observed in several experiments using different isotopes, such as ^{76}Ge, ^{100}Mo, ^{150}Nd, etc...

The neutrinoless double β decay ($0\nu2\beta$), proposed in 1939 by W.H. Furry [50] is similar to a regular double β decay ($2\nu2\beta$) with the exception that the final state does not include neutrinos:

$$ {}^A_Z\mathrm{X} \rightarrow {}^A_{Z+2}\,\mathrm{X} + 2e^- \qquad (0\nu2\beta) \tag{2.12}$$

Such a process violates the lepton number conservation and is forbidden in the Standard Model. However, it becomes an allowed process if the neutrinos are massive Majorana particles (*c.f.* Section 1.3). The absence of neutrinos in the final state would come from the absorption of the β decay emitted right-handed $\bar{\nu}_e$ as a left-handed ν_e. A sketch of the $2\nu2\beta$ and $0\nu2\beta$ decays is shown in Figure 2.4.

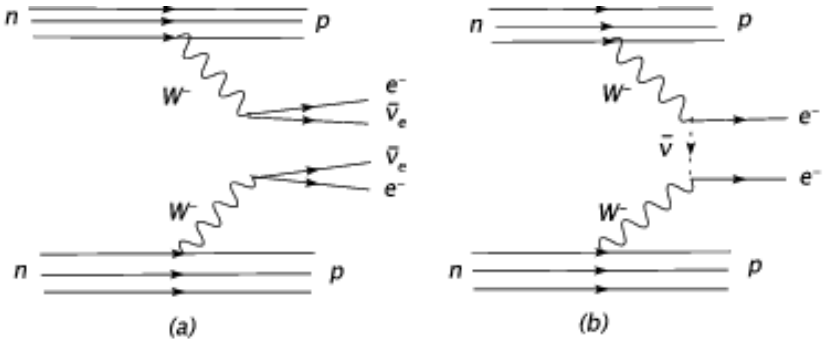

Figure 2.4: Feynmann diagrams of the $2\nu2\beta$ (left) and $0\nu2\beta$ (right) decays. Due to the Majorana assumption $\bar{\nu}_R = \nu_L$, the neutrino is re-absorbed in a $0\nu2\beta$ process [51].

The discovery potential in neutrino physics that the observation of the $0\nu2\beta$ decay could deliver is considerable and would prove the Majorana nature of neutrinos, the existence of lepton number violating processes and set strong constraints on the neutrino mass. Several experiments across the globe have therefore been designed to detect it. Most of these experiments are direct detection experiments that aim at measuring the energies of the electrons emitting in a double β decay. Since the $2\nu2\beta$ decay leads to a multiple body final state (nucleus, electrons, neutrinos), the sum energy carried by the electrons follows a distribution

with a maximum corresponding to the $\mathcal{Q}_\beta$ of the decay. On the other hand, the $0\nu2\beta$ decay gives a 2-body final state thus the summed energy carried by the electrons is supposed to be a Dirac distribution at $\mathcal{Q}_\beta$. Excellent energy resolution and very low background rates are mandatory requirements for these experiments.

From nuclear physics, the half-life of the $0\nu2\beta$ decay of a given nucleus can be computed [32]:

$$\left(\mathcal{T}_{1/2}^{0\nu2\beta}\right)^{-1} = G_{0\nu}|\mathcal{M}_{0\nu}|^2 \frac{|m_{2\beta}|^2}{m_e^2}, \tag{2.13}$$

where $G_{0\nu}$ and $\mathcal{M}_{0\nu}$ are, respectively, the nuclear matrix element and the phase factor and $m_{2\beta}$ is the effective Majorana mass.

This effective mass $m_{2\beta}$ can be expressed as a function of the mixing parameters:

$$m_{2\beta}^2 = c_{12}^2 c_{13}^2 m_1^2 + s_{12}^2 c_{13}^2 e^{i\beta} m_2^2 + s_{13}^2 e^{i\alpha} m_3^2 \tag{2.14}$$

with $e^{i\alpha}$ and $e^{i\beta}$, the two Majorana phases that have to be added to the PMNS matrix in the case a Majorana neutrino.

Past and current experiments only set upper limits on the half-life of the $0\nu2\beta$ decay giving an upper limit on the Majorana effective mass. For instance, the NEMO-3 experiment, by not observing the $0\nu2\beta$ decay of ^{100}Mo obtained $m_{2\beta} < 0.45 - 0.93$ eV [15]. A sub-part of the Heidelberg-Moscow experiment collaboration, using ^{76}Ge, claimed the observation of the $0\nu2\beta$ process leading to an effective Majorana mass determination of $0.2 < m_{2\beta} < 0.6$ eV at the 3σ level [52]. Yet, these results are the subject of a controversy and are often disapproved [53]. Recent results from the GERDA experiment [54] show no indication of this $0\nu2\beta$ signal.

Since it can be expressed as a function of the neutrino masses (*c.f.* Eq. 2.14), the effective Majorana mass carries information about the mass hierarchy and its precise determination could allow the discrimination of one scenario over the other. The favored bands at 3σ for each scenario are shown in Figure 2.5.

2.2 Neutrino oscillations

The flavor oscillation mechanism in the neutrino sector, which theory has been explained in Section 1.4, can be experimentally investigated by looking for the appearance of a flavor or its disappearance. Appearance experiments search for a non-zero probability $P_{\nu_\alpha \to \nu_\beta}$ of a neutrino ν_α oscillating into a neutrino ν_β while disappearance experiments aim at detecting a probability-driven deficit of detected ν_α with respect to the expected number of ν_α.

These two techniques, often complementary, use different sources of neutrinos on a wide scale of energy and at different distances. In order to be the most sensitive to the value of the mixing angle θ_{ij} and the mass difference Δm_{ij}^2 that the experiment aims at measuring, the propagation distance L and the energy E of the neutrino have to be carefully selected. As seen earlier in the calculation of the oscillation probability in the 2-neutrino case (*c.f.* Eq. 1.43), the amplitude and frequency of the oscillation are respectively determined by the value of the mixing angle and the mass difference. Since the mass difference remains a constant, the probability oscillation is a function of the ratio of the propagation length and the energy,

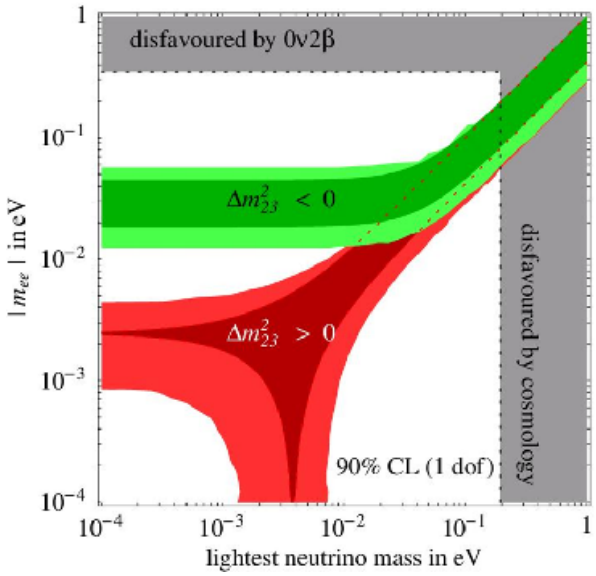

Figure 2.5: Absolute value of the effective Majorana mass as a function of the lightest neutrino mass. The red band corresponds to the normal hierarchy where $\Delta m^2_{23} > 0$ and m_1 is the lightest neutrino while the green band corresponds to the inverted hierarchy where $\Delta m^2_{23} < 0$ and m_3 is the lightest neutrino. Note that if the mass of the lightest neutrino is too large ($\gtrsim 0.1$ eV), the $0\nu2\beta$ decay looses its discrimination power with respect to the mass hierarchy determination [51].

L/E. Tuning this ratio with respect to Δm^2 is necessary to increase the sensitivity of the experiment.

From Eq. 1.44, the first minimum of survival probability in a 2-neutrino case, where the oscillation is the strongest, corresponds to a phase of $\pi/2$ leading to a ratio $L/E = 1/\Delta m^2$.

Three cases can then be considered:

- $L/E \ll 1/\Delta m^2$: it corresponds to $L \ll L_{osc}$, the oscillations are not developed yet and no appearance ($P_{\nu_\alpha \to \nu_\beta} = 0$) or disappearance ($P_{\nu_\alpha \to \nu_\alpha} = 1$) is observed;

- $L/E \gg 1/\Delta m^2$: it corresponds to $L \gg L_{osc}$, many oscillations already happened and the L/E pattern cannot be resolved by a detector with a finite energy and vertex resolution. The oscillation probability is averaged such that $\langle P_{\nu_\alpha \to \nu_\alpha} \rangle = \frac{1}{2} \sin^2 2\theta$;

- $L/E \simeq 1/\Delta m^2$: the optimal region to observe the oscillations since it is close to the first maximum of amplitude around $L \sim L_{\text{osc}}/2$.

Depending on the values of the Δm^2 their oscillations is driven by, oscillations experiments use neutrinos on a wide energy range and separate their sources from their detectors from a few meters to several thousand kilometers (millions for the Sun). This source-detector distance will be called "baseline" in the following. Accelerators-based experiments using GeV neutrinos often use baselines of several hundred kilometers while reactor-based experiments using MeV neutrinos typically use baselines of the order of the kilometer. Note that in order to be sensitive to another Δm^2, the baseline of these experiments can be varied while the neutrino energy remains constant and reciprocally.

2.2.1 Oscillation framework

The data collected by the observation of neutrino oscillations in solar, atmospheric, accelerator and reactor experiments are rather well-fitted by the three-neutrino mixing framework explained in Section 1.4, with the exception of a few anomalies. The three mixing angles have now been determined as well as the two squared mass differences. With the exception of the Majorana phase, not accessible through oscillations, only the CP violation phase is the parameter of the PMNS matrix that has yet to be discovered. Its measurement as well as the determination of the mass hierarchy will yield to a complete parametrization of the neutrino oscillation phenomenon.

Solar neutrinos

Like all stars, the Sun creates its energy via nuclear fusion processes. In the Standard Sun Model (SSM), the energy production is ruled by two processes: the p-p chain and CNO cycle. These processes are cascades of nuclear reactions leading to the creation of energy and fusion products. Among these reactions, several generate electron neutrinos with discrete or continuous energies of the order of 1 MeV, that are displayed on Figure 2.6.

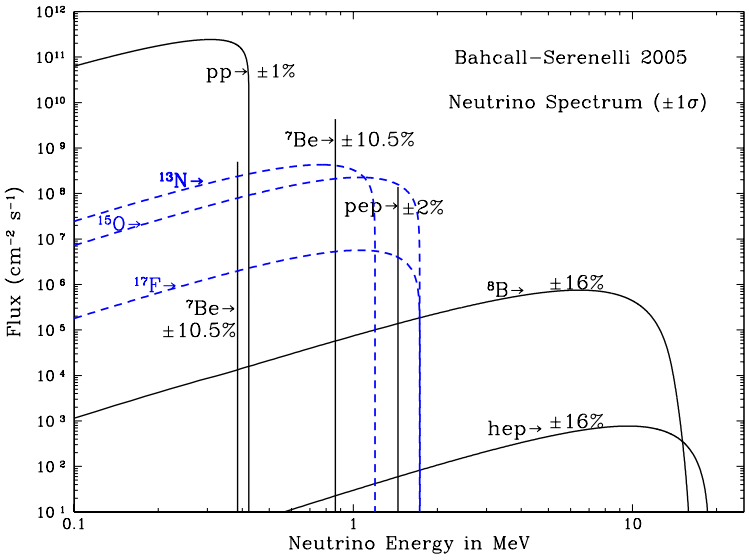

Figure 2.6: Energy spectrum of the neutrino fluxes originated from the p-p and CNO chains predicted by the SSM. The discrete or continuous nature of the spectra depends on the final state of the original reaction [55].

The Davis' Homestake experiment [18], started in 1968, is a radiochemical experiment designed to detect solar ^{8}B electronic neutrinos via the reaction:

$$\nu_e + {}^{37}\mathrm{Cl} \rightarrow {}^{37}\mathrm{Ar} + e^- \tag{2.15}$$

It consisted of a tank filled with 615 tons of perchloro-ethylene (C_2Cl_4) located deep inside the Homestake mine in South Dakota, USA. By extracting the unstable ^{37}Ar and counting them through their decay, it was possible to obtain the solar ν_e flux.

The first data, which have been confirmed and improved after 20 years of data taking [56], indicated a significant deficit of detected neutrinos with respect to the number predicted by the SSM. This was the first evidence for the so-called *solar neutrino problem*.

The Super-Kamiokande detector (SK), described in the next section, measured the solar neutrino flux (mostly from ^{8}B with a hep component) by ν_e-electron elastic scattering: $\nu + e^- \rightarrow \nu + e^-$. The cross section of this scattering, significantly larger than that of the $\nu_{\mu/\tau}$-electron scattering due to the presence of both neutral and charged current scatterings, yields to an elastic scattering rate observed in SK expressed as:

$$\phi_{\text{obs}} = \phi_{\nu_e} + \frac{1}{6.1}\left(\phi_{\nu_\mu} + \phi_{\nu_\tau}\right). \tag{2.16}$$

An oscillation of ν_e towards ν_μ or ν_τ should decrease the observed neutrino rate. This deficit has been observed, thus providing another hint of oscillation.

A few years later, the GALLEX/GNO (GALLium EXperiment [57]/Gallium Neutrino Observatory [58]) and SAGE (Soviet American Gallium Experiment [59]) radiochemical experiments confirmed the observation of this deficit, using a detection principle similar to the Davis experiment, with gallium via the reaction: $\nu_e + ^{71}\text{Ga} \rightarrow ^{71}\text{Ge} + e^-$. This reaction is sensitive to p-p and ^{7}Be ν_e.

The SNO experiment (Sudbury Neutrino Observatory) was the first one to experimentally link this deficit with flavor oscillations [25]. Its design, consisting of a one kiloton tank of heavy water, D_2O, allowed it to detect not only electronic neutrinos, like any other previous experiments, but also the other neutrino flavors via the following processes:

- Charged current (only ^{8}B ν_e sensitive): $\nu_e + d \rightarrow p + p + e^-$
- Neutral current (all $\nu_\alpha (\alpha = e, \mu, \tau)$ sensitive): $\nu_\alpha + d \rightarrow n + p + \nu_\alpha$
- Elastic scattering (all $\nu_\alpha (\alpha = e, \mu, \tau)$ sensitive): $\nu_\alpha + e^- \rightarrow \nu_\alpha + e^-$

The SNO data analysis showed that the rate of detected ν_e is about a third of the expected rate. However, by looking at the neutral current data, the total neutrino flux, all flavor combined, is in agreement with the flux predicted by the SSM. This result proves the conversion of about 2/3 of initial ^{8}B's ν_e into ν_μ and ν_τ. The two SNO results along with the previous experiments results are shown on Figure 2.7. Two regions can satisfy these measurements, the Large Mixing Angle (LMA) solution with $\Delta m^2 \sim 10^{-4}$ eV^2 and the Small Mixing Angle (SMA) solution with $\Delta m^2 \sim 10^{-7}$ eV^2.

The KamLAND detector, located in Japan, confirmed the LMA solution [60] by observing electronic antineutrinos from the surrounding nuclear reactors. With a mean baseline of 180 km, the experiment is sensitive to the so-called solar parameters $\theta_{\text{sol}} = \theta_{12}$ and $\Delta m^2_{\text{sol}} = \Delta m^2_{12}$. When observing solar neutrinos, the baseline is fixed and so large ($\sim 1.5 \times 10^8$ m) that the oscillations are averaged, the experiment is thus only sensitive to the mixing angle θ_{12} driving the amplitude of the oscillations. By having a much smaller baseline, reactor experiments such as KamLAND are sensitive to Δm^2_{12} as well as seen in Figure 2.8.

The combined results of KamLAND and the solar experiments give the set of solar parameters [15]:

$$\sin^2 2\theta_{12} = 0.857^{+0.023}_{-0.025} \quad \text{and} \quad \Delta m^2_{12} = 7.50^{+0.19}_{-0.20} \times 10^{-5} \text{ eV}^2 \tag{2.17}$$

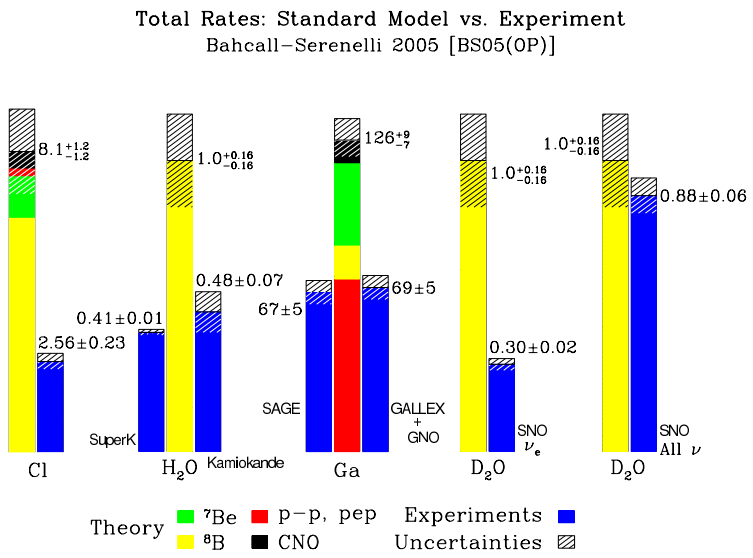

Figure 2.7: Results of the different solar experiments with detected and expected neutrino rates. Only the SNO neutral current analysis, sensitive to all flavors, is in agreement with the theoretical rate [55].

Note that this value of the squared mass difference is too large to explain the solar neutrino problem only by a Δm^2_{12}-driven oscillation[1]. Additional flavor conversion also occurs within the Sun due the MSW effect (*c.f.* Section 1.4.4). This effect led to the determination of the Δm^2_{12} sign since it affects neutrino and antineutrino in a different manner.

Atmospheric neutrinos

The interaction of cosmic rays, mostly consisting of protons, with the nuclei of the high atmosphere creates secondary particles such as pions and kaons. The pion decays:

$$\pi^{\pm} \to \mu^{\pm}\nu_{\mu}(\bar{\nu}_{\mu}), \tag{2.18}$$

along with the kaon decays:

$$\begin{aligned} K^{\pm} &\to \mu^{\pm}\nu_{\mu}(\bar{\nu}_{\mu}) \\ K_L &\to \pi^{\pm}e^{\pm}\nu_e(\bar{\nu}_e), \end{aligned} \tag{2.19}$$

create muons and primary electronic and muonic (anti)neutrinos. These decays are followed by the muon decays:

$$\mu^+ \to e^+\nu_e\bar{\nu}_{\mu} \quad \text{and} \quad \mu^- \to e^-\bar{\nu}_e\nu_{\mu} \tag{2.20}$$

generating secondary electronic and muonic (anti)neutrinos. The combination of these neutrino fluxes is called the atmospheric neutrino flux.

Being generated within the atmosphere, atmospheric neutrinos travel from ∼15 km (produced above the detector at zenith angle $\cos\theta = 1$) to ∼13000 km (produced on the other

[1] In case of vacuum oscillations, with a baseline of 1.5×10^8 m and an energy of 10 MeV, detecting this much of a deficit requires a $\Delta m^2 \sim 10^{-10}$ eV^2.

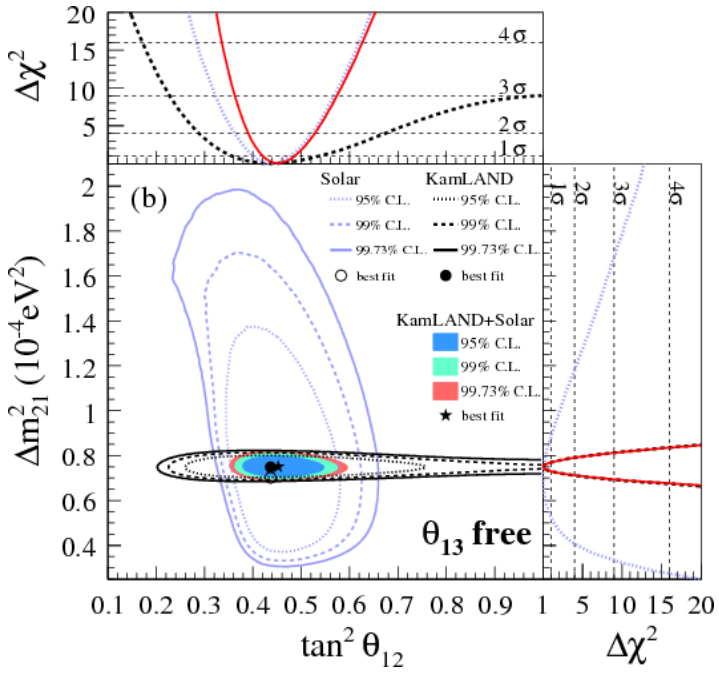

Figure 2.8: Allowed regions in a $(\tan^2\theta_{12}, \Delta m^2_{12})$ plane for the solar and KamLAND data in a 3-neutrino framework. The θ_{13} angle is here a free parameter [61].

side of Earth at zenith angle $\cos\theta = -1$).

From equations 2.18, 2.19 and 2.20, the flavor ratio "μ/e" of the atmospheric flux is close to 2:1 and seems to be constant whatever the zenith angle. However, at large energies, the muons Lorentz boost is high enough for them to reach the Earth surface before decaying. Thus at these energies of several GeV, muons contribute less to the atmospheric flux and the flavor ratio "μ/e" increases. To distinguish between these two domains, the Super-Kamiokande experiment separated their dataset into "sub-GeV" and "multi-GeV" events.

The Super-Kamiokande detector is a 50 kt water Cerenkov detector located in the Kamioka mine in Japan. An inner view of the detector is shown in Figure 2.9. By relying on the charged current detection reaction:

$$\nu_\alpha(\bar{\nu}_\alpha) + N \to \alpha^\pm + X \quad \text{with} \quad \alpha = e, \mu, \tau, \tag{2.21}$$

it is possible to retrieve the direction of the incoming atmospheric neutrino from the direction of the lepton created in the reaction. The deficit of muonic neutrinos with respect to the zenith angle led Super-Kamiokande toward the discovery of an oscillation in the atmospheric sector in 1998. This deficit is shown on Figure 2.10 for ν_e and ν_μ in the sub-GeV and multi-GeV cases. This was the first conclusive proof of neutrino oscillations.

Similarly to the determination of the solar parameters using KamLAND, the atmospheric parameters can be determined using accelerator-based experiments. Indeed, experiments using a beam of ν_μ with typical energy of the order of the GeV and a baseline of several hundred kilometers are sensitive to the atmospheric squared mass difference $\Delta m^2_{\text{atm}} = \Delta m^2_{23}$.

The combined results of accelerator experiments such as MINOS [63] and the atmospheric

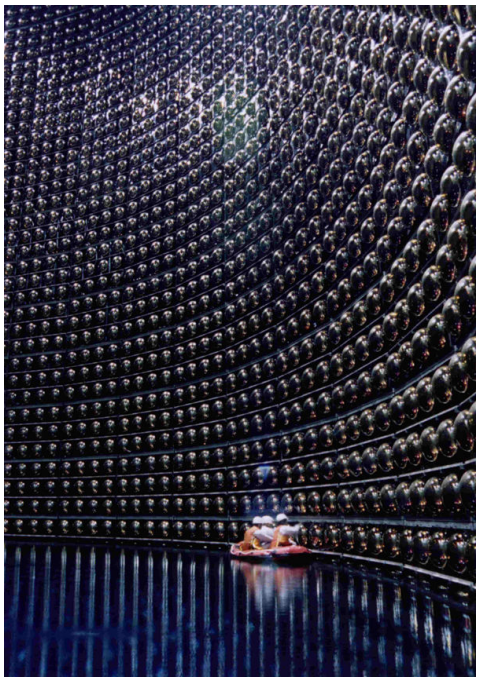

Figure 2.9: The interior of the Super-Kamiokande detector covered with 11,000 photomultiplier tubes and filled with 50 kt of pure water.

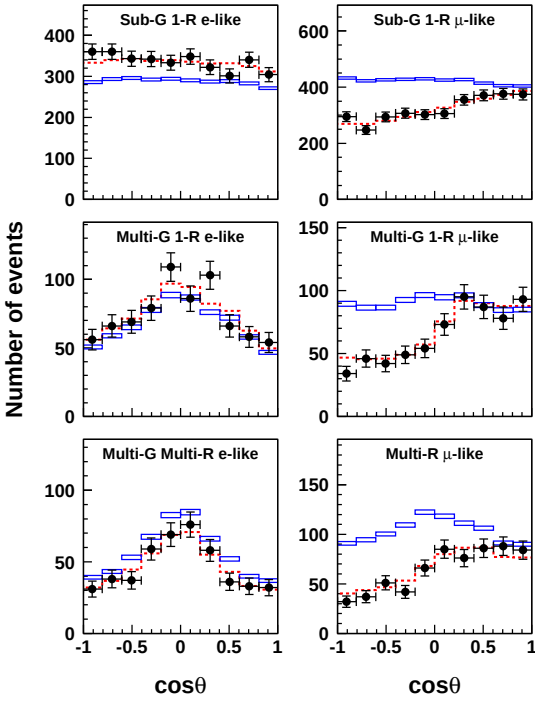

Figure 2.10: Atmospheric results of the Super-Kamiokande I experiment. The solid blue line corresponds to simulated unoscillated Monte-Carlo data, the data points are in black and the best fit to the data points is the dashed red line [62].

experiments gives the set of atmospheric parameters [15]:

$$\sin^2 2\theta_{23} > 0.95 \quad \text{and} \quad |\Delta m^2_{23}| = 2.32^{+0.12}_{-0.08} \times 10^{-3} \text{ eV}^2 \tag{2.22}$$

Unlike solar neutrinos, atmospheric neutrinos undergo relatively weak matter effects within the Earth, therefore the sign of Δm^2_{23} is yet unknown. To be able to be sensitive to these small matter effects, an outstanding energy resolution or a very long baseline are mandatory in order to observe the spectral deformation due to the effective matter Δm^2. Several future experiments such as ORCA [64], PINGU [65], JUNO [66], NOνA [67] and DUNE [68] will be carried out to solve the mass hierarchy puzzle.

Reactor neutrinos

The last PMNS matrix parameter to be measured was the θ_{13} mixing angle. As seen in Section 1.4, a null value of this angle would make the search for a CP-violation in the neutrino sector impossible using neutrino oscillations. The determination of θ_{13} thus besides enhancing our understanding of the oscillation mechanism could allow the search for a possible leptonic CP violation, key ingredient to give credit to many leptogenesis models[2]. It is important to note that, even though in the usual convention θ_{13} is the mixing angle linked to the CP-violation phase, all the mixing angles play a symmetric role in the PMNS matrix and any

[2]Leptogenesis is a process producing an asymmetry between leptons and antileptons (similarly to baryogenesis for baryons) in the very early universe, resulting in the dominance of matter over antimatter.

of them having a null value would lead to the impossibility of determining the CP violation phase using neutrino oscillations.

Long thought to be vanishing or very small, the value of the θ_{13} angle was finally measured in 2012 using electronic antineutrinos generated by nuclear reactors [26, 28, 27]. Indeed, nuclear reactors are the most intense terrestrial sources of neutrinos, created in the β decays of fission products. The physics of nuclear reactors and their generated neutrinos will be explained in more details in Chapter 3.

The study of the solar and atmospheric parameters showed the tininess of the solar mass squared difference Δm^2_{12} with respect to the atmospheric mass squared difference Δm^2_{23}. While technically the reactor mass squared difference Δm^2_{13} exists, it is by convention taken equal to Δm^2_{23}. Thus the reactor neutrino oscillation domain is driven by the atmospheric Δm^2_{23} as well. However the typical energies of reactor antineutrinos is smaller than the one for atmospheric neutrinos, which lowers the distance needed in order to keep the L/E ratio constant and be the most sensitive to the oscillation. With energies of a few MeV, reactor experiments locate their detectors a couple of kilometers away from their neutrino sources, the reactor cores of a nuclear power plant.

In the past, two experiments searched for the θ_{13} mixing angle: the CHOOZ and the Palo Verde experiments.

The CHOOZ experiment took place in the French Ardennes between 1997 and 1998 and used the B1 and B2 cores of the Chooz nuclear power plant as a 8.5 $\mathrm{GW_{th}}$ neutrino source. With a detector located under a hill (300 m.w.e.[3]) 1050 m away from the reactors, it had a rather good sensitivity to θ_{13} although its first purpose was to solve the "atmospheric neutrino anomaly" observed in SK. With an active mass of 5 tons of liquid scintillator doped with gadolinium, the $\bar{\nu}_e$ were detected via the Inverse Beta Decay reaction (*c.f.* Chapter 4):

$$\bar{\nu_e} + p \rightarrow e^+ + n \tag{2.23}$$

. Using $\sim$ 2700 neutrino candidates, the CHOOZ experiment found a ratio of measured to expected $\bar{\nu}_e$ events:

$$R = 1.01 \pm 2.8\%(\text{stat.}) \pm 2.7\%(\text{syst.}). \tag{2.24}$$

This ratio being in agreement with the non-oscillation hypothesis ($\theta_{13} = 0$), they only provided an upper limit at 90 % CL on the value of the last mixing angle [69]:

$$\sin^2 2\theta_{13} < 0.10, \tag{2.25}$$

for a large mass squared difference Δm^2.

The Palo Verde experiment took place between 1998 and 2000 near the 11.6 $\mathrm{GW_{th}}$ Palo Verde Nuclear Generating Station in the Arizona desert. Its detector, located between 750 and 890 m from the three reactor cores was, as in the CHOOZ experiment, consisting of Gd-doped liquid scintillator however segmented in order to reduce the cosmic background rate due to the low overburden of 32 m.w.e.. The ratio of measured to expected $\bar{\nu}_e$ events was found to be:

$$R = 1.01 \pm 2.4\%(\text{stat.}) \pm 5.3\%(\text{syst.}), \tag{2.26}$$

[3]The unit m.w.e. stands for *meter water equivalent* and corresponds to an overburden of one meter of water.

in agreement with the CHOOZ results and the non-oscillation hypothesis. However, due to a larger systematic error, the upper limit set on θ_{13} was less stringent with respect to the CHOOZ bound [70].

Currently, two kinds of experiments are studying the θ_{13} mixing angle: medium baseline reactor experiments and long baseline accelerator experiments.

The denomination "short", "medium" or "long" obviously depends on the length of the experiment's baseline. For reactor experiments, a short baseline is usually less than a hundred meters, a medium baseline ranges from one to several kilometers and a long baseline is bigger than a hundred kilometers. For accelerator-based experiments, the distances are bigger and a short baseline ranges from several hundred meters to a few kilometers while a long baseline is bigger than several hundred kilometers.

There are three medium baseline reactor experiments currently acquiring data: Double Chooz [71], Daya Bay [72] and RENO [73].

The three experiments have a similar design, first proposed by CHOOZ collaborators [74]. The Double Chooz detector design will be presented in details in Chapter 6.

Double Chooz

The Double Chooz experiment takes place at the same site than the previous CHOOZ experiment. Using a similar detection technique, it aims at improving the statistical and systematic uncertainties of its predecessor. The statistical improvement is mainly brought by a longer data taking and a bigger detector with a fiducial mass of about 8 tons. The systematic improvement comes from the addition of a second detector, identical to the first. This second detector called the near detector is located at about 400 m from the reactors and its major purpose is to normalize the antineutrino flux. It measures the un-oscillated antineutrino flux thus giving a reference flux, independent on the knowledge of the reactor neutrino emission, to the far detector.

Using 102 days of data with the far detector only, Double Chooz was the first reactor experiment to find an indication for the disappearance of electronic antineutrinos [26]. This deficit of $\bar{\nu}_e$, if understood as a θ_{13}-driven oscillation, gave the following result for the new mixing angle: $\sin^2 2\theta_{13} = 0.086 \pm 0.041(\text{stat.}) \pm 0.030(\text{syst.})$. A more recent analysis, still with one detector, published in 2014 [75] confirmed this indication: $\sin^2 2\theta_{13} = 0.090^{+0.032}_{-0.029}$. Several results of Double Chooz will be presented in Chapter 6.

Daya Bay

The Daya Bay experiment is located near the two nuclear reactors of the Daya Bay power station and the four reactors of the Ling Ao power station in South China. It mainly differs from the Double Chooz experiment by its size, with 6 nuclear reactors for a total thermal power of 17.4 GWth, 4 near detectors and 4 far detectors. A sketch of the Daya Bay layout in shown in Figure 2.11 (left).

Even though indications were already found by Double Chooz [26] and T2K [76], the Daya Bay experiment is the first to confirm the existence of a non-zero θ_{13} mixing angle at the level of 5σ [28]. Since then, more results have been announced and published, the most precise one being: $\sin^2 2\theta_{13} = 0.084 \pm 0.005$ using a rate and energy spectrum shape analysis [77]. The

energy spectrum is displayed in Figure 2.12 (right).

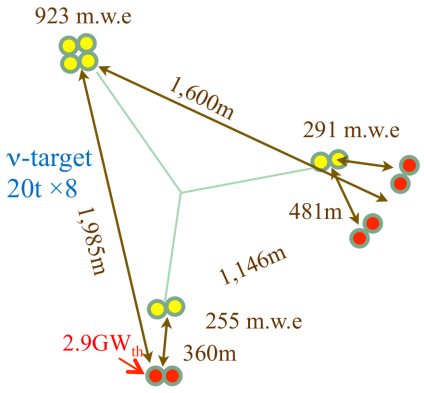

Figure 2.11: Sketch of the Daya Bay experiment layout [78]. The yellow points are detectors and the red points are the reactors.

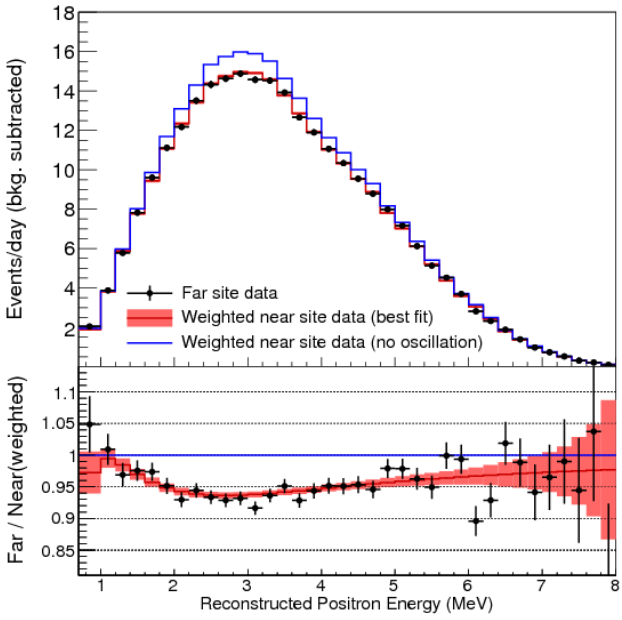

Figure 2.12: Top: Prompt energy spectrum measured by the Daya Bay detectors. The solid blue line is the spectrum measured at the near detectors (Near Halls) while the points are measured at the far detectors (Far Hall). Bottom: Ratio of oscillated over predicted spectra (far over near). The blue line is the no oscillation hypothesis while the solid red line is a best-fit solution corresponding to $\sin^2 2\theta_{13} = 0.084$ [77].

RENO

The RENO experiment is located near the six reactors of the Yonggwang power station in South Korea. Its two detectors are crossing (*c.f.* Figure 2.13 (left)) the line of reactors. This layout implies that the two detectors do not receive the same flux proportions from the reactors. Unlike in the two other experiments where the detectors are placed on isoflux lines, this has to be corrected for in the analysis hence leading to an additional systematic uncertainty. The RENO collaboration released their first results [27] shortly after Daya Bay, excluding the non-oscillation hypothesis at the level of 4.9σ (*c.f.* Figure 2.14 (right)).

Unlike reactor experiments that look for the disappearance of $\bar{\nu}_e$, accelerator-based experiments search for the appearance of the electronic flavor in a muonic neutrino beam. Since neutrino beams have typical energies ranging from several hundreds of MeV to a few GeV, their baselines are significantly bigger than for reactor experiments and can reach several hundred kilometers. This can induce non-negligible matter effects on the oscillation probability.

From the expression of the parametrized PMNS matrix in Eq. 1.24, one can derive the

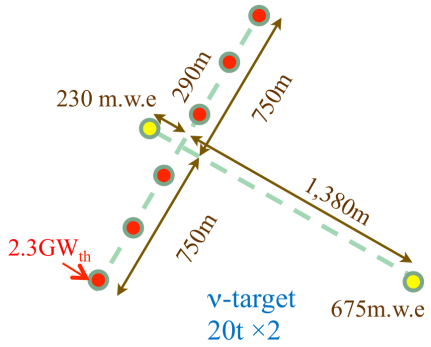

Figure 2.13: Sketch of the RENO experiment layout [78]. The yellow points are detectors and the red points are the reactors.

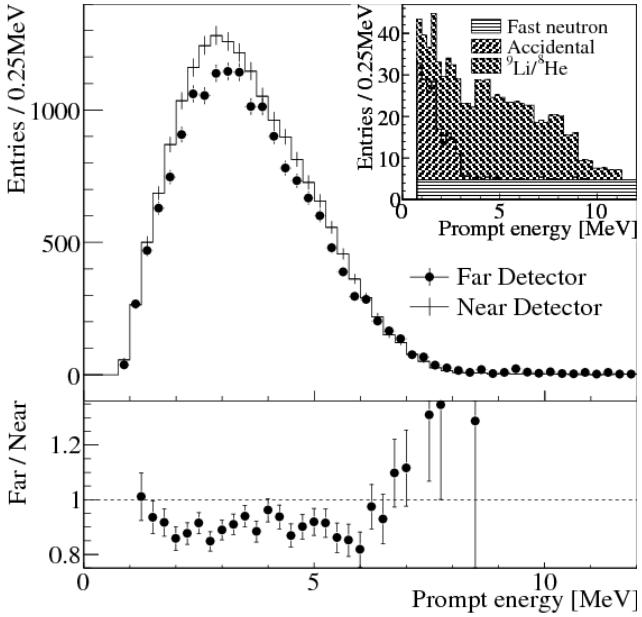

Figure 2.14: Top: Prompt energy spectrum measured by the RENO detectors. The solid line is the spectrum measured at the near detector while the points are measured at the far detector. Bottom: Ratio of oscillated over predicted spectra (far over near). The dashed line is the no oscillation hypothesis [27].

probability of a ν_μ oscillating to a ν_e:

$$P_{\nu_\mu \to \nu_e}(L, E) \simeq \sin^2 2\theta_{13} \sin^2 2\theta_{23} \sin^2 \left(\frac{\Delta^2 m_{13} L}{4E} \right) + \text{CP violation term} + \text{Matter effect term}. \tag{2.27}$$

This probability is therefore sensitive not only to θ_{13} but to θ_{23} and the CP violating phase δ_{CP} as well. The presence of a CP violating term leads to a degeneracy of the θ_{13} mixing angle with respect to δ_{CP}. Only the precise measure of θ_{13} at reactor experiments can remove this degeneracy and may provide some information on the δ_{CP} phase. The presence of a matter effect term also could allow accelerator experiments, with a sufficiently long baseline, to probe the mass hierarchy and determine the sign of Δm^2_{23}.

T2K

The T2K (Tokai to Kamioka) experiment was designed to replace the K2K experiment [79]. Its goals are the precise measurement of θ_{23}-driven ν_μ disappearance as well as the θ_{13}-driven ν_e appearance in a ν_μ beam.

The T2K experiment uses a ν_μ beam produced at the J-PARC accelerator complex in Tokai, Japan. Like all ν_μ beams, it is originated from the decays of pions and kaons generated by the interaction of a powerful proton beam with a target. In J-PARC, the 30 GeV proton beam is send on a graphite target. The secondary pions and kaons are then focused by

magnetic horns, allowing the selection of either ν_μ or $\bar{\nu}_\mu$, and sent in a hundred meter tunnel to decay. The T2K near and far detectors are placed 2.5 degrees off-axis of the neutrino beam. This narrows the neutrino energy spectrum and peaks it at 600 MeV, which enhances the sensitivity to θ_{13} in the far detector located 295 km away while minimizing beam-induced backgrounds (ν_e contamination). The T2K far detector is the Super-Kamiokande detector which is able to discriminate ν_μ from ν_e using the Cerenkov cones patterns, different for electrons and muons.

The T2K collaboration first reported an indication of ν_e appearance in June 2011, using the data acquired between January 2010 and the April 2011 earthquake [76]. Since then they resumed data taking and published enhanced results (*c.f.* Figure 2.15), refuting the $\sin^2 2\theta_{13} = 0$ hypothesis at 7.3σ [80]:

$$\begin{aligned} \sin^2 2\theta_{13} &= 0.140^{+0.038}_{-0.032} \quad \text{(Normal hierarchy)} \\ \sin^2 2\theta_{13} &= 0.170^{+0.045}_{-0.037} \quad \text{(Inverted hierarchy)} \end{aligned} \tag{2.28}$$

These results are valid under the assumptions that $|\Delta m^2_{13}| = 2.4 \times 10^{-3}$ eV^2, $\sin^2 2\theta_{23} = 0.5$ and $\delta_{\rm CP} = 0$. Slightly above the θ_{13} values obtained with reactor experiments, these results might provide an information on the $\delta_{\rm CP}$ phase by means of global fits.

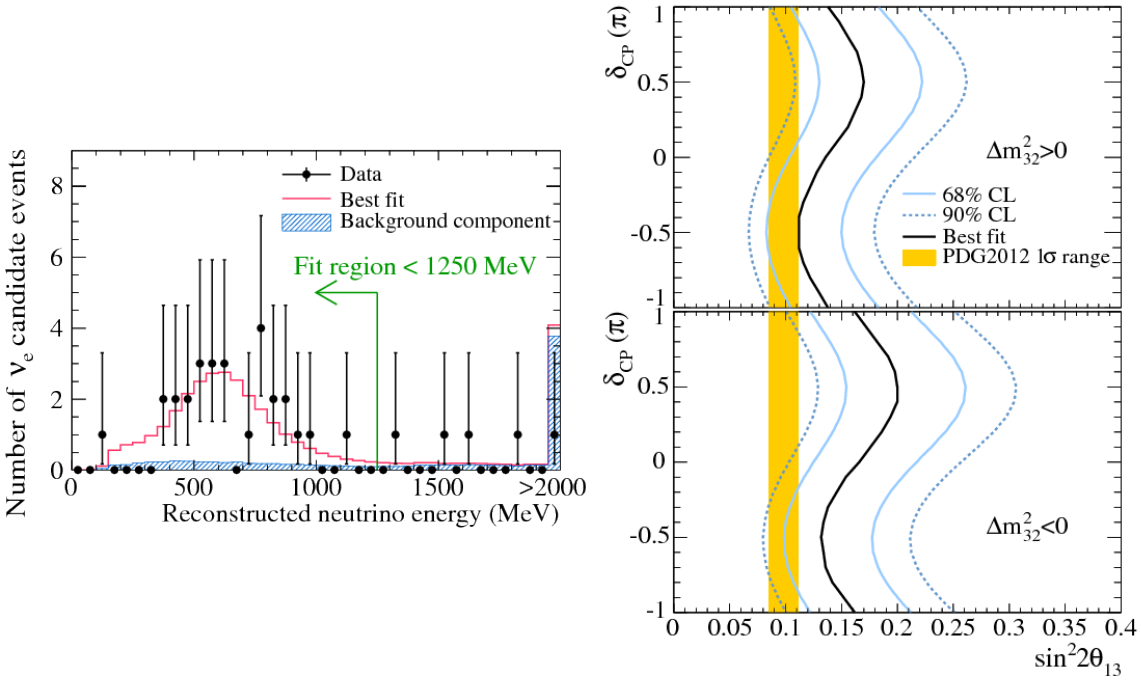

Figure 2.15: Left: Electron neutrino spectrum observed in Super-Kamiokande. 28 candidates are detected while 4.92 ± 0.55 background events are expected. The solid red line is the best-fit with $\sin^2 2\theta_{13} = 0.144$ [80]. Right: The 68% and 90% CL allowed regions for $\sin^2 2\theta_{13}$, as a function of $\delta_{\rm CP}$ assuming normal hierarchy (top) and inverted hierarchy (bottom). The solid line represents the best fit as a function of $\delta_{\rm CP}$. The shaded region shows the average $\sin^2 2\theta_{13}$ value from [15].

MINOS

While its original purpose is the study of the ν_μ disappearance and the precise measurement of the atmospheric parameters θ_{23} and Δm^2_{13} [63], the MINOS experiment (Main Injector Neutrino Oscillation Search) can look for a ν_e appearance as well.

MINOS uses a neutrino beam with an average energy of 3 GeV produced in the NuMI (Neutrino at the Main Injector) complex of Fermilab, USA. The far detector, located in the Soudan mine (Minnesota, USA) 730 km away from Fermilab, consists of 486 magnetized iron plates each separated by strips of solid scintillator for a total mass of 5.4 kt.

The analysis of the full MINOS dataset from February 2005 to April 2012 put in evidence an excess of ν_e [81] such as: $2\sin^2 2\theta_{13}\sin^2\theta_{23} = 0.051^{+0.038}_{-0.030}$ in case of normal hierarchy and $2\sin^2 2\theta_{13}\sin^2\theta_{23} = 0.093^{+0.054}_{-0.049}$ in case of inverted hierarchy. Although of lower significance, these results are in good agreement with T2K's results.

NoνA

The NoνA (NuMI Off-Axis ν_e Appearance experiment) experiment [67] was designed to be the successor of MINOS. Its primary goals are the determination of the mass hierarchy, the $\delta_{\rm CP}$ phase and the precise measurement of the θ_{13} mixing angle. It also aims at improving the precision on Δm^2_{23} by an order of magnitude compared to MINOS. NoνA uses the Fermilab NuMI beam, as MINOS did. However, their detectors are placed off-axis and the baseline has increased to 810 km. The far detector is a 14 kt segmented liquid scintillator detector.

The experiment started acquiring data in September 2013 and is scheduled to run for six years.

2.2.2 Anomalies

While the three-neutrino mixing framework is in agreement with most of the oscillation data, several experiments detected anomalous results. These anomalies found in experiments using different sources and detectors at L/E$\sim$1 m/MeV, could be related to the same physical phenomenon.

Gallium anomaly

The GALLEX and SAGE radiochemical experiments (*c.f.* Section 2.2.1) were designed to detect solar neutrinos. For the sake of understanding the detector response, intense Mega Curie[4] (MCi) ^{51}Cr (for GALLEX and SAGE) and ^{37}Ar ν_e (for SAGE) sources with known activities were deployed at the center of the detectors. Both experiments reported ratios of measured to predicted ^{71}Ge events [82, 83]:

$$\begin{aligned} R^{\rm GALLEX}_{\rm Cr1} = 0.95^{+0.11}_{-0.12} \ \text{ and } \ R^{\rm GALLEX}_{\rm Cr2} = 0.81^{+0.10}_{-0.11} \\ R^{\rm SAGE}_{\rm Cr} = 0.95^{+0.12}_{-0.12} \ \text{ and } \ R^{\rm SAGE}_{\rm Ar} = 0.79^{+0.09}_{-0.10} \end{aligned} \tag{2.29}$$

with an average ratio of:

$$R^{\rm Ga} = 0.86^{+0.05}_{-0.05}. \tag{2.30}$$

This ratio is inconsistent with the prediction R=1 at the 2.7σ level leading to the so-called Gallium anomaly. Recent reanalysis of these data have been carried out [84]. These reinterpretation takes into account new measurements of the Gamow-Teller strengths of the transitions from the ^{71}Ga ground state to the ^{71}Ge excited states. These results confirm the gallium anomaly at the level of 3σ.

[4] 1 MCi = 10^6 Ci = 3.7×10^{16} Bq

Accelerator anomalies

The LSND experiment (Liquid Scintillator Neutrino Detector) was an accelerator-based experiment designed to search for $\bar{\nu}_e$ appearance in a $\bar{\nu}_\mu$ beam [85]. It used the Los Alamos 800 MeV proton beam to generate $\bar{\nu}_\mu$ up to 300 MeV by μ^+ decay at rest. The LSND detector was a cylindrical tank filled with 167 tons of liquid scintillator placed 30 m away from the source. It detected $\bar{\nu}_e$ using the collected scintillating and Cerenkov light deposited by the Inverse beta Decay reaction products. The data collected from 1993 to 1998 indicated evidence for a $\bar{\nu}_\mu \to \bar{\nu}_e$ oscillation at the level of 3.8σ with a total excess of $87.9 \pm 22.4 \pm 6.0$ events, inconsistent with the known parameters of the 3-neutrino mixing.

The MiniBooNE experiment (Mini Booster Neutrino Experiment) was designed to test the LSND anomaly using $\bar{\nu}_\mu$ and ν_μ oscillations [86]. Using a ν_μ ($\bar{\nu}_\mu$) beam produced by the Fermilab Booster accelerator with energies up to 3 GeV and a spherical 800 tons mineral oil detector placed at 500 meters away from the source, MiniBooNE searched for an oscillation in the same L/E range than LSND by increasing both L and E by about an order of magnitude. In neutrino mode [87], the collaboration reported an excess of ν_e events of $83.7 \pm 15.1 \pm 19.3$ events with energies ranging from 300 to 475 MeV. This excess is significant at the level of 3.4σ. In antineutrino mode [88], the 24.7 ± 18.0 $\bar{\nu}_e$ events in excess in the 475 to 3000 MeV range is consistent with the $\bar{\nu}_\mu \to \bar{\nu}_e$ oscillation observed by LSND. A combined analysis [89] recently published showed a total excess of $240.3 \pm 34.5 \pm 52.6$ ν_e and $\bar{\nu}_e$ events, increasing the significance to 3.8σ.

The MicroBooNE experiment will test the origin of the MiniBooNE excess at low energy using the same beam line and a 170 tons liquid argon detector [90].

The Reactor Antineutrino Anomaly

Any reactor antineutrino spectrum is the sum of the β decay spectra of the fission products generated by the four fissioning nuclei (^{235}U,^{238}U,^{239}Pu and ^{241}Pu). Since thousands of different β branches are available to these isotopes with many of them still unknown, a simulation cannot accurately predict the total reactor antineutrino spectrum. It is thus necessary to estimate it by converting the total electron spectrum emitted by nuclear fuel into an antineutrino spectrum using energy conservation laws. Measurements of the total electron spectrum have been carried out at the ILL research reactor [91] and converted into precise reactor antineutrino spectra [92, 93].

Before the near detector started to acquire data, the Double Chooz collaboration could not normalize the flux detected in the far detector. They could only rely on the prediction of the expected flux, based on the ILL electron spectrum conversions. In 2011, T. Mueller *et al.* provided a re-analysis of the reactor antineutrino spectra accounting for the decays of thousands of fission products listed in nuclear databases [94]. Confirmed by an independent analysis [95], this calculation, while leaving the global spectral shape unchanged, re-evaluates the flux by +3.5% with respect to previous computations.

This analysis motivated a re-analysis of the 19 short-baseline (< 100 m) reactor experiments carried out in the past [96]. The corrected ratio of observed to expected events is

displayed on Figure 2.16. It also takes into account the new-estimation of the IBD cross section (depending on the neutron lifetime measurement) and off-equilibrium corrections to the reactor behavior. The latter two also re-evaluates the $\bar{\nu}_e$ flux by +1.5% and +1%, respectively. The combination of these three corrections increases the already existing 1% discrepancy between the observed and the predicted flux, at the level of 7%. The weighted average of the observed to expected ratio of events for the 19 experiments gives a ratio of:

$$R = 0.927 \pm 0.023, \tag{2.31}$$

inconsistent at 3σ with the expected value $R = 1$. This discrepancy is called the "Reactor Antineutrino Anomaly" (RAA).

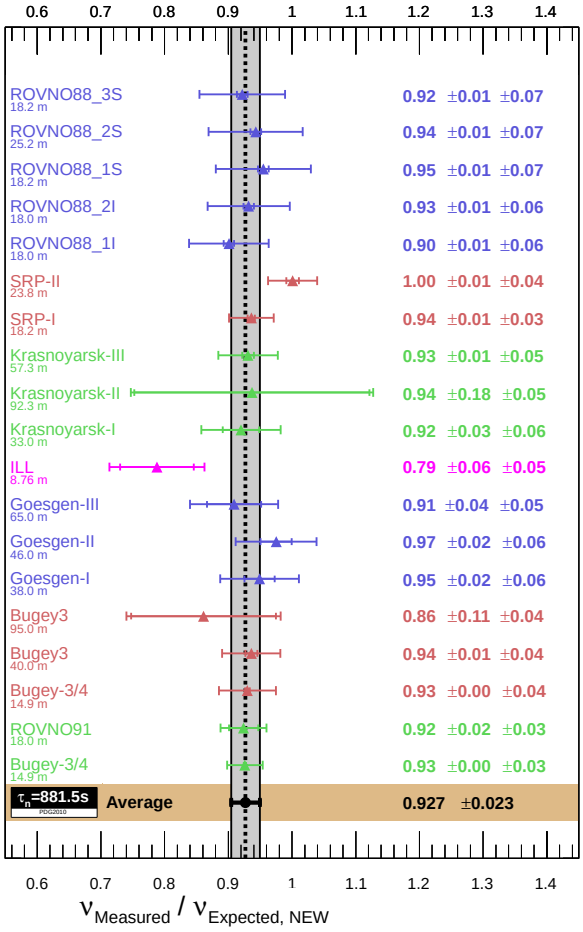

Figure 2.16: Observed to expected event ratio with respect to the baseline for short-baseline reactor experiments. The gray band corresponds to the average fit with uncertainties [96].

2.3 Sterile neutrinos

The anomalies observed in several experiments, without questioning the validity of the three-neutrino framework at first order, encourage physicists to think beyond this model. In the past, anomalies in the neutrino sector were often caused by an oscillation driven by the existence of a new neutrino mixing phenomenon. These new anomalies point toward flavor

oscillations generated by a large squared mass difference between the three current known mass states and hypothetical new mass states. While the hypothesis of new neutrino states seems tremendously attractive for new BSM physics, it is only an explanation among others. These alternative models, such as Lorentz invariance or CPT violation in the neutrino sector and extra-forces, will not be discussed in the following. Only the new neutrino states hypothesis will be considered.
Note that the possible existence of an experimental bias causing the anomalies must not be excluded yet. For instance, the significance of the RAA could be impacted by a recalculation of the reactor flux prediction or a systematic bias on the detectors' calibrations.

2.3.1 Theoretical motivations

The existence of sterile neutrino states is common to many theories beyond the Standard Model. Strictly speaking, a sterile neutrino is a neutral lepton with no ordinary weak interactions except those induced by mixing with active neutrinos. Although they can theoretically be massless, they are often considered massive particles in most see-saw models (*c.f.* Section 1.3.3).

First of all, it may be worth introducing some useful terminology from [97]. The "sterility" can be of two sorts: fully sterile or weakly sterile. A fully sterile lepton feels no gauge interaction of any sort, including hypothetical BSM interactions. A weakly sterile lepton, on the other hand, feels no Standard Model gauge interaction (strong, electromagnetic or weak) but may interact via hypothetical BSM mechanisms.

Note that in any case, sterile or not, massless or not, it necessarily couples with gravity. The full sterility still allows flavor mixing or Higgs boson exchange given the non-gauge nature of these mechanisms.

As seen in Sections 1.3.1, 1.3.2 and 1.3.3, several Standard Model extensions incorporates additional massive neutrino states in order to generate masses to the active neutrino states.

The existence of right-handed neutrino states, common to these models, provides the most obvious and naive identification of sterile neutrinos. The presence of these right-handed SU(2) singlets would, besides generating neutrino masses, satisfy a left-right similarity (each left-handed fermion has an associated right-handed partner) and a lepton-quark similarity (each quark has an associated lepton with the same chirality). Right-handed neutrinos generating Dirac masses via Yukawa couplings are considered fully sterile in the "Minimal Standard Model". This is hardly the case in most of the BSM theories, these extensions will however not be discussed in the following.

From now on, the "Minimal Standard Model" will refer to the Standard Model extended with the presence of a mechanism generating neutrino masses: the see-saw mechanism. It implies the existence of a right-handed neutrino state as well as Dirac and Majorana mass terms (*c.f.* Sections 1.3.1, 1.3.2 and 1.3.3).

From the expression of the mass Lagrangian in Eq. 1.20 and using the see-saw approximation : $M_L = 0$ and $M_R \gg m_D$, one can derive the full neutrino mass matrix:

$$\mathcal{M}_\nu = \begin{pmatrix} 0 & m_D \\ m_D^T & M_R \end{pmatrix} \tag{2.32}$$

which gives $m_1 = \frac{m_D^2}{M_R}$ and $m_2 = M_R$, eigenvalues respectively associated with the ν_L and ν_R neutrino states. Note that M_R is a $n_R \times n_R$ matrix and can accommodate any n_R, number of sterile neutrino states and masses.

While the left-handed neutrino acquire a mass $m_\nu = \frac{m_D^2}{M_R}$, the right-handed neutrino becomes very massive with $m_{\nu_R} = M_R$. This large right-handed neutrino Majorana mass is often correlated to a high symmetry breaking and its value can range from $\sim 10^{10}$ to $\sim 10^{15}$ GeV (GUT scale) or even to $\sim 10^{19}$ GeV (Planck scale[5]) [98]. This right-handed neutrino state is a very massive sterile neutrino usually called a "heavy neutral lepton". While baryogenesis models have use of such particles [31], they do no play a direct role in neutrino oscillation phenomenology.

There are several models that allow the existence of light sterile neutrino at the eV or keV scale. In what follows, some of these models and the mass range they imply for sterile neutrinos will be quickly described.

The "split see-saw model" [99] consists of the Standard Model extended with three right-handed neutrinos and a spontaneously broken $U(1)_{B-L}$ [6] gauge symmetry. Another assumption is the existence of a scale $M_C = 1/l \sim 10^{16}$ GeV over which the 4-dimensional space-time becomes a 5-dimensional space. The presence of a right-handed neutrino on a brane separated from a standard-model brane by a distance l would mean a small overlap between the two wave functions. This would lead to the suppression of the Yukawa coupling as well as the right-handed neutrino mass while still conserving the validity of the see-saw mechanism.

Because of the huge consequences of the change of the distance l between two branes on the energy scale, the split see-saw model allows the existence of light sterile neutrino in the effective 4-dimension Lagrangian, as long as its heavy progenitor is originally located on a distant brane. This model provides a wide range of hypothetical sterile neutrino masses, depending of the original heavy right-handed mass, the distance l and other 5-dimensional couplings parameters. It is interesting to note that the split see-saw model provides satisfying dark matter candidates with keV-scale sterile neutrinos, the predicted abundance of such particles being in agreement with the current observations.

The Froggatt-Nielsen (FN) mechanism [100] is a way to associate light right-handed neutrinos to the typical BSM high energy scales by introducing a new high-energy sector of fermions, all charged under a specific $U(1)_{FN}$ symmetry. Originally used to account for the pattern of quark masses and mixing, the FN mechanism could as well be used to generate eV or keV scale light right-handed neutrinos. Basically, the mass suppression factor of a heavy particle exponentially depends on its charge under $U(1)_{FN}$. By varying the charges of the three heavy right-handed sterile neutrinos, several promising results have been achieved [101]: the generation of two heavy neutrinos to account for leptogenesis and a keV-scale neutrino as a warm dark matter candidate, the generation of one eV-scale to solve the oscillation anomalies and another as a dark matter candidate, etc..

The νMSM (Neutrino Minimal Standard Model) [102] provides a satisfactory explanation

[5] Similarly to the GUT scale, at the Planck scale, gravity should unite with the other forces.

[6] B-L is the difference between the baryon and lepton numbers. Unlike a B or L symmetry alone, this hypothetical symmetry should not be violated by chiral anomalies.

accounting for a wide range of sterile neutrino masses, each being the solution to an observational problem. By adding $\mathcal{N}$ right-handed neutrino singlets to the Standard Model, it could allow the generation of keV to GeV-scale sterile neutrinos while still using the see-saw mechanism and a heavy right-handed state to give active neutrinos their masses. While this model does not solve the oscillation anomalies via light ev-scale sterile neutrinos, it incorporates dark matter in the form of keV sterile neutrinos. To do so, the νMSM requires a number of right-handed singlets bigger than 2, $\mathcal{N} = 3$ being the favored scenario.

Other models such as mirror models [103] or SuperSymmetry (SUSY) [104] provides attractive solutions but, since they require the existence of a "mirror" or "symmetric" Standard Model, they are considered a step further than the MSM and will not be discussed here.

2.3.2 Neutral Leptons: Light, keV, MeV or more

Oscillation favored masses

The anomalies put in evidence with flavor oscillation experiments might be explained by the existence of a new oscillation happening at small L/E$\sim$1 m/MeV. This oscillation would thus be driven by a mass squared difference $|\Delta m^2_{\text{new}}|$ of unknown sign larger than the known Δm^2_{sol} and Δm^2_{atm} leading to $|\Delta m^2_{\text{new}}| > 10^{-2}$ eV^2.

As seen in Section 2.2.2, several accelerator-based experiments observed an excess of electronic (anti)neutrinos while looking at disappearance in a muonic (anti)neutrino beam (*c.f.* Figure 2.17). This excess, when interpreted in terms of a new oscillations in a 3 (active) + 1 (sterile) neutrino framework gives limits on the $\sin^2 2\theta_{\text{new}}$-$\Delta m^2_{\text{new}}$ parameter space as shown in Figure 2.18. The MiniBooNE analysis of ν_μ and $\bar{\nu}_\mu$ disappearances gives best fit points for the set of parameters [98]:

$$\begin{aligned} \sin^2 2\theta_{\text{new}} = 0.16 \;\text{ and }\; |\Delta m^2_{\text{new}}| = 17.50 \text{ eV}^2 \;\text{ for } \nu_\mu \text{ disappearance (at 47\% CL)} \\ \sin^2 2\theta_{\text{new}} = 0.96 \;\text{ and }\; |\Delta m^2_{\text{new}}| = 31.32 \text{ eV}^2 \;\text{ for } \bar{\nu}_\mu \text{ disappearance (at 99.5\% CL)} \end{aligned} \tag{2.33}$$

Combining these two analyses gives the following best fit:

$$\sin^2 2\theta_{\text{new}} = 0.44 \;\text{ and }\; |\Delta m^2_{\text{new}}| = 31.32 \text{ eV}^2 \text{ (at 99.2\% CL)} \tag{2.34}$$

A recent analysis combining results from MiniBooNE and SciBooNE [105] yields the following best fit [106]:

$$\sin^2 2\theta_{\text{new}} = 0.086 \;\text{ and }\; |\Delta m^2_{\text{new}}| = 5.9 \text{ eV}^2, \tag{2.35}$$

excluding the null oscillation hypothesis at 81.9%.

A similar analysis of the appearance of ν_e and $\bar{\nu}_e$ have been carried out as well [107, 88] giving the best fit (*c.f.* Figure 2.18):

$$\sin^2 2\theta_{\text{new}} = 10^{-3} \;\text{ and }\; |\Delta m^2_{\text{new}}| = 4 \text{ eV}^2 \text{ (at 99\% CL)} \tag{2.36}$$

The Gallium and reactor experiments (c.f. Sections 2.2.2 and 2.2.2) both observed a deficit of electronic (anti-)neutrino events with respect to the expected number of events. In both types of experiments, energies ($\sim$ 1 MeV) and baselines ($\sim 10 - 100$ m) were quite similar. The L/E ratios are thus similar ($\sim$ 1 m/MeV) and both kind of experiments are sensitive to

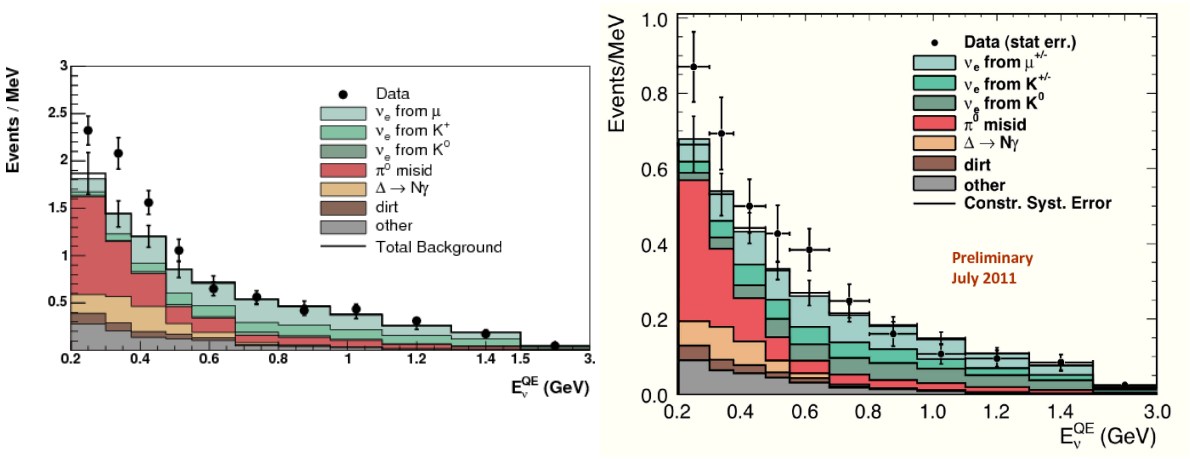

Figure 2.17: Left: Neutrino (left) and antineutrino (right) reconstructed energy spectra in MiniBooNE. The data points (black points with error bars) and the expected backgrounds (histograms) are displayed.

the same Δm^2_{new}. For this reason, they are often combined together on the $\sin^2 2\theta_{\text{new}}$-$\Delta m^2_{\text{new}}$ parameter space as shown in Figure 2.20.

Interpreting the results of all short-baseline reactor experiments as an oscillation toward a sterile neutrino state modifies the $\bar{\nu}_e$ survival probability as seen on Figure 2.19. At short distances (< 100 m), the oscillation probability is driven by the new mass squared difference Δm^2_{new} until it reaches the Δm^2_{13} dominated region at ~ 1 km. Afterwards, the Δm^2_{new} driven oscillation becomes negligible as the Δm^2_{12} region becomes dominant.

The combination of this interpretation of the reactor experiments with the Gallium experiments results gives the following best fit on the angle-mass parameter space:

$$\sin^2 2\theta_{\text{new}} = 0.17 \pm 0.04 \quad \text{and} \quad |\Delta m^2_{\text{new}}| = 2.3 \pm 0.1 \text{ eV}^2, \tag{2.37}$$

with:

$$|\Delta m^2_{\text{new}}| > 1.5 \text{ eV}^2 (\text{at } 99\% \text{ CL}). \tag{2.38}$$

This 3+1 neutrino hypothesis disfavors the no-oscillation hypothesis at 99.97% CL. (3σ).

Figure 2.20 shows the allowed $\sin^2 2\theta_{\text{new}}$-$\Delta m^2_{\text{new}}$ regions for the combination of reactor, Gallium and accelerator anomalies. It is worth noting that while Gallium and reactor data favor $\Delta m^2_{\text{new}} \sim 1$ eV^2, accelerator experiments tend to point toward a higher squared mass difference $\Delta m^2_{\text{new}} \sim 10 - 30$ eV^2.

Even though anomalies in oscillation experiments data sometimes prefer different $\sin^2 2\theta_{\text{new}}$-$\Delta m^2_{\text{new}}$ regions, they point toward the existence of a sterile neutrino with a squared mass difference $\Delta m^2_{\text{new}} \sim 1$ eV with the active flavors.

Cosmology favored masses

Cosmological observations can also be used as a tool to probe the existence of possible sterile neutrinos.

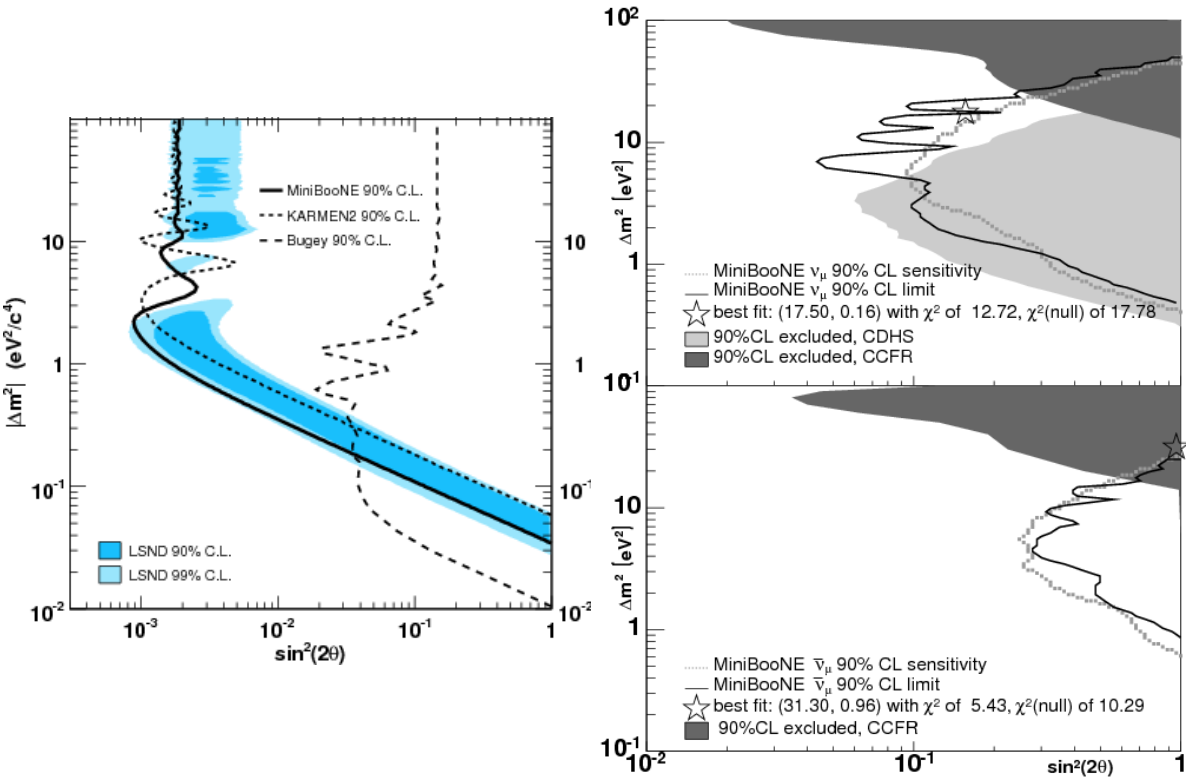

Figure 2.18: Left: 90% CL sensitivity (dashed line) and limit (solid line) for the ν_e and $\bar{\nu}_e$ appearance analysis in a 2-neutrino (active-sterile) mixing case [107]. Right: 90% CL sensitivity (dashed line) and limit (solid line) for the ν_μ (top) and $\bar{\nu}_\mu$ (bottom) disappearance analyses in MiniBooNE. Results from previous experiments are shown as well in dark (CCFR) and light (CDHSW) gray [98].

In the early Universe, neutrinos are considered at thermal equilibrium with the other particles. During the expansion of the Universe, the thermal plasma cools and its density drops, thus less and less neutrinos interactions occur. As the plasma reaches a temperature of 1 MeV, the neutrino interaction rate becomes lower than the Universe expansion rate and neutrinos decouples from the thermal plasma. The ultra-relativistic behavior of neutrinos is conserved after this decoupling and their energy spectrum can be parametrized by a Fermi-Dirac distribution. The expansion rate of the Universe during the epoch following this decoupling, called the radiation dominated era, depends on the energy density of relativistic particles such as photons and neutrinos. This expansion $H\left(t\right)$ is given by:

$$H^2\left(t\right) \simeq \frac{8\pi G}{3}\left(\rho_\gamma + \rho_\nu\right) \tag{2.39}$$

with G the gravitational constant and $\rho_{\gamma,\nu}$ the energy densities of photons and neutrinos, respectively.

Since neutrinos decoupled before the e^+e^- annihilation process that occurred at a plasma temperature ~ 0.2 MeV, they are not reheated by the energy released in this process, unlike photons. Therefore, the neutrino temperature is lower than the photon temperature such as $T_\nu = \left(\frac{4}{11}\right)^{1/3} \times T_\gamma \simeq 1.9$ K.

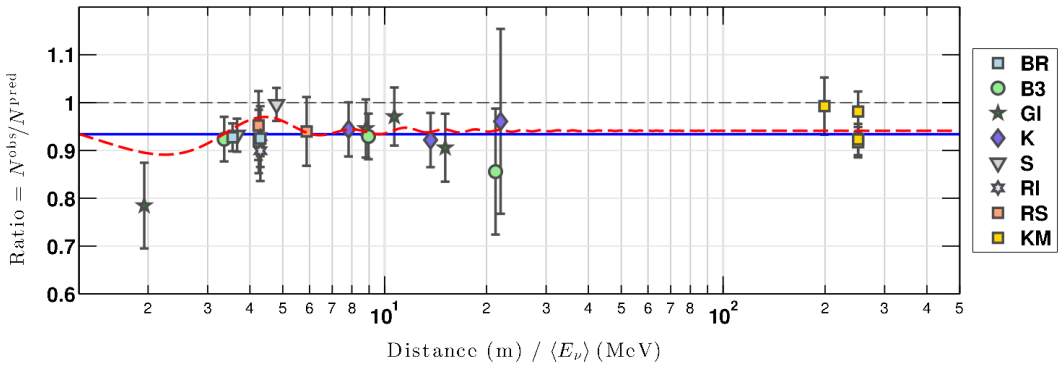

Figure 2.19: Ratio of observed over expected event rates for several reactor experiments as a function of the distance over the average $\bar{\nu}_e$ energy. All ratios are normalized to the expected flux corrected for the θ_{13}-driven deficit measured by Daya Bay [108]. The solid blue line represents the global average. The dashed red line corresponds to the best fit oscillation with $\sin^2 2\theta = 0.15$ and $\Delta m^2 = 0.48$ [96].

From this temperature, the energy density can be derived leading to:

$$\rho_\nu = N_{\text{eff}} \frac{7\pi^2}{120} T_\nu^4 \tag{2.40}$$

with N_{eff} the effective number of neutrino families.

According to the standard model of cosmology [15, 110], the effective number of neutrino is $N_{\text{eff}} = 3.046$ rather than $N_{\text{eff}} = 3$ as the Standard Model and its 3 neutrino flavors would suggest. This discrepancy is due to the fact that not all neutrinos were decoupled during the e^+e^- annihilation. Adding sterile neutrinos to the already existing three neutrino flavors would lead to an increase of N_{eff} since, even though they do not interact by weak interactions, they could still increase the relativistic energy density through oscillation-based thermal production.

Note that the addition of any light particle can contribute to the relativistic energy density. The observation of a $N_{\text{eff}} > 3.04$ could be due to sterile neutrinos but also to the existence of axions, gravitons, etc...

Several cosmological observations can be carried out to measure N_{eff}. Results from measurements of the CMB (Cosmic Microwave Background) temperature anisotropies, observations of large-scale structure distributions and computations of light element abundance from BBN (Big Bang Nucleosynthesis) are shown on Figure 2.21. While being consistent with the standard $N_{\text{eff}} = 3.04$, these data do not exclude $N_{\text{eff}} > 3.04$. Note that most of the cosmological results are model-dependent, they cannot alone prove or refute the existence of a sterile neutrino.

These observations, when combined with the current understanding of the cosmological constant with cold dark matter, can deliver informations on the hypothetical sterile neutrino mass m_s. A recent analysis [111] of the WMAP-7 and LRG (Luminous Red Galaxy) from the SDSS data along with the Hubble's constant H_0 gave the following constraint on m_s (*c.f.* Figure 2.21):

$$m_s < 0.45 \text{ eV (95\% CL.)} \tag{2.41}$$

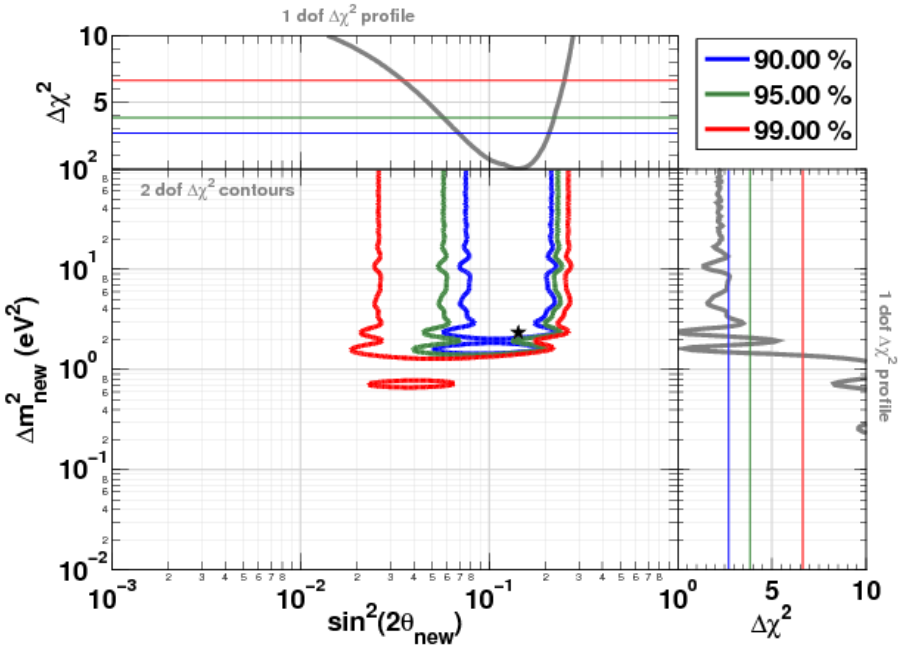

Figure 2.20: Allowed regions in the $\sin^2 2\theta_{\text{new}}$-$\Delta m^2_{\text{new}}$ plane from the combination of short-baseline reactor neutrino experiments, Gallium experiments, MiniBooNE reanalysis of [109], and the ILL-energy spectrum distortion. The data are consistent with a 3+1 neutrino oscillation framework with $\sin^2 2\theta_{\text{new}} = 0.14 \pm 0.08$ (95% CL) and $|\Delta m^2_{\text{new}}| > 1.5$ eV^2 [96].

This upper bound is inconsistent with the observations in oscillations experiments, favoring a $\Delta m^2_{\text{new}} \sim 1$ eV^2, and thus $m_s > 1$ eV, and fully thermalized neutrinos. However, in a $3 + N_S$ framework, cosmological data could accommodate the existence of a heavier non-thermalized neutrino at the eV-scale.

The nature of dark matter is one of the hottest issue in modern cosmology. While several models postulate exotic particle such as axions or supersymmetric particles, neutrinos are the most obvious candidates as dark matter candidates. However, the formation of large scale structures detected by cosmological observations [112] tends to set a lower limit on the mass of the dark matter particles. Indeed, ultra relativistic light particles such as Standard Model neutrinos prevent the formation of small structures in the Universe. In order to be compatible with the observations, dark matter candidates need to be qualified as "cold dark matter" or "warm dark matter" whereas Standard Model neutrinos are classified as "hot dark matter". The temperature classification depends on relativistic motion of the particle, which is equivalent to the mass in this case, at the radiation-matter transition time. Heavy particles are considered cold dark matter while light particles are considered hot dark matter.

While standard neutrinos are too light to be considered as dark matter candidates, sterile neutrinos and their wide hypothetical mass range might. Recent observations of the phase-space distribution in dwarf spheroidal galaxies [113] put a lower bound on the mass of a dark matter particle $M_{DM} > 1$ keV. Another observation using the X-ray spectrum emitted by the Andromeda galaxy [114] constrained this same mass and provided an upper limit

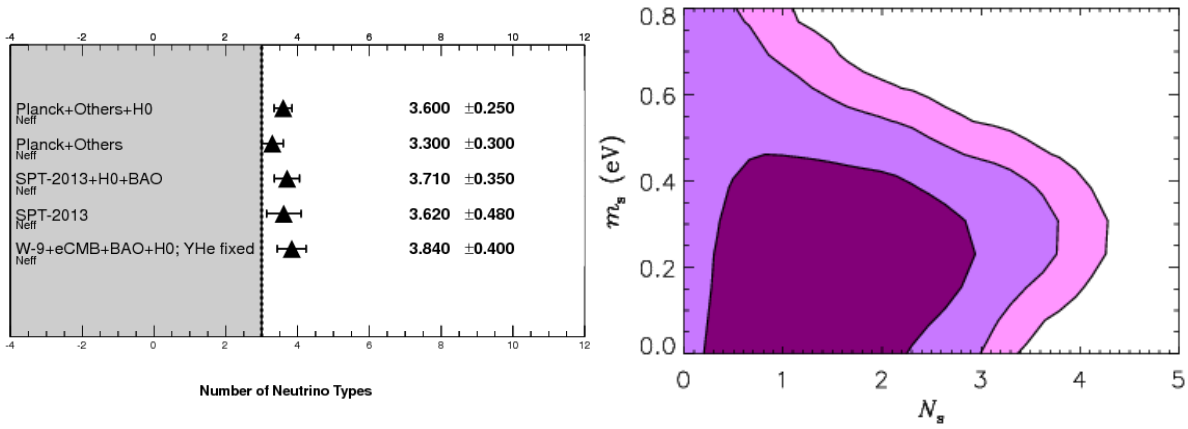

Figure 2.21: Left: Constraints on the number of effective neutrino families N_{eff} from cosmological observations. W-9 stands for the 9-year dataset of WMAP, BAO for Baryonic Acoustic Oscillations, SPT is the South Pole Telescope and H0 refers to the Hubble constant with $H_0 = 74.2 \pm 3.6$ km.s^{-1} [98]. Right: 68%, 95% and 99% allowed regions for the sterile neutrino mass and the number of sterile neutrinos such that $N_{\text{eff}} = 3 + N_S$. In this analysis, the standard neutrinos are considered massless [111].

$M_{DM} < 4$ keV.

This energy region is allowed in the νMSM (*c.f.* Section 2.3.1) even though it requires a large asymmetry generated by the two other sterile neutrinos, each responsible respectively for baryogenesis and flavor oscillations. A sterile neutrino having a mass $m_s \sim 1 - 20$ keV is thus a suitable candidate for warm dark matter in the νMSM model as pictured on Figure 2.22. Recent X-ray observations of the Andromeda galaxy and the Perseus galaxy cluster by the XMM-Newton telescope reported the detection of a weak line at 3.52 ± 0.02 keV [115, 116]. As explained in Ref. [117], this line could provide a hint of the existence of a 7 keV sterile neutrino, potential dark matter candidate.

The cold dark matter hypothesis is more and more disfavored by observations, such as the absence of dwarf satellites galaxies around massive ones such as the Milky Way [118]. Corresponding to particle masses above the MeV scale, cold dark matter is generally thought to be constituted of axions or WIMP's (Weakly Interacting Massive Particles), more popular. Sterile neutrino masses of the order of the MeV and above are often discarded. Indeed this mass is too high to be generated, using an even heavier sterile neutrino, without reaching the GUT scale.

2.3.3 Light sterile neutrino oscillation phenomenology

In the previous Section 2.3.2, we provided a review of the different mass scales open to sterile neutrinos from oscillation and cosmological inputs. However, since this thesis is focused on the study of $\bar{\nu}_e$ emitted by radioactive or natural nuclear sources, only the mass favored by gallium and reactor anomalies will be considered. In the following, only the 3 (active) + 1 (sterile) mixing framework will be studied with $\sin^2 2\theta_{\text{new}} \sim 1$ and $\Delta m^2_{\text{new}} \sim 1$ eV^2.

The addition of a new flavor ν_s and a new mass state m_4 transforms the PMNS matrix

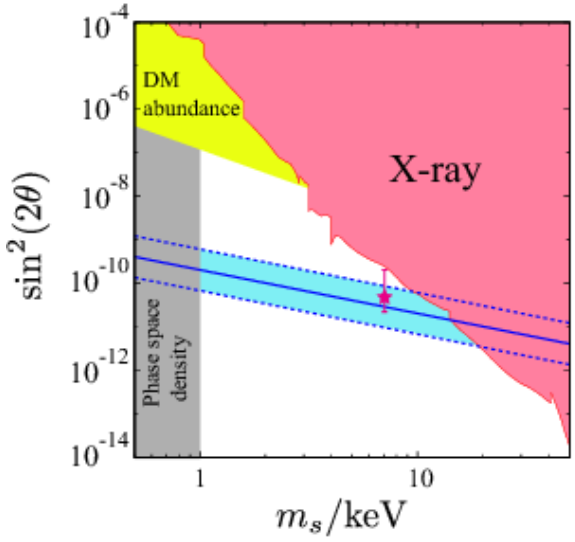

Figure 2.22: Bounds on the mass m_s and the mixing angle θ of a hypothetical sterile neutrino as a dark matter candidate in the νMSM model [117]. The red star represents the values of the mass and the mixing angle explaining the 3.5 keV X-ray line.

into a 4×4 matrix such as:

$$|\nu_\alpha\rangle = \sum_k U^*_{\alpha,k}|\nu_k\rangle \quad \text{or} \quad \begin{pmatrix}\nu_e\\ \nu_\mu\\ \nu_\tau\\ \nu_s\end{pmatrix} = U_{PMNS}\begin{pmatrix}\nu_1\\ \nu_2\\ \nu_3\\ \nu_4\end{pmatrix} \tag{2.42}$$

with:

$$U_{\text{PMNS}} = \begin{pmatrix}U_{e1} & U_{e2} & U_{e3} & U_{e4}\\ U_{\mu1} & U_{\mu2} & U_{\mu3} & U_{\mu4}\\ U_{\tau1} & U_{\tau2} & U_{\tau3} & U_{\tau4}\\ U_{s1} & U_{s2} & U_{s3} & U_{s4}\end{pmatrix} \tag{2.43}$$

As in the 3-neutrino case, this 4×4 PMNS can be parametrized using 6 mixing angles $(\theta_{12}, \theta_{23}, \theta_{13}, \theta_{14}, \theta_{24}, \theta_{34})$ and 3 CP-violation phases. An additional squared mass difference Δm^2_{34} needs to be taken into account in the oscillation as well.

Given the relative smallness of the three standard squared mass differences ($\Delta m^2_{12} < \Delta m^2_{23} < 10^{-2}$ eV^2) with respect to the new one ($\Delta m^2_{\text{new}} \sim 1$ eV^2), the standard mass states can be approximated at short-baselines as $m_1 \approx m_2 \approx m_3$. Using the PMNS elements of Eq. 2.43, one can derive the appearance and disappearance probabilities [119]:

$$\begin{aligned} P_{\nu_\alpha \to \nu_\beta} &= 4|U_{\alpha4}|^2|U_{\beta4}|^2 \sin^2 \frac{1.27\Delta m^2_{14} L}{E} \\ P_{\nu_\alpha \to \nu_\alpha} &= 1 - 4\left(1 - |U_{\alpha4}|^2\right)|U_{\alpha4}|^2 \sin^2 \frac{1.27\Delta m^2_{14} L}{E} \end{aligned} \tag{2.44}$$

In the case of $\bar{\nu}_e$ disappearance, the disappearance probability becomes:

$$P_{\bar{\nu}_e \to \bar{\nu}_e} = 1 - \sin^2 2\theta_{14} \sin^2 \frac{1.27\Delta m^2_{14} L}{E}, \tag{2.45}$$

an expression similar to the survival probability observed by reactor experiments looking for the θ_{13} oscillation.

Chapter 3

MeV (Anti)Neutrino generators

The following chapter is dedicated to the different MeV-scale (anti-)neutrino generators. First, we will focus on nuclear reactors from their basic characteristics to the spectrum of the antineutrino they generate. We then describe the principles and different types of radioactive sources, another kind of man-made (anti-)neutrino generator. Finally, we review the powerful astrophysical process of core-collapse supernova, also generating a tremendous amount of (anti-)neutrinos. These three generators, although very different in terms of mechanisms, intensity or signatures, have in common that they emit (anti-)neutrinos at the MeV scale.

3.1 Nuclear reactors

Since the Reines and Cowan experiment, nuclear reactors have played a predominant role in neutrino physics. Their strong intensity and pure $\bar{\nu}_e$ emission make them cheap [1], efficient [2] and reliable antineutrino sources.

3.1.1 Basic fission principles

Nuclear reactors exploit the principle of nuclear chain reaction to continuously generate energy via fission reactions. Nuclear fission is a process where a heavy nucleus splits into several, usually two, lighter nuclei while emitting energy. It can be assimilated to a nuclear decay (spontaneous fission) or induced by an incident particle such as a neutron. When a heavy nucleus with typically $Z > 90$ undergoes a fission process, it leaves its two fission fragments excited and very rich in neutrons. These highly unstable nuclei consequently evaporate several neutrons and emit gammas in order to become more stable. The energy liberated during this whole process, including the fission fragments kinetic energy, is confined within the reactor vessel and recovered as heat in a nuclear power station. Among these ~ 200 MeV, depending on the fissioning isotope, only the small fraction of energy carried away by neutrinos escapes the reactor.
While several natural isotopes are considered fissionable, i.e. they are likely to undergo fission when struck by an energetic neutron with more than 1 MeV of kinetic energy, only ^{235}U is found in nature and fissile, i.e. it undergoes fission when struck by thermal neutrons

[1] While the construction of a nuclear reactor is incredibly expensive, it is at the charge of the power plant operator not the experiment.

[2] Nuclear reactors, especially commercial ones, usually run at full power and only shutdown to refuel.

(E∼0.025 eV). Other fissile nuclei such as ^{239}Pu and ^{233}U can artificially created by neutron irradiation of ^{238}U or ^{232}Th. The isotopic composition of natural uranium is 99.3% of ^{238}U , 0.7% of ^{235}U and traces of ^{234}U. Using enrichment techniques, the concentration of ^{235}U can be improved to about 5% for uses in most civil nuclear reactors. Some research reactors run on fuel enriched to about 20%. Uranium further enriched is no longer used in common nuclear reactors but in nuclear weapons where the ^{235}U concentration can rise up to 85% or more. In order to deliver a constant flux of thermal energy, the chain fission reaction needs to be kept in a sustained state where the flux of fission-induced neutrons is constant. A system operating in such a sustained state reached its *criticality*. While the fading neutron emission of a subcritical system does not allow it to maintain sustained chain fissions, a supercritical state emits a rapidly increasing number of neutrons and might end up in an uncontrollable fission chain reaction if not correctly operated. Nuclear reactors operate in a critical state where fission-induced neutrons induce more fissions and so on. Since it is the most widely used fissile isotope, let's focus on the fission reaction of ^{235}U :

$$^{235}\mathrm{U} \; + \; {}^{1}_{0}\mathrm{n} \; \rightarrow \; {}^{A1}_{Z1}\mathrm{FP1} \; + \; {}^{A2}_{Z2}\mathrm{FP2} \; + \; k \, {}^{1}_{0}\mathrm{n} \; + \; \gamma' s, \tag{3.1}$$

with $^{A1}_{Z1}$FP1 and $^{A2}_{Z2}$FP2, the two fission products and k the mean number of emitted neutrons. For ^{235}U , k = 2.4 meaning that while 2.4 neutrons are emitted per ^{235}U fission, only one induces another fission. The remaining fraction of neutrons is usually lost during the thermalization or *moderation* process, needed to decrease the energy of fission-induced neutrons from several MeV to several meV, thermal energy where the ^{235}U fission cross section becomes higher (*c.f.* Figure 3.1). To be thermalized, fast neutrons of several MeV undergo consecutive elastic scatterings until they reach thermal energies of the order of the meV. The medium used to thermalize neutrons is called the moderator and is usually composed of light nuclei such as H or D [3] to increase the mean energy loss per neutron scattering.

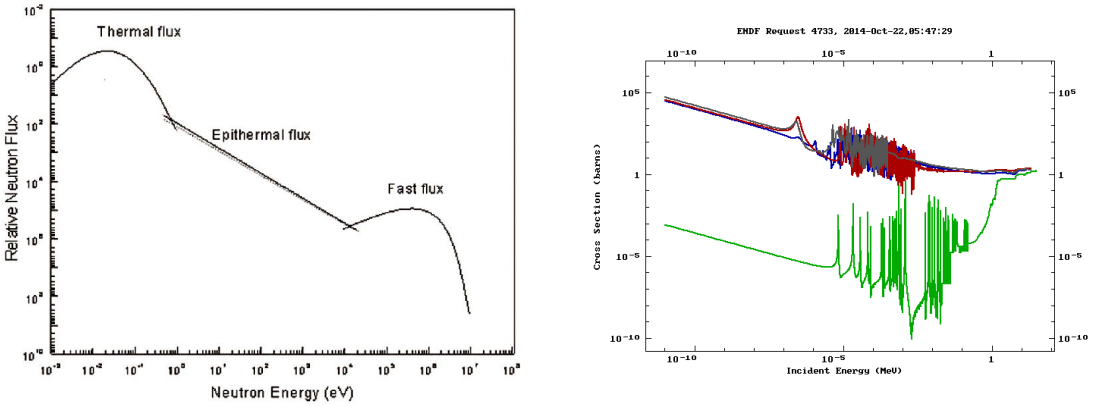

Figure 3.1: Left: Energy spectrum of neutrons in the moderator [120]. Their energy at emission and after thermalization can be represented as Maxwell distributions peaked respectively around 1 MeV and 50 meV. Right: Fission cross sections of ^{235}U (blue), ^{238}U (green), ^{239}Pu (red) and ^{241}Pu (gray). The non-fissile nature of ^{238}U can clearly be seen on its fission cross section, orders of magnitude lower than the others at thermal energies but comparable at fast neutrons energies.

[3] Deuterium ($^{2}_{1}$H) is an hydrogen atom with an additional neutron. It is the main component of heavy water (D_2O).

3.1.2 Reactor mechanisms

A nuclear reactor is characterized by 3 main components: the fuel made of the fissioning isotope sustaining the fission chain reaction, the coolant used to recover the heat produced by fissions and the moderator slowing down and thermalizing fast neutrons. These three elements can be of several types and each combination brings different advantages and drawbacks. Nuclear reactors can be simply divided into two classes:

- *Thermal reactors*: These reactors use a moderator to thermalize fission-induced neutrons. As stated above, the moderator needs to be composed of light nuclei and located as close as possible to the fuel in order to minimize neutron losses and maximize the probability of inducing fissions (*c.f.* Figure 3.2). To satisfy these requirements, this moderator is usually used as coolant as well. Water (H_2O) and heavy water (D_2O) are widely used as such in most thermal reactors, usually in a pressurized vessel to increase its boiling point. Given the high fission cross section of ^{235}U at thermal energies, thermal reactors allow the use of lowly enriched uranium (between 1 and 4%) or even natural uranium (with the use of D_2O as a moderator) as a fuel. They are the most common nuclear reactors.

- *Fast neutrons reactors*: Unlike the previous ones, these reactors use fast neutrons to induce more fissions. In order to keep the fast neutrons flux constant, they do not use a moderator and need to be compact to minimize neutron energy losses between fuel elements. Since water acts as a moderator, heavier coolants such as molten metals (sodium or lead) or gases (helium or carbon dioxide) need to be adopted. Though these mediums are more delicate to operate, they allow the reactor to run at higher temperatures thus increasing its efficiency. The relatively low fission cross section of ^{235}U to fast neutrons requires a higher fuel enrichment than in the case of thermal reactors (of the order of 20%). However the high neutron flux allows the *breeding* of fertile isotopes such as ^{238}U into fissile isotopes such as ^{239}Pu leading to a fuel regeneration. Fast neutron reactor can also transmute actinides considered nuclear waste, into less problematic elements in terms of disposal.

In the following, we will focus on thermal reactors and especially the most common type: light-water-moderated reactors (LWR). They can be divided into two kinds: Pressurized Water Reactors (PWR) and Boiled Water Reactors (BWR). Their main difference lies in the heat exchange system. In a PWR, the water coolant is kept pressurized to 155 bars while passing through the reactor, preventing it to boil at 350°C. It then transfers its heat to a secondary system that generates steam, finally evacuated through a third cooling system. In a BWR, water is vaporized into steam when in contact with the reactor and is then evacuated though the secondary cooling system.

3.1.3 Antineutrino production

As explained earlier, fission reactions in the reactor create neutron-rich fission fragments (*c.f.* Figure 3.3). In order to reach the band of stability, these fission products undergo a series of β-decays thus emitting several electronic antineutrinos. On average, each fission releases 6 antineutrinos along with the 200 MeV of thermal energy. A 1 GW_{th} reactor thus delivers a total of 2×10^{20} $\bar{\nu}_e$ $.s^{-1}$ thus making a nuclear reactor the most intense source of neutrinos on Earth.

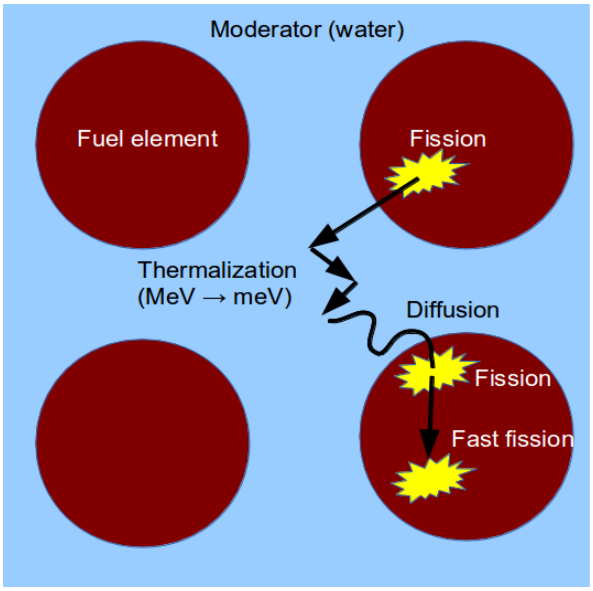

Figure 3.2: Moderation process in a thermal reactor. After thermalization, the neutron diffuses (random Brownian walk) before inducing another fission. Fast neutrons induced fissions on ^{238}U usually occur within the same fuel element without moderation.

Although it is the only fissile isotope in fresh fuel, composed of ^{235}U and ^{238}U , ^{235}U is not the only element which fission releases antineutrinos. Even in thermal reactors, the breeding of fertile ^{238}U can occur after a fast neutron radiative capture on ^{238}U transforming it into ^{239}U which β-decays twice into a fissile ^{239}Pu . While the radiative cross section of ^{238}U is higher than its fission cross section, fast neutron induced fissions of ^{238}U still occur. In some cases, ^{239}Pu can undergo two neutron captures and transmutes into ^{241}Pu, another fissile isotope. During a reactor operation cycle, the four fissioning isotopes ^{235}U , ^{238}U , ^{239}Pu and ^{241}Pu contribute to the antineutrino emission. However, their structures and masses cause them to split into different fission fragments as displayed on Figure 3.3 leading to different fission energies and antineutrino emission as summarized in Table 3.1.

Isotope	Total fission energy [MeV]	Number of emitted $\bar{\nu}_e$ per fission
^{235}U	201.7 ± 0.6	1.92 ± 0.036
^{238}U	205.0 ± 0.9	2.38 ± 0.048
^{239}Pu	210.0 ± 0.9	1.45 ± 0.030
^{241}Pu	212.4 ± 1.0	1.83 ± 0.035

Table 3.1: Total energy and number of antineutrinos emitted above the detection threshold of 1.8 MeV (*c.f.* Chapter 4) per fission of the four fissioning elements: ^{235}U , ^{238}U , ^{239}Pu and ^{241}Pu [123].

The fuel composition evolves over time and as the fraction of ^{235}U decreases, the fraction of ^{239}Pu and ^{241}Pu increases. This is known as the *burnup* effect, displayed on Figure 3.4. Since the average antineutrino yield of the two fissioning Pu isotopes is lower than the one of ^{235}U, the number of emitted $\bar{\nu}_e$ decreases over time, even for a reactor operating at constant power. This characteristic of the burnup effect drives current studies in nuclear non-proliferation.

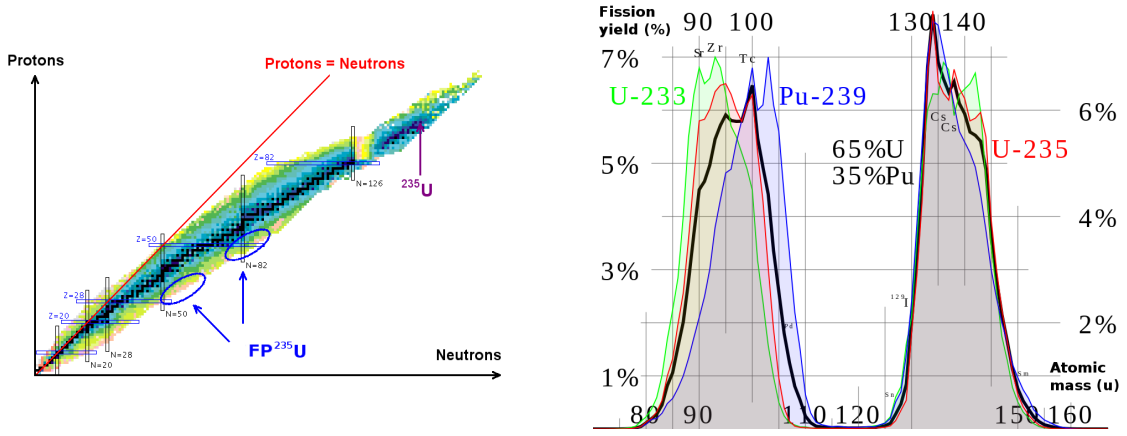

Figure 3.3: Left: Localization of the ^{235}U fission products in the chart of nuclides [121]. Right: Distribution of the fission products originated from the fissions of the 3 fissile elements ^{235}U ,^{239}Pu and ^{233}U and an hybrid fuel (65% U, 35% Pu) [122].

3.1.4 Antineutrino energy spectrum

Electronic antineutrinos are generated through β-decays such as:

$$ {}^{A}_{Z}X \rightarrow {}^{A}_{Z+1}Y + e^{-} + \bar{\nu}_e \ . \tag{3.2} $$

By considering a decay at rest and a negligible recoil of the daughter nucleus, two reasonable assumptions, the principle of energy conservation gives the relation between the electron and antineutrino energies:

$$ E_e + E_{\bar{\nu}_e} = m_X - m_Y - E^*, \tag{3.3} $$

with m_X and m_Y the respective rest masses of the ${}^{A}_{Z}X$ and ${}^{A}_{Z+1}Y$ nuclei and E^* the excitation energy of the daughter nucleus ${}^{A}_{Z+1}Y$. The electron and the antineutrino share the total energy $E_0 = m_Y - m_X + E^* = \mathcal{Q}_\beta + E^*$. Their energy spectra are continuous and each can be computed knowing the other as displayed in Figure 3.5. Although, for a given nucleus, $\mathcal{Q}_\beta$ is a constant, the excitation energy E^* varies depending on the energy level. For each value of E^*, a β-branch is associated with an electron spectrum $S_{e,b}(E)$ and an antineutrino spectrum $S_{\bar{\nu}_e\ ,b}(E)$ sharing an energy $E_{0,b}$ such as:

$$ S_{\bar{\nu}_e\ ,b}(E) = S_{e,b}(E_{0,b} - E). \tag{3.4} $$

This is a zeroth-order approximation, with no corrections to Fermi's theory of β-decay [125].

During the decay of a given nucleus, all branches must be taken into account and the electron and antineutrino spectra are combination of all of them weighted by their branching ratio:

$$ S_{\bar{\nu}_e}(E) = \sum_{b=1}^{N_b} \alpha_b S_{\bar{\nu}_e\ ,b}(E) \quad \text{and} \quad S_e(E) = \sum_{b=1}^{N_b} \alpha_b S_{e,b}(E), \tag{3.5} $$

with N_b the total number of branches and α_b the branching ratio of the b branch.

Since the fissions of each of the four nucleus ^{235}U , ^{238}U , ^{239}Pu and ^{241}Pu creates a wide variety of fission products, the antineutrino spectrum emitted per fissile isotope is the

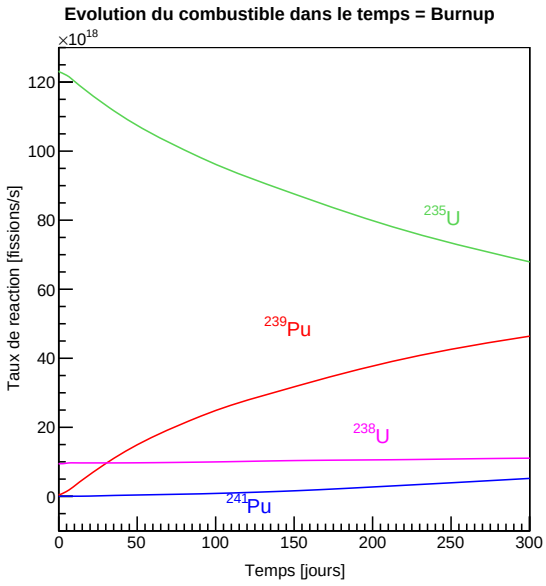

Figure 3.4: Simulated fission rates of the four fissioning isotopes as a function of time for a PWR reactor operating at constant power [124].

weighted sum of each fission product spectrum. For instance, the antineutrino spectrum of ^{235}U can be expressed as:

$$S_{\bar{\nu}_e\ ,^{235}\mathrm{U}}(E,t) = \sum_{FP=1}^{N_{FP}} \mathcal{A}_{FP}(t) \sum_{b=1}^{N_b} \alpha_b S_{\bar{\nu}_e\ ,b}(E), \tag{3.6}$$

with $\mathcal{A}_{FP}(t)$, the activity of the fission product of interest.

Given the large range of fission products created in a nuclear reactor, we estimate the number of β-branches to be of the order of 10000, each contributing to the total antineutrino spectrum.

Accurate knowledge of each branch of each fission product is thus mandatory in order to compute a total antineutrino spectrum with the so-called *ab initio* method. This approach requires the use of all β-branches, whether theoretically computed or experimentally measured and listed in nuclear databases. Given the current state of these databases, the ab initio method is limited by a 10% uncertainty up to 7 MeV and larger above it [124] mainly driven by the pandemonium effect [126]. This large uncertainty motivated the experimental measurements of these branches. Since an individual identification is nearly impossible, only the total electron energy spectrum, sum of the contribution of each branch, is measured.

Measurements of the electron spectra originated from ^{235}U , ^{239}Pu and ^{241}Pu fissions have been carried out in the eighties at the Institut Laue-Langevin (ILL) in Grenoble [127, 93]. To do so, thin foils of these isotopes were placed 80 cm from the ILL reactor core where the neutron flux was exclusively thermal. The high neutron flux induced fissions and the electron spectra of the subsequents fission products were measured in the BILL high resolution spectrometer [128].

In order to compute an antineutrino spectrum from these measurements, Schreckenbach et al. used an effective method and fitted the ILL electron spectrum with 30 virtual β-

branches [92] as displayed in Figure 3.6. While none of those branches corresponded to an actual β-decay, each had an associated electron and hence antineutrino spectrum. The sum of these spectra gave the total antineutrino spectrum from ^{235}U , ^{239}Pu and ^{241}Pu fissions with an uncertainty at the level of 3%. Since the fission of ^{238}U is triggered by fast neutrons, it could not be measured at the ILL reactor and its contribution to the antineutrino spectrum was computed only from theoretical models assumptions. Since then, Haag et al. measured the ^{238}U electron spectrum using the FRM II fast neutrons source in Garching [129] and the antineutrino spectrum extracted from it is now taken into account in recent predictions [75].

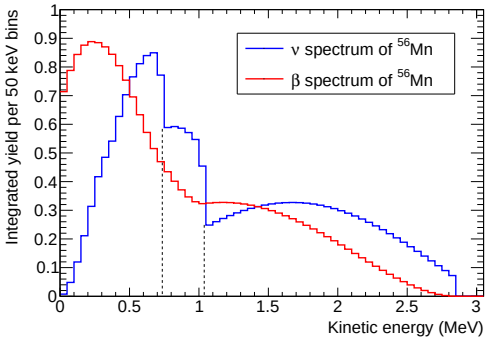

Figure 3.5: Example of conversion between the electron and $\bar{\nu}_e$ spectra of ^{56}Mn [124].

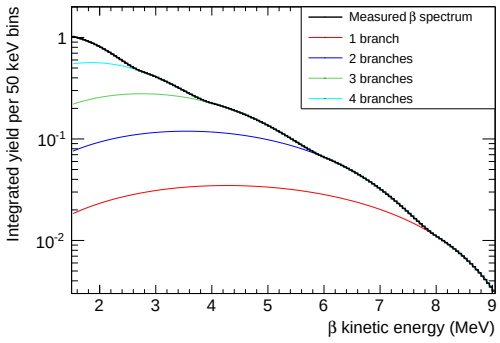

Figure 3.6: Conversion of electron spectra (black) into $\bar{\nu}_e$ spectra using an effective method on 4 virtual branches (color) [124].

In order to increase the understanding of the reactor antineutrino spectrum, members of the Double Chooz collaboration in Saclay performed a complete re-analysis of the spectrum predictions in 2011 [94]. This work was driven by the fact that at that time, the Double Chooz experiment was only running with one detector and therefore needed lower systematic uncertainties on the $\bar{\nu}_e$ spectrum before oscillation. It was based on a mixed approach combining experimental inputs of the effective method and theoretical models of the ab initio method. Instead of fitting the electron spectrum measured at ILL with a few virtual branches, Mueller et al. made full use of the ten thousand real branches available in the nuclear databases. However, these real branches accounted only for 95% of the total energy spectrum measured at ILL and the remaining 5% had to be fitted using an effective method with only 5 virtual branches. This new technique put in evidence a +3% systematic normalization shift with respect to the previous estimations of [92] as shown in Figure 3.7. This discrepancy is understood as an effect due to non-physical corrections induced by the use of virtual branches.

An independent study carried out by Huber et al. [95] the same year and using only virtual branches with corrections is in agreement with this re-analysis.

3.2 Radioactive sources

The advantages of nuclear reactors in terms of intensity and $\bar{\nu}_e$ purity makes them highly effective neutrino sources for the study of short to long range neutrino oscillations.

However, at shorter distances, drawbacks quickly arise and sometimes hinder the reliability of reactors as a $\bar{\nu}_e$ source. At kilometer-scale distances, the construction of a detector is a

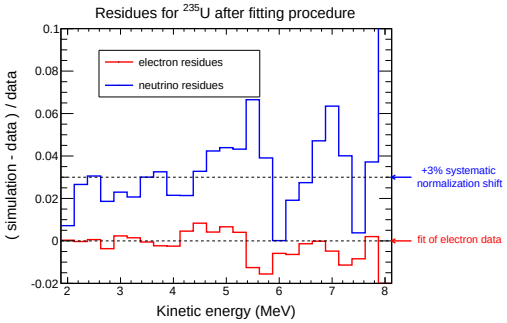

Figure 3.7: Residues of ^{235}U electron and antineutrino spectra after the fitting procedure of [94]. The +3% systematic shift only arises after conversion [124].

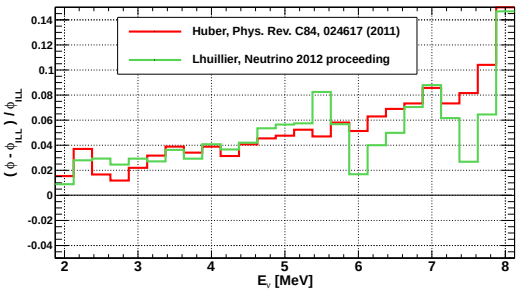

Figure 3.8: Residues between previous and current predictions of the ^{235}U antineutrino spectrum. Reanalysis from [94] is displayed in green while results from [95] are displayed in red [130].

much simple matter than inside a power plant area or within the reactor building.

Besides, nuclear reactors, for commercial or research purposes, do not operate continuously at their designed full power. They sometimes run at lower power and have to stop to refuel. These shutdowns, lasting from several days for a research reactor to several months for a commercial one, as well as any changes on the reactor power must be monitored and shared between the operator and the scientific community. The precise knowledge of a reactor power and hence of its $\bar{\nu}_e$ flux can be tricky since it also depends on the fuel composition.

Finally, the study of short range oscillations forces detectors to be located inside reactors buildings, a few meters away from the core. Along with possible complications on safety and privacy, this also implies to install a low background detector in a highly irradiated area hence tremendously reducing the detector efficiency as well as increasing systematic uncertainties.

For short baseline studies, the use of a compact, transportable and yet intense source of neutrinos is appealing. Such an object made of an isotope emitting ν_e or $\bar{\nu}_e$ is a radioactive source and its principle will be discussed in the following section.

3.2.1 History

Radioactive sources have been long used in neutrino physics for the sake of calibrating detectors. From the study of the quenching factor in liquid scintillator detectors using α emitters, the energy scale measurement using γ sources and the study of coincidences using neutron emitters, they are a part of neutrino physics since its beginning. However, it is only in the 90s that physicists first used radioactive sources as neutrino emitters.

As described in Section 2.2.1, GALLEX and SAGE were radiochemical experiments designed to detect solar neutrinos via the $\nu_e + ^{71}\mathrm{Ga} \rightarrow ^{71}\mathrm{Ge} + e^-$ reaction. In order to calibrate their detectors, both collaborations manufactured and deployed intense ν_e sources with known energy and intensity. While the initial goal of energy calibration was a success, both experiment reported an anomaly as presented in Section 2.2.2.

Twenty years later, these anomalies contribute to the regain of interest towards the use of intense neutrino emitters in neutrino physics. Experimental concepts to test this Gallium anomaly consists of deploying a source of ν_e /$\bar{\nu}_e$ in the vicinity of large monolithic detectors in order to observe an oscillation pattern, explained by a mixing between active and sterile

neutrino states [131]. A detailed study of such an experiment using an $\bar{\nu}_e$ source in KamLAND or Borexino will be thoroughly described in Chapter 7.

3.2.2 Neutrino sources

Neutrino sources emit ν_e through electron capture process of unstable nuclei:

$$ {}^{A}_{Z}X + e^- \rightarrow {}^{A}_{Z-1}Y + \nu_e, \tag{3.7} $$

in which the proton-rich ${}^{A}_{Z}X$ nucleus absorbs an inner orbital electron thereby transforming a proton into a neutron and emitting an electron neutrino. This reaction being a 2-body decay at rest, the energy spectrum of the outcoming ν_e follows a discrete distribution.

Electron neutrinos can be detected through elastic scatterings off electrons:

$$ \nu_e + e^- \rightarrow \nu_e + e^-. \tag{3.8} $$

Its initial and final states being identical, this reaction does not have a threshold. The energy and momentum of the incoming neutrino are redistributed among the two particles of the final state. The total neutrino-electron elastic scattering cross section for the process of Eq. 3.8 can be predicted and expressed as:

$$ \sigma_{tot} = \sigma_0 \left(\frac{3}{4} + 3\sin^2\theta_W + 4\sin^4\theta_W \right) = 9.49 \times 10^{-45} \mathrm{cm}^2 \frac{E_\nu}{\mathrm{MeV}}, \tag{3.9} $$

with θ_W the Weinberg angle and E_ν the electron neutrino energy. This cross section, computed for $< E_\nu >= 31.7$ MeV was found in good agreement with a measurement performed by LSND [132] resulting in:

$$ \sigma_{tot} = 10.1 \pm 1.1(\mathrm{stat.}) \pm 1.0(\mathrm{sys.}) \times 10^{-45} \mathrm{cm}^2 \frac{E_\nu}{\mathrm{MeV}}. \tag{3.10} $$

Note that this cross section increases linearly with the neutrino energy E_ν.

Compared to the one of IBD used to detect $\bar{\nu}_e$, this cross section is relatively small. Besides, the detection of ν_e in the MeV range via electron scattering is very sensitive to backgrounds from the natural radioactivity β and γ rays. Only a few low-background detectors, designed to study low energy solar neutrinos, could efficiently distinguish ν_e electron scattering signals from backgrounds. Finally, to provide a sufficient amount of neutrino interactions in the current kiloton-scale detectors, activities of the order of tens of MCi [4] are required from such ν_e sources.

Candidates isotopes: Ar and Cr

Two nuclei were used by the Gallex and SAGE collaborations and are still under considerations for radioactive sources experiments: ^{51}Cr and ^{37}Ar.

^{51}Cr decays to ^{51}V with a 27.7 days half-life. 90.1% of the time, it decays to the ground state of ^{51}V and emits a monochromatic 751 keV ν_e while in the remaining 9.9%, it decays toward an excited state thus emitting a 413 keV ν_e followed by a 430 keV gamma ray. A decay scheme of ^{51}Cr is displayed in Figure 3.9. ^{37}Ar decays to ^{37}Cl with a half-life of 35.0 days and produces 814 keV ν_e with a branching ratio of 100%.

[4] 1 Ci = 3.7×10^{10} Bq

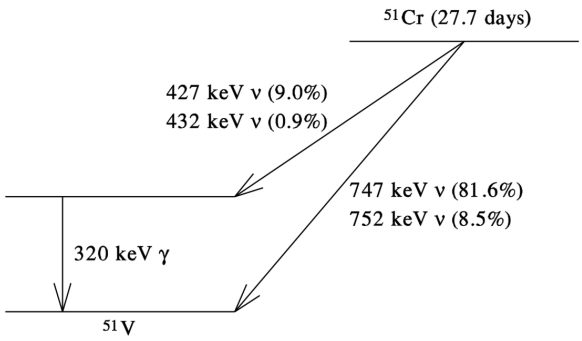

Figure 3.9: Decay scheme of ^{51}Cr to ^{51}V through electron capture [133].

Natural chromium is mainly composed of ^{52}Cr (83.8%) and contains 4.35% of ^{50}Cr. The ^{50}Cr thermal neutron capture cross section of 17.9 barn allows the large scale production of ^{51}Cr by neutron irradiation inside nuclear reactor cores through the $^{50}\mathrm{Cr}\,(n,\gamma)^{51}\,\mathrm{Cr}$ reaction. However, the higher concentration of ^{53}Cr in natural chromium (9.5%) along with its thermal neutron capture cross section of 18.7 barn leads to a lowering of the ^{51}Cr yield since neutrons are more likely to be absorbed by ^{53}Cr than by ^{51}Cr.

^{37}Ar is also produced by neutron irradiation in reactor cores but through the $^{40}\mathrm{Ca}\,(n,\alpha)^{37}\,\mathrm{Ar}$ reaction. This (n,α) reaction has a 1.75 MeV threshold and thus requires irradiation with fast neutrons instead of thermal neutrons.

Advantages and drawbacks

Both sources constitute a challenge from their production to their deployment.

In terms of heat release and gamma ray production, ^{37}Ar is easier to handle than ^{51}Cr since it requires a smaller shielding to dissipate its heat and attenuate its gamma activity. However, the solid metallic state of ^{51}Cr makes it easier to extract and manipulate than gaseous ^{37}Ar. The ^{53}Cr concentration reduces the efficiency of the neutron irradiation of chromium and leads to the need of several consecutive irradiations. Likewise, the threshold of the (n,α) reaction in the case of ^{37}Ar implies a fast neutron irradiation taking place in the close vicinity of the reactor fuel elements. Though Ar benefits from a slightly longer half-life than Cr, both are a challenge regarding transportation. With only a few nuclear reactor available for material irradiation, there is a significant probability that it will be located far from the deployment site. The half-lives of both isotopes in the order of a few tens of days require a fast transportation followed by a prompt deployment in order to provide a sufficient number of neutrino events. Finally, from the physics point of view, ^{37}Ar's higher neutrino energy could help better discriminate against natural radioactivity.

With all these arguments in consideration, the global effort on the use of neutrino sources tends to be directed toward ^{51}Cr.

3.2.3 Antineutrino sources

Antineutrino sources emit $\bar{\nu}_e$ via β^- decay:

$$ {}^{A}_{Z}X \rightarrow {}^{A}_{Z+1}\,Y + e^- + \bar{\nu}_e \ . \tag{3.11} $$

This reaction is a 3-body decay and, as explained in Section 3.1.4, electron and $\bar{\nu}_e$ are produced over a broad energy spectrum up to the maximum endpoint energy ($\mathcal{Q}_\beta$) of all the available β branches.

In liquid scintillator, $\bar{\nu}_e$ are detected via the IBD reaction that will be described in details in Chapter 4. Its cross section being higher than the one of electron scattering along with its dependency on E_ν^2 instead of E_ν allows the detection of a larger number of events. Furthermore the IBD signature, a time and space coincidence between a prompt positron energy deposition and a delayed neutron capture, allows a very efficient background discrimination that tends to reduce the requirements on the source activity as well. Hence, the required activity of a $\bar{\nu}_e$ source tends to be smaller by a factor of ~ 50.

Candidates isotopes

With an energy threshold of 1.806 MeV, the IBD reaction requires the use of a source isotope with a high $\mathcal{Q}_\beta$. Moreover, in order to avoid the transportation and deployment issues raised by the low half-lives of ν_e sources, isotopes will longer half-lives of the order of hundreds of days are preferable. Unfortunately, these two physical characteristics are strongly anti-correlated and nuclei with high enough $\mathcal{Q}_\beta$ for efficient IBD detection have half-lives typically shorter than a day, thus preventing the use of a $\bar{\nu}_e$ source made of a single radioisotope. However, to bypass this difficulty, one might look for a cascading couple of β^- isotopes with a long-lived parent nucleus and a short-lived daughter isotope. While finding a parent isotope with a half-life of the order of hundreds of days is an easy task, the daughter isotope must be carefully selected to provide a $\mathcal{Q}_\beta$ as high as possible above the IBD threshold to maximize the IBD reaction rate. A thorough search in nuclear databases led to the identification of several pairs of isotopes displayed in Table 3.2.

Couple	$\tau_{1/2}$ of parent	Q_β of daughter
^{42}Ar - ^{42}K	33 y	3.53 MeV
^{90}Sr - ^{90}Y	28.9 y	2.28 MeV
^{106}Ru - ^{106}Rh	372 d	3.55 MeV
^{144}Ce - ^{144}Pr	285 d	3.00 MeV

Table 3.2: Suitable couple for an $\bar{\nu}_e$ radioactive source [121].

The elected one: ^{144}Ce -^{144}Pr

With only $\sim$500 keV between the IBD threshold and its $\mathcal{Q}_\beta$, ^{90}Sr provides a modest reaction rate. Furthermore, its long half-life leads to a reduction of the reaction rate for typical experiment running periods between 1 and 2 years. While the half-life of ^{42}Ar is also quite long, its high $\mathcal{Q}_\beta$ compensates the loss of reaction rate and makes it a suitable candidate. ^{106}Ru and ^{144}Ce share both reasonable half-lives and high $\mathcal{Q}_\beta$ making them the best choices of isotope pairs with a small advantage for ^{106}Ru due to its higher endpoint energy.

However, the choice of the best couple is not only driven by physical arguments but by production feasibility at the industrial scale as well. Like its isotope ^{37}Ar, ^{42}Ar is produced through fast neutron irradiation on ^{40}Ar thus raising similar issues. Besides, the chances of a double neutron capture required to transform ^{40}Ar into ^{42}Ar are lowered by the fact that ^{41}Ar

has a very short half-life ($\tau_{1/2}$ = 109 ms). In addition, ^{42}Ar is produced in a gaseous state, very hard to manipulate. ^{42}Ar has thus been rejected from the possible candidates. ^{90}Sr , ^{106}Ru and ^{144}Ce are fission products created in nuclear reactors that could be extracted from nuclear spent fuel. However, in a reactor core, each fission products has a specific production rate expressed as the cumulative fission yield and corresponding to the number of nuclei produced per fission with a reactor core considered at equilibrium. Although this is only an approximation since long lived isotopes may never reach equilibrium during fuel irradiation, this quantity is a good indicator of the abundance and concentration of each fission product in reactor spent fuel. Table 3.3 summarizes the cumulative fission yield of the three isotopes of interest for thermal fissions of ^{235}U and ^{239}Pu , the two main fissile isotopes in commercial nuclear reactors. Due to its low fission yield for ^{235}U , ^{106}Ru is strongly disfavored compared to ^{90}Sr and ^{144}Ce .

	Cumulative fission yield (%)		
	^{106}Ru	^{90}Sr	^{144}Ce
^{235}U	0.401(6)	5.78(6)	5.50(4)
^{239}Pu	4.35(9)	2.10(4)	3.74(3)

Table 3.3: Cumulative thermal fission yields of ^{106}Ru , ^{90}Sr and ^{144}Ce [121] for the two main fissile isotopes fueling nuclear reactors.

Given their comparable fission yields for both ^{235}U and ^{239}Pu , ^{90}Sr and ^{144}Ce are the most probable candidates for a $\bar{\nu}_e$ source. However, as stated earlier, the low endpoint energy of ^{90}Sr and its long half-life tend to reduce both reaction rate and source activity, thus definitely rejecting the ^{90}Sr - ^{90}Y couple. Only the ^{144}Ce - ^{144}Pr pair remains as the most suitable couple for a $\bar{\nu}_e$ source. Though it will be explained in details in Chapter 7, note that the ^{144}Ce extraction from spent nuclear fuel has been proven feasible at an industrial scale.

3.3 Supernovae

While the two neutrino generators previously described were both man-made objects, there exist intense MeV (anti-)neutrino generators that can be found in nature called supernovae (SNe). Considered one of the most violent and spectacular astronomical events ever observed along with active galactic nuclei (AGN) and gamma-ray bursts (GRB), these stellar explosions emit a tremendous amount of light and neutrinos.

Due to their incredible luminosity, several supernovae have been observed with the naked eye throughout the history of mankind [134]. Records of such observations have been found in archives mostly from the European, Arabic, Chinese, Japanese and Korean civilizations and their existence is mentioned as well in Native American paintings and Maori culture. While the most famous is the SN1054[5] supernova which produced the Crab nebula and the Crab pulsar, the brightest of all historical times was SN1006 which stayed visible for about 3 years (21 months for SN1054). The two last galactic SN were observed with the naked eye in

[5]In the 1960s, Zwicky and his collaborators suggested the current naming scheme for supernovae: the prefix "SN" followed by the year of discovery with, in case of several discoveries per year, an upper-case letter from A through Z for the first 26 SN discovered that year. In case of more discoveries the upper-case letter is replaced by the lower-case sequences "aa,bb...".

1572 by Tycho Brahe and 1604 by Joannes Kepler. Since then, the invention of the telescope allowed the observation of many SNe in other galaxies. Another step has been taken in 1987 with the observation of SN1987A with the detection of both light and neutrinos coming from the same supernova (*c.f.* Section 3.3.2).

Supernovae can be classified into two types: type I and type II. Each of these two types can itself be divided into subgroups depending on the spectroscopic properties and luminosity features. Type I and II SNe are respectively characterized by the absence or presence of hydrogen lines in their spectra. However, SNe could also be classified with respect to their explosion mechanism: thermonuclear or core-collapse.

Thermonuclear SNe (or type Ia) are produced when a white dwarf that has been accreting mass from a companion star, reaches its instability limit and collapses. This collapse triggers the fusion of carbon and oxygen into heavier elements thus causing the thermonuclear explosion of the star [32]. Since they are all generated through the same process, all type Ia SNe have very similar characteristics. They emit the same amount of energy and have very similar light curves. This property, verified by the observation of numerous type Ia SNe in nearby galaxies, allows their use as *standard candles* for the measurement of galactic distances. The measurement of the Hubble constant and the Universe's matter density constant can be carried out using this technique as explained in Ref. [135].

However, while being useful for cosmological studies, thermonuclear SNe have a limited interest in neutrino physics since they do not produce a large amount of neutrinos compared to core-collapse supernovae. Only core-collapse SN will be considered hereafter.

3.3.1 Core-collapse supernova

Core-collapse SNe arise from the collapse of the core of a massive star ($M \geq 8\ M_\odot$). The wide mass and size ranges of these stars called *progenitors* implies a large variety of supernova explosion with very different visible effects. Core-collapse are thus classified into subtypes depending on their envelope composition (He or H) and/or light emission [136].

Core-collapse supernova dynamics

All stars undergo a long phase of hydrogen burning through the p-p and the CNO cycles [137]. These fusion cycles, represented on Figure 3.10, respectively account for 98.4% and 1.6% of the energy production in the Sun[6].

After the hydrogen is burned off and depleted, the star is no longer at equilibrium and its energy production is not sufficient to withstand gravitation. It starts to contract thus increasing its inner pressure and temperature, according to the equation of state of non-degenerate ideal gas $p \sim \rho \times T$. When a high enough temperature has been reached, helium starts to fusion to ^{12}C via a triple α-process. After all the helium has been fused into carbon, nitrogen and oxygen, the star undergoes another contraction leading to the fusion of these elements. Depending on the star mass, additional fusion processes may occur as shown in Table 3.4. The last reaction occurring in most stars with mass higher than 12 $M_\odot$ is the burning of silicon to produce nickel and iron. This phase, extremely fast compared to the previous ones, corresponds to the last phase of the star's burning process since, in the region of iron and nickel, the maximum binding energy per nucleon, of about 8 MeV/nucleon, has been reached. No energy can be gained by further fusion processes of heavier stable elements.

[6]Note that the ratio between these two production fractions depends on the type of the star.

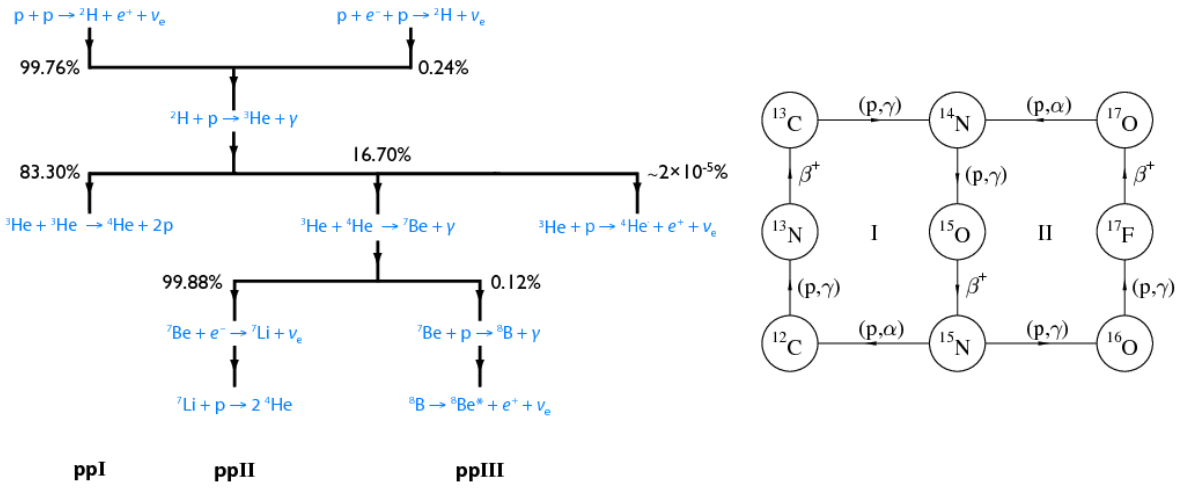

Figure 3.10: Left: Representation of the proton fusion processes in the Sun's p-p cycle. Right: Representation of the CNO cycle [137].

At this point, the star has an onion-like structure with a small and dense iron core surrounded by shells composed by elements of decreasing atomic number (Si, O, Ne, C, He).

Fuel	T_c [10^9K]	ρ_c [g.cm^{-3}]	Main product	T [yr]
H	0.04	5.81	He, N	1.11×10^7
He	0.18	1.39×10^3	C, O, Ne	1.97×10^6
C	0.83	2.39×10^5	Ne, Na, Mg	2.03×10^3
Ne	1.63	7.24×10^6	O, Mg, Si	0.732
O	1.94	6.66×10^6	Si, S	2.58
Si	3.34	4.26×10^7	Fe, Ni, Cr	5.01×10^{-2}

Table 3.4: Central temperature T_c, central density ρ_c and burning time T of the chronological burning phases of a 15 $M_\odot$ star [32].

The stability of the star's iron core is maintained by the pressure of the degenerate electron gas ruled by the Pauli exclusion principle at high densities. However, the creation of massive elements through fusion increases the core mass until it reaches the Chandrasekhar mass of about 1.4 $M_\odot$. At this point, the constantly increasing density and temperature due to gravitation can no longer be compensated by the electron pressure and the core starts to contract, causing an increase of the photodissociation process on iron:

$$\gamma + {}^{56}\text{Fe} \rightarrow 13\alpha + 4\text{n}. \tag{3.12}$$

This endothermic reaction absorbs about 124 MeV leading to a reduction of the thermal pressure and electron kinetic energy. The electron capture (EC) on nuclei and free protons:

$$e^- + {}^{56}\text{Fe} \rightarrow {}^{56}\text{Mn} + \nu_e \tag{3.13}$$

$$e^- + p \rightarrow n + \nu_e \ , \tag{3.14}$$

further contributes to the reduction of the electron density and pressure. These two reactions called *neutronization processes* create mainly neutron-rich nuclei, unable to balance the gravitational pressure previously compensated by the electron gas pressure. The core starts to collapse faster and, when the core density reaches 10^{12} g.cm^{-3}, neutrinos can no longer escape since, due to neutrino-nucleus coherent scattering, their mean free path is smaller than the core's radius.

This effect, referred to as *neutrino trapping*, causes neutrinos to move with the surrounding collapsing environment while being at thermal equilibrium with it. The envelope separating the region opaque to neutrinos and the external free-streaming region is defined as the *neutrinosphere* in analogy with the Sun's photosphere. In this transition region, the neutrino energy spectrum is thermal and can be approximated with a Fermi-Dirac distributions as detailed in Section 3.3.1.

In the meantime, the collapse continues and the iron core is now in freefall at supersonic speed. Finally, the collapsing core reaches a density higher than nuclear densities ($\rho \gtrsim 10^{14}$ g.cm^{-3}). At such densities, the nuclear force becomes strongly repulsive and the matter incompressibility causes the collapse to stop and reverse. While the inner core reaches an hydrostatic equilibrium and forms a *proto neutron star* (PNS), a strong shockwave is sent outwards and propagates though the core's outer layers with a velocity of the order of 100 km.ms^{-1} thus slowing its free-fall. This causes the PNS to form an unshocked core, with a radius of roughly 10 km and a density of about 10^{14} g.cm^{-3}, surrounded by a shocked mantle extending up to 200 km at a decreasing density.

As it propagates through the outer PNS core, the shockwave dissipates its energy via the photodissociation of Fe nuclei into nucleons. The high electron capture rate on protons leads to a huge production of neutrons and electronic neutrinos, piling up behind the dense medium of the shockwave. After a few ms, when the shock reaches layers with density lower than 10^{11} g.cm^{-3}, a shock *breakout* occurs and all the trapped neutrinos are released within a few ms time window. This prompt emission called the *neutronization burst* carries about 10^{51} ergs in ν_e. Nonetheless, this burst is too short to emit a significant amount of neutrino since it only originates from the neutronized periphery of the PNS, not its inner core. With most of its energy expelled in the form of neutrinos, the shockwave is now weakened and stalls at a radius of about 200 km, 100 ms after the initial bounce, without reaching the star's outer layers. At that point, different scenarii can occur depending on the star mass. If the progenitor star weights less than 10 solar masses, the shockwave, even though weakened, is able to eject the star envelope thus generating a supernova explosion. This is the prompt SN scenario. If however, the progenitor mass is so high that the shockwave fails to reach its envelope, the surrounding medium continues to fall on the PNS. At some point the pressure of the degenerate nucleon gas cannot withstand gravitation anymore and the core collapses into a black hole without a supernova explosion [32].

In order to revive the stalled shock and generate a supernova explosion in the case of massive stars, a new mechanism has to be introduced. Recent computations carried out with the help of powerful supercomputers [138] allowed 2D and 3D simulations of core-collapse supernovae and helped strengthen the neutrino-driven explosion hypothesis[7]. In this scenario, the shock is revived by the energy deposition of the neutrino flux produced in the PNS, between 0.5 and 1 s after the bounce. Inside the PNS core, neutrinos of all six flavors are

[7]Note that, given their preliminary nature, most of the current 3D core-collapse simulations do not yield a SN explosion.

created through thermal processes,

$$e^- + e^+ \rightleftharpoons \nu + \bar{\nu} \tag{3.15}$$
$$N + N \rightleftharpoons N + N + \nu + \bar{\nu}, \tag{3.16}$$

scatterings,

$$\nu + n, p \rightleftharpoons \nu + n, p \tag{3.17}$$
$$\nu + A \rightleftharpoons \nu + A \tag{3.18}$$
$$\nu + e^{\pm} \rightleftharpoons \nu + e^{\pm} \tag{3.19}$$

and neutrino-neutrino reactions,

$$\nu_e \ + \nu_x \rightleftharpoons \nu_e \ + \nu_x \, (\nu_x = \nu_\mu, \bar{\nu}_\mu, \nu_\tau, \bar{\nu}_\tau) \tag{3.20}$$
$$\nu_e \ + \bar{\nu}_e \ \rightleftharpoons \nu_{\mu,\tau} + \bar{\nu}_{\mu,\tau}., \tag{3.21}$$

with A a nucleus, N a nucleon and ν any kind of neutrino flavor. In addition, electron neutrinos are produced in the highly degenerated nucleon gas via the electron capture process in Eq. 3.14 and electron antineutrinos are produced via the positron capture on neutron:

$$e^+ + n \rightarrow p + \bar{\nu}_e \ . \tag{3.22}$$

This huge amount of neutrinos is still trapped in the PNS core and cannot escape the neutrinosphere. However, since neutrino interactions are flavor and energy dependent, there are different neutrinospheres for different flavors. Given the composition of the SN medium (n, p, e^-) and the neutrino energy, insufficient to create muons and taus, ν_e and $\bar{\nu}_e$ can interact via both charged and neutral current processes whereas $\nu_x \, (\nu_\mu, \bar{\nu}_\mu, \nu_\tau, \bar{\nu}_\tau)$ can only interact through the flavor-independent neutral current processes. Therefore, one can define three different energy-dependent neutrinospheres respectively corresponding to ν_e , $\bar{\nu}_e$ and ν_x. As previously stated, the neutrino emission spectrum on the surface of these neutrinospheres is thermal at the corresponding energies.

Neutrino heating and cooling is dominated by the two absorption reactions and their inverse:

$$\nu_e \ + n \rightleftharpoons p + e^- \tag{3.23}$$
$$\bar{\nu}_e \ + p \rightleftharpoons n + e^+. \tag{3.24}$$

However, due to the neutron-rich matter composing the PNS, the opacity of ν_e at a given energy is larger than the opacity of $\bar{\nu}_e$ at the same energy and the ν_e neutrinosphere has a larger radius than the $\bar{\nu}_e$ neutrinosphere. Similarly, due to their inability to interact through charged current, the ν_x neutrinosphere radius is even smaller. Typical neutrinosphere radii vary between 50 and 100 km. The temperature being a function of the decreasing SN radius, the average time-integrated neutrino energy follows the relation $\langle E_{\nu_e} \rangle < \langle E_{\bar{\nu}_e} \rangle < \langle E_{\nu_x} \rangle$. Curves of luminosities and average neutrino energies are displayed on Figure 3.11.

The emission of neutrinos lasts for about 10 seconds and carries most (99%) of the lepton number and energy of the PNS. One can thus approximate the energy released in a supernova explosion using the expression of the neutron star binding energy:

$$E_B \simeq \frac{3}{5} \frac{G_{\rm grav} M_{\rm PNS}^2}{R_{\rm PNS}} = 3 \times 10^{53} {\rm ergs} \left(\frac{10 \text{ km}}{R_{\rm PNS}} \right) \left(\frac{M_{\rm PNS}}{1.4 \text{ M}_{\rm PNS}} \right)^2 , \tag{3.25}$$

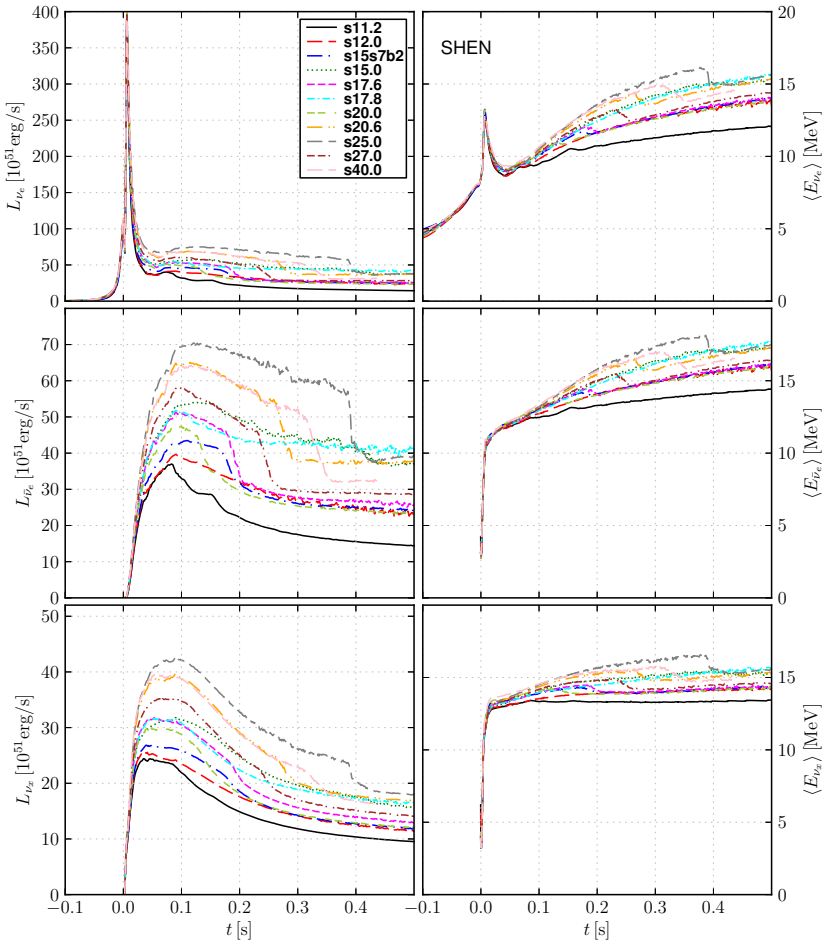

Figure 3.11: Time evolution of radiated luminosities (left) and average neutrino energies (right) fo ν_e (top), $\bar{\nu}_e$ (middle) and ν_x (bottom). Time is normalized to the moment of the bounce. The different color curves correspond to (non-exploding) 1D simulations of several solar-metallicity progenitors and a 15 $M_\odot$ progenitor referred to as "s15s7b2" [139].

with G_{grav} the gravitational constant and R_{PNS} and M_{PNS} the radius and mass of the proto neutron star. This value of the energy carried away by neutrinos will be used in the simulations described in Section 5.4.

Only a fraction varying from 5 to 10% of this incredible amount of energy is sufficient to revive the shock and finally cause the supernova explosion. The remaining fraction of neutrinos leaves the supernova medium and propagates through space. Then, given their lower mean free path, photons are able to escape the dense supernova medium several hours after neutrinos. Finally, the envelope surrounding the PNS is expelled by the shockwave, ejecting the massive elements heavier than iron created by neutron capture in the neutron-rich supernova medium.

As they travel through the supernova medium and later through space, neutrinos or antineutrinos can oscillate and undergo MSW resonances. Additional flavor conversion phenomena occur due to neutrino self-interaction as well as the presence of shock waves and turbulence. The computation of these oscillation phenomena can differ from one model to

the other, as explained in the next section. While many features concerning the mechanisms and the occurrence of such flavor conversion phenomena have been unraveled, important open questions remain [140]. Note also that the recently discovered lepton-number emission self-sustained asymmetry (LESA) is expected to produce a dipole pattern during the accretion phase [141].

Expected signals on earth

For an observer on Earth, the most obvious SN signals are optical photons. Indeed, although only 1% of its energy is carried away by photons, the visible luminosity of a core-collapse SN reaches the amount 10^{36} W, 10 orders of magnitude greater than the solar luminosity, making it as bright as an entire galaxy as displayed in Figure 3.12. To this value, one can add the sum of the luminosities in all the regions of the electromagnetic spectrum.

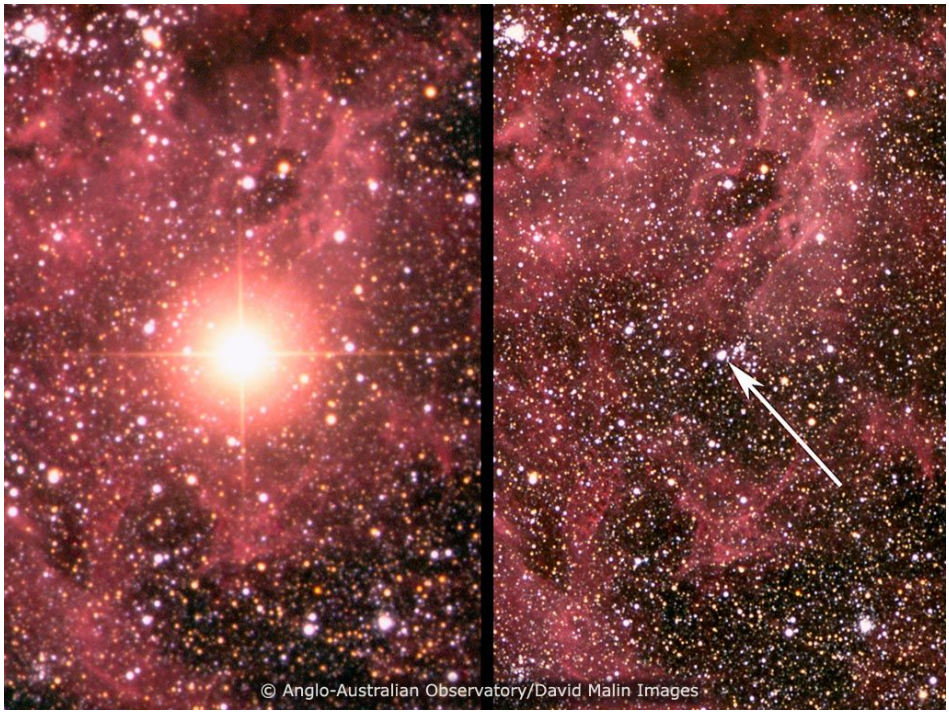

Figure 3.12: Picture of SN1987A taken in the visible spectrum before it exploded (right) and 10 days after the explosion (left) [142].

The light emitted during a supernova explosion peaks quickly after the shock. The peak typically lasts from a few hours to a few days depending on the progenitor star mass and shock temperature. This peak is followed by a quick cooling phase preceding a longer phase when temperature and luminosity remain rather constant, thus showing as a plateau in luminosity curves. This behavior originates from a balance between the contracting photosphere and the expanding star ejecta. While supernovae with massive enough progenitors reach this plateau right after the cooling phase, smaller supernovae such as SN1987A first undergo a strong decline before brightening again to reach the plateau. After this phase lasting roughly 100 days, the luminosity follows an exponential decay since it is dominated by the radioactive decay of unstable nuclei, mainly ^{56}Ni and ^{56}Co, emitting γ rays that are captured in the

ejecta and converted into optical photons. The light curve of SN1987A and other observed SN is displayed in Figure 3.13.

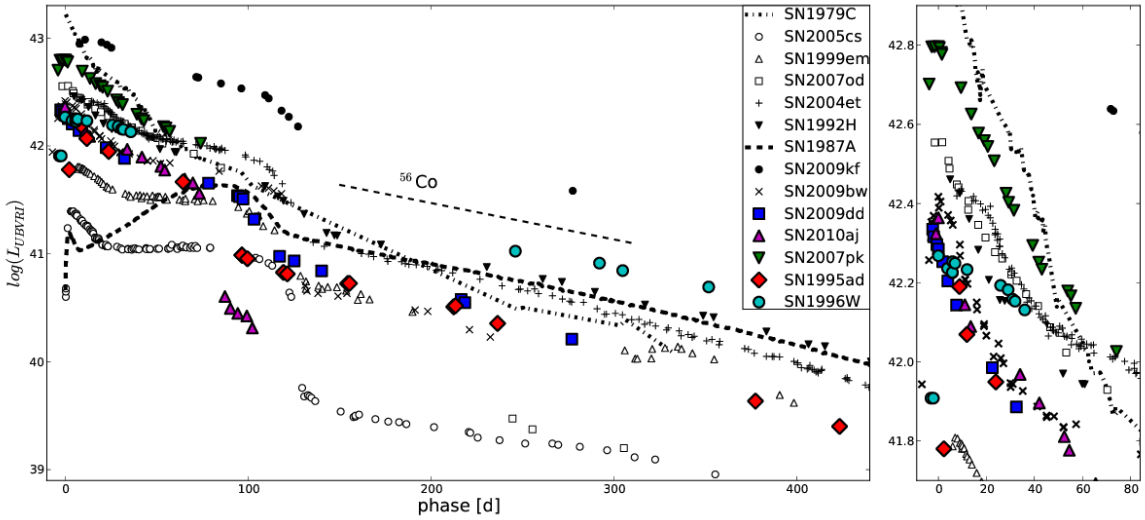

Figure 3.13: Left: Integrated light curves (over the visible spectrum) obtained using bolometric measurements for different type II SN. The phase expressed in days is taken with respect to the peak or, for SN1987A with respect to the bounce. Right: Close-up of the light curve in the first 80 days [143].

While the observation of light from supernovae is quite straightforward and has been carried out for centuries, there is another messenger whose observation can nowadays be performed: the neutrino. The detection of the neutrinos emitted by SN1987A opened the field of extrasolar neutrino astronomy and is the origin of many models[8] of neutrino emission and behavior within the complex and poorly known supernova medium.

In this work we will focus on two of them: the so-called Livermore [144] and Gava-Volpe-Kneller-McLaughlin (GVKM) [145] models.

In 1997, T. Totani, K. Sato, H.E. Dalhed and J.R. Wilson published a model of supernova neutrino energy spectrum, commonly referred to as the "Livermore" model, the latter two authors belonging to the Lawrence Livermore National Laboratory. Previous models were based on the assumption the neutrino energy followed a Fermi-Dirac (FD) distribution due the thermal nature of their emission. However, as explained in Section 3.3.1, the neutrino opacity changes with the neutrino energy. Considering this, the neutrino energy spectrum can be modeled as a blackbody radiation from a spherical surface at temperature $T_{\bar{\nu}_e}$ whose radius depends on the neutrino energy $E_{\bar{\nu}_e}$. The energy spectrum thus differs from a FD distribution with zero chemical potential and becomes somewhat "pinched" with a deficit in both low and high energy ranges. The $\bar{\nu}_e$ energy spectrum $\frac{dF_{\bar{\nu}_e}}{dE_{\bar{\nu}_e}}$ can be written as:

$$\frac{dF_{\bar{\nu}_e}}{dE_{\bar{\nu}_e}} = \frac{L_{\bar{\nu}_e}}{4\pi D^2} \frac{1}{T_{\bar{\nu}_e}^4 \; F_3(\eta)} \frac{E_{\bar{\nu}_e}^2}{e^{E_\nu / T_{\bar{\nu}_e}} \; ^{-\eta} + 1}, \tag{3.26}$$

where $L_{\bar{\nu}_e}$ is the supernova $\bar{\nu}_e$ luminosity, D is the supernova distance, η is the degeneracy

[8] On average over the last 27 years following the detection of the SN1987A neutrinos, they are the subject of one paper every ten days !

or "pinching parameter" and $F_3(\eta)$ is defined as:

$$F_3(\eta) = \int_0^\infty \frac{x^n}{e^{x-\eta}+1} dx. \tag{3.27}$$

Figure 3.14 shows all the relevant characteristics of the neutrino emission for the Livermore model, such as luminosities, average energies and energy spectra.

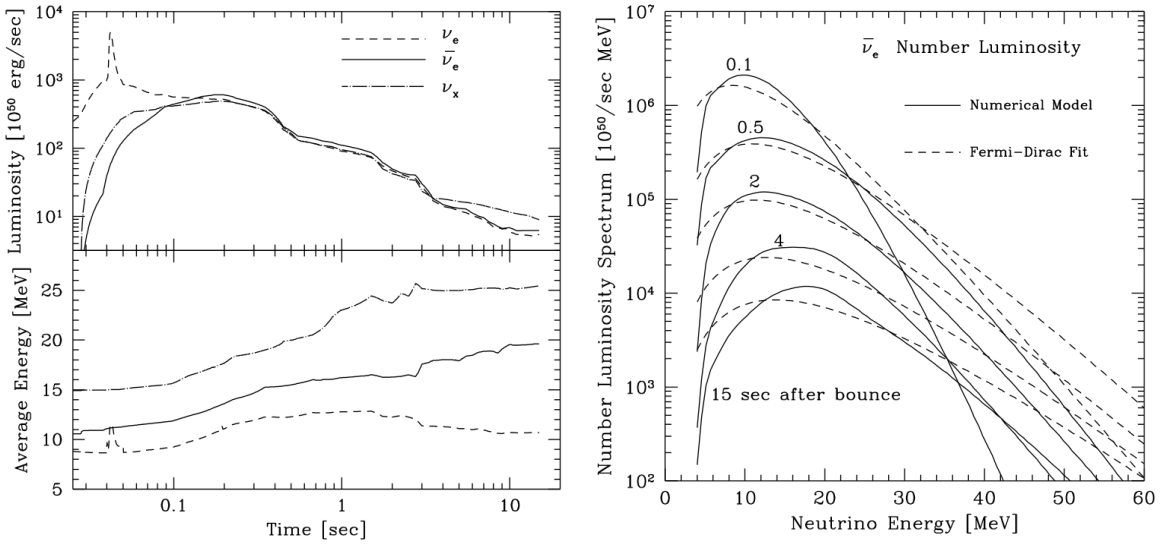

Figure 3.14: Left: Evolution of the neutrino luminosity and average energy over a 10 s window for all flavors. Right: Energy spectra of $\bar{\nu}_e$ for several periods of time after the core bounce. The dashed lines are the non-pinched FD distributions that have the same luminosity and average energy than the calculations in solid lines [144].

At the time the model was developed, neutrino oscillations were not discovered yet (*c.f.* Section 1.1). However the existence of the solar and atmospheric neutrino anomalies seemed to point towards the existence of an oscillation phenomenon. Possible effects on the energy spectrum arising from these oscillations in vacuum and matter via the MSW mechanism have been discussed at that time but not thoroughly studied.

A first numerical calculation including both self-interaction and shockwave effects have been published in 2009 by a group composed of J. Gava, C. Volpe, J. Kneller and G.C. McLaughlin thus being referred to as the "GVKM" model. By taking into account neutrino-neutrino processes, dynamic MSW effects with time-dependent supernova density profiles and decoherence, this model provides a more realistic $\bar{\nu}_e$ flux as expected on Earth. Computations with oscillations requires a knowledge of all PMNS parameters however, at that time, the last mixing angle θ_{13} was yet to be discovered. With the assumption of a "large" angle ($\theta_{13} > 10^{-4}$) and a zero δ_{CP} phase, antineutrinos undergo an adiabatic MSW resonance during the explosion early times (< 1 s). The neutrino spectrum is then considered "cold" respectively to the average neutrino energy. When passing through the MSW high resonance region, the shockwave causes neutrino conversion to become non-adiabatic and the neutrino spectrum becomes "hot". Figure 3.15 shows the $\bar{\nu}_e$ energy spectrum for both conversions. Note that in the case of a normal mass hierarchy, the antineutrino flux does not change while traveling through the star and its energy spectrum remains "cold".

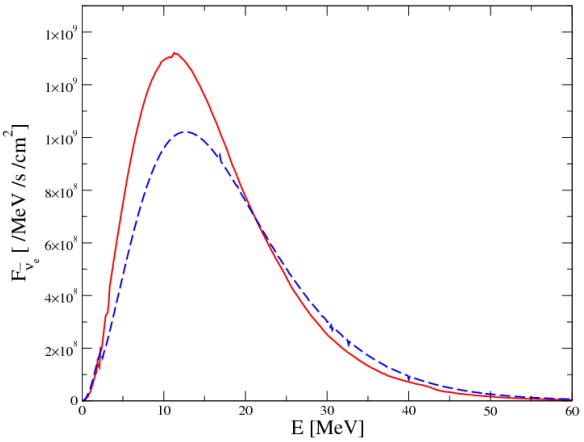

Figure 3.15: Energy spectra of $\bar{\nu}_e$ on Earth in case of adiabatic (solid line) and non-adiabatic (dashed line) conversions in the star [145].

3.3.2 SN1987A - An observed supernova

On the 23$^{\text{rd}}$ of February 1987 the brightest supernova since Kepler's in 1607 was observed. This type II supernova, called SN 1987A since it was the first one observed that year, occurred in the Large Magellanic Cloud (LMC) about 50 kpc, or 160'000 light-years, away from Earth. Its progenitor was identified as Sanduleak -69° 202, a blue supergiant, with a mass of about 20 $M_\odot$ [146]. While SN1987A provided a huge amount of information in all regions of the electromagnetic spectrum, the most interesting feature was the first detection of neutrinos from the actual gravitational collapse[9].

At that time, four neutrino detectors were operating and claimed the observation of an unusual rate of neutrinos 2.5 hours before the optical discovery of the SN1987A supernova [147, 148, 149, 150]. Two of these detectors were water Čerenkov detectors, Kamiokande-II and IMB, the other two, Baksan and Mont-Blanc, being liquid scintillator detectors. While the events observed in Kamiokande-II, IMB and Baksan occurred within a time window accounting for the time calibration uncertainties between the detectors, the events observed by the Mont-Blanc experiment have been recorded about five hours earlier. Considering that these events lie close to the experiment trigger threshold of 5 MeV, it is usually assumed that they are a statistical fluctuation unrelated to the supernova signal. The analyses of the SN1987A neutrino signal thus only consider the data from Kamiokande-II, IMB and Baksan.

From the characteristics of the neutrino events listed in Table 3.5, several theoretical predictions have been tested. All 29 observed events were due to $\bar{\nu}_e$ interactions and a combined analysis led to the determination of the $\bar{\nu}_e$ luminosity $L_{\bar{\nu}_e}$ and average temperature $T_{\bar{\nu}_e}$ [151]:

$$L_{\bar{\nu}_e} = 4.8^{+2.3}_{-1.0} \times 10^{52} \text{ ergs} \qquad \text{and} \qquad T_{\bar{\nu}_e} = 3.9^{+0.5}_{-0.3} \text{MeV}. \tag{3.28}$$

These results are in good agreement with the theory described in Section 3.3.1 that postulated a $\bar{\nu}_e$ luminosity of $L_{\bar{\nu}_e} = 1/6 \times L_{tot} = 5 \times 10^{52}$ ergs. With all 29 events spread over a time interval of about 10 s, the observation is in agreement with the numerical calculations of the emission time depending on the cooling time and accretion time.

[9]For designing the Kamiokande detector that detected these neutrinos, Masatoshi Koshiba was rewarded by the 2002 Nobel Prize in Physics

Detector	Relative time [ms]	E [MeV]	Detector	Relative time [ms]	E [MeV]
Kamiokande-II	0	20.0±2.9	IMB	0	38±7
Kamiokande-II	107	13.5±3.2	IMB	412	37±7
Kamiokande-II	303	7.5±2.0	IMB	650	28±6
Kamiokande-II	324	9.2±2.7	IMB	1141	39±7
Kamiokande-II	507	12.8±2.9	IMB	1562	36±9
Kamiokande-II	686	6.3±1.7	IMB	2684	36±6
Kamiokande-II	1541	35.4±8.0	IMB	5010	19±5
Kamiokande-II	1728	21.0±4.2	IMB	5582	22±5
Kamiokande-II	1915	19.8±3.2			
Kamiokande-II	9219	8.6±2.7			
Kamiokande-II	10433	13.0±2.6			
Kamiokande-II	12439	8.9±2.9	Baksan	0	12.0±2.4
Kamiokande-II	17641	6.5±1.6	Baksan	435	17.9±3.6
Kamiokande-II	20257	5.4±1.4	Baksan	1710	23.5±4.7
Kamiokande-II	21355	4.6±1.3	Baksan	7687	17.5±3.5
Kamiokande-II	23814	6.5±1.6	Baksan	9099	20.3±4.1

Table 3.5: Characteristics of the SN1987A neutrino events observed in Kamiokande-II, IMB and Baksan. The relative time is expressed in ms with respect to the first event detected in each detector [151].

Although the data from SN1987A neutrinos was too sparse to provide detailed information on the supernova mechanism, it brought several interesting results on neutrino properties. While these results are nowadays more constrained, they were competitive when first discovered. The first property that can be easily extracted from the data is the neutrino lifetime. Since no significant discrepancy between the expected and observed flux of neutrinos has been observed, one can assume no neutrino decay occurred during their transit to Earth thus setting a lower limit on the $\bar{\nu}_e$ lifetime of approximatively 1.5×10^5 years [152].
From the arrival time and energy dispersion, one can set an upper bound on the neutrino mass since while the latter remains constant, the time of flight is shorter as the energy increases. A more recent Bayesian analysis of the SN1987A neutrino events has been performed in Ref. [153] and set an upper bound on the $\bar{\nu}_e$ mass of 5.7 eV (95% C.L). This shows as well that neutrinos travel nearly at the speed of light.
Other bounds on properties such as the $\bar{\nu}_e$ magnetic moment, electric charge or decay into heavy neutrino are summarized in [32].

With only 29 detected events, the observation of SN1987A neutrinos already brought an incredible amount of information. Considering all current neutrino detectors, the next supernova, if occurring in our galaxy or its dwarf satellites, will provide us a statistic larger by several orders of magnitude along with a detailed picture of the supernova mechanisms. Hence the need to quickly and efficiently detect neutrinos from the next supernova. This is the goal of the SNEWS network.

3.3.3 The SNEWS network

The SNEWS (SuperNova Early Warning System) [154] collaboration gathers experimenters from neutrino experiments capable of supernova detection. Its primary goal is to provide the astronomical community with an early alert in case of a supernova occurring.
To do so, each experiment that belongs to the network needs to implement a neutrino burst monitoring system. Since each experiment has different detection features (detection technique, energy threshold, expected rate, etc..), each burst trigger system needs to fit criteria defined by the experiment's collaboration. When these criteria are met and a burst of events is detected by an experiment, a client sends out an alert to the SNEWS coincidence server. If the server finds a coincidence between several alerts in a 10 s time windows, an alert is sent to the SNEWS alert mailing list, hosted at snews.bnl.gov. These alerts are classified as "gold" and "silver" depending on their robustness. Gold alerts require higher quality requirements and a low false alert rate from the experiments involved in the coincidence, unlike silver alerts. Gold alerts are thus sent to both experimentalists and astronomers while silver alerts are only sent to experimentalists for a possible upgrade after human checking. The flowchart of the SNEWS alert system is shown in Figure 3.16.

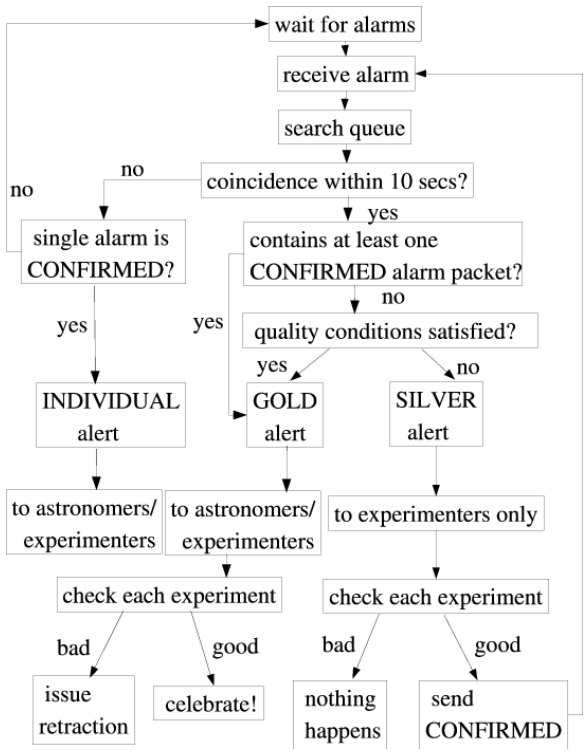

Figure 3.16: Flowchart of the sequence of events leading to the sending of a gold or silver alert [155].

As of today, a total of seven detectors belong to the SNEWS network: KamLAND, Borexino, SNO, Daya Bay, LVD, Super-Kamiokande and IceCube. These detectors, while based on different technologies as summarized in Table 3.6, have to provide an early warning fulfilling requirements known as "The 3 P's":

- Prompt: Providing an early supernova alert is equivalent to running against the clock. With only a few hours between the arrival time of neutrinos and light on Earth, a

complete automation of the process is mandatory to avoid any time-consuming human checking of an individual detector's alert.

- Pointing: While the prompt detection of a supernova would already be a success, having the ability to point towards its location would be even better. With a majority of the detected events being Inverse Beta Decay (IBD) events, pointing becomes challenging but not unreachable (*c.f.* Chapter 4). However, it is generally considered that only Super-Kamiokande, sensitive to the neutrino-electron elastic scattering reaction (ES), is currently capable of reconstructing a supernova location. The simulations I conducted, presented in Section 5.4, aimed at proving the feasibility of a supernova pointing by combining the directional information carried by the IBD interactions in large liquid scintilllator detectors. With the SNEWS detectors scattered over the globe, triangulation might be possible but, in practice, it requires high statistics coupled with a very precise time calibration between detectors.

- Positive: With an estimated rate of galactic core-collapse supernovae of 3 per century, the rate of accidental fake alerts is required to be set very low, fewer than one per century. For instance, in the case of a gold alert, each individual experiment's false alarm rate should not exceed one per week.

Detector	Technology	Mass [kt]	Location	Events (10 kpc)
KamLAND	Liquid scintillator	1	Japan	300
Borexino	Liquid scintillator	0.3	Italy	100
SNO	Liquid scintillator	1	Canada	300
Daya Bay	Liquid scintillator	6×0.05	China	100
LVD	Liquid scintillator	1	Italy	300
Super-Kamiokande	Water Čerenkov	32	Japan	7'000
IceCube	Ice Čerenkov	∼3000	South Pole	∼500'000

Table 3.6: Main characteristics of the detectors currently belonging to the SNEWS network. A expected number of detected neutrinos in the event of a supernova occurring at 10 kpc, with an average energy of 12 MeV and a $\bar{\nu}_e$ luminosity of 5×10^{52}ergs, is displayed.

To test its response in case a real supernova event, SNEWS can issue fake alerts, advertised as such, to the astronomical community. There is however a difference of opinion between astronomers and neutrino physicists. The former often ask for a lower coincidence threshold, thus improving the detection sensitivity at the price of an higher false alarm rate while the latter are often skeptical to the increase of the rate of "false positives" given the rarity of true events they usually deal with. In reality, lowering the detection threshold would not significantly increase the sensitivity, most detectors already being sensitive to the entire Milky Way. On the other hand, an increase of the false alerts rate would help exercise the system and keep the interest of the astronomical community high. As of today, SNEWS has not issued any SN alerts.

Chapter 4

Inverse Beta Decay process: Theory and Simulation

While the distinction between antineutrino and neutrino has been carefully made in the previous chapters, the following chapters will mostly deal with antineutrinos. For a simpler reading, the term 'neutrino' will thus be used in both cases, except if stated otherwise.

4.1 Inverse Beta Decay reaction

First used in 1956 to prove the existence of the neutrino, the Inverse Beta Decay (IBD) reaction is still the most used interaction to detect electron antineutrinos. Its characteristics will be explained in details in the following.

4.1.1 Theoretical basis

In the framework of the Standard Model of particle physics, neutrinos only interact via electroweak processes, through the exchange of neutral (Z^0) or charged ($W^{\pm}$) gauge bosons. These processes are then referred as *neutral* (NC) or *charged* (CC) currents. Like the other flavors, electronic antineutrinos can thus interact on electrons or nucleons via these currents.

The neutrino-electron elastic scattering presented in Section 3.2 brings little interest to the detection of $\bar{\nu}_e$ since it does not yield a specific signature other than the energy deposited by the ionizing electron. The NC $\bar{\nu}_e$ interaction on a nucleon is even harder to detect since, while having the same signature as the neutrino-electron elastic scattering, it implies a nucleus recoil with an energy in the keV range for MeV neutrinos. Finally, the CC $\bar{\nu}_e$ interaction on a proton or quasielastic scattering of $\bar{\nu}_e$ on proton, i.e. the IBD interaction:

$$\bar{\nu_e} + p \rightarrow e^+ + n \tag{4.1}$$

yields the most distinguishable signature with the simultaneous emission of a positron and a neutron. Besides, its high cross section places it above almost all others in terms of detection rate.

Let us now review some of the IBD reaction features such as the total cross section and the secondary particles energies. In the following, only the first order approximations, precise enough at low energies, will be taken into account. The precise IBD kinematics with second order corrections will be thoroughly described in Section 4.2.

The IBD reaction has a threshold depending on the nucleus the target proton is bound to. The lighter the target nucleus is, the lower the IBD threshold is set. Neutrino detectors relying on the IBD detection widely use organic liquid scintillator, very rich in hydrogen atoms. Considering an IBD reaction of a $\bar{\nu}_e$, whose mass can be neglected, on a hydrogen nucleus, called free proton from now on, assumed at rest, the energy threshold of the reaction can be expressed in the laboratory frame as:

$$E_{thr} = \frac{(m_e + m_n)^2 - m_p^2}{2m_p} \simeq 1.806 \text{ MeV}, \tag{4.2}$$

with m_p, m_n and m_e respectively the proton, neutron and electron masses. Note that the threshold of this reaction occurring on a proton bound to a ^{12}C carbon atom is 14 MeV, quite high with respect to the energy spectrum of reactor neutrinos, for instance.

Above this threshold, the relation between the neutrino and positron energies is, at zeroth order, given by:

$$E_e^{(0)} = E_\nu - \Delta, \tag{4.3}$$

with $\Delta = m_n - m_p$, the nucleon mass difference.

From this expression of the energy, one can compute the momentum $p_e = \sqrt{E_e^2 - m_e^2}$. Both can then be used to express a zeroth-order approximation of the cross section:

$$\sigma \approx \kappa_{IBD} \times \frac{p_e E_e}{\text{MeV}^2} \text{ cm}^2, \tag{4.4}$$

with $\kappa_{IBD} = 9.61 \times 10^{-44}$ cm^2 the IBD prefactor, which uncertainty is driven by the neutron lifetime measurement. It is important to emphasize that, however convenient and easy to handle, this cross section is strongly biased at energies higher than 10 MeV. A more precise expression will be derived in Section 4.2.

4.1.2 Observables

The successful detection of a $\bar{\nu}_e$ via IBD relies on the observation of two distinct signals, respectively corresponding to the energy deposition of the positron and the neutron. While both particles are emitted simultaneously, their energy depositions are separated in time.
The ionizing nature of the positively charged positron leads it to loose its energy as it propagates in the surrounding medium. When its kinetic energy becomes null, it annihilates with an electron thus creating two gamma rays with a total energy of 2m_e, m_e being the electron mass. The overall energy deposited by the ionization and annihilation of the positron is called the *visible* energy $\text{E}_{\text{vis}} = E_e + m_e$ with E_e the total positron energy, sum of its kinetic energy T_e and mass m_e. This first energy deposition is called the *prompt* event.

After its emission, the neutron, given its neutral charge, can only loose its energy via scattering off surrounding nuclei. This process called *moderation* decreases its energy until it reaches typical thermal equilibrium at ∼0.025 eV (300 K). The neutron then scatters at thermal energies before it gets captured on a nucleus. This process called *diffusion* is a random walk centered around the thermalization point with a duration depending on the medium average neutron capture cross section. The neutron capture leads to the emission of secondary particles, usually gamma rays or alpha particles. The energy deposited by those particles is called the *delayed* event, as opposed to the prompt event, since it occurs several microseconds later.

Since both events originate from the same neutrino interaction, they are correlated. Since the actual delayed energy deposition comes from the neutron capture and not its previous interactions, the amount of deposited energy only depends on the capture reaction. This reaction usually occurs at thermal energies and does not depend on the initial neutron energy. The prompt and delayed amount of energy deposited are thus uncorrelated. However, this is not the case for the time and locations of these events. Indeed, being emitted at the same time-space location, both particles will yield to events related in time and position, depending on their respective behavior in the medium.

A sketch, displaying the basic of the IBD kinematics from the emission of both particles to their annihilation or capture, is shown in Figure 4.1

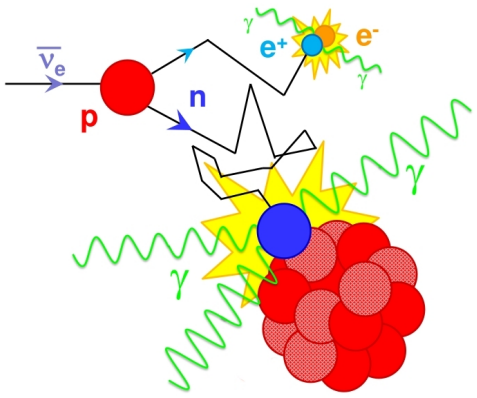

Figure 4.1: Sketch of basic kinematics of the IBD interaction. In this picture, the positron annihilates with an electron thus creating a pair of gamma rays and the neutron gets captured on a heavy (A,Z >> 1) nucleus such as gadolinium [156].

4.2 Detailed IBD kinematics

While first-order approximations of the IBD characteristics are sufficient enough to obtain trustworthy results at low energies such as reactor energies, one needs to account for second-order corrections at higher energies.

Several computations have been carried to obtain precise expressions of the IBD cross sections. Indeed the precision required both in spectral shape and norm from reactor experiments made mandatory the use of second order corrections to the IBD cross section. In the following, I will focus on the computation performed by Alessandro Strumia and Francesco Vissani [157]. This expression, valid in most of the whole sub-GeV energy range, is relevant when detecting neutrinos emitted by the generators described in Chapter 3.

4.2.1 Total cross section: Interaction rate

The total cross section drives the interaction rate of the IBD reaction. Indeed, the $\bar{\nu}_e$ energy spectrum observed in a detector is proportional to the product of the emission $\bar{\nu}_e$ energy spectrum and the total cross section as displayed in Figure 4.2.

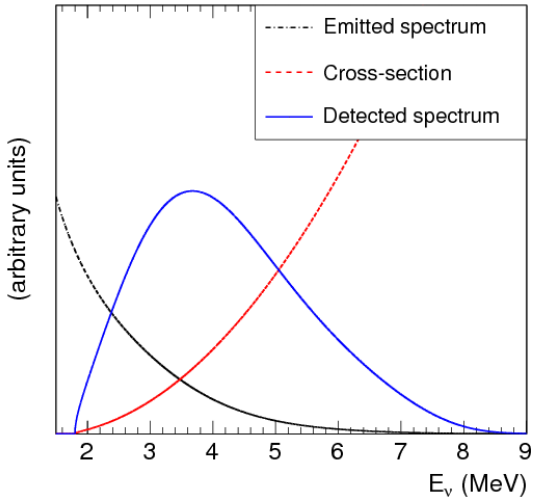

Figure 4.2: Illustration of the $\bar{\nu}_e$ detected energy spectrum as the product of the IBD cross section and the $\bar{\nu}_e$ energy spectrum emitted by a nuclear reactor [94].

The total IBD cross section computed by P. Vogel and J.F. Beacom in Ref. [8] is expressed as a function of the positron energy:

$$\sigma\left(E_e\right) = \frac{2\pi^2}{m_e^5 f^R \tau_n} p_e E_e, \tag{4.5}$$

where m_e is the electron mass, $\tau_n = 880.3 \pm 1.1$ s is the most recent measured neutron lifetime [15] and $f^R = 1.7152$ is the phase space factor including the Coulomb, weak magnetism, recoil and outer radiative corrections. The constant term of this expression, called the IBD prefactor κ, is thus directly related to the neutron lifetime and is subject to possible modifications over time.

This expression of the cross section is widely used in the reactor energy range, below 20 MeV. However, while being accurate at those energies, it gets strongly suppressed at higher energies ($E_\nu \gtrsim 60$ MeV) and starts decreasing until it reaches non-physical negative values for $E_\nu \gtrsim 150$ MeV. This effect is due to the recoil terms in $1/m_p$, dominant at high energy.
In the energy range $E_\nu \gtrsim 40$ MeV, relevant for supernova or accelerator neutrino detection, one needs to use a more precise computation of the IBD cross section. Starting from a differential expression of the cross section, the authors of Ref. [157] were able to obtain an expression valid, up to at least 200 MeV. In addition, the use of a differential expression allows the determination of the angular distributions of the reaction products.

4.2.2 Differential cross section: Angular distributions

The differential IBD cross section can be written as:

$$\frac{\mathrm{d}\sigma}{\mathrm{d}t} = \frac{G_F^2 \cos^2\theta_C}{2\pi(s-m_p^2)^2}|\mathcal{M}|^2, \tag{4.6}$$

where G_F is the Fermi constant, $\cos\theta_C$ is the Cabbibo angle, $\mathcal{M}$ is the invariant amplitude for the IBD reaction, $s = (p_\nu + p_p)^2$ and $t = (p_\nu - p_e)^2$ are expressed as functions of the

neutrino, proton and positron 4-momenta p_ν, p_p and p_e in the laboratory frame. The complete expression of $\mathcal{M}$ can be found in Ref. [157].

By inserting the 4-momenta expressions in the proton rest frame:

$$s - m_p^2 = 2m_p E_\nu \tag{4.7}$$

$$s - u = 2m_p \left(E_\nu - E_e\right) - m_e^2 \tag{4.8}$$

$$t = m_n^2 - m_p^2 - 2m_p \left(E_\nu - E_e\right), \tag{4.9}$$

in the differential cross section $\frac{\mathrm{d}\sigma}{\mathrm{d}t}$, one can express the latter as a function of the neutrino and positron energy:

$$\frac{\mathrm{d}\sigma}{\mathrm{d}E_e}\left(E_\nu, E_e\right) = 2m_p \frac{\mathrm{d}\sigma}{\mathrm{d}t}, \tag{4.10}$$

The total cross section, displayed in Figure 4.3 (left), can be expressed after including the following one-loop radiative corrective:

$$\mathrm{d}\sigma\left(E_\nu, E_e\right) \rightarrow \mathrm{d}\sigma\left(E_\nu, E_e\right)\left[1 + \frac{\alpha}{\pi}\left(6 + \frac{3}{2}\log\frac{m_p}{2E_e} + 1.2\left(\frac{m_e}{E_e}\right)^{1.5}\right)\right], \tag{4.11}$$

where α is the fine-structure constant. This correction, valid at $\mathrm{E}_\nu \ll m_p$, amounts to a $\sim$2% correction.

Note that the authors of Ref. [157] computed an approximation of the total cross section:

$$\sigma\left(\bar{\nu}_e\ , p\right) \simeq 10^{-43} p_e E_e E_\nu^{-0.07056 + 0.02018\ln E_\nu - 0.001953\ln^3 E_\nu}\,\mathrm{cm}^2. \tag{4.12}$$

This approximation, valid for positron energies given by Eq. 4.3, is in agreement within a few per-mille for $E_\nu \lesssim 300$ MeV with the previous expression.

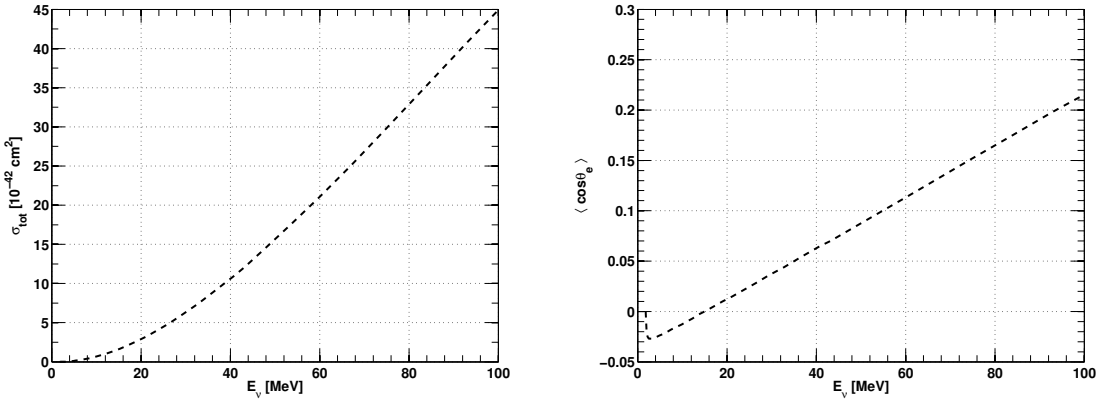

Figure 4.3: Left: Total cross section of the IBD reaction after second order corrections. Right: Average cosine of the positron scattering angle θ_e.

The differential cross section can be expressed with respect to the scattering angle θ_e between the neutrino and the positron directions after including the Jacobian coming from $t = m_e^2 - 2E_\nu\left(E_e - p_e\cos\theta_e\right)$ in $\frac{\mathrm{d}\sigma}{\mathrm{d}t}$:

$$\frac{\mathrm{d}\sigma}{\mathrm{d}\cos\theta_e}\left(E_\nu, \cos\theta_e\right) = \frac{p_e\epsilon}{1 + \epsilon\left(1 - \frac{E_e}{p_e}\cos\theta_e\right)}\frac{\mathrm{d}\sigma}{\mathrm{d}E_e}, \tag{4.13}$$

where $\epsilon = E_\nu/m_p$ quantifies the nucleon recoil effects.

This dependence in θ_e implies that E_e and p_e are now functions of not only E_ν but θ_e as well:

$$E_e = \frac{(E_\nu - \delta)(1+\epsilon) + \epsilon\cos\theta_e\sqrt{(E_\nu-\delta)^2 - m_e^2\kappa}}{\kappa}, \quad p_e = \sqrt{E_e^2 - m_e^2} \tag{4.14}$$

with $\kappa = (1+\epsilon)^2 - (\epsilon\cos\theta_e)^2$ and $\delta = \left(m_n^2 - m_p^2 - m_e^2\right)/2m_p$.

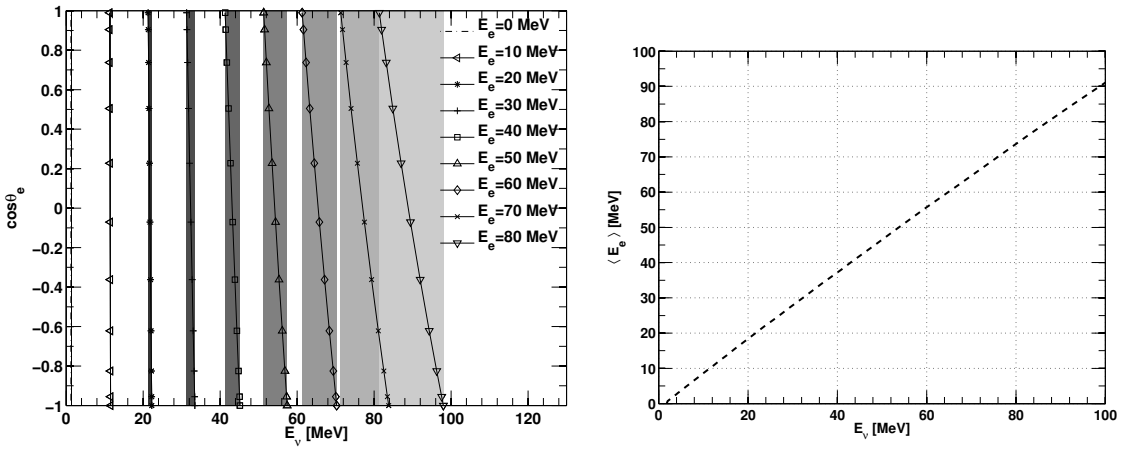

Figure 4.4: Left: Relationship between E_ν and E_e as a function of the positron emission angle, $\cos\theta_e$. The gray bands correspond to the range of possible reconstructed neutrino energies for a given positron energy [158]. Right: Average positron energy as a function of the neutrino energy.

Given the large mass difference between the proton and the positron, the latter is strongly pulled along the motion of the interaction's center of mass. It can thus be emitted in any direction. However, as the neutrino energy increases, the average positron direction, characterized by $\langle\cos\theta_e\rangle$, is modified. The behavior of the direction with respect to the neutrino energy is shown on Figure 4.3 (right).
At low energies, $E_\nu < 15$ MeV, the positron is emitted slightly backward on average and the behavior of the average scattering angle cosine can be approximated by:

$$\langle\cos\theta_e\rangle \simeq -0.034\frac{p_e}{E_e}. \tag{4.15}$$

This is a first order approximation, only valid a low energies, below 10 MeV. The apparent upward "hook" right above the IBD threshold is the result of the finite positron mass, strongly decreasing the p_e/E_e ratio at very low neutrino energies.

As the neutrino energy rises, corrections due to weak magnetism and nuclear recoil depending on E_ν/m_p need to be taken into account. The average cosine expression:

$$\langle\cos\theta_e\rangle \simeq -0.034\frac{p_e}{E_e} + 2.4\frac{E_\nu}{m_p} \tag{4.16}$$

is an excellent approximation for $\langle\cos\theta_e\rangle$ from threshold to $E_\nu \simeq 150$ MeV, beyond the supernova energy range.

The effects of Eq. 4.16 on the mean positron direction combined with the angle-dependent expression of the positron energy in Eq. 4.14 yield to a energy-dependent shift between the

positron and the neutrino energies as shown in Figure 4.4. While the previous relation between the neutrino and the positron energy (Eq. 4.3) only induced a 1.8 MeV difference between the two energies, the introduction of the scattering angle in the relation offers a range of available values to the positron energy for a given neutrino energy. When emitted along the neutrino direction, the positron takes the maximum available energy. On the other hand, it goes backwards when taking the minimum of available energy. The average positron energy for each neutrino energy is displayed in Figure 4.4 (right). Although the average neutrino-positron energy difference is close to 1.8 MeV at low energies, it increases with the neutrino energy to finally reach ∼10 MeV for $E_\nu \simeq 100$ MeV.
On the detection point of view, since only the positron energy can be measured, a degeneracy appears in the neutrino energy estimate. As shown in Figure 4.4 (left), this degeneracy is weak at reactor energies ($E_\nu < 10$ MeV) and strengthens at higher energies to finally induce an error of up to 10% in the $\bar{\nu}_e$ energy reconstruction at 100 MeV.

While, as explained above, the positron angular distribution behavior is quite peculiar and counterintuitive, the neutron angular distribution is rather simple to understand.
Since we considered an IBD interaction on a proton at rest in the laboratory frame, there is a direct correlation between the neutron and positron angular distributions through the principle of momentum conservation:

$$\vec{p_\nu} = \vec{p_e} + \vec{p_n}. \tag{4.17}$$

Kinematics dictate the neutron must always be emitted in the forward hemisphere with an angle θ_n depending on the positron emission angle. A simple analytical estimation of the maximum neutron emission angle is given in Ref. [8]:

$$\cos\theta_{nmax} = \frac{\sqrt{2E_\nu\Delta - (\Delta^2 - m_e^2)}}{E_\nu}, \tag{4.18}$$

with Δ the nucleon mass difference. At threshold, the neutron is emitted in the neutrino direction and, as the neutrino energy increases, its emission angle increases as well as shown in Figure 4.5 (left).

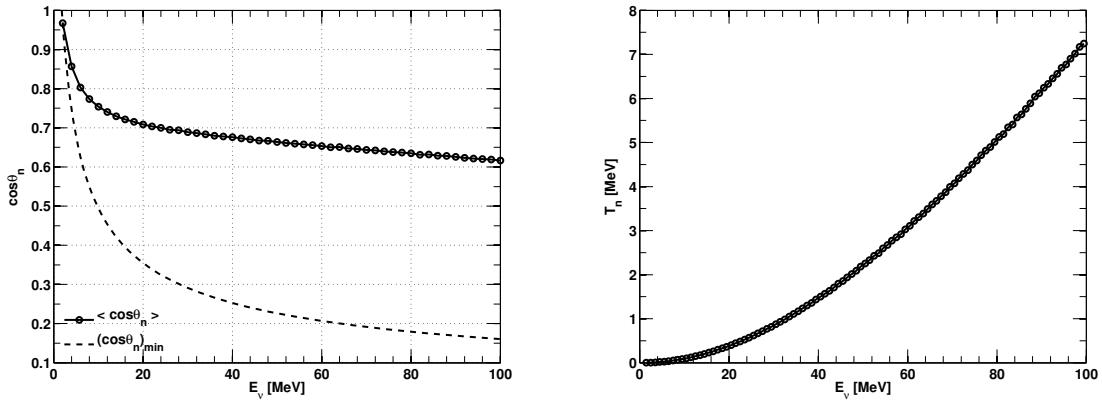

Figure 4.5: Left: Average (circles) and maximum (dashed line) value of the outgoing neutron angle cosine, $\cos\theta_n$, as a function of the neutrino energy. Right: Average neutron kinetic energy T_n as a function of the neutrino energy.

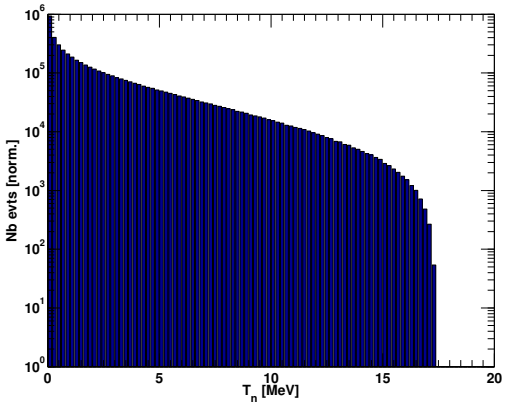

Figure 4.6: Neutron kinetic energy distribution extracted from the simulation of a neutrino energy spectrum uniform between 0 and 100 MeV.

Finally, the momentum conservation principle allows the analytical computation of the neutron kinetic energy:

$$T_n = \frac{E_\nu E_e}{m_p}\left(1 - \frac{p_e}{E_e}\cos\theta_e\right) + \frac{\Delta^2 - m_e^2}{2m_p}. \tag{4.19}$$

This energy increases quadratically with the neutrino energy as shown in Figure 4.5 (right). At reactor energies, the neutron kinetic energy is of the order of 10-100 keV while, as displayed on Figure 4.6, some neutrons can carry up to ∼18 MeV of kinetic energy at $E_\nu \sim 100$ MeV.

4.3 IBD simulation codes

Neutrino experiments based on the IBD detection are usually required to reach very high levels of sensitivity, especially in the low energy range. Efficient and reliable simulations of the detector are thus mandatory, starting from the IBD reaction itself.

4.3.1 NuMC for GEANT4

The NuMC[1] code, written in C++, has been developed by Jonathan Gaffiot during his PhD thesis [156]. During my thesis, I used it to perform several simulations and contributed to its development by including additional features. The main purpose of NuMC is to simulate the neutrino propagation from the source to the detector with the Monte Carlo method. While originally used in the Nucifer experiment to better understand and take into account the impact of the source and detector size and boundary effects, other sources and detectors have been implemented since then. It can now be used to simulate neutrino transport from various sources, such as reactors (Osiris, ILL, VVER, etc..), radioactive sources (^{144}Ce ,^{51}Cr) and supernovae (GVKM, Livermore), to various detectors (Nucifer, KamLAND, Borexino, etc...). NuMC operates in two distinct modes, namely *path* and *spectra*. The *path* mode performs the Monte Carlo calculation of the mean neutrino path while the *spectra* mode computes the expected neutrino spectrum.

[1]NuMC stands for *Neutrino Monte Carlo*

To propagate neutrinos from their source to a detector and compute a mean neutrino path, NuMC first picks a point in the source, depending on a probability distribution function, if provided. This distribution, although mandatory for precise reactor simulations, has a limited impact as the source-detector distance increases. For instance, when simulating supernova neutrinos (*cf.* Section 5.4), we will not take it into account and the source will be considered point-like. From this creation point, a random vector normal to the unit sphere is generated and its intersection length with the detector volume is computed and saved. The sum of these intersection lengths finally gives the mean source-detector length and the geometrical normalization factor, later used to renormalize the neutrino flux. More details can be found in Jonathan Gaffiot's thesis.

After running NuMC in *path* mode, the mean neutrino path is fixed and serves as input in *spectra* mode. In this mode, two points are randomly chosen, one in the source and another in the detector, and their distance is compared to a $1/L^2$ law normalized to the smallest source-detector distance. This determines if the pair of points is discarded or kept for the spectrum computation. In the latter case, NuMC picks an energy in the detected neutrino energy spectrum, product of the IBD spectrum with the emitted neutrino spectrum, the latter depending on the source. From the L/E ratio, NuMC is able to compute an oscillation probability using a user-defined Δm^2. This functionality is of interest when propagating neutrinos in short-distance neutrino experiments such as Nucifer or CeSOX. After this step, NuMC provides a detected neutrino energy and an interaction point in the detector that can be saved and later used to compute oscillation contours or simulate IBD reaction products. In the following, we will focus on the latter: the generation of positron-neutron pairs by NuMC.

Since it was mainly used to propagate low energy neutrinos, the IBD cross section originally coded in NuMC was the Vogel and Beacom expression described in Section 4.2.1. Later, the need for precise interaction rates required for the CeSOX experiment pushed the implementation of additional corrections as well as more precise cross sections such as the one computed by A.N. Ivanov et al. [159]. This total cross section takes into account several first and second order corrections such as weak magnetism, screening effects, etc... The implementation of these cross sections was performed by Jonathan Gaffiot, using corrections computed by Matthieu Vivier and Mathieu Durero [160].

Although very precise at low energies, these cross sections, as previously explained, provide wrong or even non-physical results at higher energies as shown on Figures 4.7 and 4.8. Furthermore, they do not always allow a differential computation of the cross section, mandatory to recreate IBD kinematics. To solve both issues, I decided to implement the Strumia-Vissani total and differential cross sections in NuMC.
In order to obtain both total and differential cross sections, I decided to first implement the angular-dependent expression of Eq. 4.13 in NuMC. To do so, using a precise expression of the IBD invariant amplitude $|\mathcal{M}|^2$ is mandatory. Although Strumia and Vissani claimed in their paper that the next-to-leading order (NLO) approximation of this quantity provided a description accurate enough to describe the detection of supernova neutrinos, discrepancies with the complete model arise as the neutrino energy increases. Figure 4.9 shows the behavior of the model and the NLO approximation in terms of total cross section and average positron angle cosine.

Since these tedious form factors formulas have been implemented, NuMC has been able to provide precise IBD interaction rates and kinematics for neutrino energies up to 200 MeV, the latter being of interest when using NuMC to generate datafiles later injected into a simulation

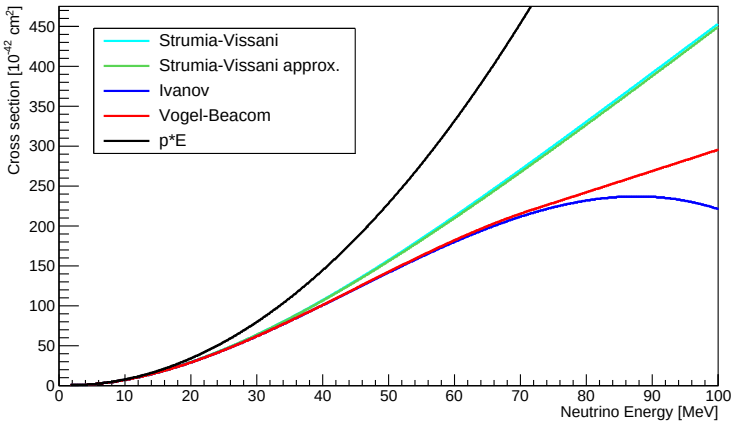

Figure 4.7: IBD cross sections computed in NuMC for 5 different models: the basic "p*E" expression of Eq. 4.4, the Vogel-Beacom expression of Eq. 4.5 without corrections, the Ivanov expression found in Ref. [159], the precise approximation in Eq. 4.12 and the Strumia-Vissani model.

package such as GEANT4.

GEANT4 [161] is a simulation tool developed worldwide by the high energy physics community. Its main purpose is to simulate particle transport through elementary physical processes in a given detector. Like ROOT [162], it consists of a large C++ library rather than a self-contained software. Its classes, defined by the prefix **G4**, are suitable for a wide variety of uses from the generation of the detector geometry and physical models (embedded in *physics lists*) to the visualization and the input/output management.
The basic flowchart of a GEANT4 simulation is the following:

- A particle is generated with defined characteristics (type, mass, charge, etc..), at a defined position (x_0,y_0,z_0) and with a defined momentum (p_x,p_y,p_z)
- The particle travels through the detector geometry divided into volumes, each made of a defined material with specific density, mass and composition
- It interacts in the material through different physical processes described in the **G4Process** classes
- The interaction information (position, deposited energy, secondary particles) are stored and the process is repeated

While GEANT4 has the ability to generate particles by itself (using the **G4ParticleGun** class), it can also read input files containing particle information. In particular, NuMC generates HEPEvt files, one of the most used file format. HEPEvt files consist of comment and event data lines. An event data is built on the following format: a line containing the number of particles in the event and a line containing the information of each event such as type, position, time, momentum and polarization. More information on the HEPEvt format applied to the KamLAND simulation can be found in Ref [163].
Although it can generate and propagate neutrinos, GEANT4 does not handle their interactions due to their tiny cross sections. An IBD event thus needs to be created via its products, the positron and neutron.

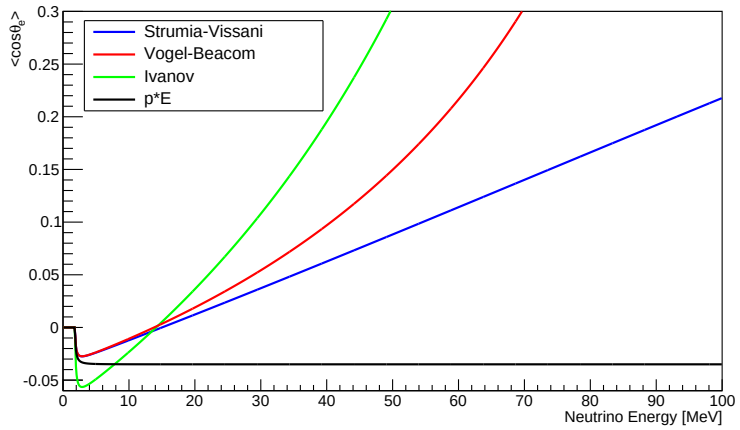

Figure 4.8: Average cosine of the positron scattering angle θ_e computed in NuMC for 4 different models: the basic "p*E" expression, the Vogel-Beacom model, the Ivanov model and the Strumia-Vissani model.

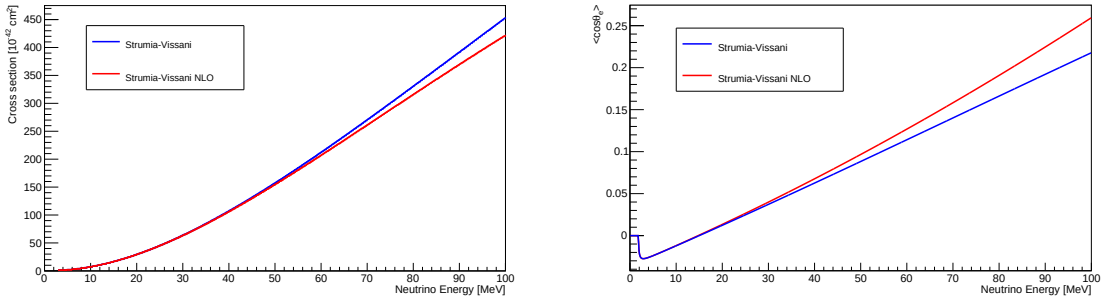

Figure 4.9: Cross section (left) and average cosine of the positron angle computed in NuMC for the complete Strumia-Vissani model (blue) and its NLO approximation (red).

To generate a typical IBD event and save it in HEPEvt format, NuMC follows a series of steps:

- A neutrino energy E_ν is picked at random in an energy spectrum
- A positron scattering angle θ_e is chosen in a distribution depending on E_ν
- The positron energy E_e is computed from Eq. 4.14 and its momentum p_e expressed in Cartesian coordinates
- From Eq. 4.17, the neutron energy E_n and momentum p_n are calculated
- An interaction point (x_0,y_0,z_0) is picked in the detector volume as a function of a distribution computed earlier when running NuMC in *path* mode

The previous steps are then repeated a number of times corresponding to the user-defined number of IBD events expected in the simulation. In the end, here is what a typical IBD HEPEvt looks like after being generated by NuMC and before being read by GEANT4:

2
1 −11 0 0 $p_e(x)$ $p_e(y)$ $p_e(z)$ m_e 0 x_0 y_0 z_0
1 2112 0 0 $p_n(x)$ $p_n(y)$ $p_n(z)$ m_n 0 x_0 y_0 z_0

The first line only contains the number of particles to generate in the event, two in the case of IBD. The second and third line contain the positron and neutron information starting from their PDG codes[2]: -11 and 2112 respectively. Note that the mass and momenta are expressed in GeV, the default HEPEvt unit.

Let us now focus on the GEANT4 simulation itself.
Unless stated otherwise in the HEPevt line, all particles in the event are generated at once, likewise an actual IBD event. As a charged lepton, the positron behavior is ruled by electromagnetic processes such as ionization, Bremsstrahlung and annihilation. In the simulation, these processes belong to the G4EmLivermorePhysics physics list, describing the interaction of electrons, positrons and gamma-rays at low energies (down to about 250 eV). After losing its energy mainly through ionization, the positron annihilates with an electron thus creating a pair of gamma rays. The energy deposited by the positron, sum of the annihilation and ionization energies is stored on an event-by-event basis.
The neutron loses its energy through elastic scattering off nuclei of the medium until it thermalizes and reach energies of ∼0.025 eV. It then diffuses as explained in Section 4.1.2 before its capture and the subsequent emission of secondary particles.

At this stage, GEANT4 still considers the two initial particles and their respective energy depositions as a single event. Therefore, it adds up all their energy in a non physical "prompt+delayed" event. To solve this issue, a feature had been implemented in the GLG4sim[3] package: the DeferTrac process (called DeferTracProc).
The default configuration of GEANT4 treats a neutron, from its creation to its capture as a single event. The purpose of DeferTracProc is to set an event time window corresponding to the prompt energy deposition and to delay any persisting depositions to the following event. Technically speaking, when DeferTracProc is activated in a simulation, the positron energy deposition and the neutron thermalization belong to the prompt event, these two processes occurring in a few-tens-of-nanoseconds time scale. The neutron diffusion being longer than the event time window, all secondary particles the neutron could create afterwards are delayed to the next event. This is the case for the particles arising from neutron capture.

At the end of a "NuMC + GEANT4" simulation, an IBD interaction is characterized by two events, a prompt and a delayed, as it is in actual data.

4.3.2 SuperNustradamus for MATLAB

Although GEANT4 provides a very precise simulation of a detector, it is sometimes not suitable or feasible in a reasonable time for all simulations.

[2]Each particle listed in the Particle Data Group [15] has its own and unique PDG code for simplicity purposes.

[3]GLG4sim is a Generic Liquid-scintillator Anti-Neutrino Detector ("GenericLAND") Geant4 simulation, developed by Glenn Horton-Smith [164]. It is derived from the general parts of the KamLAND simulation and is available freely for the neutrino community. For instance, the Double Chooz simulation package is based on it (*c.f.* Section 6.4).

For instance, given the complexity of their interaction processes with respect to their energy ranges, neutron physics is tricky to properly simulate in GEANT4[4]. The need for high-precision neutron transport in low-energy experiments led to the development of dedicated or external neutron simulation packages as we will see in Chapter 6.
Another drawback of GEANT4 is its execution speed. Indeed, since it tracks and propagates every primary and secondary particles from their creation to their final interaction, GEANT4 is quite time-consuming. This makes it unsuitable for long simulations of radiation shielding as explained in Chapter 7 or simulations of large number of IBD events such as needed in Section 5.4. Therefore, we developed a standalone simulation package: SuperNustradamus.

SuperNustradamus has been developed by myself and Théophile Chirac during his internship at CEA Saclay between September 2013 and May 2014 [165]. It is written in MATLAB [166]. Its main purpose is the simulation of a supernova process detected in a liquid scintillator detector. To achieve this goal, SuperNustradamus is divided into three main programs:

- SNSpectra, dedicated to the computation of energy spectra and cross sections
- Nustradamus, dedicated to the computation of event rates in liquid scintillator detectors
- SuperTOY, dedicated to the generation of neutrinos and subsequent (e^+,n) pairs

SNSpectra

SNSpectra handles the conversion of emitted neutrino spectra into detected spectra in neutrino or positron energy. To do so, it takes a neutrino spectrum and multiplies it with an IBD cross section. Both are user-defined and chosen among several choices. The neutrino flux can be picked among the following:

- a GVKM spectrum
- a Livermore spectrum
- a simple Maxwellian thermal distribution, describing the energy of neutrinos immediately after the burst
- a pinched Fermi-Dirac spectrum as shown in Eq. 3.26 with user-defined parameters

Figure 4.10 (left) displays the first three energy spectra, the pinched Fermi-Dirac distribution being similar to the Livermore spectrum. All these spectra describe the energy distributions of supernova neutrinos, relevant to the main purpose of SuperNustradamus. However, other spectra can be implemented and studied. For instance, I added a spectrum of $\bar{\nu}_e$ from ^{235}U fissions for testing purposes. Since SNSpectra works with binned distributions, only the energy spectrum histogram, binned from 0 to 100 MeV and scaled by the flux intensity, needs to be provided. The cross section in SNSpectra is computed quite similarly to NuMC. As displayed in Figure 4.10 (right), several cross sections models can be chosen by the user.

After computing both, SNSpectra multiplies the neutrino flux with the cross section to obtain the detected energy spectrum. In order to be easily used as input for other programs,

[4]At least until the 9.4 version of GEANT4. Since the 9.5 version, lots of improvements have been performed in neutron simulations.

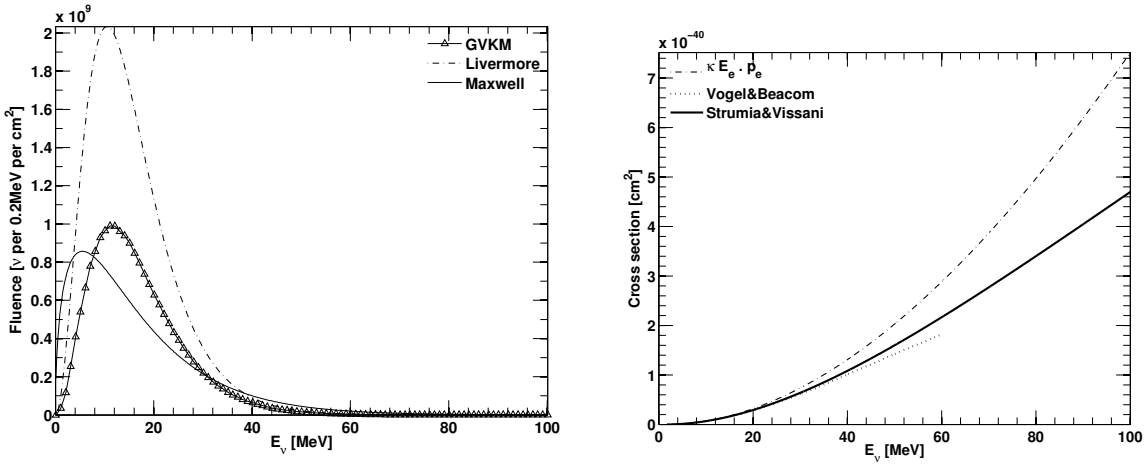

Figure 4.10: Left: Expected core-collapse supernova $\bar{\nu}_e$ emission spectra (integrated over 10 s) based on the Maxwell, Livermore, and GKVM fluxes at 10 kpc. The three spectra are normalized to the same energy released by the supernova, 3×10^{52} ergs (2×10^{58} MeV), equally distributed among each neutrino and antineutrino species. The integrated fluxes of the three distributions are respectively 9.7×10^{10} $\bar{\nu}_e$ .cm^{-2}, 1.9×10^{11} $\bar{\nu}_e$ .cm^{-2} and 9.7×10^{10} $\bar{\nu}_e$ .cm^{-2}. Right: IBD cross section based on three different approximations computed by SNSpectra. Both figures are extracted from Ref. [158].

this detected spectrum is expressed in neutrino energy and normalized to an IBD interaction on one free proton. Figure 4.11 displays the detected neutrino spectrum for a GVKM spectrum multiplied by different cross sections, previously described.

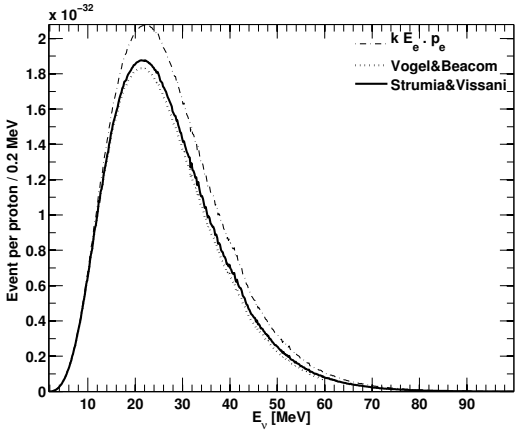

Figure 4.11: Expected neutrino spectrum for a supernova located at 10 kpc, normalized to the interaction on one free proton.

After running SNSpectra, a text file is generated, filled line by line by the detected energy spectrum bins and whose title contains both flux and cross section names. This file is later to be used as input by Nustradamus and SuperTOY.

Nustradamus

Nustradamus is mainly dedicated to the computation of interaction rates in neutrino detectors. It is based on a code first developed by Matthieu Vivier at Saclay and dedicated to the study of source experiments such as CeLAND (*c.f.* Chapter 7). Nustradamus has been developed to serve as a full supernova simulation package such as SNOwGLoBES [167]. Incidentally, before we developed SuperNustradamus, we first used the latter to estimate the interaction rate per detector. However, due to its lack of flexibility for the studies we had planned, we then decided to develop our own simulation tool, benchmarked with SNOwGLoBES.

To compute interaction rates, Nustradamus takes detected neutrino spectra (computed by SNSpectra) as inputs as well as detector information. The relevant detector information are gathered in a table and read by Nustradamus. Since each spectrum is normalized to an IBD interaction on a proton, the most relevant characteristic of each detector is its proton number, i.e. the number of free protons in its volume. This quantity is obtained by multiplying the proton (H nucleus) density, expressed in $\mathrm{H.m^{-3}}$ (or $\mathrm{H.kg^{-1}}$) by the detector volume (or mass). While the latter depends on the detector size, the former depends on the liquid scintillator composition. Both information are written in the table and Nustradamus computes the proton number for each detector.

By applying this proton number normalization factor along with a distance normalization factor, following a $1/\mathrm{L}^2$ law, on the input detected spectrum, Nustradamus is able to provide detected spectra with respect to detector size (mass) and supernova distance. The IBD interaction rate is then obtained by simply integrating the spectrum. Applications of Nustradamus to actual detectors will be studied in Section 5.4.

Additional features have been implemented in Nustradamus as well. For instance, by taking as input each detector's GPS coordinates (latitude and longitude) over the globe as well as supernova position (right ascension and declination) over the galactic sky, Nustradamus is able to generate maps of the detectors and supernovae locations, as shown on Figure 4.12. Seemingly unrelated to the interaction rate computation, this feature might be useful for further analyses, such as triangulation or Earth matter effects studies. This is beyond the scope of the work presented in Section 5.4.

SuperTOY

SuperTOY has been developed to simulate IBD interactions in liquid scintillator detectors, thus offering an alternative to a full GEANT4 simulation chain. It was the main program of the analysis presented in Section 5.4 and several routines have been added to it for the sake of avoiding cross-talks between programs. However, in the following, I will focus on SuperTOY's core concept: the IBD simulation with state of the art kinematics description.

First, SuperTOY generates a supernova, represented by its position over the sky and its emitted energy spectrum. The former defines the neutrino direction in the detector frame and is usually fixed at (x,y,z)=(0,0,1) in Cartesian coordinates so that the supernova is located at the detector's zenith and the neutrino direction points toward the negative z axis. The neutrino energy of each IBD event is picked at random in the energy spectrum emitted by the supernova. The energy range, chosen by default between the IBD threshold of 1.806 MeV and 100 MeV can be modified by the user. From its energy and direction, the neutrino momentum p_ν is computed such that $p_\nu = E_\nu$, in agreement with the assumption of an ultrarelativistic neutrino.

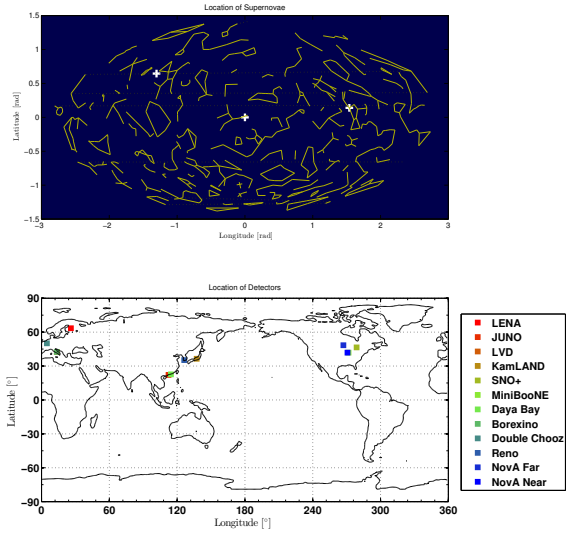

Figure 4.12: Representation of the galactic sky (top) and world map (bottom) in Nustradamus. Among the three supernovae, represented over the sky by white crosses, only Betelgeuse (right), located 0.2 kpc away from Earth, is an actual candidate, the other two being generated at arbitrary positions. The detectors displayed on the world map are current or future detectors used in the following analyses.

Positron and neutron momenta are then computed in a way very similar to NuMC, depending as well on the user-defined cross section. Figure 4.13 shows the mean value of $\cos\theta_e$ obtained from a SuperTOY simulation, in agreement with the Vogel-Beacom analytic computation.

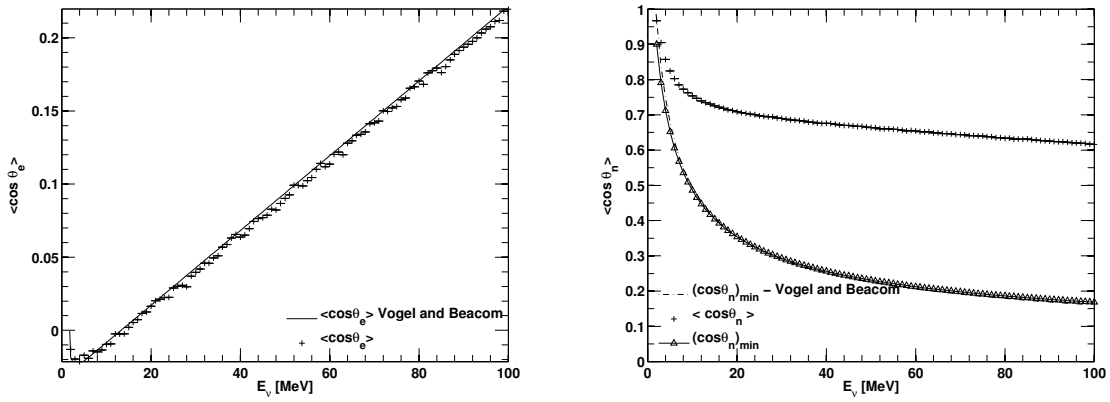

Figure 4.13: Left: Average cosine of the outgoing positron angle, $\cos\theta_e$, as a function of neutrino energies between E_{th} and 100 MeV. Right: Average cosine of the outgoing neutron angle, $\cos\theta_n$. Both panels show results of SuperTOY based on the Strumia-Vissani cross section compared to the analytical evaluations of Vogel-Beacom [158].

A the end of this step, SuperTOY provide the same information than NuMC: the event-by-event momentum information of the positron-neutron pairs. Note that, while NuMC handled the spatial distribution of IBD events in the detector, all SuperTOY events are lo-

cated at the detector center: (0,0,0) in Cartesian coordinates. At this point, the relevant IBD information are gathered in an array whose length is the number of neutrino events such that:

$$E_{e1}\ \mathrm{p}_e(x)_1\ \mathrm{p}_e(y)_1\ \mathrm{p}_e(z)_1\ E_{n1}\ \mathrm{p}_n(x)_1\ \mathrm{p}_n(y)_1\ \mathrm{p}_n(z)_1$$
$$E_{e2}\ \mathrm{p}_e(x)_2\ \mathrm{p}_e(y)_2\ \mathrm{p}_e(z)_2\ E_{n2}\ \mathrm{p}_n(x)_2\ \mathrm{p}_n(y)_2\ \mathrm{p}_n(z)_2$$
$$E_{e3}...$$

While its C++ structure allows fast computations, NuMC works on an event-by-event basis, each IBD event being treated one after another. This is not the case of SuperTOY. Indeed, MATLAB's structure, based on arrays manipulation, allows parallel array processing. SuperTOY's arrays containing all the events are manipulated at once thus eliminating the need for iteration loops and strongly reducing execution speed.

From now on, SuperTOY will act as a simulation tool and propagate the (e^+,n) pairs it generated, as in GEANT4 with the NuMC-generated pairs.
In order to obtain an accurate description of the behavior of both particles in the detector, I ran GEANT4 simulations and used their outputs as inputs for SuperTOY in the form of arrays in text datafiles. To speed up simulations while still maintaining a satisfactory level of accuracy, only the path length probability density function or the free path mean value with respect to the particle energy will serve as inputs. The angular distribution, effect of the scatterings the particles undergo in the detector medium, will not be taken into account. However, a test simulation performed with a neutron angular spread showed no significant discrepancies with our "unscattered" results.
While I had access to several GEANT4 simulations (Double Chooz, KamLAND, Nucifer), I decided to use KLG4sim, the simulation of the KamLAND detector (*c.f.* Chapter 7), for this study. My choice was driven by two reasons: robustness and simplicity. SuperTOY has been developed to study neutrino directionality in large liquid scintillator detectors and in the context of this study, KamLAND is the biggest detector currently in operation while Double Chooz is the smallest. It seemed more than reasonable to use the former simulation package in this case. Furthermore, its use is rather convenient and allows fast simulations and analyses. These two reasons influenced my choice toward the use of KLG4sim as a provider of inputs for SuperTOY. To ensure the validity of these results, I performed all simulations using DCGLG4sim, the Double Chooz simulation package, based on GLG4sim as well but using a different liquid scintillator doped with gadolinium (Gd) (*c.f.* Chapter 6). Aside from the neutron capture process, no significant discrepancies between the two simulations have been observed.

First, I simulated positrons with energies ranging from 0 to 100 MeV, with a 0.5 MeV binning. Using the data analysis software developed for the CeLAND experiment (*c.f.* Chapter 7), I extracted the path length of each positron and wrote it into an histogram for each energy. The path length distribution between the positron creation at the interaction point and its annihilation is displayed in Figure 4.14 (top), for different positron energies. As seen on Figure 4.14 (bottom), the positron range increases rather linearly with the energy, as expected for an ionizing particle.

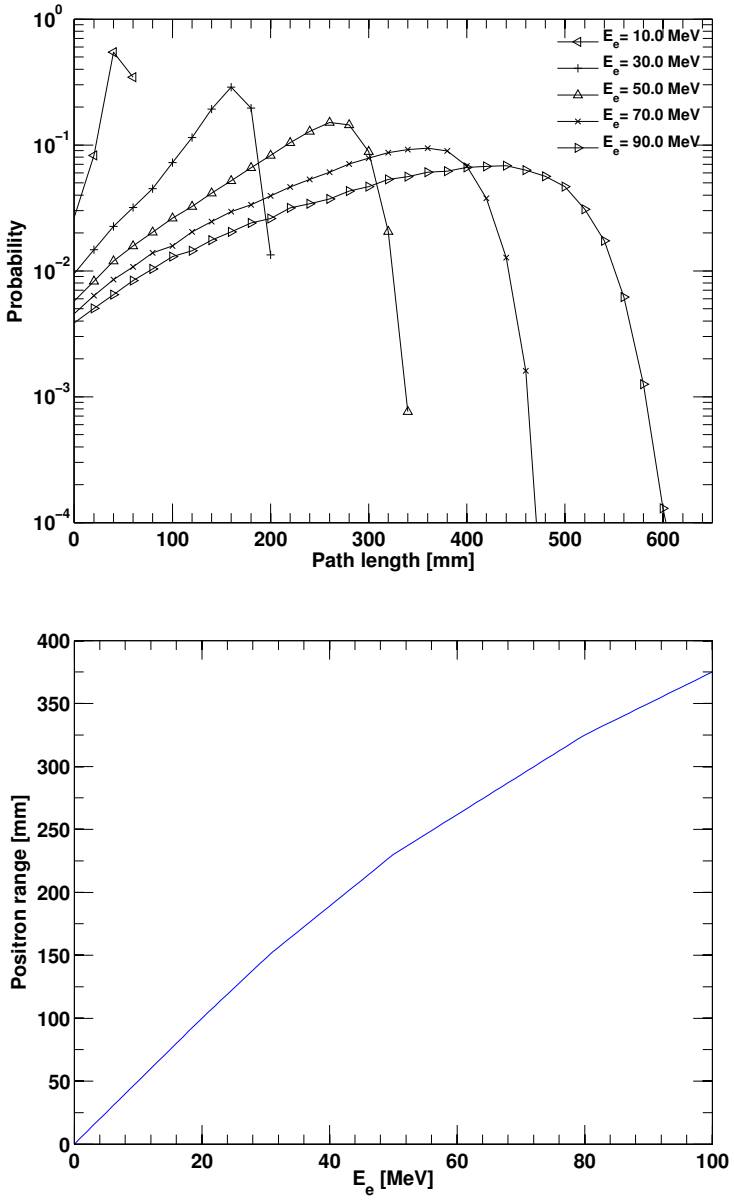

Figure 4.14: Top: Probability density function of the path length of positrons with different kinetic energies. Bottom: Mean positron path length as a function of the positron energy E_e.

Similarly, I simulated neutrons with kinetic energies ranging from 0 to 20 MeV, with a 10 keV binning between 0 and 1 MeV and a 100 keV binning between 1 and 20 MeV. Since the diffusion process smears the "thermalization location" i.e., the point where we consider the neutron as thermal after its moderation, SuperTOY separates the delayed event generation into two parts: moderation and diffusion. As stated earlier, neutron simulation has often been GEANT4's pet peeve. However, the implementation of new low energy neutron models and cross sections [168] based on the ENDF BVII database, improved neutron physics since

the 9.5 version of GEANT4. KLG4sim being compatible with the 9.5 version of GEANT4, the neutron behavior is considered accurate enough for our studies.

The main difficulty when trying to obtain the moderation path length i.e., the distance between the neutron creation and its thermalization comes from the very nature of the thermalization process. Indeed, a neutron is considered thermal when reaching kinetic energies of ∼0.025 eV. However, at such energies, the ratio between the neutron kinetic energy and its mass (and the mass of the surrounding medium nucleons) is of eleven orders of magnitude. The slightest scattering leads the neutron to acquire a sufficient amount of kinetic energy to not be considered thermal anymore. To take this effect into account, I chose not to look at the path length of each neutron on an event-by-event, which was my first approach, but rather look at the average path length at a given neutron kinetic energy. Instead of considering the neutron path length as the distance between its creation and the point where its kinetic energy first reached 0.025 eV, I looked at the neutron endpoint and computed the barycenter of the neutron captures in (X,Y,Z). The validity of this approach comes from the fact that, when diffusing after being moderated, the neutron direction is isotropic. The barycenter of the neutron captures thus gives the average moderation path length, displayed in Figure 4.15 (left), for different neutron kinetic energies. While it only yields an average path length rather than a distribution, this approach better mimics the true neutron behavior.
The diffusion length is quite easier to obtain since it only concerns thermal neutrons. To that end, I generated thermal neutrons with T_n=0.025 eV isotropically and stored each path length from creation to capture. Since KamLAND's liquid scintillator is not doped with gadolinium, a large fraction of neutron captures occur on hydrogen (H) atoms with a small component of captures on carbon atoms (C). The cross section of thermal neutron capture on C being significantly lower than the others, I will not consider it in the following. To obtain a diffusion path length before capture on Gd, I ran simulations using DCGL4sim and its Gd-doped liquid (0.1%). The diffusion path length before capture in an unloaded or a Gd-loaded liquid is displayed in Figure 4.15 (right). In the case of a neutron capture on H, a 2.2 MeV gamma ray is emitted upon capture. The path length distribution of this gamma is obtained by shooting isotropic 2.2 MeV gamma rays, in a way similar to the previous one. It is worth noting that since SuperNustradamus was developed to study large detectors, with mostly undoped liquid scintillator, it does not efficiently handle neutron captures on Gd. Given the low yield of captures arising on Gd when summing all detectors of interest for the study presented in Section 5.4, I decided not to take them into account. Furthermore, the cascade of gamma rays arising from neutron captures on Gd, while leading to an ∼8 MeV energy deposition cannot be precisely predicted in terms of number of gammas and energy carried individually. However, this isotropic multi-emission actually "focuses" the delayed event energy deposition closer around the capture point and limits the smearing brought by a single gamma ray detection.

The path length distributions extracted from positron and neutron simulations are written in text datafiles in the form of arrays and stored in a dedicated subfolder in the SuperTOY main repository. At the beginning of each SuperTOY execution, the datafiles specified by the user are loaded into MATLAB's workspace so that any local function or script would be able to access them. This is the case of the SuperTOY's scripts acting as simulation tools to transform (e^+,n) pairs into prompt and delayed events. By picking a path length in the positron range distribution corresponding to an energy E_e and multiply it with the normalized positron momentum p_e, one can obtain a realistic positron range at E_e. On the other

hand, since the neutron path length before thermalization is not a distribution, its range is obtained only by multiplying the discrete energy-dependent path length at T_n with the normalized neutron momentum. From this thermalization point, a first vector, whose length is randomly chosen from the neutron capture distribution, is drawn isotropically thus giving the neutron capture point. Likewise, a second vector is shot isotropically to account for the path length distribution of the gamma ray arising from neutron capture.

At this point, each neutrino event is defined as such:

$$E_{e1}\ \mathrm{X}_{e1}\ \mathrm{Y}_{e1}\ \mathrm{Z}_{e1}\ \mathrm{X}_{n1}\ \mathrm{Y}_{n1}\ \mathrm{Z}_{n1}$$
$$E_{e2}\ \mathrm{X}_{e2}\ \mathrm{Y}_{e2}\ \mathrm{Z}_{e2}\ \mathrm{X}_{n2}\ \mathrm{Y}_{n2}\ \mathrm{Z}_{n2}$$
$$E_{e3}...$$

with $(\mathrm{X,Y,Z})_{e,n}$ the prompt and delayed vertex coordinates. Since SuperTOY is supposed to mimic a GEANT4 simulation, only the observables available in data and simulation such as positron energy and event locations are returned.

Now that the prompt and delayed events have been generated, corrections are to be applied to account for detector-dependent effects. The main effects considered in SuperTOY are position reconstruction and vertex/energy resolutions.

Energy depositions in liquid scintillator detectors are usually due to low energy ionizing particles and are thus considered point-like within the reconstruction uncertainty brought by the detector's intrinsic vertex resolution. However, as an ionizing particle energy rises, its range increases accordingly. As shown on Figure 4.14, the positron mean path length, while being negligible at reactor energies, increases to ∼25 cm on average at 50 MeV. At that point, the energy deposition can no longer be considered point-like but rather track-like with

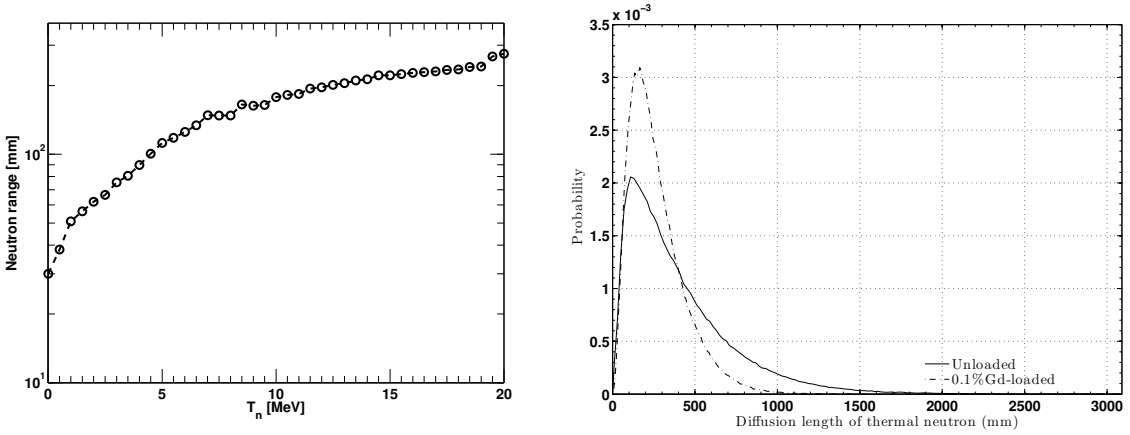

Figure 4.15: Left: Mean neutron path length before diffusion as a function of the neutron kinetic energy T_n. Right: Diffusion length of thermalized neutrons in liquid scintillator with and without Gd-doping. Both figures are extracted from Ref. [158].

a larger deposition at the positron endpoint, corresponding to its annihilation. However, since most reconstruction softwares in data acquisition and simulation chains have been developed and trained to reconstruct point-like events, the track-like structure of the deposition will not be taken into account. In most cases, the reconstructed vertex is the barycenter of the photon emission along the track, not the particle endpoint. Since only the latter is provided to SuperTOY, a correction has to be applied to obtain a realistic prompt vertex reconstruction. To compute the value of this correction factor, I compared the positron path length between creation and annihilation with the distance between the positron creation and its KLG4sim-reconstructed point-like vertex for the whole energy range [0-100] MeV. It has been put in evidence that an independent scaling factor of 0.72 could reconcile both distances. The track width leads to a smearing of the reconstructed charge barycenter by a Gaussian-like distribution with a standard deviation of $\sim$2 cm. The "track reconstruction" correction factor along with the 2 cm Gaussian smearing are applied to each prompt location in SuperTOY thus decreasing the length of the positron track by a factor 0.72.

In liquid scintillator, the energy is converted into scintillation light, detected by photomultipliers. The energy and position reconstruction of an event thus depend on the number of photons detected by the photomultipliers and their reconstructed position in (X,Y,Z) coordinates. More details and an application to Double Chooz can be found in Chapter 6.
This dependence to the number of photons or *photostatistic*, expressed as a charge, leads to energy-dependent and detector-dependent effects. For that matter, energy and vertex reconstruction resolutions are often expressed at 1 MeV with a $1/\sqrt{\text{E (MeV)}}$ dependence. For instance, in a large liquid scintillator detector such as KamLAND, energy and vertex resolutions are of the order of $6\%/\sqrt{\text{E (MeV)}}$ and 12 cm$/\sqrt{\text{E (MeV)}}$, respectively. These reconstruction effects are being described by a Gaussian smearing with a standard deviation equal to the resolution value. In SuperTOY, a vector picked in a Gaussian distribution corresponding to a user-defined vertex resolution is added to the prompt and delayed location to account for detector resolution. A similar smearing is applied to the energy distribution.

After applying the above corrections, SuperTOY provides a set of neutrino events with visible energies and reconstructed vertices as expected in actual data extracted from a liquid scintillator detector.

Chapter 5

Exploiting the directionality of the IBD Process

In this chapter, we will study the concept of neutrino directionality, i.e. the possibility of retrieving the direction of a neutrino flux from the kinematics of the interactions it induced. These studies are focused on the IBD reaction, relevant for the detection of low-energy neutrinos in liquid scintillator detectors. First, we will review the reasons that motivate the study of neutrino directionality. We will then look in detail at three applications of this concept: the localization of nuclear reactors with the Double Chooz detectors, the directional detection of supernovae using several IBD-sensitive detectors and the detection of geoneutrinos.

5.1 Motivations

Exploiting the directional information carried by detected particles is of interest for numerous neutrino experiments. When the source location is known, it might help discriminate between signal and background while, if not, it allows a possible reconstruction of the source position. The need for a strong background rejection in short baseline experiments or geoneutrinos detection recently increased the global interest of the neutrino community in neutrino directionality. However, since the observation of the first extrasolar neutrinos at the end of the last century (*c.f.* Section 3.3.2), the astronomical scientific community started to consider neutrinos as an additional messenger to better understand astrophysical phenomena such as core-collapse supernovae [169]. The observation of a supernova neutrino signal and the reconstruction of its source location would bring a tremendous amount of information about this astrophysical process. This concept will be further developed is Section 5.4.

Neutrino directionality might also benefit the detection of geoneutrinos, which requires a strong and robust background rejection. Since geoneutrinos are emitted within the Earth crust and mantle, their reconstructed direction should point towards the lower hemisphere in spherical coordinates with an angular distribution depending on the crust and mantle geochemical compositions. On the other hand, reactor neutrinos, one of the main background in the search for geoneutrinos, are scattered over the globe at different known locations, mostly in the Northern Hemisphere. The rejection of neutrino events coming from those locations might help increasing the signal over background rate, critical for geoneutrino observation. A detailed study of neutrino directionality with geoneutrinos in the Borexino experiment can be found in Romain Roncin's thesis [170].

A nuclear reactor in operation emits an intense, power-dependent and unalterable flux of neutrinos. These characteristics, crucial for reactor experiments, have been noticed by the International Atomic Energy Agency (IAEA) which, in the past decade, took an interest in neutrino detection to carry out its missions. Indeed, the detection of neutrinos originating from a reactor core provides an indication of the reactor power and core composition thus allowing a reliable reactor monitoring able to detect unusual or illegal operations. Furthermore, the long-range detection of neutrinos and the reconstruction of their source could allow the detection of rogue nuclear reactors and possibly locate it. Ref. [171] and [172] provide detailed studies of such application.

5.2 Methods

Since the invention of the cloud chamber in 1911 by Charles Thomson Rees Wilson [173], one has been able to recover the direction of charged ionizing particles by observing the track-like structure of the energy deposition pattern. However, in the case of neutral particles, the pattern might look quite different. While the detection of energetic (fast) neutrons relies on the observation of the subsequent proton recoils providing an ionization track, neutrinos are significantly harder to detect in such manner. First, due to the low cross sections of neutrino interactions, the large dedicated low-energy detectors do not usually provide an easy observation of the event pattern. Besides, depending on the interaction and its products, the direction reconstruction might not be straightforward. Let us take the example of the two neutrino interactions previously described: the neutrino scattering off electrons and the Inverse Beta Decay.

Neutral current neutrino scattering off electrons leads to the emission of an electron. Similarly, charged current neutrino scattering leads to the emission of a charged lepton, whose type ($e^{\pm}$,$\mu^{\pm}$,$\tau^{\pm}$) directly depends on the interacting neutrino ($\overset{(-)}{\nu}_e$,$\overset{(-)}{\nu}_\mu$,$\overset{(-)}{\nu}_\tau$). From the kinematics inherent to these processes, one can expect the outgoing charged particle to be emitted along the direction of the incoming neutrino. The observation of the product particle direction thus provides a direct estimate of the source location on an event-by-event basis. In a practical case, this observation is made possible by the use of specific detection techniques as Čerenkov imaging or segmented calorimetry as shown in Figure 5.1.

Incoming neutrino direction reconstruction is not as obvious in the case of Inverse Beta Decay. As explained in Section 4.2, the angular distributions ruling IBD kinematics are widely spread. Besides, unlike scatterings that lead to the emission of a charged lepton only, the IBD reaction also generates a neutron, whose position is much harder to reconstruct since only the secondary particle created upon capture can be detected. Finally, at the relatively low energy range usually observed with IBD, a precise track or vertex reconstruction is hardly achievable with respect to the detector's intrinsic resolution. These limitations prevent an event-by-event estimation of the source location thus only allowing a statistical estimation.

As shown previously in Section 4.3.2, for IBD events at typical reactor energies, the positron is emitted slightly backwards and its mean path length is of the order of a few mm, much smaller than most detectors spatial resolution. It is thus considered fixed and the vertex of the prompt event is viewed as the IBD interaction position. Neutrons, on the other hand, can travel several centimeters along the neutrino direction (*c.f.* Figure 4.5)

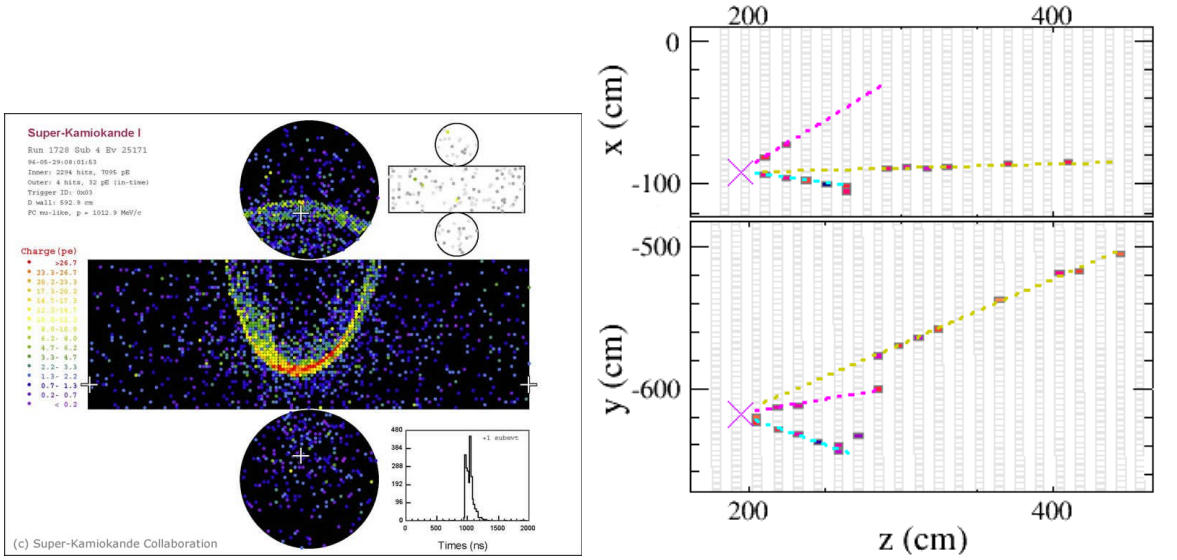

Figure 5.1: Left: Čerenkov ring created by a neutrino-induced muon in Super-Kamiokande [174]. Right: Event display of the first neutrino candidate event selected in the segmented NoνA's far detector [175].

before being thermalized. Although their diffusion smears this so-called neutron displacement, a statistical analysis of the reconstructed prompt and delayed vertices provides the average neutron thermalization location and its direction with respect to the IBD interaction position. This is the basis of the directionality analysis used in Double Chooz and detailed in Section 5.3. At higher energies, additional angular and reconstruction effects need to be taken into account in these analyses as explained in Section 5.4 in the case of supernovae detection.

5.3 Application: Double Chooz

In this section, I will present the directionality studies performed with the Double Chooz experiment by the dedicated "Neutrino directionality" working group, composed of Erica Caden (Drexel University - Philadelphia, P.h.D degree awarded in 2012), Romain Roncin (APC Laboratory - Paris, P.h.D degree awarded in 2014), Yaroslav Nikitenko (INR RAS - Moscow, P.h.D ongoing) and myself.

5.3.1 Results of past experiments

The directionality studies performed with Double Chooz were first driven by the goal of improving the results of the past CHOOZ experiment [176].
In 1999, the CHOOZ experiment, previously described in Section 2.2.1, provided a location of the two reactors of the Chooz nuclear power plant, using only the sample of neutrinos they detected. With their dataset of ∼2500 neutrinos, they were able to reconstruct the direction of the cores within a 18° half-aperture cone. CHOOZ was the first monolithic experiment to demonstrate the feasibility of directional neutrino detection in unsegmented detectors.

The Palo Verde experiment performed a similar measurement [177], extracted the directionality information from its data and, using the segmentation of their detector, used it as a

variable for cross-checking background subtraction methods. Indeed, the anisotropy of IBD events, however weak, tends to stick them out above background events, mostly isotropic by nature. By defining an asymmetry coefficient $A = \frac{R-L}{R+L}$ in terms of the numbers of neutrons captured in a segment away from the source R and in a segment facing the source L, an asymmetry $A_{\text{data}} = 0.050 \pm 0.017$ was found in data while the Monte Carlo gave $A_{\text{MC}} = 0.134$. This discrepancy is due to the presence of isotropic background events in the data sample while the simulation consisted of neutrinos events only. The estimation of the signal over noise ratio given by:

$$\frac{S}{N} = \frac{A_{\text{data}}}{A_{\text{MC}} - A_{\text{data}}} = 0.6^{+0.4}_{-0.3} \tag{5.1}$$

was found in agreement with the value of 0.81 ± 0.03 computed using a more precise background subtraction analysis. While the directional information was never used as an input for the oscillation parameters determination, it paved the way for future segmented detectors where similar analyses are expected to be performed in order to discriminate signal over background. The PROSPECT experiment [178], dedicated to sterile neutrino searches in the vicinity of a nuclear reactor, showed an interest in exploiting directionality [179] to further discriminate neutrinos from backgrounds events.

Prior to CHOOZ and Palo Verde, the Gösgen experiment [180] was the first one ever to experimentally demonstrate the anisotropy of the IBD reaction. Their segmented detector, made of scintillator and ^{3}He layers in alternation allowed the detection of both positrons in the scintillator material and neutrons in the ^{3}He neutron detectors. By observing a neutron deficit in the layers facing the reactor, they were able to prove the existence of neutrino directionality in IBD at the 10σ level.

5.3.2 The Double Chooz layout

Although the applications of neutrino directionality aim at recovering the location of a completely unknown neutrino source, this is not the case of Double Chooz in which we know where the neutrinos are coming from. However, to demonstrate the feasibility of the directionality measurement and reach an high enough precision on its results, one needs to accurately understand the source-detector layout of the experiment.

Among the three reactor experiments, Double Chooz possesses the simplest site layout. Indeed the important number of reactors scattered around the Daya Bay detectors (*c.f.* Figure 2.11) and the wide distribution of the RENO reactors (*c.f.* Figure 2.13) do not allow to consider the neutrino source as point-like, a specificity of the Double Chooz layout as displayed on Figure 5.2. With this configuration, the two Double Chooz detectors are nearly located at the isoflux positions with respect to the reactors, which means each detector, near and far, receives almost the same flux fraction from the two reactor, B1 and B2, when operating at equal power. This characteristic, unique to Double Chooz, allows a strong suppression of the flux systematics, thus increasing the precision of the θ_{13} measurement.

To further enhance the understanding of the flux systematics, the determination of the reactors and detectors coordinates on a single and unique reference frame is crucial as well. Indeed, the 2-neutrino survival probability of a ν_e, expressed in Equation 1.44 and valid for Double Chooz, directly depends on the propagation distance L. This distance, referred to as the baseline, is one of the inputs that drives the measurement of the mixing angle and thus needs to be accurately known.

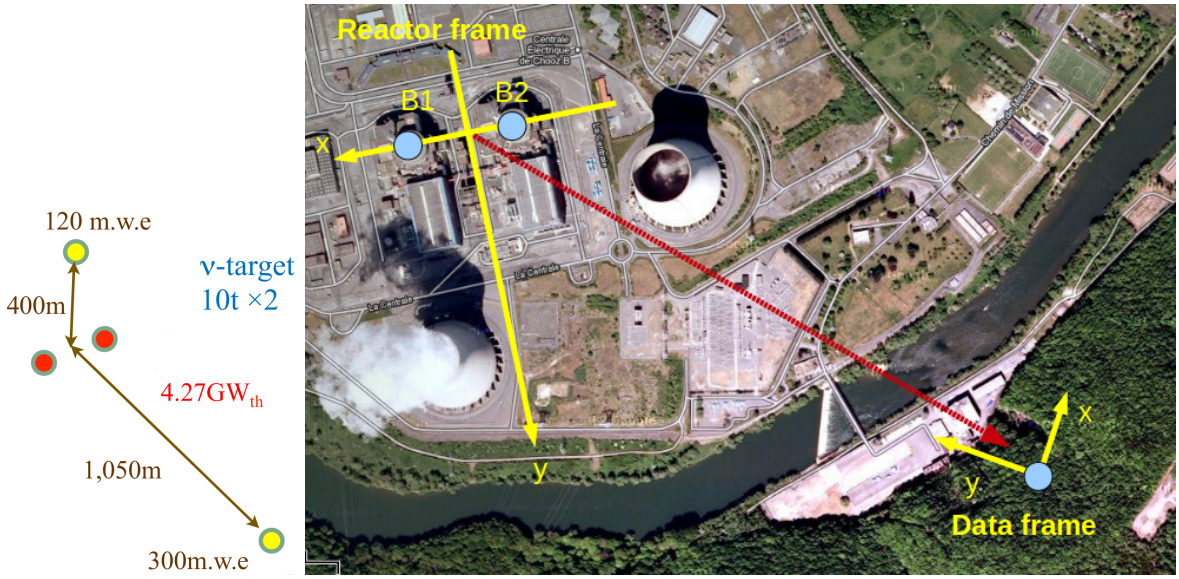

Figure 5.2: Left: Sketch of the layout of the Double Chooz experiment [78]. Right: Satellite view of the Double Chooz layout. The reactor (or "EDF ") frame and the detector (or "Data") frame are not aligned.

In January 2013, the Fit-Esic company, under the supervision of Matthieu Vivier from the Saclay group, performed a geodetic survey of the Double Chooz layout [181]. To do so, the positions of 3 reference pillars placed in front of the far laboratory entrance, where the Double Chooz's far detector is located, were measured via GPS. To obtain their positions within the plant coordinate system, referred to as "EDF frame" and centered between the B1 and B2 reactors, another GPS measurement was performed on 3 other reference pillars whose positions was already accurately known in the EDF frame. A picture of such pillars and a sketch of their positions are shown on Figure 5.3. Finally, a laser-based polygonation was performed to connect the front of the far laboratory to the actual detector, whose positions was already known from several markers. A picture of one of the step of the polygonation and a sketch of the method are shown on Figure 5.4. The results of this survey are summed up in Table 5.1.

	New coordinates (m)			Old coordinates (m)		
	x	y	z	x	y	z
B1	82.048	-0.008	121.660	82.5	0	120
B2	-82.048	0.008	121.660	-82.5	0	120
DCfar	-751.856	738.956	90.129	-747.1	744.4	84.0

Table 5.1: New and old coordinates of the Double Chooz layout expressed in cartesian coordinates in the EDF reference frame.

While the old and new coordinates differ by more than a few meters, the new baselines between the B1 and B2 cores and the far detector were found in agreement with the old ones as shown in Table 5.2. However, their associated uncertainties are now much lower and the systematical error they induce on the θ_{13} measurement is negligible.

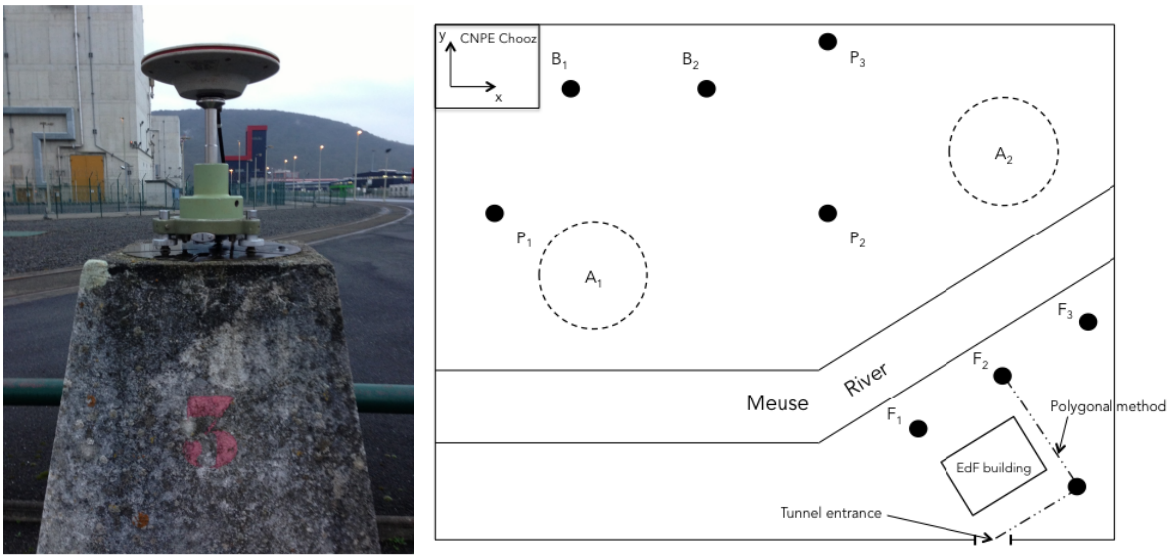

Figure 5.3: Left: Reference pillar of the Chooz power plant during a GPS measurement. Right: Sketch of the reference pillars scattered over the plant site and the far laboratory entrance.

	Baselines (m)		Angles (°)	
	New	Old	Azimuthal	Zenith
B1-DCfar	1114.656 ± 0.015	1114.6 ± 0.1	87.190 ± 0.072	88.379 ± 0.001
B2-DCfar	997.839 ± 0.015	997.9 ± 0.1	80.929 ± 0.072	88.188 ± 0.001

Table 5.2: Baselines and angles between the far detector and the two reactors. The azimuthal and zenith angles are expressed in the detector frame.

At the time the survey had been performed, the near laboratory was still in construction and the near detector markers were not ready to be accurately measured. The Fit-esic company thus only performed a GPS measurement on the reference pillars in front of the near laboratory. The measurement of the markers positions has been performed a few months later [182] and, in 2015, the polygonation was conducted [183], thus achieving the complete geodetic survey of the Double Chooz layout. Although the final positions of the near detector are still being checked, they seem to agree with the expected values.

Besides their importance for the θ_{13} measurement, the results extracted from this geodetic survey are of interest for directionality studies, especially the angles between the detectors and the reactors in the detector frame. These angles are the main unknowns that need to be determined using only the neutrino events in order to prove the experiment's capability to perform a directional detection.

5.3.3 Double CHOOZ results

In order to thoroughly study the directionality of the IBD process, one has to perform an analysis on a sample of neutrinos as pure as possible. Indeed, given the small anisotropy of the reaction, the presence of background would smear and possibly bias the direction reconstruction. For that matter, I decided to use the datasets of neutrino candidates used

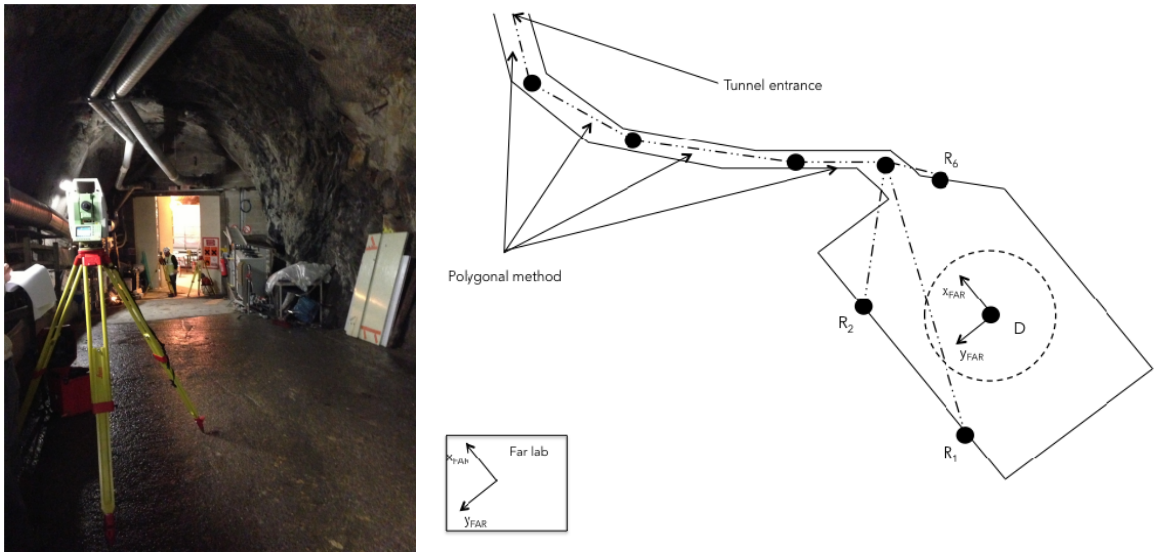

Figure 5.4: Left: Laser polygonation between the far detector and the entrance of the far laboratory. Right: Sketch of the laser polygonation used to measure the positions of the far detector reference markers.

in the Double Chooz final fit, i.e. the determination of the oscillation parameters. These datasets, in the form of ROOT trees, contain the information relevant to all the Double Chooz analyses for each neutrino event (prompt and delayed energies, positions, charge, etc...). The selection performed to generate these datasets is described in Section 6.5. While designed to tag neutrino events using the neutron capture on Gd (n-Gd), the Double Chooz experiment demonstrated its capability to perform a θ_{13} measurement using neutron captures on H (n-H) [184]. The following directionality studies will thus be conducted on two datasets, "n-Gd" and "n-H", both compared with corresponding Monte-Carlo simulations (MC) with higher statistic. A preliminary directionality analysis on a near detector's n-Gd dataset will be presented as well.

Direction reconstruction

Among the considerable list of variables available for each neutrino event, the most relevant information for directionality are the prompt and delayed reconstructed vertices, referred to as $\vec{X}_p$ and $\vec{X}_d$, three-dimensional vectors in (X,Y,Z) Cartesian coordinates. From these vertices, one can construct the neutrino vector $\vec{X}$ such that:

$$\vec{X} = \vec{X}_d - \vec{X}_p, \tag{5.2}$$

$\vec{X}$ being the vector having its origin at the prompt event and pointing toward the delayed event. The small anisotropy of the IBD reaction prevents this vector from providing a directional information on an event-by-event basis. We thus a have to sum these vectors in order to obtain an estimate of the neutrino direction. The average sum of the neutrino vectors $\vec{p}$ is defined as:

$$\vec{p} = \frac{1}{N}\sum_{i=1}^{N} \vec{X}_i, \tag{5.3}$$

with N the number of neutrino candidates in the dataset. Sometimes called the "neutrino wind", $\vec{p}$ corresponds to the average neutrino direction pointing away from the reactors and towards the detector. An estimate of the reactors' direction, expressed in azimuthal (ϕ) and zenith (θ) angles in the detector frame, can be obtained from $\vec{p}$ using:

$$\phi = \tan^{-1}\left(\frac{p_y}{p_x}\right) \tag{5.4}$$

$$\theta = \tan^{-1}\left(\frac{p_z}{\sqrt{p_x^2+p_y^2}}\right) \tag{5.5}$$

Note that the azimuthal and zenith angles can be obtained on an event-by-event basis by applying the above formulas to each neutrino vector $\vec{X}$.

Upon retrieving the reactors direction, one has to provide an uncertainty on the reconstructed angles. In their analysis, the CHOOZ collaboration evaluated this uncertainty using the normalized average sum of the neutrino vectors $\vec{p}/|\vec{p}|$. Assuming that the true neutrino direction (given by the layout geometry) is parallel the z-axis of the detector frame, the central limit theorem induces that the three components p_x, p_y and p_z are Gaussian distributions centered at $(0, 0, |\vec{p}|)$ with $\sigma \propto 1/\sqrt{3N}$. The 1σ uncertainty (68% C.L.) on the neutrino direction can thus be given as the half-aperture of the cone enclosing 68% of the events. One has to keep in mind that this uncertainty is, by definition, two-dimensional, which means it can be considered as the quadrature addition of the azimuthal and zenith uncertainties. This method will be referred to as the "CHOOZ method" in the following.
Another way of computing this uncertainty has been provided by Hochmuth et al. [185] in their study aiming at separating the two Chooz reactors using directionality with the Double Chooz near detector, then planned to be located closer to the cores. Being more statistically driven than the previous one, this approach is based on the neutron-positron spatial distribution. By defining two quantities l and L, l corresponding to the mean neutron path before thermalization, described in the next section, and L the weighted average of the widths of the p_x, p_y and p_z distributions, one can express the angular uncertainty as:

$$\sigma = \tan^{-1}\frac{L}{l\sqrt{N}}, \tag{5.6}$$

with N the number of events. Unlike the previous one, this uncertainty is mono-dimensional and can be applied to both azimuthal and zenith angles. This method will be referred to as the "Hochmuth method" from now on.
The third and last method is the one I chose to use by default in the following analyses, the previous methods will be given only for comparison purposes. The computation of the angular uncertainty in this approach is analytical and consists of deriving the equations of Eq. 5.5 for both azimuthal and zenith angles. After tedious calculations, I obtained the following errors:

$$\sigma_\phi = \frac{1}{1+\tan^2\phi}\sqrt{\left(\frac{\delta(p_x)p_y}{p_x^2}\right)^2+\left(\frac{\delta(p_y)}{p_x}\right)^2} \tag{5.7}$$

$$\sigma_\theta = \frac{1}{1+\tan^2\theta}\sqrt{\left(\frac{\delta(p_z)}{\sqrt{p_x^2+p_y^2}}\right)^2+\left(\frac{p_z}{\left(p_x^2+p_y^2\right)^{3/2}}\right)^2\left((\delta(p_x)p_x)^2+(\delta(p_y)p_y)^2\right)} \tag{5.8}$$

with $\delta(p_x)$, $\delta(p_y)$ and $\delta(p_z)$ the uncertainties on the p_x, p_y and p_z components. Like the "Hochmuth method", this approach provides a mono-dimensional angular uncertainty on the azimuthal and zenith angle.

n-Gd analysis

The 17,358 neutrino candidates in this analysis belong to the dataset used to perform the θ_{13} measurement of the Double Chooz third publication [75]. The corresponding n-Gd MC dataset contains about 1,900,000 events.

The first observable one can look into to demonstrate the IBD anisotropy is the average spatial difference between the interaction point and the neutron capture location. Indeed, as explained in Section 4.3.2, the positron mean path length at reactor energies can be considered negligible. This allows to regard the prompt event vertex as the neutrino interaction point. While the diffusion and gamma emission upon capture are isotropic processes, they occur after the moderation which keeps the memory of the neutron direction. Furthermore, at such energies, the neutron is emitted forward in the neutrino direction. To obtain the mean path length between the neutron creation and its loss of directional information, the so-called neutron displacement, one can look at the positron-neutron spatial separations along the x, y and z-axis, as shown in Figure 5.5. The behavior of each of these components is best-fitted by a Gaussian convoluted with two exponentials functions accounting for the tails of the distributions.

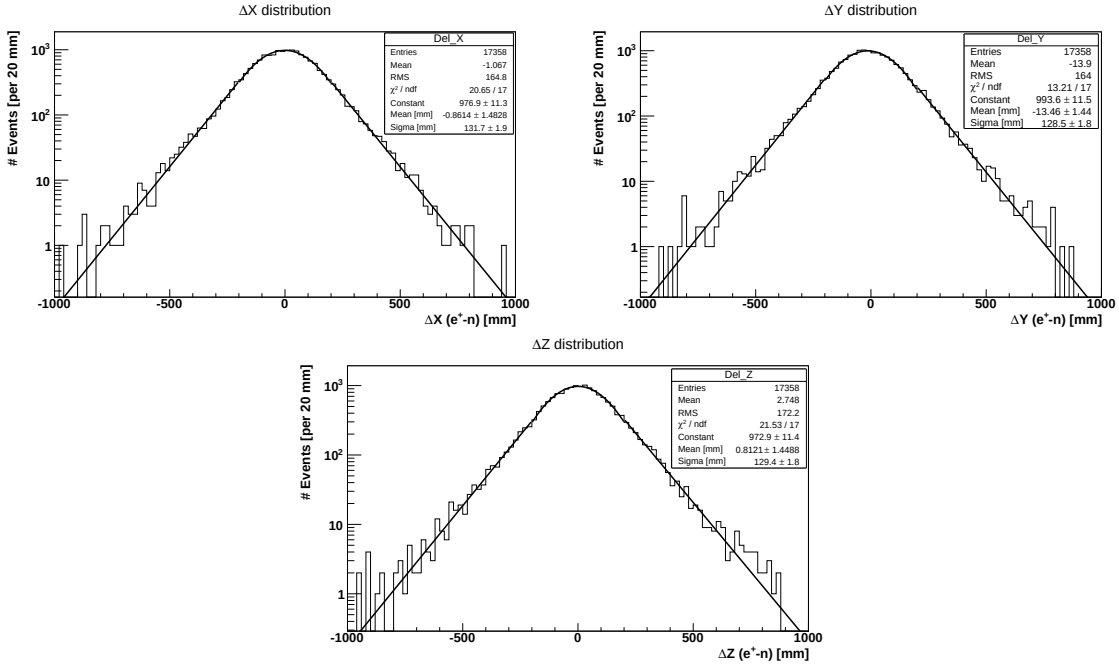

Figure 5.5: X, Y and Z components of the spatial separation of the (e^+-n) pairs. The data histogram is fitted by a "Gaussian+exponential" function, in solid black.

The displacement in each direction is provided by the mean of the Gaussian fitting the distribution. By adding these individual displacements in quadrature, one can recover the

total neutron displacement as such:

$$\mathrm{l_{DATA}} = \sqrt{\mu_{\mathrm{x}}^2 + \mu_{\mathrm{y}}^2 + \mu_{\mathrm{z}}^2} = 13.51 \pm 2.52 \text{ mm}, \tag{5.9}$$

in agreement with the MC computation:

$$\mathrm{l_{MC}} = 13.81 \pm 0.26 \text{ mm}. \tag{5.10}$$

From the means and variances of the p_x, p_y and p_z distributions, one can express the neutrino wind $\vec{p}$:

$$\vec{p}_{\mathrm{DATA}} = (-1.125; -13.890; +2.801) \pm (1.250; 1.244; 1.307) \tag{5.11}$$

$$\vec{p}_{\mathrm{MC}} = (-1.469; -14.120; -0.309) \pm (0.121; 0.122; 0.126)\,, \tag{5.12}$$

in mm for both n-Gd data and MC samples. Note that, while the x and y components are in agreement between data and MC, the z components are inconsistent. As displayed in Table 5.1, the Double Chooz far detector is positioned below the two reactors in term of altitude. One thus expect the z component of the $\vec{p}$ to be negative, as observed in the MC sample. This discrepancy has yet to be explained however, we suspect that it might come from a bias in the vertex reconstruction. This hypothesis has been investigated by Romain Roncin who put in evidence a bias in the position reconstruction along the z axis. More details can be found in Ref. [170].

After applying Eq. 5.5 on the $\vec{p}_{\mathrm{DATA}}$ and $\vec{p}_{\mathrm{MC}}$ neutrino wind vectors, one can obtain the reconstructed azimuthal and zenith angles of the reactors direction in the detector frame, summarized in Table 5.3.

n-Gd analysis	Azimuthal ϕ (°)	Zenith θ (°)	δ_{CHOOZ}(°)(2-D)	$\delta_{\mathrm{Hoch.}}$(°)(1-D)
Data	85.37 ± 5.16	11.37 ± 5.30	7.0	5.1
MC	84.06 ± 0.49	-1.25 ± 0.51	0.7	0.5

Table 5.3: Azimuthal and zenith angles with associated uncertainties of data and MC for the n-Gd analysis. The uncertainties δ_{CHOOZ} and $\delta_{\mathrm{Hoch.}}$ obtained via the bi-dimensional "CHOOZ" and mono-dimensional "Hochmuth" methods are shown for comparison.

The event-by-event azimuthal and zenith distributions, displayed in Figure 5.6, as well as its two-dimensional representation in (ϕ,θ), shown in Figure 5.7, both exhibit a behavior consistent with the angles reconstructed with the neutrino wind.

Using an approach similar to the Gosgen and Palo Verde directionality measurements, one can estimate the directional information carried by a neutrino dataset in a single distribution. This distribution is generated by evaluating the angle between each neutrino vector $\vec{X}$ and the known direction of the neutrino flux, or in other words the angle between the reconstructed and true neutrino direction. The cosine of this angle is expressed as:

$$\cos\alpha = \frac{\vec{X} \cdot \vec{\nu}}{||\vec{X}|| \times ||\vec{\nu}||}, \tag{5.13}$$

with $\cos\alpha$ the normalized scalar product of $\vec{X}$ the neutrino vector and $\vec{\nu}$ the neutrino direction. If a direction is favored, as expected in case of a forward non-anisotropy, the $\cos\alpha$ distribution

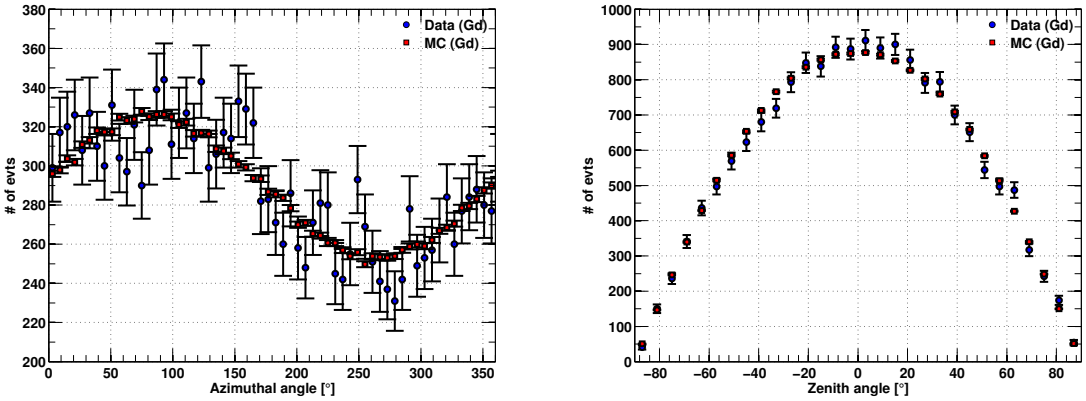

Figure 5.6: Azimuthal (left) and zenith (right) angle distribution of each event of the n-Gd dataset (blue circles) and normalized MC (red squares).

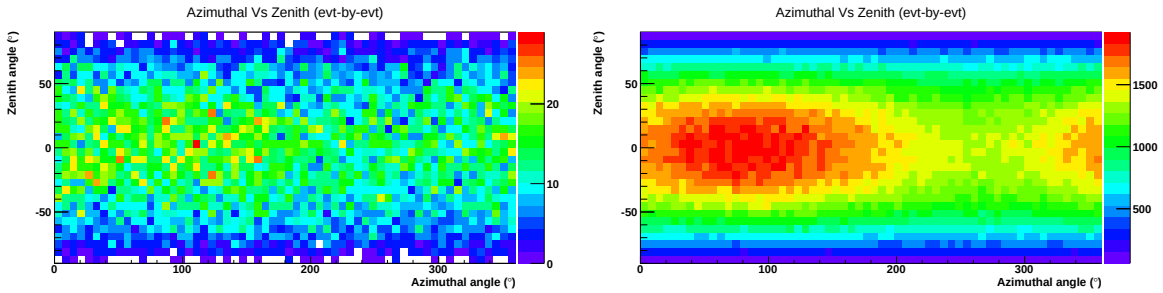

Figure 5.7: Azimuthal vs zenith angle distribution for both n-Gd data (left) and normalized MC (right).

is more peaked toward the positive values (+1) than the negative values (-1), as shown in Figure 5.8. The existence of an anisotropy, however weak, along the true neutrino axis is proven in both data and MC.

This distribution has the potential to provide a confidence level on the observation of neutrino directionality. Indeed, if no directional information were carried by the neutrinos of the sample, one would expect the $\cos\alpha$ distribution to be flat. The mean of a flat distribution between -1 and +1 is equal to 0 while the means of the distributions displayed in Figure 5.8 are equal to:

$$\mu_{\text{DATA}}\left(\cos\alpha\right) = 0.05383 \pm 0.0.00433 \tag{5.14}$$

$$\mu_{\text{MC}}\left(\cos\alpha\right) = 0.05320 \pm 0.00041, \tag{5.15}$$

quite off from that value, due to their asymmetry. From these values and their associated errors, one can naively estimate a confidence level by computing the difference between the reconstructed $\cos\alpha$ and flat distributions in terms of errors. By doing so, the n-Gd dataset excludes the non-directionality hypothesis by 12.42σ while the MC, due to higher statistic, excludes it by more than 120σ. Please keep in mind that this is a naive interpretation of the results. A dedicated χ^2 analysis is expected to provide more robust confidence levels.

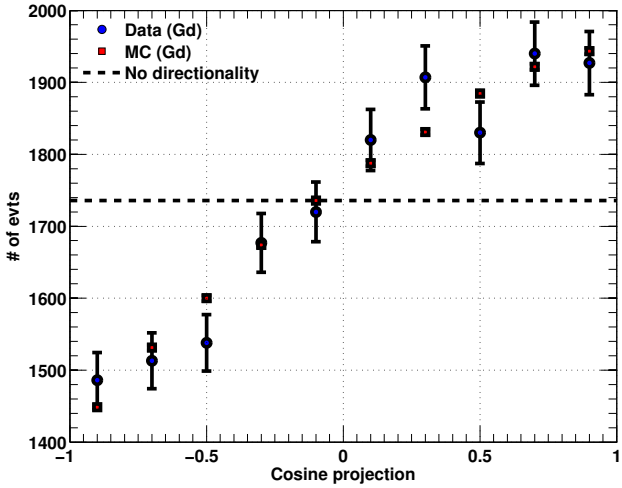

Figure 5.8: $\cos\alpha$ distribution of each event of the n-Gd dataset (blue circles) and normalized MC (red squares). The dashed black line represents the behavior of $\cos\alpha$ in case of IBD isotropy.

n-H analysis

The Double Chooz's directionality measurement with neutron capture on Gd is currently the most precise ever to be achieved. However, most liquid scintillator detector, especially at large scales, are not doped with Gd and only rely on the neutron capture on H to tag and detect neutrino events. Since no directionality measurement with n-H has ever been performed, its feasibility has yet to be proven. This measurement would pave the way for large liquid scintillator detectors such as JUNO [66] or LENA [186] in terms of potential for directional detection. The directionality analysis with n-H in Double Chooz aim to prove the feasibility of such a measurement.
The 31,898 neutrino candidates in this analysis belong to the dataset used to perform the second θ_{13} measurement from neutron capture on hydrogen that will be presented in an impending publication . The corresponding n-H MC dataset contains about 3,200,000 events.

Computed as in the n-Gd analysis, the total neutron displacement in the n-H data is found equal to:

$$\mathrm{l_{DATA}} = \sqrt{\mu_{\mathrm{x}}^2 + \mu_{\mathrm{y}}^2 + \mu_{\mathrm{z}}^2} = 10.84 \pm 2.33 \text{ mm}, \tag{5.16}$$

in agreement with the MC computation:

$$\mathrm{l_{MC}} = 11.68 \pm 0.22 \text{ mm}. \tag{5.17}$$

The neutrino wind $\vec{p}$ can be expressed as:

$$\vec{p}_{\mathrm{DATA}} = (-2.737; -11.610; -0.955) \pm (1.045; 1.037; 1.072) \tag{5.18}$$

$$\vec{p}_{\mathrm{MC}} = (-1.117; -10.992; -0.102) \pm (0.101; 0.101; 0.103)\,, \tag{5.19}$$

in mm for both n-H data and MC samples.

After applying Eq. 5.5 on the $\vec{p}_{\mathrm{DATA}}$ and $\vec{p}_{\mathrm{MC}}$ neutrino wind vectors, one can obtain the reconstructed azimuthal and zenith angles of the reactors direction in the detector frame, summarized in Table 5.4.

n-H analysis	Azimuthal ϕ (°)	Zenith θ (°)	δ_{CHOOZ}(°)(2-D)	$\delta_{\mathrm{Hoch.}}$(°)(1-D)
Data	76.74 ± 5.03	-4.58 ± 5.17	8.9	5.0
MC	84.20 ± 0.52	-0.53 ± 0.54	1.1	0.5

Table 5.4: Azimuthal and zenith angles with associated uncertainties of data and MC for the n-H analysis. The uncertainties δ_{CHOOZ} and $\delta_{\mathrm{Hoch.}}$ obtained via the bi-dimensional "CHOOZ" and mono-dimensional "Hochmuth" methods are shown for comparison.

Although computed with a twice larger statistic, the uncertainties on the azimuthal and zenith angle are similar in both analyses. Considering the IBD directional information as statistically driven, one should expect an uncertainty reduction from n-Gd to n-H by a factor $\sqrt{2}$. This discrepancy is due to the neutron diffusion after thermalization, much longer and spatially extended for captures on H. In addition, the neutron capture on H emits a single gamma ray of 2.2 MeV whose spatial reconstruction is wider than in the case of the 8 MeV gamma cascade generated upon a neutron capture on Gd.

The event-by-event azimuthal and zenith distributions, displayed in Figure 5.9, as well as its two-dimensional representation in (ϕ,θ), showed in Figure 5.10, both exhibit a behavior consistent with the angles reconstructed with the neutrino wind. The $\cos\alpha$ distribution for n-H is shown in Figure 5.11.

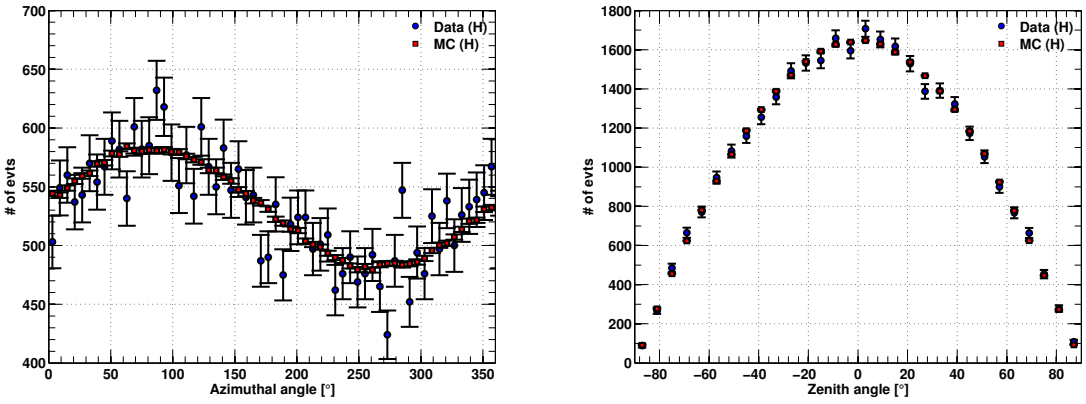

Figure 5.9: Azimuthal (left) and zenith (right) angle distribution of each event of the n-H dataset (blue circles) and MC (red squares).

From the standard deviations of the $\cos\alpha$ distributions and their associated errors:

$$\sigma_{\mathrm{DATA}}(\cos\alpha) = 0.04167 \pm 0.00321 \quad (5.20)$$

$$\sigma_{\mathrm{MC}}(\cos\alpha) = 0.04040 \pm 0.00032, \quad (5.21)$$

the n-H dataset excludes the non-directionality hypothesis by 12.98σ while the MC, due to higher statistic, excludes it by more than 120σ. Likewise the n-Gd analysis, please keep in mind that this is a naive interpretation of the results.

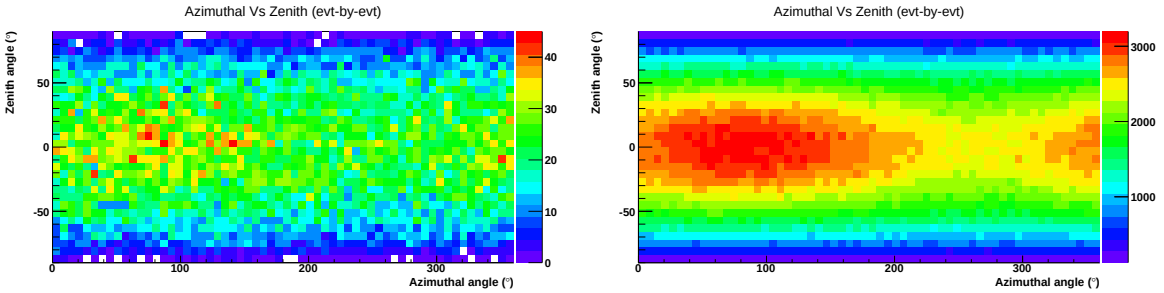

Figure 5.10: Azimuthal vs zenith angle distribution for both n-H data (left) and MC (right).

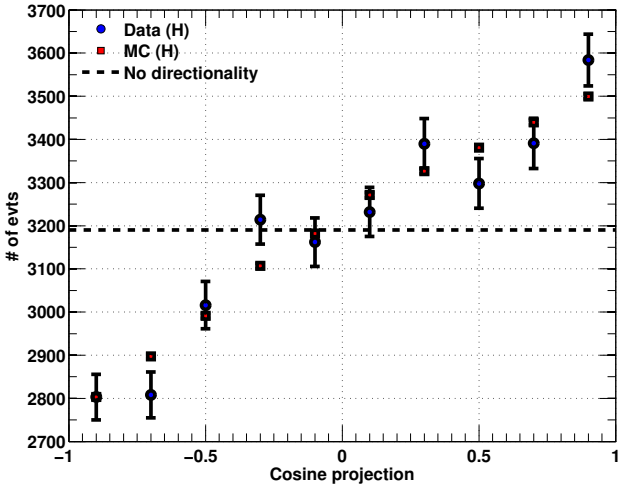

Figure 5.11: Cosine projection distribution of each event of the n-H dataset (blue circles) and MC (red squares). The dashed black line represents the behavior of $\cos\alpha$ in case of IBD isotropy.

Near detector

With only 1883 neutrino candidates extracted from its data (*c.f.* Section 6.5.3), the near detector and its n-Gd dataset do not provide a directional information as precise as the far detector. However with an expected rate of $\bar{\nu}_e$ candidates of $\sim$300 d^{-1}, it will quickly accumulate an important statistic. It is foreseen that the near detector directionality studies might provide an angular separation of the two reactors [185]. The following results will only consist of data since the MC dataset of the near detector has not been generated yet.

Computed as in the far detector, the total neutron displacement in the n-Gd data is found equal to:

$$\mathrm{l}_{\mathrm{DATA}} = \sqrt{\mu_{\mathrm{x}}^2 + \mu_{\mathrm{y}}^2 + \mu_{\mathrm{z}}^2} = 18.19 \pm 8.46 \text{ mm}, \tag{5.22}$$

in agreement, though a bit higher, with the previous displacements.

The neutrino wind $\vec{p}$ can be expressed as:

$$\vec{p}_{\mathrm{DATA}} \quad = \quad (-3.65; -17.22; 1.21) \pm (3.10; 3.23; 3.32)\,, \tag{5.23}$$

in mm.

After applying Eq. 5.5 on the $\vec{p}_{DATA}$ neutrino wind vector, one can obtain the reconstructed azimuthal and zenith angles of the reactors direction in the detector frame, summarized in Table 5.5.

n-Gd analysis	Azimuthal ϕ (°)	Zenith θ (°)	$\delta_{\text{Hoch.}}$(°)(1-D)
Data	78.05 ± 10.12	3.92 ± 10.77	10.02

Table 5.5: Azimuthal and zenith angles with associated uncertainties for the near detector's n-Gd analysis. The uncertainty $\delta_{\text{Hoch.}}$ obtained via the mono-dimensional "Hochmuth" method is shown for comparison.

The event-by-event azimuthal and zenith distributions, displayed in Figure 5.12 exhibit a behavior consistent with the angles reconstructed with the neutrino wind. The $\cos\alpha$ distribution has not been computed since it relies on the knowledge of the reactor-detector layout, still unraveled at this time.

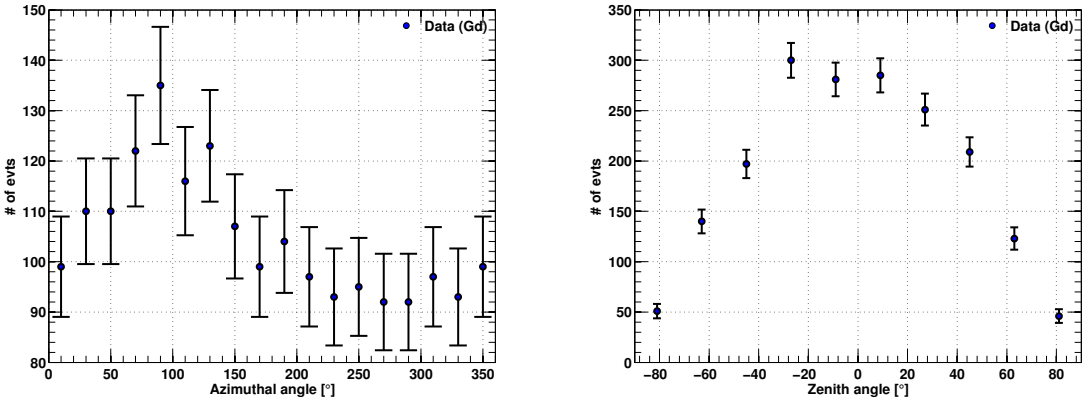

Figure 5.12: Azimuthal (left) and zenith (right) angle distribution of each event of the near detector's n-Gd dataset.

As explained in Section 6.5.3, the near detector's $\bar{\nu}_e$ candidates have been selected with basic cuts and without the usual background rejection techniques. Further directionality analyses with a larger statistic and a better understanding of backgrounds will soon provide better direction measurements with both n-Gd and n-H data sets.

The agreement between the n-Gd and n-H analysis is the conclusive proof that directionality is achievable in undoped large scale liquid scintillator detectors. The Double Chooz directionality measurements could thus lead the way for various applications such as reactor localization, supernovae pointing or geoneutrino directional detection.

5.4 Application: Supernovae detection

The early arrival of SN1987A neutrinos on Earth (*c.f.* Section 3.3.2) raised a strong interest in the neutrino and astronomical communities leading to the development of the SNEWS

network *c.f.* Section 3.3.3). An early pointing could allow the astronomical community to quickly locate the supernova and consequently study the explosion early phases with the world's telescope armada.

The estimated core-collapse supernova rate in our Galaxy is a few per century. The possible progenitor could be located anywhere, nevertheless the supernova probability distribution computed from the red giant stars distribution is centered around 11.9 kpc with a RMS dispersion of 6 kpc [187].

Neutrino scattering on electrons in a very large water Čerenkov detector, such as Super-Kamiokande, provides the best way to locate a supernova through neutrinos, with an accuracy of about 8 degrees at 10 kpc (95% C.L.) [188]. However, the pointing accuracy is degraded by the IBD reactions, with a neutrino scattering signal over IBD noise ratio of about 1/30. On the other hand, the large cross section of the IBD reaction compared to neutrino scattering allows the detection of supernova $\bar{\nu}_e$ in smaller detectors.

During my thesis, I worked on the early pointing of a core-collapse supernova using the IBD reaction in Large Liquid Scintillator Detectors (LLSD). Although it does not provide an event by event pointing ability, the high cross section of this reaction leads to a high number of interactions, almost free of backgrounds. The statistical analysis of the angular distributions of the reaction products (positron and neutron) can be correlated to the neutrino direction and its associated uncertainty, enabling an early pointing of the supernova.

The following study has been condensed in the form of an article [158].

5.4.1 Toy Monte Carlo for supernova position reconstruction

The main purpose of this work is to associate a reconstruction uncertainty to the pointing of a supernova using the IBD detection in liquid scintillator detectors. To do so, I simulated supernova neutrino datasets using the SuperNustradamus simulation package, described in Section 4.3.2. Since it describes the neutrino spectrum as expected on Earth, these datasets were generated from a GVKM energy spectrum convoluted with the Strumia-Vissani cross section, default cross section for all SuperNustradamus simulations. As previously explained, these datasets consist of prompt and delayed events, associated to a neutrino event, with corresponding visible energies and reconstructed vertex positions.

In order to estimate the direction of incoming neutrinos, I now define the Delayed-Prompt vector $\vec{X}$ for each neutrino event, as displayed in Figure 5.13. This unit vector has its origin at the positron reconstructed position and points toward the neutron capture reconstructed location.

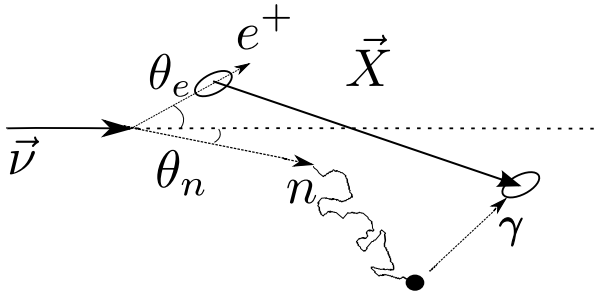

Figure 5.13: Sketch of the Delayed-Prompt vector $\vec{X}$ along the direction of the incoming neutrino.

A direction (ϕ, θ) is then computed for each event with ϕ and θ respectively the azimuthal and zenith angles in the detector reference frame. The angular distributions extracted from a supernova simulation are displayed in Figure 5.14. These distributions are respectively the azimuthal angle distribution, the zenith angle distribution and the cosine projection on the neutrino axis expressed in Eq. 5.13. All simulations were carried out using a conservative vertex resolution of 20 cm. Tests with a 15 cm vertex resolution were performed without yielding significant improvements.

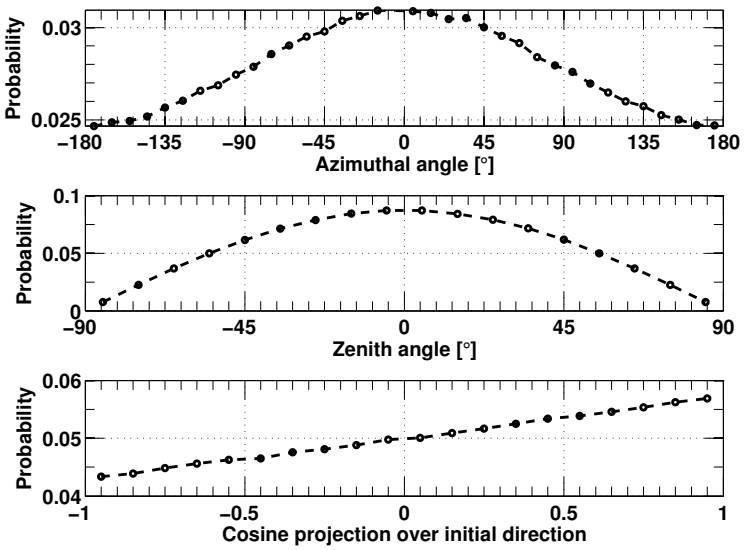

Figure 5.14: Probability density functions of azimuthal angle (top), zenith angle (center) and cosine projection on the neutrino direction (bottom) distributions extracted for a supernova pointing towards the (0,0) spherical coordinates. The angular distributions are centered on the (0,0) spherical coordinates. Neutrino energies are drawn from a GVKM spectrum.

In order to consider all the relevant features of the IBD kinematics the direction is reconstructed using a χ^2 minimization method comparing a model and a supernova dataset, both simulated with SuperNustradamus. The model dataset is computed with a large number of events, typically of the order of 500,000 events, in order to smooth statistical effects and generated along an arbitrary direction. On the other hand, the supernova dataset has a realistic statistic corresponding to the number of IBD interactions in a given detector and is generated along a user-defined direction (ϕ_0, θ_0). By rotating the model distribution across the sky, the fit algorithm finds the best-fit angles (ϕ, θ) corresponding to the minimum value of the χ^2 expressed as:

$$\chi^2(\phi,\theta) = \sum_i^N \sum_j^N \left(Y_i - M_i(\phi,\theta)\right) \left(V^{-1}\right)_{ij} \left(Y_j - M_j(\phi,\theta)\right), \tag{5.24}$$

where Y_i and $M_i(\phi,\theta)$ are the concatenation over N bins of the three angular distributions (azimuthal, zenith and cosine projection) of the supernova and model datasets, respectively. V_{ij} is the N×N covariance matrix made of two independent blocks accounting for the bin-to-

bin statistical uncertainty of the azimuthal and zenith angle distribution and a third block, correlated to the first two, accounting for the bin-to-bin statistical and systematical uncertainties of the cosine projection distribution expressed in Eq. 5.13. The V_{ij} covariance matrix, displayed in Figure 5.15 has been generated using 2,000 independent datasets of 5,000 neutrino events each, then normalized to one event. The resulting unitary covariance matrix is then normalized to the number of events in the supernova dataset being used in each χ^2 minimization.

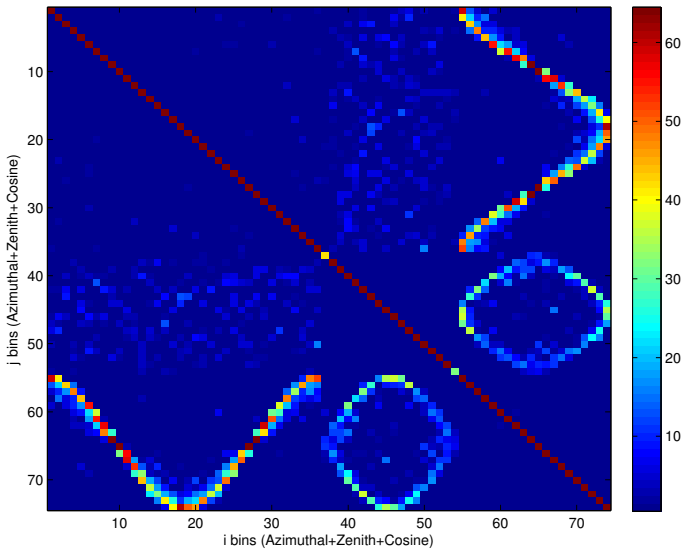

Figure 5.15: Covariance matrix of the concatenated azimuthal, zenith and cosine projection distributions.

The best-fit angles (ϕ, θ) corresponding to a minimum of χ^2 are then stored and the process is repeated with a new supernova dataset having the same statistic. From all these trials, I obtain distributions of reconstructed azimuthal and zenith angles whose means and variances correspond to the reconstructed supernova directions and associated angular errors.

5.4.2 Detectors of interest

The detection of supernova neutrinos in liquid scintillators relies on the existence of numerous large scale detectors with a mass larger than several tens of tons. These volumes are large enough to detect a significant number of events and tag a supernova in our Galaxy or its closest satellites, such as the Small and Large Magellanic Clouds, with a negligible fake detection rate, thanks to the coincidence between detectors. The non-exhaustive list of detectors considered in this work and their relevant characteristics are collected in Table 5.6. Their respective expected event rates, computed with Nustradamus (*c.f.* Section 4.3.2) are displayed on Figure 5.16 and Table 5.7.

NOνA (NuMI Off-Axis $\bar{\nu}_e$ Appearance) is an experiment dedicated to observe ν_e appearance using Fermilab's ν_μ beam NuMI [67]. It operates above ground with two detectors, each made of individual cells of liquid scintillator of 3.87 cm $\times$ 6.00 cm $\times$ 15.7 m. With 12'480 cells, NOνA's near detector consists of 145 tons of active material while the far detector and its

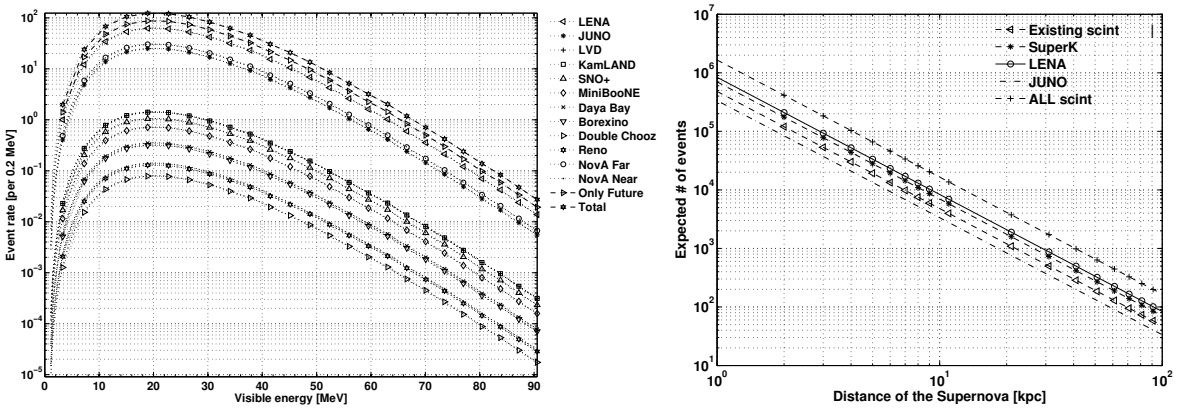

Figure 5.16: Left: IBD interaction rate in various LLSD as a function of the visible energy, for a core collapse supernova located at 10 kpc. "Future only" and "All" are respectively the combination of LENA and JUNO and the combination of all LLSD, current and future. Right: IBD interaction rate for LLSD as a function of the supernova distance. The number of expected IBD events in Super-Kamiokande is shown for comparison.

Table 5.6: Main detector features used in the simulation.

Detector	Dimensions (m)	Shape	V (m^3)	free H/m^3	# free H
LVD	a=10,b=13.2,c=22.7	Box	1020	7.46 $.10^{28}$	7.6 $.10^{31}$
KamLAND	r=6.50	Sphere	1150	6.60 $.10^{28}$	7.6 $.10^{31}$
SNO+	r=6.00	Sphere	904	6.24 $.10^{28}$	5.6 $.10^{31}$
Borexino	r=4.25	Sphere	321	5.30 $.10^{28}$	1.7 $.10^{31}$
Daya Bay	r=2.00,h=4.00	Cylinder	50(× 6)	6.24 $.10^{28}$	1.8 $.10^{31}$
Double Chooz	r=1.70,h=3.55	Cylinder	32(× 2)	6.55 $.10^{28}$	0.4 $.10^{31}$
Reno	r=2.00,h=4.40	Cylinder	55(× 2)	6.24 $.10^{28}$	0.7 $.10^{31}$
NOνA (far)	a=15.7,b=15.7,c=132	Box	32500	6.24 $.10^{28}$	2.0 $.10^{33}$
NOνA (near)	a=3.5,b=4.8,c=9.58	Box	161	6.24 $.10^{28}$	1.0 $.10^{31}$
MiniBooNE	r=5	Sphere	523	7.31 $.10^{28}$	3.8 $.10^{31}$

761'856 cells encloses 24 ktons of liquid scintillator. Its important background rate at sub-GeV energies and its energy threshold, above the neutron capture on H at 2.2 MeV, does not allow an efficient neutrino burst detection nor a neutron vertex reconstruction yet. NOνA will thus not be taken into account in the following direction reconstruction analyses.

The Large Volume Detector (LVD)[189] is located at the Laboratori Nazionali del Gran Sasso (42° 27' 10" N, 13° 34' 30" E), at the depth of 3600 m.w.e.. It is a 1 kt liquid scintillator detector in the form of an array of 840 scintillator counters, 1.5 m^3 each. While its active mass allows the detection of an important number of neutrinos, the size of LVD's individual scintillating counters prevents any precise position reconstruction. Hence, like NOνA, it will not be taken into account in the following directionality analyses.

From now on, the following detectors will be considered in our directionality analyses. The KamLAND experiment [190] is a 1 kton liquid scintillator (80% dodecane and 20% pseudocumene) balloon located within the Kamioka mine in Japan (36° 25' N, 137° 18' E), at 2700 mwe under the Ikenoyama mountain.

The SNO+ experiment [191] is currently in its final construction phase at the SNOLab

laboratory (46° 28' 30" N, 81° 12' 04"), shielded with an overburden of 6000 m.w.e.. SNO+ will be filled with 780 tons of Linear Alkyl Benzene (LAB).

The Borexino experiment [192] is located at the Laboratori Nazionali del Gran Sasso in Italy (42° 27' 10" N, 13° 34' 30" E) and shielded with an overburden of 3800 m.w.e.. It consists of 278 tons of pseudocumene-based liquid scintillator.

Three reactor neutrino oscillation experiments, Daya Bay [108], Double Chooz [71], and RENO [73] are currently taking data to measure the θ_{13} mixing angle. They all consists of several identical detectors located within two kilometers from several powerful nuclear power plant cores used as intense electron antineutrino sources. The Daya Bay experiment is located in the Guang-Dong Province, on the site of the Daya Bay nuclear power station (22° 36' 59" N, 114° 32' 28.1" E). Each of the six cylindrical identical detector modules contains an effective volume of 20 tons of 1 g/l Gd-loaded liquid scintillator, and 22 tons of non-doped scintillator. The Double Chooz experiment is located close to the twin reactor cores of the Chooz nuclear power station located in the French Ardennes (50° 08' 43" N, 4° 80' 165" E). The two cylindrical identical detectors contain a 8-ton fiducial volume of liquid scintillator doped with 1 g/l of Gd and 18 tons of non-doped scintillator. The RENO experiment is located on the site of the Yonggwang nuclear power plant in Korea, about 400 km south of Seoul (35° 24' 04" N, 126° 25' 31.5" E). The two cylindrical identical detectors contain a 16-ton fiducial volume of liquid scintillator doped with 1 g/l of Gd and 39 tons of non-doped scintillator. Given the relatively low number of events expected from capture on Gd in those three detectors, in the following we only consider the events expected from neutron capture on H. Considering the energy and vertex reconstruction enhancement brought by neutron capture on Gd, this is a conservative approach.

The MiniBooNE detector [193], located at Fermilab (41° 83' N, -88° 26' E), is a spherical volume containing 680 tons of mineral oil built at ground level. The project of adding PPO in the mineral oil proposed in Ref. [194] indicates the detector might still be running for a few years. The addition of PPO would enhance scintillation and set MiniBooNE in our LLSD list.

Table 5.7: Expected number of interactions taking into account the exact liquid scintillator chemical compositions and densities, for a 10 kpc core-collapse supernova.

	Livermore	GVKM
LVD	319	190
KamLAND	318	189
SNO+	237	141
Borexino	71	43
Daya Bay	79	47
Double Chooz	18	11
RENO	29	17
NOνA far	6811	4057
NOνA near	32	19
MiniBooNE	161	96

Beyond the currently running detectors, two projects of large-scale liquid scintillator detectors are being considered: JUNO and LENA. These detectors, besides providing an answer to some of the major open questions remaining in the neutrino field, are perfect apparatus for studying core-collapse supernovae.

JUNO (Jiangmen Underground Neutrino Observatory) is under construction and will consist of a 20 kt LAB-based liquid scintillator detector located at Jiangmen (22°37' N,

112°70' E) in South China [66]. Being 20 times as massive as SNO+, the same factor on the expected event number is expected.

LENA (Low Energy Neutrino Astronomy) is a project designed to be a next-generation liquid scintillator detector on the scale of 50 kt [186]. Its location is still under investigation but the most probable is the Pyhäsalmi mine (63°39' N, 26°2' E, 4000 m.w.e.), located in the Pyhäjärvi province in Finland.

Note that, although their masses are one order of magnitude bigger than the current detectors, JUNO and LENA will only observe a couple of neutrino events from the closest galaxy, M31.

5.4.3 Combined multi-detectors fit

I applied the method previously described to a single detector. I considered KamLAND in this first application. I generated several datasets with different numbers of events and computed their associated angular uncertainty using the method previously described. Figure 5.17 (left) shows the interpolation of these results, best fitted by an inverse square root function, and describes the behavior of the angular uncertainty with respect to the number of detected events. Using this curve and the expected number of events computed with Nustradamus, I associated an angular uncertainty on the supernova reconstructed direction for KamLAND at different distances as shown in Figure 5.17 (right). Several simulations were carried out using the different flux shapes presented in Section 3.3.1 and no sensible differences in the results have been found. With a number of events leading to an angular uncertainty greater than 90°, I consider that no directional information can be extracted and consequently discard the concerned detector from the directionality reconstruction. On the other hand, the detection of more than 50,000 events would lead to a trigger rate too high to be withstood, hence I arbitrarily consider it as the detection limit. Therefore, any observation of a higher neutrino rate in a single detector would, in the analyses, not bring additional direction information and the reconstruction error could not reach lower values. Between these two limits, the angular uncertainty increases with the distance and with the inverse of the number of events. The statistical nature of the IBD directionality process is well shown since several thousands of events are required to obtain a decent reconstruction uncertainty. As a consequence, the pointing potential of a single detector such as KamLAND gets degraded as soon as the distance exceeds a few kpc, hence the interest of combining several detectors to improve the accuracy.

Higher sensitivities on supernova position reconstruction are reachable adding the directional information provided by several detectors. Each of the detectors previously described in Section 5.4.2 could detect a supernova assuming it leads to a sufficient amount of detected events. The combination of these signals increases the supernova detection potential in two ways.

First, observing a coincident supernova signal in several detectors across the globe strengthens the confidence that a supernova has occurred. This is the current role of the SNEWS network, described in Section 3.3.3. Furthermore the time difference between the supernova signals coming from those detectors could give us a first hint of localization using the triangulation method as discussed in [169]. This method might not be accurate enough at typical supernova distances since it requires a good understanding of the luminosity time distribution and is strongly statistic dependent. A significant work of precise time calibrations between detectors would also be mandatory.

Second, one can combine the reconstructed angular directions and errors provided by

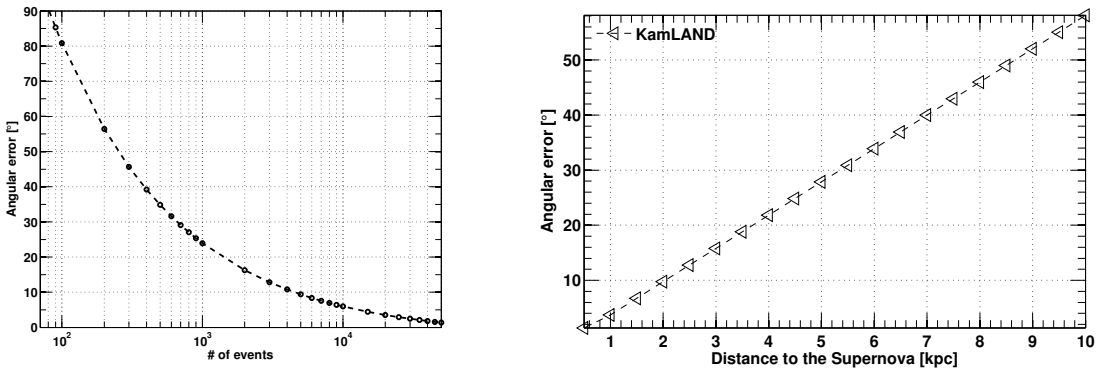

Figure 5.17: Left: Angular uncertainty as a function of the number of detected events. Right: Angular uncertainty as a function of the distance in kpc in the KamLAND detector.

those detectors to improve the localization of the detected supernova.

Table 5.8: List of individual detectors and their corresponding datasets.

	Existing	SNEWS	Near future	All
LVD				
KamLAND	×	×	×	×
SNO+	×	×	×	×
Borexino	×	×	×	×
Daya Bay	×	×	×	×
Double Chooz	×		×	×
RENO	×		×	×
NOνA (far)				
NOνA (near)				
MiniBooNE			×	×
JUNO			×	×
LENA				×

In the context of a global analysis with N detectors combined, all the individual angular "cones" of 1σ azimuthal and zenith uncertainties must be combined into a single one. To do so, I combined the individual angular errors and expressed the average angular uncertainty as:

$$\bar{\sigma} = \left(\sum_{i=1}^{N} \frac{1}{\sigma_i^2} \right)^{-\frac{1}{2}}, \tag{5.25}$$

with σ_i the 1σ uncertainty on the supernova direction reconstructed in the i^{th} considered detector.

In the following analysis, I considered 4 sets of combined detectors, summed up in Table 5.8. The "Existing" dataset is the combination of all current LLSD, "SNEWS" consists of the four LLSD belonging to the SNEWS network as detailed in Section 3.3.3, "Near future" is the sum of all current LLSD with the addition of MiniBooNE and JUNO, planned to operate within the next 5 years and finally "All" consists of the sum of all detectors, current and future. Results are displayed in Figure 5.18 for individual detectors and Figure 5.19 for the sets of combined detectors.

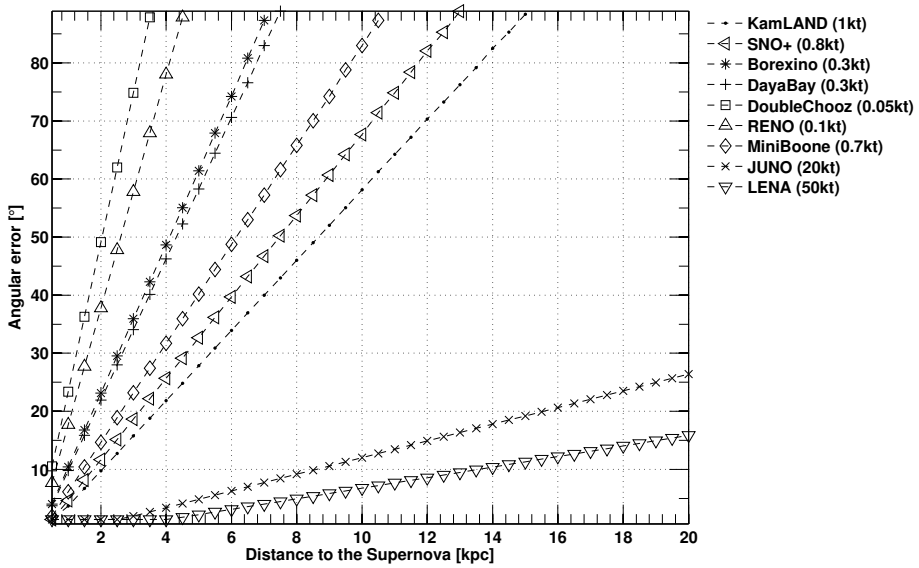

Figure 5.18: Angular uncertainty as a function of the supernova distance for different detectors and their associated masses.

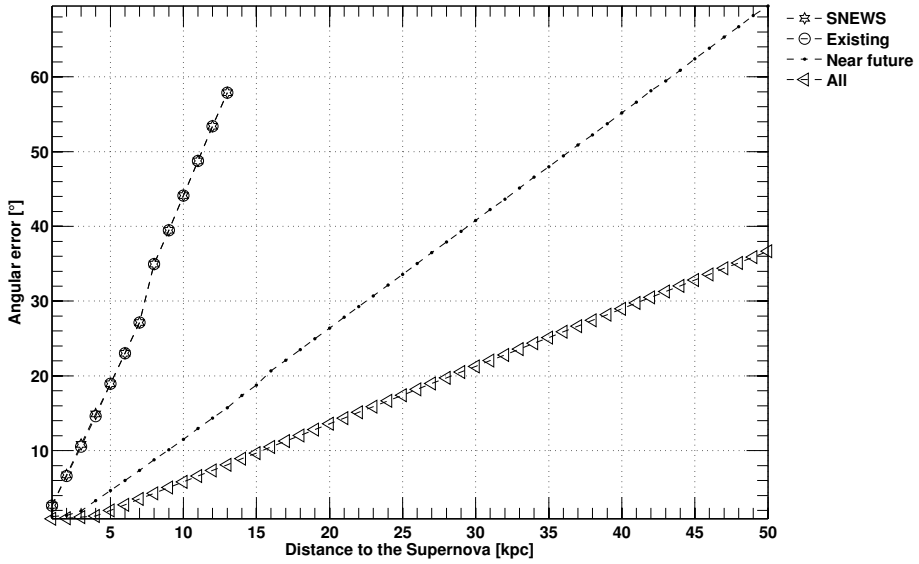

Figure 5.19: Angular uncertainty as a function of the supernova distance for different detector combinations. The mean reconstruction error for combined detectors is computed using the combination of the angular reconstruction error associated with each individual detector. Due to the small event rate expected in Double Chooz and RENO, the "SNEWS" and "Existing" datasets yield very similar results.

Considering a supernova located at 10 kpc, no current detector could provide a valuable direction information other than the hemisphere in which the supernova occurred. However, when combining several of these detectors, this same supernova direction is likely to be reconstructed within a 45°(68% C.L.) cone. While this angular opening is still larger than most of the optical instruments can accommodate, the addition of JUNO in a near future would reduce the uncertainty to 12°(68% C.L.), hence reaching a relevant level, almost competitive with the current Super-Kamiokande detector. With the conservative assumption that any galactic gravitational stellar collapse will occur within a 20 kpc radius, the addition of current and future detectors could reconstruct its position within a 14°(68% C.L.) cone.

5.4.4 Discussion

The coincident observation of a burst in several neutrino detectors would be a robust early warning of a forthcoming visible galactic core-collapse supernova. The main goal of the SuperNova Early Warning System (SNEWS) is to provide the astronomical community with this early alert of a supernova [154]. Each experiment belonging to SNEWS has its own supernova real-time trigger system dedicated to detect a burst of events that might be linked to a supernova. When the trigger requirements are met, an alert is sent to the global SNEWS server and is compared with possible alerts coming from other experiments. If a coincidence is found within a time window of 10 seconds, a global alert is sent to the SNEWS mailing list, universally accessible via snews.bnl.gov. In 2014, Daya Bay joined the SNEWS network already composed of Super-Kamiokande, LVD, Borexino, SNO+, KamLAND and IceCube. Adding Double Chooz, RENO and NOνA to the network would increase the number of detected supernova neutrinos, thus strengthening the confidence level of an hypothetical alert.

The SNEWS network is set up to provide information that a supernova has been detected via its neutrinos to astronomers. Although this information is mostly characterized by the observation of a burst of events in coincidence in several experiments, a directional information could be sent as well, if provided. Without this information, the supernova location remains unknown until its observation. Knowing this position, even roughly, over the sky would give astronomers a consequent head start and could lead to the observation of a complete supernova process, including its early luminosity rise.

Even though current LLSD in SNEWS can provide directional information for nearby supernovae, Super-Kamiokande remains the best detector to locate them. However, with the replacement of SNO heavy water with liquid scintillator and before the construction of Hyper-Kamiokande [195], it stands alone as the world's only large Čerenkov detector. Relying solely on Super-Kamiokande might not be enough to ensure a permanent watch on supernovae. Any maintenance operation or reconstruction software issue could put astronomers in the blind in case of a long-awaited supernova detection.

With the help of SNEWS's current and future liquid scintillator detectors, this scenario is unlikely to happen as the directional information of several detectors that observed the supernova can be combined. In the case of all SNEWS detectors operating at once, the Super-Kamiokande direction reconstruction will be improved by the combined reconstruction of all LLSD. With only 4 LLSD (KamLAND, Borexino, SNO+ and Daya Bay) capable of direction reconstruction, SNEWS is currently able to locate a 8 kpc supernova within a barely practical 35°(68% C.L.) wide cone. However, with the addition of all current LLSD as well as JUNO and MiniBooNE in a near future, the opening of this cone could be reduced to 9°(68% C.L.) thus reducing by a factor 15 the area of the sky region of interest.

In order to join the SNEWS network, each experiment would have to meet a few requirements, one of the most important being the robustness of its data acquisition system (DAQ), i.e. its capability to quickly and efficiently tag a supernova burst. In order to send a reliable alert to the SNEWS global server, each detector's DAQ needs to be modified to operate on real-time mode and detect any unusual trigger rate increase. In the case of NOνA, the detector's trigger is directly synchronized with the NuMI beam trigger hence the necessity of operating the detectors in a "free" mode without any external trigger as presented in Ref. [67]. An example of the implementation of such a trigger for the Daya Bay detectors is detailed in Ref. [196].

Implementing a combined pointing ability within the network might be more challenging. While the detection of a supernova burst solely relies on the observation of a burst of events in several detectors in coincidence, its pointing towards the sky requires energy and position reconstructions of these events. Most detectors operate on a run-by-run basis and usually analyze large datasets after long periods of data taking. Providing a neutrino direction within a time scale of a few hours would require off line and real time data analysis. This might be achieved by installing separate and independent online data acquisition and analysis chains capable of supporting large data rates and fast energy and position reconstruction based on the current analysis.

In this work, I discussed the interest of combining worldwide large liquid scintillator detectors to efficiently reconstruct a supernova location. Such an information would be precious to the SNEWS network in order to provide not only an alert that the optical observation of a supernova is imminent but also that it is likely to occur in a restricted region of the sky. While for a typical supernova located at 10 kpc, a 45°(68% C.L.) reconstruction cone would be currently too large to be entirely enclosed within the aperture of an optical telescope[1], it would focus astronomers attention to a particular field of view, enhancing the probability for a comprehensive optical observation. The impending Zwicky Transient Facility (ZTF) [197] will be able to completely scan this region of the sky within two hours. The presence of several telescopes based on the design described in Ref. [198] would provide a high probability of successful observation as well. The implementation of future detectors would soon reduce the region of interest to a 12°(68% C.L.) radius cone. In the case of a nearby supernova 2 kpc away, a single detector such as KamLAND could point its direction within a 10°(68% C.L.) cone and the combinations of current and/or future detectors could reduce this uncertainty below 5°(68% C.L.).

Though it has hardly been discussed in this work, the observation of a large quantity of neutrinos in several large detectors will help improve the direction reconstruction via triangulation technique. The combined data from several time-calibrated detectors scattered over the globe would be contained within the 40 ms time window corresponding to the Earth's crossing. The detection of a full neutrino spectrum at each moment of the supernova luminosity rise and decay would decrease any statistical uncertainty related to the luminosity rise time thus making triangulation a viable technique as explained in Ref. [169]. Since only IceCube, Super-Kamiokande and NOνA's far detector are currently operating with active masses relevant for triangulation, it might not be a suitable method as we speak. However, with the impending construction of large detectors such as JUNO, LENA or Hyper-Kamiokande, it could be considered as reliable as the other methods. Another pointing method relying on the observation of spectral distortions caused by matter effects in Earth is discussed in Ref. [199].

[1]Note that the Moon's angular diameter over the sky is 0.5° hence enclosed in a 0.25° radius cone.

Recent technological developments have been successfully carried out in the field of detection materials. For example, detectors using liquid scintillators mixed and dissolved into water are currently being designed. A detailed study of such technology and its potential physics applications can be found in Ref. [200]. Besides combining the technical advantages of both materials, a water-based liquid scintillator (WbLS) detector also provides two directional information. Indeed, enhanced by the possible use of fast photodetectors such as LAPPD's (Large Array Picosecond PhotoDetectors), the collection of Čerenkov and scintillation light produced by the both IBD and electron scattering processes would exploit the full directional information carried by neutrinos. Another promising concept is the hydrogeneous Time Projection Chamber (TPC) described in Ref. [201]. Consisting of a detection volume filled with an organic liquid at room temperature and covered by a layer of noble gas under an electric field, it could allow a 3D imaging of the IBD interaction occurring in the liquid with the use of pixelated light detectors. Such a detector could in principle provide an almost event-by-event directional information for each IBD interaction, since it allows the reconstruction of the positron track and energy and the first neutron-induced proton recoil. Besides, its simple design and capability to be operated at room temperature could help its development at large scales.

I would like to draw attention to technical issues that might arise along with the high event rates in large detectors. Underground detectors are designed to operate in an ultra low background environment with typical trigger rates of a few hundred Hz. The detection of tens of thousands of neutrinos even distributed in time over a 10 s window with a strong peak at 1 s may lead to a non-negligible dead-time or, worst case scenario, to a DAQ crash. On the other hand, the NOνA far detector, since it operates at the surface, is subjected to a 300 kHz background rate from cosmic rays at 10 MeV. While thanks to its fine-grained segmentation, it could separate IBD events from cosmic muons tracks, an efficient supernova tagging would place significant demands on the DAQ in terms of dead-time and data readout and analysis rates. In order for any of these detectors to efficiently collect a large number of neutrinos in a short period of time and increase its pointing ability, consequent efforts will be required to improve the current state of data acquisition. For instance, the MicroBooNE detector operates with an untriggered continuous readout and saves its data on a disk for several hours, in case an alert from the SNEWS network is issued, thus running without dead-time [202].

5.4.5 Retrieving astrophysical information from supernova neutrinos

Beyond the main goal of determination of the supernova direction, I will now address in this section additional information that could be retrieved by LLSD, using the IDB process. In particular, I will consider the determination of the supernova distance and then the assessment of the neutron star mass. The latter was investigated in Ref. [203] in the case of SN1987A. I also briefly address the possible discrimination between distinct supernova neutrino energy spectra.

Measurement of the supernova distance

Since, for a given supernova, the number of detected events varies with the inverse of the squared distance, the determination of its distance sounds straightforward in principle. To better understand the impact of statistical and systematic uncertainties, I developed a Monte-

Carlo simulation to generate and fit the detected energy spectra with a χ^2 minimization method. This simulation is independent from the direction retrieval fit presented in Section 5.4.1 and allows the comparison between fake data fitted with the GVKM flux under various hypotheses. While the energy spectra are generated by SuperTOY, as before, only the χ^2 minimization differs. In this case, the minimization is based on a Pearson's χ^2 such that:

$$\chi^2 = -2\sum_i^N Y_i - M_i + Y_i \ln M_i/Y_i, \tag{5.26}$$

with Y_i and M_i are the respective energy spectra over N bins of the supernova and model datasets. I chose this statistical test rather than a Gaussian's χ^2 test due to the low number of events expected at large distances. In these cases, several bins of the energy spectrum were empty or too low to be following a Gaussian statistic, thus leading to a bias of up to 10% in the distance reconstruction at 10 kpc.

The main systematics considered are uncertainties on the neutron star features. Indeed the number of emitted neutrinos depends on the difference between the progenitor star and the neutron star gravitational binding energies. However, the first term can be considered negligible and the neutrino flux therefore depends on the neutron star binding energy[2] $E_B = \frac{3}{5}\frac{M_{ns}^2}{R_{ns}}$ with M_{ns} and R_{ns}, being the mass and radius of the neutron star [29]. In the literature these parameters are usually set to $M_{ns} = 1.4\ M_\odot$ and $R_{ns} = 10$ km [32]. From the average observed neutron star masses and radii computed in Ref. [204] and Ref. [205], I conservatively consider a relative uncorrelated systematic uncertainty of 10% for both parameters. I simulated GVKM-based supernovae bursts located from 1 to 10 kpc away and reconstructed their distances and associated uncertainties (stat. + syst.). Hereafter, a conservative energy resolution of 6% in the whole energy range is taken into account. The distance is reconstructed without bias and with an uncertainty of 40% and 15% at 10 kpc for a 1 kt and a 20 kt detector, respectively. These results are valid for the spectral shapes of the GVKM and Livermore fluxes presented in Section 3.3.1.

Measurement of the neutron star mass

A large set of neutron star masses have been previously measured and are listed in Ref. [204]. These measurements provide relative uncertainties at the 0.1% level on the neutron star mass for binary systems. However, an isolated system such as a single supernova without companion would not provide as much precision. Hence, our interest to retrieve the neutron star mass from the number of detected neutrino events. I now fix the supernova distance, assumed to be known by another conventional technique and try to retrieve the neutron star mass from the number of detected events and the expression of the neutron star gravitational energy. In a practical case, the measurement of the distance could be achieved through the Expanding Photosphere Method [206]. This technique led to a 10 % uncertainty of the SN1987A distance. Using this as a reference, I fix the uncertainty on the reconstructed distance to 10%. I also fix the neutron star radius and associated uncertainty, as in Section 5.4.5. I can thus assess how well one could measure the neutron star mass by fitting the energy distribution of incoming neutrino events as in Section 5.4.5. I generated neutrino supernova spectra with statistics

[2]In Sections 5.4.5 and 5.4.5 an approximated relation of the gravitational binding energy of a sphere of uniform density is employed. I use it here for illustrative purposes, since the determination of the supernova distance and of the neutron star mass are not the main purposes of the present work.

corresponding to different masses between 1 and 2 solar masses. For a canonical supernova located at 10 kpc, the mass could be measured with an uncertainty of 16% and 13% for a 1 kt and a 20 kt scintillator detector respectively.

An example: Disentangling different supernova flux shapes

The far location of SN1987A in the Large Magellanic Cloud has provided information on the total gravitational energy radiated as neutrinos and on the neutrino temperatures, consistent with predictions (see Ref. [151] and references herein). However, the statistic was not large enough to precisely determine the supernova neutrino energy spectrum. In what follows I study the possibility to discriminate between two flux shapes, GVKM and Livermore, with the current and future generation of LLSD. I statistically compare spectra generated from a GVKM distribution with both GVKM and Livermore fluxes. To simplify the problem as well as remain conservative, I normalize both fluxes to the same integral, only their spectral shapes differ. I then compare the χ^2 distributions of 5,000 simulated experiments fitted with the GVKM and Livermore fluxes. The two χ^2 distributions are generated for supernova distances ranging from 0 to 10 kpc. The separation power between the two is expressed through the following figure of merit: F.o.M. $= \frac{\mu_2 - \mu_1}{2.35 \times (\sigma_2 + \sigma_1)}$ with $\mu_{1,2}$ and $\sigma_{1,2}$ the respective mean and standard deviation of the two distributions. This figure of merit has been carefully chosen for its efficiency in disentangling Gaussian-like probability distributions. It has been used in the Nucifer experiment to separate neutron and gamma backgrounds via the Pulse Shape Discrimination (PSD) technique. More details can be found in Ref. [156]. Figure 5.20 shows the behavior of this separation power parameter as a function of the increasing distance for a 1 kt and a 20 kt detector. The reconstruction of a GVKM spectrum at 95% C.L. can be achieved up to a distance of 2.2 kpc for a 1 kt detector such as KamLAND and 9.5 kpc for a 20 kt detector such as JUNO.

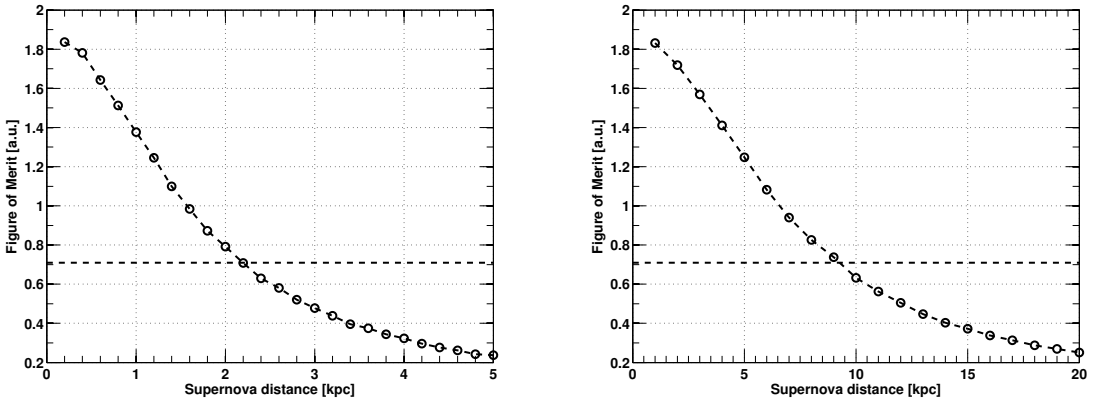

Figure 5.20: Figure of merit for disentangling GVKM and Livermore energy distributions as a function of the supernova distance for a 1 kt (left) and a 20 kt (right) detector. The dotted line represents the upper limit over which a GVKM spectrum is reconstructed with at least 95% C.L.

5.5 Application: Geoneutrinos detection

Besides its application in reactor monitoring/detection and supernova pointing, both covered in the previous sections, neutrino directionality with IBD could be applied to a field linking particle physics and geophysics: the detection of geoneutrinos.

This study was motivated by the invitation to give a talk I received from the organizers of the "Neutrino Geoscience 2015" conference in June 2015. Given its strong versatility, I used the same toy Monte Carlo used to retrieve supernovae positions and modified its inputs in order to perform a directionality measurement with geoneutrinos. The following analysis is summarized in my presentation entitled "Neutrino Directionality with Large Liquid Scintillator Detectors - Application to geoneutrinos detection" [207]. The following analysis by no means intends to be a complete overview of the potential of directionality using geoneutrinos.

5.5.1 Geoneutrinos

Radioactive elements present in the Earth contribute to the radiogenic heating of the Earth. These elements mostly consist of ^{238}U,^{232}Th,^{235}U and ^{40}K, however given the smaller half-life of ^{235}U ($\tau_{1/2} = 0.7 \times 10^9$ y), its contribution is weaker. The radioactive β-decays of these elements emit heat as well as several electron antineutrinos[3] as summarized in Eq. 5.31.

$$^{238}\mathrm{U} \rightarrow {}^{206}\mathrm{Pb} + 8\alpha + 8e^- + 6\bar{\nu}_e + 51.7 \text{ MeV} \quad (5.27)$$

$$^{232}\mathrm{Th} \rightarrow {}^{208}\mathrm{Pb} + 6\alpha + 4e^- + 4\bar{\nu}_e + 42.7 \text{ MeV} \quad (5.28)$$

$$^{235}\mathrm{U} \rightarrow {}^{207}\mathrm{Pb} + 7\alpha + 4e^- + 4\bar{\nu}_e + 46.4 \text{ MeV} \quad (5.29)$$

$$^{40}\mathrm{K} \rightarrow {}^{40}\mathrm{Ca} + e^- + \bar{\nu}_e + 1.31 \text{ MeV } (89.3\%) \quad (5.30)$$

$$^{40}\mathrm{K} + e^- \rightarrow {}^{40}\mathrm{Ar} + \nu_e + 1.505 \text{ MeV } (10.7\%) \quad (5.31)$$

The detection of those neutrinos could allow the computation of the amount of radiogenic heat produced within the Earth, a quantity of crucial importance for the field of geoscience. Since they originate from the consecutive β-decays of the U and Th chains elements, the $\bar{\nu}_e$ energy spectra of ^{238}U, ^{232}Th and ^{235}U possess characteristic and well-known shapes displayed in Figure 5.21 along with the $\bar{\nu}_e$ energy spectrum of ^{40}K. ^{40}K can decay toward ^{40}Ar via electron-capture thus emitting a monoenergetic ν_e, however since this neutrino is not detectable by IBD, I will not consider it in the following. While the overall geoneutrino energy spectrum extends up to 3.26 MeV, only $\bar{\nu}_e$ produced by the ^{238}U carry energies larger than 2.25 MeV. Furthermore, ^{235}U and ^{40}K $\bar{\nu}_e$ energies do not reach the IBD threshold of 1.8 MeV thus making their detection via IBD impossible. The detection of neutrinos from ^{40}K and the computation of its radiogenic heat is of interest for geophysicists and geochemists. For that matter, the detection of ^{40}K ν_e's via elastic scattering could come in handy, granted that the solar neutrino background have been properly subtracted.

The Bulk Silicate Earth (BSE) models can predict the mass ratios (called chondritic ratios) of ^{232}Th/^{238}U and ^{40}K/^{238}U and typical values of Th/U = 3.9 and K/U ∼ 13,000 are expected, as explained in more details in Ref [209]. Since the IBD cross section increases with the neutrino energy, this Th/U mass ratio of 3.9 leads to an expected neutrino flux ratio $\bar{\nu}_e$ (Th) /$\bar{\nu}_e$ (U) of 0.27. These models also predict that uranium and thorium, lithophile

[3]The ^{40}K can decay toward ^{40}Ar via electron-capture thus emitting a monoenergetic ν_e

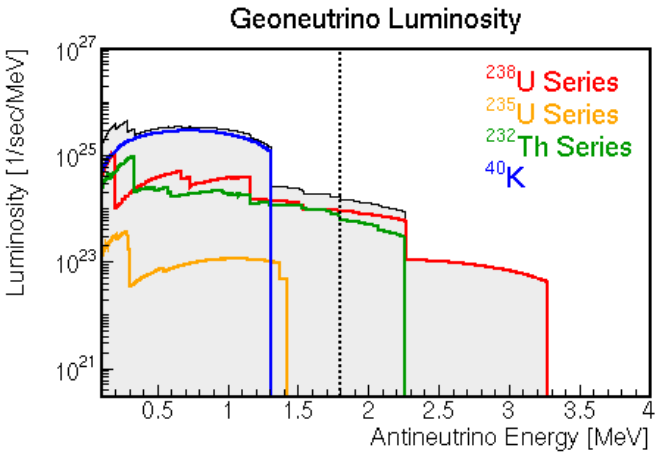

Figure 5.21: Geoneutrino luminosity as a function of the energy for the four most important decay chains:^{238}U,^{232}Th,^{235}U and ^{40}K [208]. The 1.8 MeV IBD threshold is represented by the vertical dashed line.

elements, are not present in the Earth's core but only in the crust and mantle. Potassium however, might melt with iron and sulfur, two elements largely dominant in the core, thus leading to its possible role as a heat source in the core. Therefore, according to the most popular measurable models, geoneutrinos are thought to be originated from the Earth's crust and mantle.

Although the surface heat flux of the Earth has been estimated quite precisely to 47 ± 2 TW [210], the contribution of radiogenic heat to this global flux remains unknown in the absence of hints coming from the detection of geoneutrinos. The cosmochemical, geochemical and geodynamical BSE models respectively predict radiogenic heats of 11 ± 2, 20 ± 4 and 33 ± 3 TW, distributed in the crust and mantle. The discrimination of a model with respect to another will depend on the amount of heat estimated from the detection of geoneutrinos. While the crust radiogenic power determination is achievable via the extraction of rock samples at several depths[4] and the analysis of their isotopic composition, the mantle radiogenic power remains inaccessible via such conventional means. This is where the detection of geoneutrino fits in, since by subtracting the expected geoneutrino flux originating from the crust to the whole neutrino flux detected by an experiment, one can infer the fraction of the geoneutrino flux emitted by the mantle.

Geoneutrinos have been previously detected via IBD by the KamLAND and Borexino experiments. In order to estimate the geoneutrino flux at different locations over the globe, a new measurement unit, expressed as a normalized event rate, has been introduced: the Terrestrial Neutrino Unit (TNU). It is defined as the number of IBD interactions detected in one year with a target of 10^{32} protons[5] and 100% detection efficiency. After fix-

[4]The deepest borehole ever drilled is 12 km deep, in the Kola peninsula in Russia.

[5]Although it depends on the liquid composition as well, the quantity of 10^{32} protons is often approximated as 1 kton of liquid scintillator

ing the chondritic ratio and the overall geoneutrino spectrum, one can express the flux as: 1 TNU $=$ 0.113 $\times$ 10^6 $\bar{\nu_e}$.cm^{-2}.s^{-1} [208].
The Borexino experiment reported a geoneutrino measurement from 2056 days of data taking (before selection cuts), between December 15, 2007 and March 8, 2015. After applying adequate selection cuts and fixing the chondritic ratio to 3.9, the best-fit extracted from the candidates displayed in Figure 5.22 (left) estimated that $23.7^{+6.5}_{-5.7}$(stat.)$^{+0.9}_{-0.6}$(sys.) geo-$\bar{\nu}_e$ events were detected, equivalent to $43.5^{+11.8}_{-10.4}$(stat.)$^{+2.7}_{-2.4}$(sys.) TNU. The same fit led to an estimation of the number of reactor $\bar{\nu}_e$ of $52.7^{+8.5}_{-7.7}$(stat.)$^{+0.7}_{-0.9}$(sys.), equivalent to $96.6^{+15.6}_{-14.2}$(stat.)$^{+4.9}_{-5.0}$(sys.) TNU. From this measurement, they provided an estimate of the radiogenic heat produced in the Earth. This value is displayed in Figure 5.23 (left) and could be used to validate or discard several BSE models.
Similarly, during 2991 days of data taking between March 9, 2002 and November 20, 2012, the KamLAND experiment detected 116^{+28}_{-27} geo-$\bar{\nu}_e$ events, equivalent to $3.4^{+0.8}_{-0.8} \times 10^6$ $\bar{\nu_e}$.cm^{-2}.s^{-1} in term of un-oscillated flux. The energy spectrum of these events is displayed in Figure 5.22 (right) and the amount of radiogenic heat predicted is displayed in Figure 5.23 (right).
At this moment, none of these two experiments can rule out a model over another. However, with higher statistic, this seems possible within the next decade.

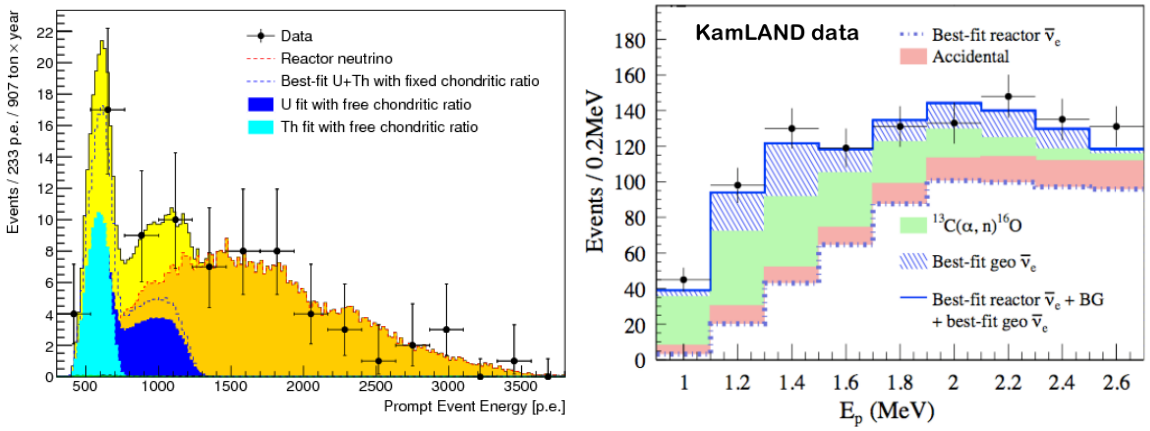

Figure 5.22: Left: Prompt energy spectrum, expressed in photo-electrons (p.e.) of $\bar{\nu}_e$ candidates in Borexino [211]. The dotted line shows the best-fit of geo and reactor $\bar{\nu}_e$ assuming a chondritic ratio of 3.9. The two blue domains show additional fits with U and Th separately taken as free parameters. Right: Prompt energy spectrum, expressed in MeV, of the $\bar{\nu}_e$ candidates in the geoneutrino energy region in KamLAND [212]. The dashed blue domain shows the best-fit of geo-$\bar{\nu_e}$.

In the late nineties, J.M. Herndon predicted the possible existence of uranium at the center of Earth's core and postulated the existence of an hypothetical natural nuclear reactor, self-sustained by the chain fission of the uranium isotopes. While the existence of such reactors is possible under several conditions and has been confirmed by the discovery of the Oklo natural nuclear reactor in Gabon [122], the hypothesis assuming the presence of uranium in the Earth's core is strongly debated among geophysicists. Though no conventional technique allows to test this hypothesis, the detection of neutrinos emitted by this reactor might validate/discard its existence. The reactor imagined by Herndon has an expected radius of about 4 km, as displayed in Figure 5.24, and could deliver up to 30 TW of thermal

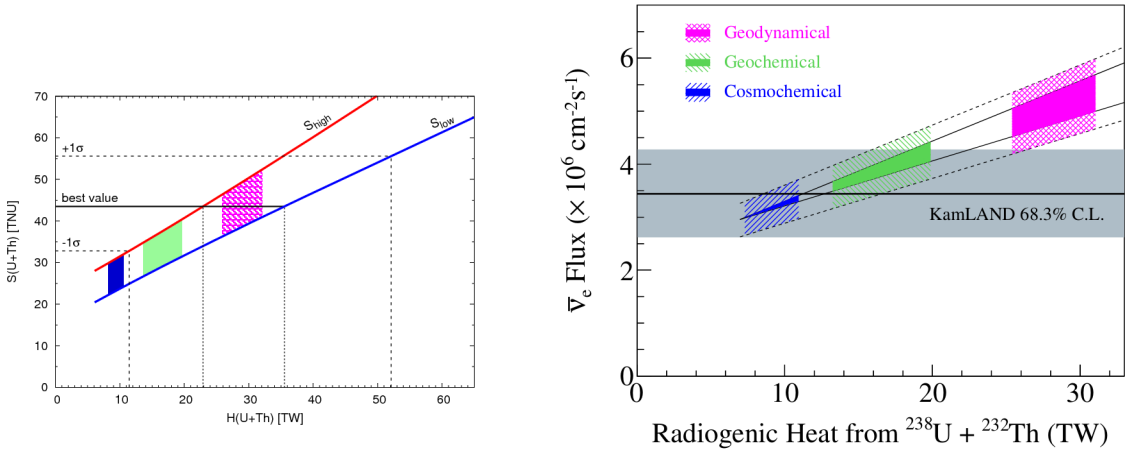

Figure 5.23: Geoneutrino flux measured in TNU Borexino [211] (left) and in $\bar{\nu}_e$ .cm^{-2}.s^{-1} in KamLAND [212] (right) versus radiogenic heat expected from the three BSE models: cosmochemical, geochemical and geodynamical.

power. Its composition was suggested to be ^{235}U/^{238}U = 0.76:0.23, thus making it a ^{235}U-rich reactor with an emitted neutrino energy spectrum strongly driven by the fission products of ^{235}U. Given the similarities between the georeactor and "regular" nuclear reactors neutrino spectra, the Borexino and KamLAND experiments set limits on the thermal power of the georeactor by adding a $N_{\text{georeac.}}$ component to their best-fit while constraining the nuclear reactors component $N_{\text{reac.}}$ with its expected value, well-known from the thermal output of commercial reactors. By doing so, the Borexino and KamLAND collaborations respectively set upper limits of 4.5 TW (95% C.L.) [213] and 3.7 TW (95% C.L.) [212] on the georeactor thermal power.

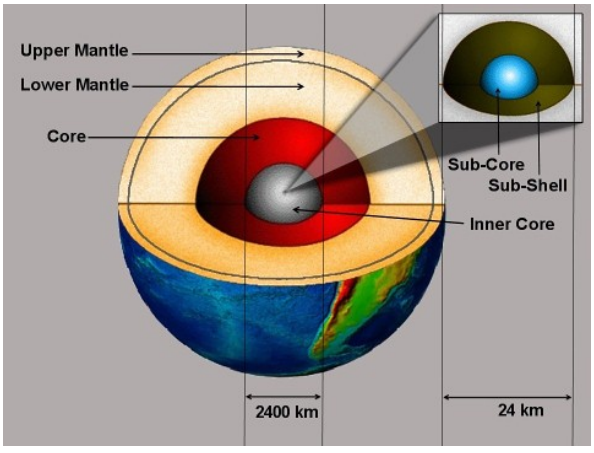

Figure 5.24: Sketch of the georeactor (referred to as "sub-core" in the picture) at the center of the Earth.

As previously stated, one of the main goal of geoneutrino detection is the estimation of the mantle geoneutrino component. This is achieved by subtracting the crust component to

the total detected geoneutrino flux. Such computations were performed by the two collaborations and lead to an estimate of $20.9^{+15.1}_{-10.3}$ TNU in Borexino [211] and $11.2^{+7.9}_{-5.1}$ TNU in KamLAND [212]. While the error, dominated by the subtraction of the crust component, is still quite big, the null hypothesis, based on the assumption that no geoneutrino signal originates from the mantle, is rejected at more than 90% C.L.. The very location of the two experiments makes difficult the determination of the mantle signal since most of the geoneutrino signal comes from the crust, with a strong component of local crust, within the 500 km surrounding the detector. The contribution of the local crust (LOC), rest of the crust (ROC) and mantle is displayed in Figure 5.25. While the KamLAND, Borexino and SNO+ experiments are mainly sensitive to crust geoneutrinos due to their construction on thick continental crust[6], the HanoHano experiment [214], a project of a 10 kt liquid scintillator detector on a barge planned to be operated underwater off the coast of Hawaii, is largely sensitive to mantle geoneutrinos. A sketch of the HanoHano detector is shown in Figure 5.26.

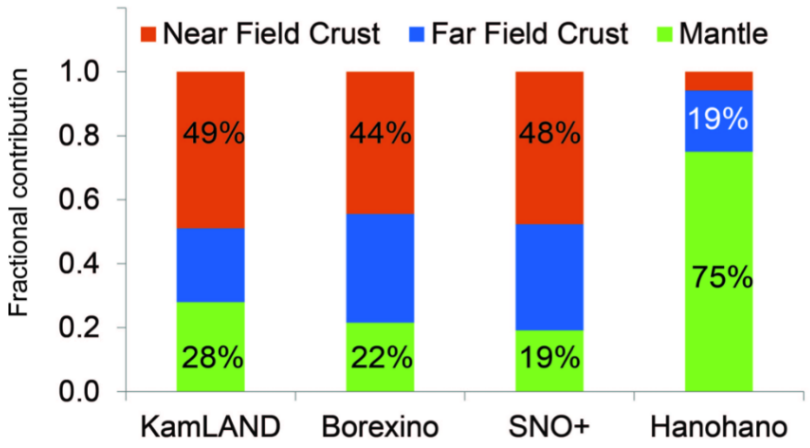

Figure 5.25: Predicted fractions of geoneutrino contributions from the near field crust (LOC), the far field crust (ROC) and the mantle at various detector locations: Japan (KamLAND), Italy (Borexino), Canada (SNO+) and Hawaii (HanoHano) [214].

Besides its sensitivity to mantle geoneutrinos, one of the main advantages of HanoHano is its very low exposure to the background of reactor neutrinos. Indeed, while Borexino and KamLAND are located in regions of the world with a high nuclear activity[7] as shown in Figure 5.27, Hawaii is located far away from any declared reactor.

5.5.2 Results and limitations

For this study of geoneutrino directionality, I chose to focus on two goals: the retrieval of the direction of the hypothetical georeactor and the discrimination between mantle and crust geoneutrinos. The latter is often mentioned and is considered as an important goal of neutrino directionality applied to geoneutrinos. To perform these two analyses, I applied the same

[6]The continental crust thickness is of the order of 35 km while the oceanic crust is about 8 km thick.

[7]The reactor background has been strongly reduced at KamLAND due to the shutdown of all Japanese commercial reactors in 2012.

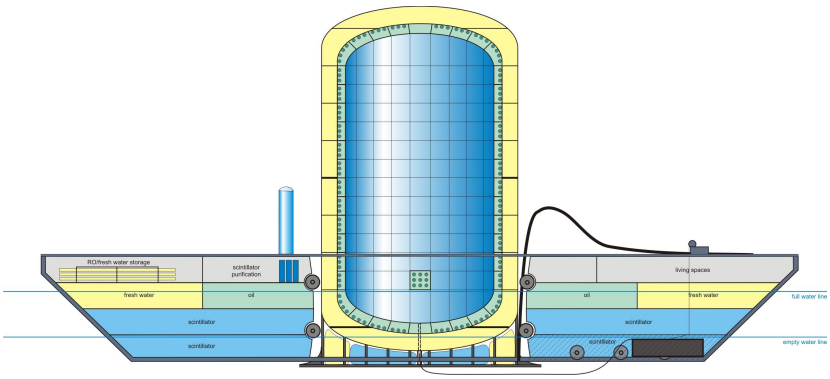

Figure 5.26: Cross sectional sketch of HanoHano detector and its barge [215].

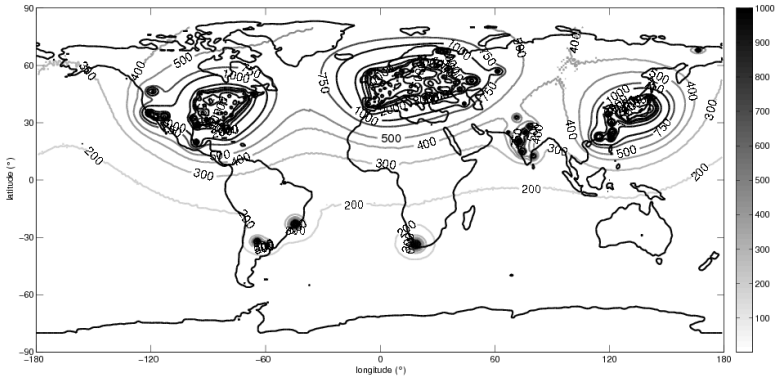

Figure 5.27: Known reactor background expressed in $\bar{\nu_e}.y^{-1}$ per 10^{34} protons [172]. 201 nuclear power stations have been included.

method than for supernova neutrinos, as explained in Section 5.4.1. The main difference lies in the fact that different energy spectra were used: a Th/U neutrino spectrum describing the geoneutrino flux and a reactor spectrum describing the georeactor flux. Both these spectra are displayed on Figure 5.28 and have been added to SuperNustradamus for further analyses.

In the simulation, the georeactor was, like a supernova, considered a point-like source, a rather safe assumption given its 4-km radius with respect to the 6400-km radius of the Earth. Since its thermal power directly impacts the number of detected events, it was used to compute the expected rate of IBD interactions. For a 4 TW georeactor, current upper limit set by Borexino and KamLAND, the computation of the number of expected IBD events led to 15.2 $\bar{\nu_e}.y^{-1}.k^{-1}$. In order not to be dominated by the geoneutrino background from Th/U decays, dominant in the low energy region, I applied an energy cut to select only events with $E_\nu = 3.3$ MeV. While rejecting all Th/U geoneutrino events, this cut only rejects 27% of the georeactor events.

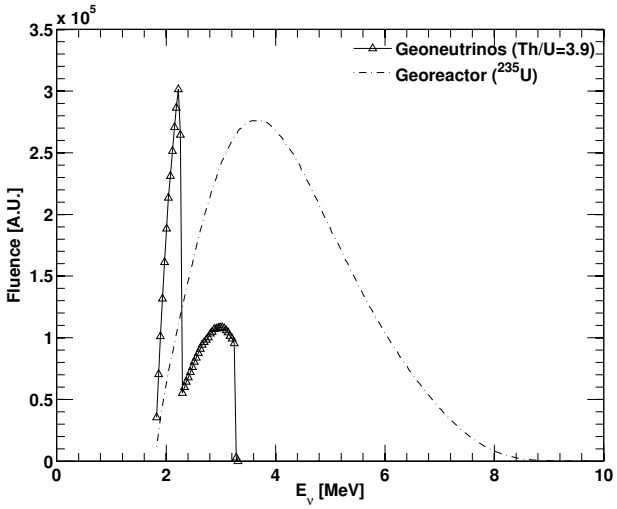

Figure 5.28: Geoneutrinos and georeactor energy spectra (not normalized). The geoneutrino flux assumes a chondritic Th/U ratio of 3.9 and the georeactor flux is based on a ^{235}U neutrino spectrum.

Relevant for supernova neutrinos given the large number of events detected over a short period of time and their broad energy spectrum, the fact that no backgrounds are taken into account in the SuperNustradamus simulations is questionable when dealing with geoneutrinos. Indeed, as previously stated, geoneutrinos detection is subject to a significant background, mainly from reactor neutrinos. This is especially true when looking at georeactor neutrinos, having an energy spectrum almost identical to nuclear reactor neutrinos. Since only the HanoHano detector and its advantageous location could consider not taking this background into account, the following results have to be considered as optimistic. The results of the directionality analysis of georeactor neutrinos is displayed in Figure 5.29.

Assuming a realistic exposure time between 10 and 20 years, only HanoHano could reconstruct the position of the georeactor within a 15°(68% C.L.) cone. Given the low reactor background rate in Hawaii, this directional information, combined with a fit of the energy spectrum constraining the reactor component displayed in Figure 5.27, could definitely confirm or discard the existence of a TW-scale georeactor at the center of Earth's core.

The simulation of the crust and mantle geoneutrinos was more complex. SuperNustradamus being developed for supernovae simulations, it is by default designed to generate point-like neutrino sources and reconstruct point-like positions. In the case of geoneutrinos, the emission is distributed in the crust and mantle surrounding the detector hence the whole hemisphere below the detector can be considered as the source. To simulate this emission, I generated random neutrino directions over the unit sphere with a negative zenith angle (south hemisphere). While the actual geoneutrino emission in the Earth seen in a detector is not as smooth and shows structures corresponding to the different layers of crust and mantle, this approximation is relevant enough for the following analysis. Since the neutrino source is quite broad, the angular distributions of the neutrino direction vectors are not as peaked as in a point-like source case and this directly impacts the reconstruction precision as displayed in Figure 5.30. The expected event rates used to generate this figure are different for each

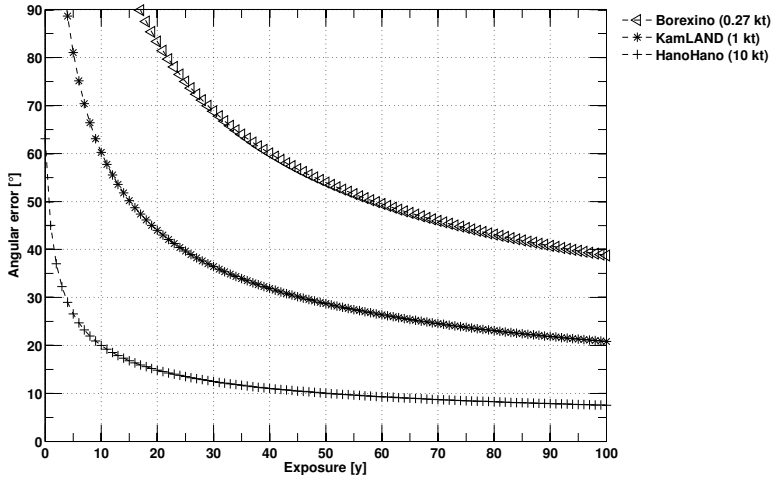

Figure 5.29: Angular uncertainty of the reconstruction position as a function of the exposure time for an hypothetical 4 TW georeactor. The three detectors considered are Borexino (0.27 kt), KamLAND (1 kt) and HanoHano (10 kt).

detector. I considered respective detected geoneutrino rates of 43.5 and 30.1 TNU for the Borexino and KamLAND experiments. For HanoHano, mostly sensitive to mantle geoneutrinos, I decided to use a geoneutrino rate of 20.9 TNU, the most recent expected mantle signal computed by Borexino.

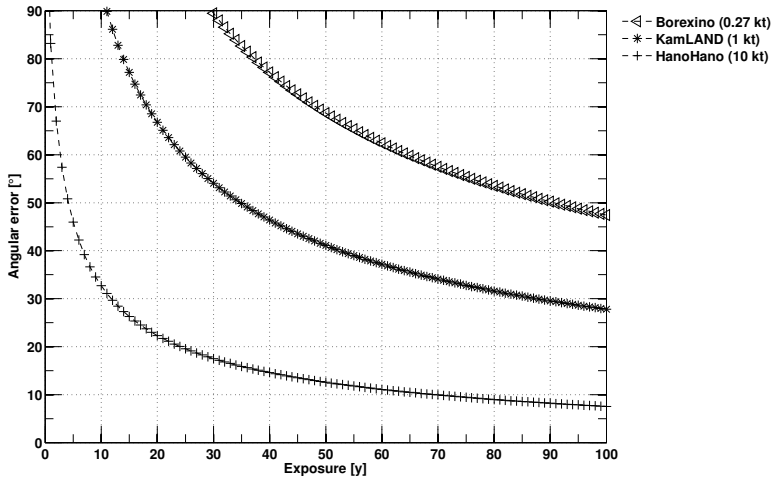

Figure 5.30: Angular uncertainty on the reconstructed barycenter of the geoneutrino distribution as a function of the exposure time. The three detectors considered are Borexino (0.27 kt), KamLAND (1 kt) and HanoHano (10 kt).

The interpretation of these results is not as straightforward as before. Given the geoneu-

trino hemispherical distribution, the reconstruction of a single direction coming from a point-like source seems irrelevant. However, since the distribution is invariant in azimuthal angle (symmetrical with respect to the vertical z-axis of the detector), the single direction reconstructed by the χ^2 minimization method is in fact the barycenter of the distribution. By definition, the distribution is centered around the vertical z-axis. The reconstruction uncertainty displayed in Figure 5.30 thus describes how well can a detector reconstruct the mean direction of an incoming, broadly distributed, geoneutrino flux.

Considering no backgrounds were taken into account to compute these results, one can doubt the potential of IBD directionality in term of geoneutrino direction reconstruction. For instance, after 20 years of data taking, KamLAND could only reconstruct the mean direction of the geoneutrino flux at the level of 65°(68% C.L.), making impossible any attempt to separate crust and mantle geoneutrinos. Showing this limitation was actually the implicit goal of this analysis.

Unlike the potential of IBD directionality applied to supernova detection, somewhat disregarded due to its weak anisotropy, the potential of directional geoneutrino detection with IBD is often overestimated in the community. While the IBD process is currently the most suitable reaction to detect geoneutrinos in terms of event rates and background rejection, its directionality potential is very limited and, despite the global idea strongly anchored in the community, cannot achieve an efficient crust-mantle discrimination in reasonable timescales with the current and forthcoming neutrino detectors.

The first limitation comes from the statistical nature of the IBD directionality, only reliable using large datasets of thousands of neutrinos and strongly incompatible with the low expected geoneutrino flux. While it can be compensated using larger and larger detectors such as HanoHano (10 kt), JUNO (20 kt) or LENA (50 kt), it requires long exposure times as well, barely reachable by the current Borexino and KamLAND experiments, already a decade old.
The second limitation comes from the distribution of the geoneutrino directions. As previously explained, the reconstruction of a point-like georeactor might be achievable, however the discrimination between two similarly distributed fluxes might not, even in the unlikely scenario of a background-free measurement. In the case of geoneutrinos and for the majority of neutrino events of interest in neutrino experiments, the expected flux comes from below the detector, including both signal and backgrounds. The addition of a reactor neutrino background would only worsen the direction reconstruction, already imprecise without any backgrounds.
For these two reasons, an application of IBD directionality to geoneutrinos detection and more especially to a crust-mantle differentiation seems very optimistic, if not unachievable. Nonetheless, other detection reactions or improved detection techniques might provide a better directionality measurement and bring an event-by-event directional information.

Improvements such as segmented detectors or WbLS, both presented in Section 5.4.4, might strengthen the directional information, however at such low energies, their potential is still to be demonstrated. Indeed, while at supernova energies the positron travels several centimeters and deposits its energy along a track, it's not the case at low energies, where the positron displacement can be considered negligible. At such energies, the neutron is the

particle carrying the directional information since, as IBD kinematics dictate, it is emitted strongly forward in the neutrino direction.
An efficient IBD directional geoneutrino detector would have to retrieve the neutron direction before its moderation. The only way to do so is to detect the first neutron interaction to happen after its emission and to compare it to the positron energy deposition in order to obtain the neutrino direction. While regular liquid scintillator detectors are not sensitive enough to detect this first neutron-induced proton recoil, the hydrogeneous TPC concept, presented in Section 5.4.4 might achieve this goal. As displayed in Figure 5.31, the 3D imaging capabilities of the TPC enhanced by its mm-scale spatial resolution would provide an event-by-event neutrino directionality with IBD, especially at low energies.

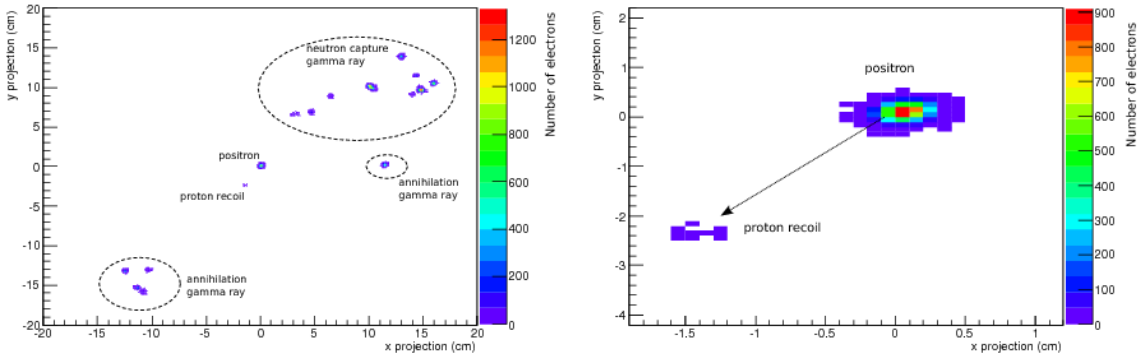

Figure 5.31: Left: Simulated event topology of a typical low energy IBD interaction [201]. Right: Close-up view of the simulated event topology centered on the positron energy deposition and the first proton recoil. The vector between the two depositions provides an accurate estimation of the direction of the incoming neutrino.

Chapter 6

Measurement of θ_{13} with Double Chooz

Although it has been previously mentioned, this chapter will provide a detailed overview of the Double Chooz experiment. After a description of the experiment's design in Section 6.1, all the steps leading to the oscillation parameters determination will be presented, in "chronological" order, from the data acquisition in Section 6.2.1 to the final θ_{13} computation in Section 6.6.

6.1 The Double Chooz experiment

Double Chooz is a neutrino experiment designed to perform a measurement of the PMNS matrix's θ_{13} mixing angle, unmeasured until 2012. It consists of two identical detectors located on the site of the Chooz nuclear power plant in the French Ardennes as displayed in Figure 6.1.

6.1.1 The experimental design

When the Double Chooz initiative started in 2003, the current best limit on the θ_{13} mixing angle was set by the CHOOZ experiment, limited by its relatively high statistical and systematic uncertainties. The design of Double Chooz was such that, using the same source of neutrinos, i.e. the reactor cores of the Chooz nuclear power plant, it would lower these uncertainties to a level sufficient for a discovery of θ_{13} if $\sin^2 2\theta_{13} > 0.09$ (90% C.L.). To do so, the experiment runs with two identical detectors, both based on an improved design.

As explained in Section 2.2.1, Double Chooz is a neutrino disappearance experiment. It aims at measuring the θ_{13} angle by observing a deficit of neutrino events driven by the following survival probability:

$$P_{\nu_e \to \nu_e}(L, E) = 1 - \sin^2 2\theta_{13} \sin^2 \left(1.27 \frac{\Delta^2 m_{13}[eV^2] \times L[m]}{E[MeV]} \right). \tag{6.1}$$

One of the two detectors of the experiment, called the far detector, is located about 1 km away from the reactor cores, thus maximizing this deficit. However, this observation requires a precise understanding of the neutrino flux originating from the reactors, a quantity still

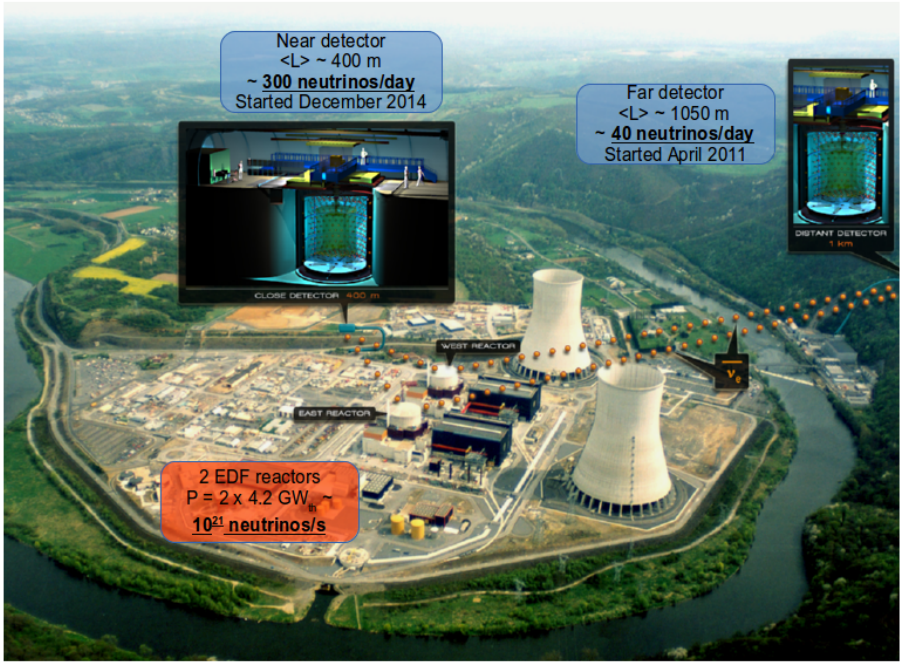

Figure 6.1: Experimental site of the Double Chooz experiment, displaying the two reactors and the locations of the near and far detectors.

subject to debates. The deployment of a second identical detector, called the near detector, located closer to the reactors in order to observe a non-oscillated flux of neutrinos is thus mandatory to renormalize the neutrino flux and cancel the major uncertainty. The positions of the two detectors with respect to the $\bar{\nu}_e$ survival probability is displayed in Figure 6.2.

The near detector serves as a reference point of the unoscillated neutrino flux, to be compared with the deficit expected in the far detector. However, the oscillation being dependent on both distance and energy, it also acts as a reference of the unoscillated energy spectrum.

The far detector has been built at the location where the CHOOZ detector was placed. It lies beneath an overburden of 300 m.w.e within a 20 m long, 7 m large and 3.5 m high laboratory. Located 1115 m and 998 m away from the B1 and B2 reactors, respectively, its weighted baseline with respect to the reactor barycenter is 1050 m. The far detector's construction started in May 2008 and it started acquiring data since April 2011.
The near detector is located beneath an overburden of 150 m.w.e, in a laboratory excavated and built from scratch for the needs of the Double Chooz collaboration. The civil construction work began in April 2011 with the digging of the tunnel leading to the future near laboratory and finished in 2012. Since then, the laboratory has been prepared to receive the near detector whose construction lasted until the end of 2014 with the detector filling and the upper shieldings' installation. Finally, the data taking and detector commissioning started in December 2014. The near detector is located 466 m and 351 m away from the B1 and B2 reactors, respectively, for a weighted baseline of 400 m. Figure 6.3, 6.4, 6.5 and 6.6 depict several stages of the near detector's construction in chronological order.

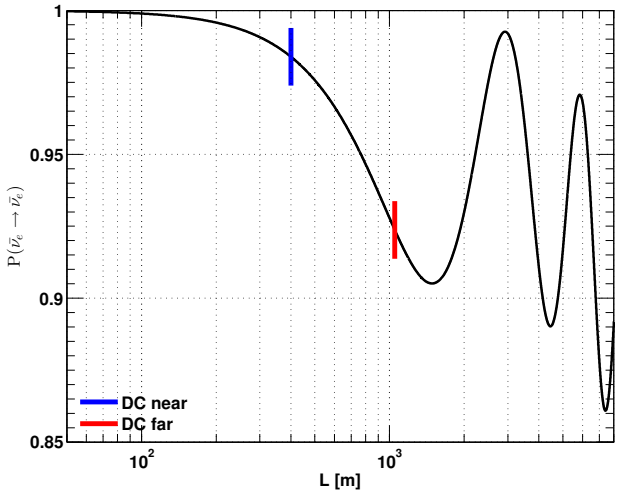

Figure 6.2: Survival probability of a $\bar{\nu}_e$ as a function of the detector distance to the reactors. The $\bar{\nu}_e$ energy is fixed at 3 MeV and the oscillation parameters $\sin^2 2\theta_{13}$ and $\Delta^2 m_{13}$ are respectively equal to 0.093 and 2.52×10^{-3} eV^{-2}. The solar oscillation parameters are taken as $\sin^2 2\theta_{12} = 0.846$ and $\Delta^2 m_{12} = 7.53\times10^{-5}$ eV^{-2}. The baselines of the near and far detectors of Double Chooz are respectively 400 and 1050 m.

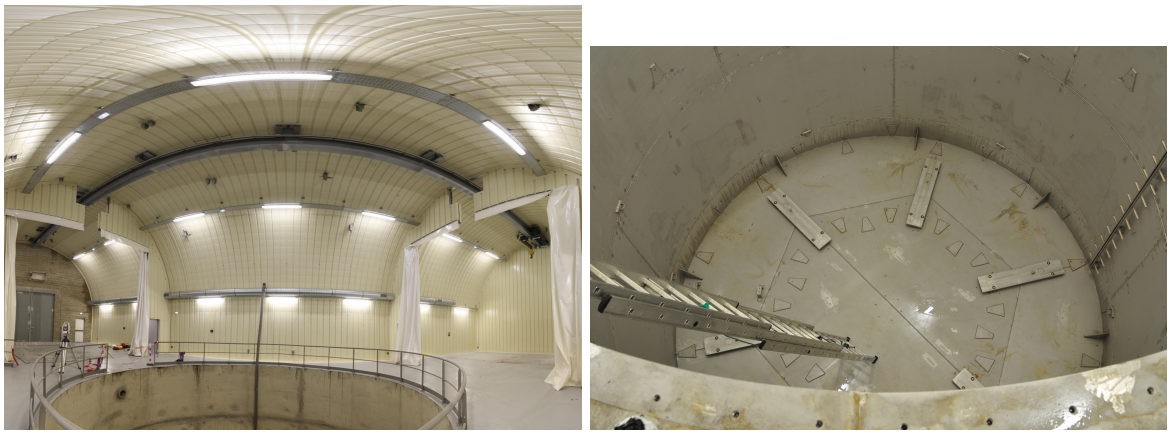

Figure 6.3: Left: Near laboratory upon delivery. Right: Inner Veto supports installed in the pit.

6.1.2 Chooz power plant

The Chooz B[1] nuclear power plant is located along the Meuse river, a few kilometers away from the Belgian border, in the Champagne-Ardennes region. Its two reactors, B1 and B2, of the most recent N4 generation of PWR, are among the most powerful ever built and can deliver a total thermal power of 2×4.25 GW$_{\rm th}$, equivalent to an electrical power of 2×1.5 GW$_{\rm e}$. Their respective construction began in 1984 and 1985 and their operation by the EDF com-

[1]Chooz A, the first French PWR in operation from 1967 to 1991, was build under the hill located 1 km away from the current power plant.

Figure 6.4: Left: Buffer vessel integration. Right: Installation of the Inner Detector PMTs.

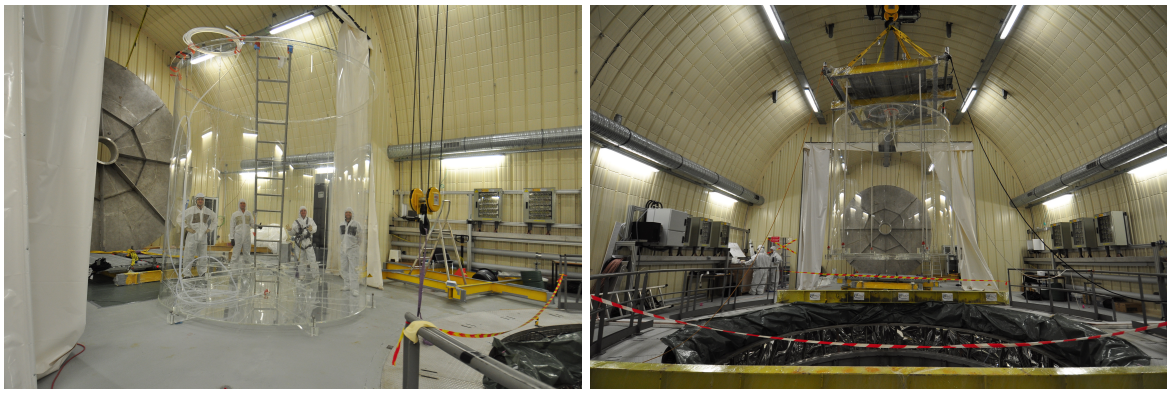

Figure 6.5: Left: Acrylic vessel of the Gamma Catcher. Right: Integration of the Target acrylic vessel.

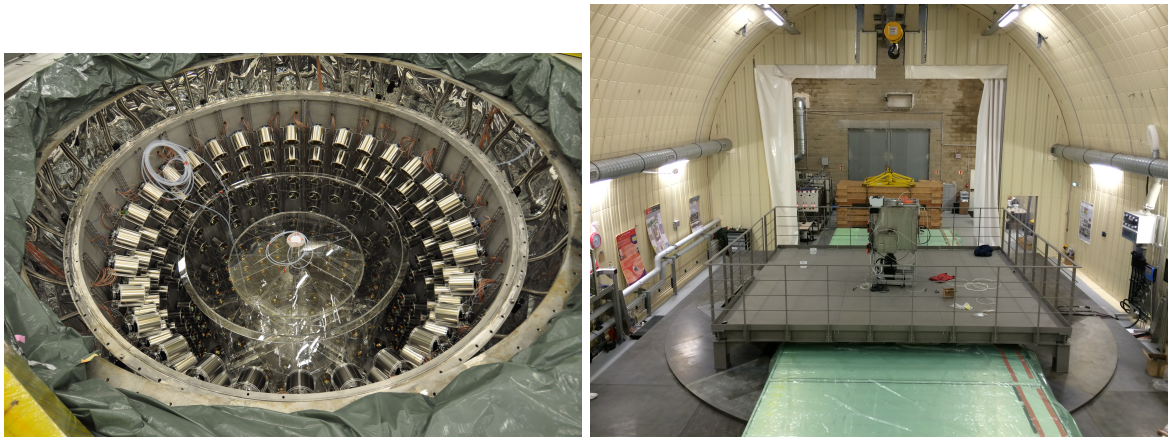

Figure 6.6: Left: Picture of the complete Inner Detector taken before the closing of the Buffer top cap. Right: Complete detector upon installation of the Outer Veto and the Glove Box.

pany (*Electricité de France*) started in 1996 and 1997. Each reactor core is made of 205 fuel assemblies, each enclosing 264 corrosion-resistant zirconium fuel rods filled with cylindrical

pellets of uranium dioxide (UO_2). The uranium used in PWRs such as Chooz B is enriched in ^{235}U up to 4%. Pictures of a PWR's fuel assembly and core are displayed in Figure 6.7. The two reactors regularly undergo maintenance and refueling operations thus giving to the Double Chooz experiment the opportunity to perform a measurement of the neutrino flux in the three following main configurations: (2-On), (1-Off;1-On), (2-Off). The thermal power of each reactor core is provided by EDF on a minute-by-minute basis with an uncertainty of 0.5% at 4.25 GW_{th}.

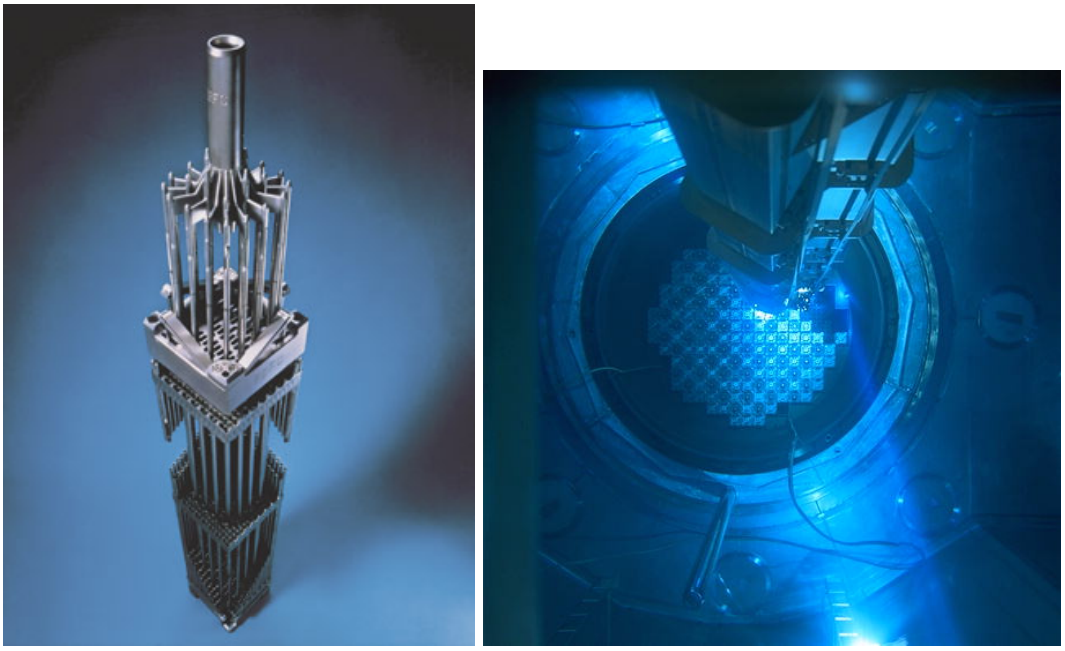

Figure 6.7: Left: Fuel assembly of a PWR [216, 217]. Right: PWR's core during a refueling operation [217, 218].

The simulation of each reactor core in terms of fuel evolution and fission rates is performed with the dedicated MURE code [219, 220] using inputs provided by EDF. The $\bar{\nu}_e$ spectra emitted by the fission products of the four main fissioning isotopes (^{235}U , ^{238}U , ^{239}Pu and ^{241}Pu), accounting for more than 99.7% of the fissions, are predicted using the method described in Section 3.1.4. To suppress the normalization uncertainty of this $\bar{\nu}_e$ prediction, Double Chooz uses the Bugey4 measurement of the $\bar{\nu}_e$ rate at 15 m from the Bugey reactor core [221] as an anchor point. Additional corrections accounting for the differences of fuel composition between the Bugey and the Chooz reactors are applied. This renormalization reduces the systematic uncertainty of the interaction rate associated to the flux prediction to 1.7%, largely dominated by the 1.4% uncertainty in the Bugey4 measurement. Not renormalizing the flux would have increased this uncertainty to 2.8%.

6.1.3 The Double Chooz detector

The Double Chooz detector design is based on the previous CHOOZ design but has been improved in terms of size, stability and background rejection to reduce both statistical and

systematical uncertainties.
The detector design is based on the "nesting dolls" concept, each volume being fully enclosed in one another, as displayed in Figure 6.8.

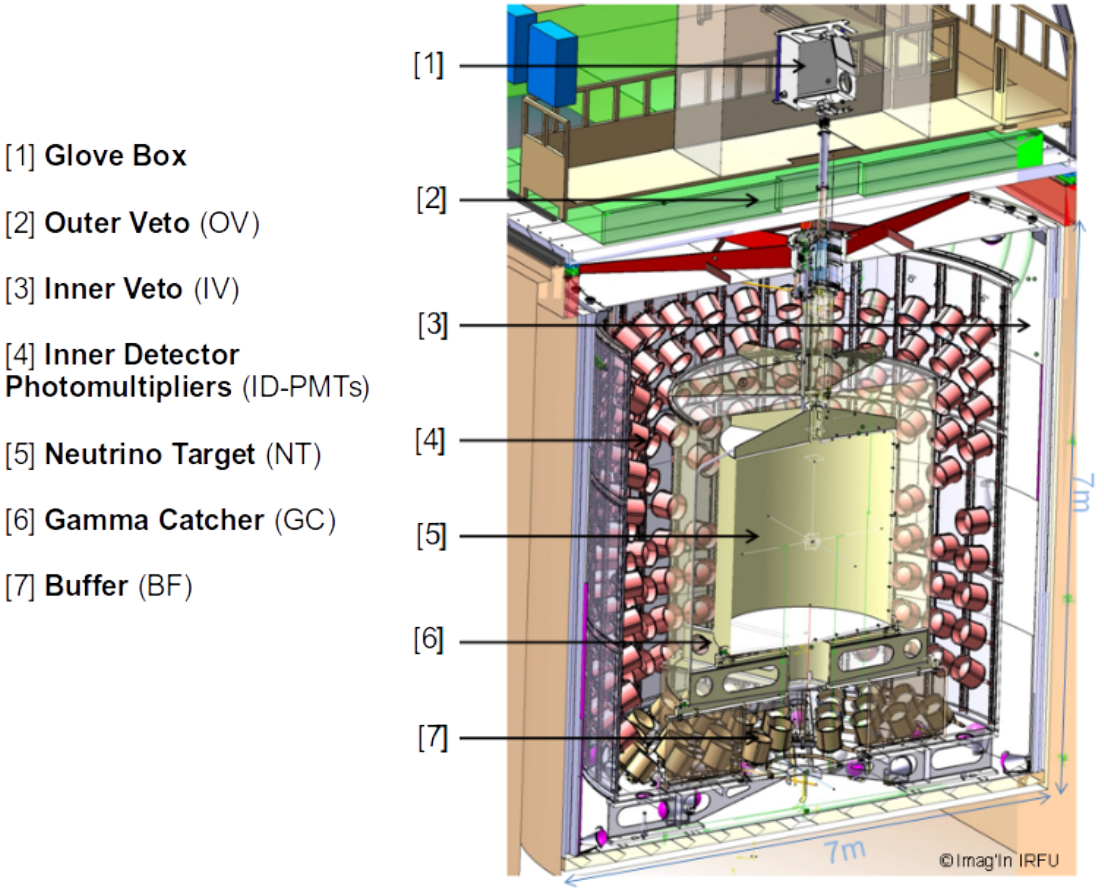

Figure 6.8: Cross sectional view of a Double Chooz detector with its main detection volumes.

Each Double Chooz module consists of three main sub-detectors. The Inner Detector (ID) where the $\bar{\nu}_e$ interaction are detected, the Inner Veto (IV) dedicated to detect and tag external backgrounds and the Outer Veto (OV) whose purpose is to tag incoming cosmic muons.

The Inner Detector is composed of three independent and optically coupled concentric cylindrical volumes: the Neutrino Target (NT), the Gamma Catcher (GC) and the Buffer (BF).

- Neutrino Target: The NT is the utmost central part of the detector where neutron captures on Gd are detected. Enclosed in a 8 mm thick acrylic vessel of 2300 mm diameter and 2458 mm height, it is filled with 10.3 m^3 of Gd-loaded liquid scintillator. It is composed of 80% n-dodecane ($C_{12}H_{26}$) and 20% PXE (ortho-phenylxylylethane,$C_{16}H_{18}$), with a concentration of PPO (2,5-diphenyloxazole), bis-MSB (4-bis-(2-methylstyryl)) and Gd of 7 g/L, 20 mg/L and 1 g/L, respectively. PXE is a scintillator solvent and emits light upon its de-excitation. This light is then re-absorbed by PPO and bis-MSB,

a fluor and a wavelength shifter, whose purpose is to re-emit this light in the blue and UV wavelengths, where the PMTs are the most sensitive. Learning from CHOOZ's misfortune, a lot of effort has been put in the development of the Gd-loading in terms of transparency and stability [222].

- Gamma Catcher: Surrounding the NT with a 55 cm thick layer of undoped liquid scintillator encompassed in a 12 mm thick acrylic vessel of 3416 mm diameter and 3572 mm height, the GC is designed to contain the gamma rays emitted from the positron annihilation and neutron capture. The detection of these energy depositions limits edge effects at the border of the NT, thus increasing the detection efficiency and reducing its associated uncertainty. The 22.6 m^3 of GC's liquid, composed of 66% mineral oil, 30% n-dodecane and 4% PXE with a 2 g/L and 20 mg/L concentration of PPO and bis-MSB, has been tuned to provide a light yield[2] similar to the NT's. The undoped GC liquid serves as a detection volume when performing the neutrino analysis using neutron capture on hydrogen.

- Buffer: The BF is the outermost part of the inner Detector. Enclosed in a 3 mm thick stainless steel vessel of 5516 mm diameter and 5675 mm height, it is filled with 110 m^3 of non-scintillating mineral oil, composed of medicinal white oil (53% in volume) and n-dodecane (47% in volume). Its vessel supports 390 low background 10-inch Hamamatsu R7081 photomultiplier tubes (PMTs) of the Inner Detector [223, 224], which detect the light emitted upon energy depositions in the NT and the GC. Each PMT is enclosed in a mu-metal shield to reduce the disturbances caused by external magnetic fields. The BF 105-cm thick layer of transparent oil serves the purpose of shielding the NT and the GC from the external and PMT radioactivity, the latter mostly from ^{40}K, contained in the PMTs glass. This addition of the BF volume is a major improvement with respect to the CHOOZ detector, only consisting of a NT and a GC.

Surrounding the Inner Detector with a 50-cm layer of liquid scintillator, the Inner Veto is a stainless steel vessel of 6500 mm diameter and 6830 mm height. It is filled with 90 m^3 of scintillating liquid, composed of 50% n-dodecane, 50% LAB (Linear Alkyl Benzene) mixed with 2 g/L of PPO and 20 mg/L of bis-MSB. The scintillation light emitted in the liquid is collected by 78 8-inch Hamamatsu R1408 PMTs. The role of the IV is to tag any background external to the detector, such as muons, spallation neutrons and natural gamma radioactivity.

The IV is surrounded by a shielding, built to protect the detector from external radioactivity of the surrounding rock. Its design differs from one detector to the other. In the far detector, 15 cm thick stainless steel bars cover the detector top and lateral parts. However, in the near detector, only the top is covered with 15 cm thick steel bars, the sides of the detectors being surrounded by a 50 cm thick layer of water. While maintaining the gamma attenuation required in the detector design, the low density of water being compensated by its larger thickness, water acts as a neutron moderator thus reducing the rate of spallation neutron backgrounds in the detector. Given the shallower location of the Double Chooz near detector and its higher muon rate, this upgrade has a positive impact on the background

[2]The light yield represents the quantity of scintillation light emitted for a given energy deposition. It is usually given in units of photoelectrons (p.e.) per MeV.

rejection.

Above the IV and, by construction, the ID lies the Outer Veto, another additional feature with respect to the CHOOZ experiment, whose purpose is to detect and tag the muons that pass through or around the detector. Unlike the other volumes, the OV is not made of liquid scintillator but plastic scintillator strips coupled with Hamamatsu H8804 multianode PMTs. Modules of 64 strips, each strip measuring $5 \times 1 \times 320$ or 360 cm, cover an area of 91 m^3 above the stainless steel shielding, enough to detect any muon likely to induce, directly or through spallation, a signal in the detector. Its strips alternatively disposed along the x and y-axis, the OV is able to provide the coordinate of a passing muon in the detector plane, with a much higher precision than the IV. To detect and tag muons passing through the glove box and the chimney, used to deploy calibration sources in the ID, two additional layers of strips have been mounted above the glove box. Combining both IV and OV leads to a muon rejection efficiency larger than 99.99%.

6.2 Data acquisition and calibration

6.2.1 Data acquisition

The data acquisition system of the Double Chooz experiment is depicted on Figure 6.9. The scintillation light collected by the PMTs is transformed into an electric signal of a few mV amplitude. The signal of each PMT is transported through a single cable along with the ∼1.3 kV high voltage (HV) supplying the PMT. A custom-made HV-splitter circuit then decouples each component. The low amplitude PMT high frequency signals are amplified by the Front-End Electronics (FEE) modules in order to be ready for digitization, a task performed by the Flash-Analog-To-Digital (ν-FADC) converters.

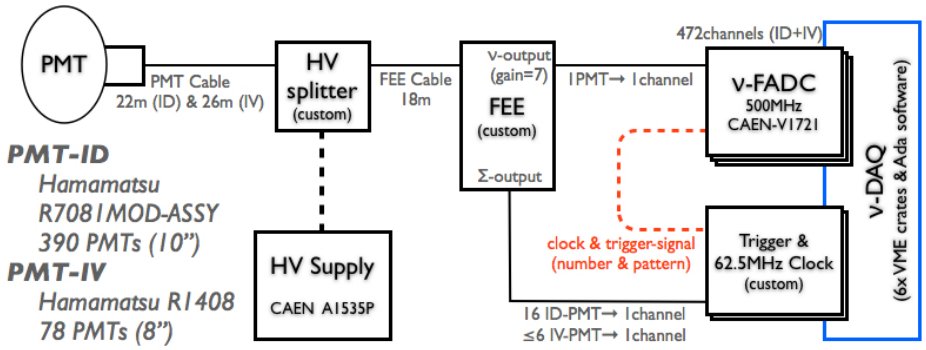

Figure 6.9: Scheme of the Double Chooz data acquisition system [75].

ν-FADC

The Double Chooz ν-FADC system relies on 64 CAEN-Vx1721(VME64x) [225, 226] waveform digitizers developed in collaboration with the CAEN company and the "AstroParticules et Cosmologie" (APC) laboratory. Each card possesses 8 channels with 8-bit FADC with a sampling rate of 500 MS/s, able to separate PMT signal separated by more than 2 ns. Each

of those channels holds 2 MB of internal memory, split into 1,024 buffers of 4,096 ns. As long as no external trigger is received, the digitization process occur continuously in a buffer. Upon receiving a trigger signal, the digitization moves to the next buffer, leaving the previous one for readout. Up to 1,024 events can be recorded and stored in memory. Over the 4,096 ns available per buffer, a 256 ns waveform is recorded, containing more than 90% of the scintillation light received by the PMTs. The trigger rate, of the order of 300 Hz, is lower than the readout rate thus allowing a dead time free acquisition.

Trigger system

While amplifying each PMT signal and sending it to the ν-FADC, the FEE also delivers a sum signal, whose amplitude is proportional to the addition of the charges seen in each channel, fed into the trigger system. The trigger system consists of three trigger boards (TB) and one trigger master board (TMB). Two of the TB are dedicated to the ID PMTs and one to the IV PMTs.
The ID PMTs are separated into 12 sectors, each one consisting of 32 PMTs. Among these 12 sectors, 6 are for the upper part of the ID, while the other 6 are for the lower part. The PMTs' connection to the trigger system is such that half of the PMTs from a given sector are connected to the TB A trigger board, while the other half are connected to the TB B trigger board. The FEE sums the signals by groups of 16 PMTs before sending this sum to the corresponding trigger board. The grouping is such that a PMT belonging to a given TB is surrounded by PMTs belonging to the other one. With this configuration, each TB observes the same detector volume, though it is only connected to half of the PMTs. The trigger decisions of both TB should thus be identical, within statistical fluctuations. Given the lower number of PMTs in the IV and their disposition, the IV trigger board receives trigger signals from groups of 3 to 6 PMTs only. Finally, the trigger master board receives trigger decisions from the three TBs and sends a signal to the digitization system to store the event in its memory. The TMB is synchronized to the FADC and the OV via a 62.5 MHz clock.
The trigger decisions for all trigger boards are based on energy and group multiplicity, e.g. if more than two sectors are hit, and these conditions can be modified in order to lower or increase the detection threshold. The ID starts to trigger at energies of about 350 keV and the trigger efficiency reaches 100%, with a negligible uncertainty, above the 0.7 MeV threshold, often used for analysis. The IV triggers at about 10 MeV which corresponds to an 8 cm muon track at minimum ionizing energy.

6.2.2 Calibration system

To precisely determine the θ_{13} mixing angle from the detected neutrino rate and energy spectrum, each Double Chooz detector needs to be understood as accurately as possible. In order to suppress most of the systematic uncertainties associated with the detector response, it is utterly important to master the detector response to the different particles involved in the physical processes relevant to the experiment (α, $\beta^{\pm}$, γ and neutrons) as well as the optical properties of the liquid (refraction index, attenuation length) and the PMTs' responses (offsets, gains, quantum and geometrical efficiencies). The precise knowledge of the detector response, obtained via several calibration devices installed within each module, allows Double Chooz to reach percent-level uncertainties on the detector efficiency.

Radioactive sources

The understanding of the detector response to an energy deposition as well as its energy scale is performed through the deployment of radioactive sources in the detector vessels. Two devices are used for this deployment: the Z-axis deployment system (ZADS) and the guide tube (GT). The installation of an articulated arm (AA) is under investigation since its deployment raises several technical concerns. The ZADS consists of a motorized pulley-and-weight system called *fish line*, used to place sources along the z-axis of the target. A source in the ZADS can be deployed from the chimney down to 1 cm above the NT bottom cap, with a source position uncertainty below 1 mm. The GT is a rigid hermetic loop installed in the GC in which the sources are guided through using a motor-driven wire. While the ZADS provides the detector response for all heights in the NT, the GT allows the characterization of the detector in the GC and at the boundaries of the NT and the buffer region. Both devices are displayed in Figure 6.10. The AA consists of a robotic arm whose segments are attached with joints. If installed in the NT through the chimney, it will be able to deploy sources within the whole volume of the NT thus providing a complete characterization of the detector response in the NT. All these calibration devices are operated from a clean tent above a detector. The ZADS and the eventual AA need to be operated using a glove box under nitrogen atmosphere at the detector pressure.

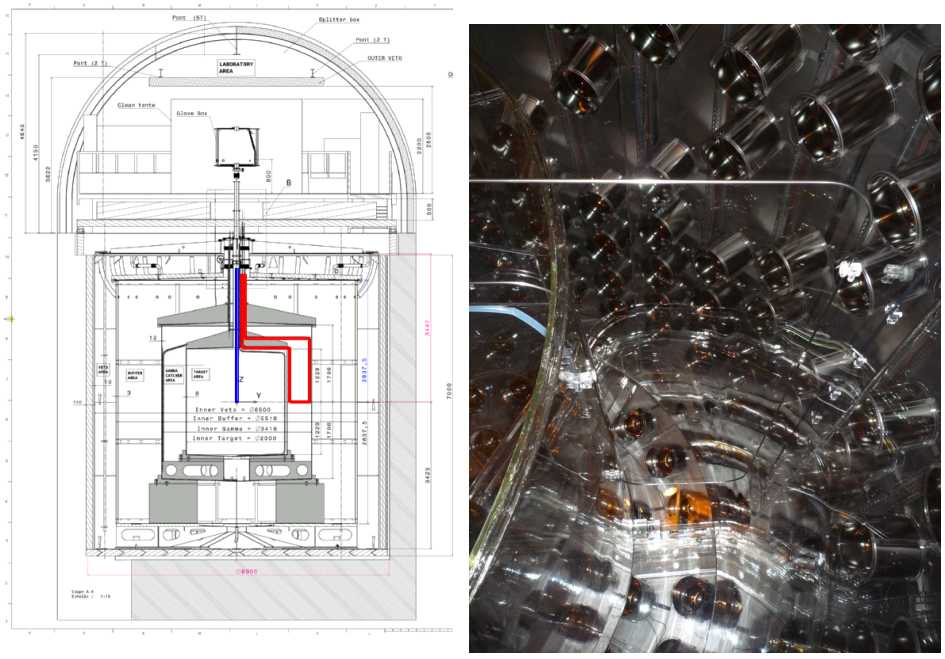

Figure 6.10: Left: Cross sectional sketch of the detector. The ZADS deployment through the chimney and the GT are highlighted in blue and red, respectively. Right: Photograph of the guide tube in the gamma catcher. The target acrylic vessel is visible on the left and the buffer wall covered with PMTs is visible on the right.

So far, four radioactive sources, sealed in capsules built to fit in the calibration devices, have been deployed in the NT and GC. Each of the four radioisotopes, ^{137}Cs, ^{68}Ge, ^{60}Co and

^{252}Cf has been selected with respect to its emitted radiation and its corresponding detector response.
The ^{137}Cs source emits a gamma ray of 662 keV upon its β^--decay to ^{137}Ba. This low energy gamma only has little interest for the $\bar{\nu}_e$ selection but provides a reference point between the threshold of 300 or 500 keV and the IBD detection threshold[3] of 1.022 MeV. The ^{68}Ge source emits pairs of 511 keV gammas upon the decay of ^{68}Ge toward ^{68}Ga via electron capture and the subsequent β^+-decay of ^{68}Ga. The positron emitted by the latter decay annihilates with an electron of the capsule and leads to the creation of two 511 keV gammas, an energy signature relevant for the detector characterization at the IBD detection threshold. By emitting two simultaneous gamma rays of 1.173 and 1.333 MeV each, the ^{60}Co provides a calibration of the energy between 1 and 2.5 MeV. The ^{252}Cf source emits gammas and neutrons by spontaneous fission[4] (SF) thus sometimes mimicking an $\bar{\nu}_e$ event. While the prompt energy spectrum, corresponding to the sum of the gamma energies, is of no interest for calibration due to its rough shape, the delayed event energy, corresponding to the neutron capture on Gd/H helps evaluating the systematic uncertainties of the neutron captures on Gd/H.
In addition to these known sources, the detector response is also evaluated using the captures of spallation neutrons, created by the interaction of energetic cosmic rays within or in the vicinity of the detector. The Bi-Po processes in the scintillator, leading to the observation of an electron from ^{212}Bi followed by a delayed 8 MeV α particle, which yields a $\sim$1 MeV signal due to quenching, from ^{212}Po, can be used as well for calibration purposes.

Light sources

While the radioactive sources help understanding the detector response to various radiations, a light injection system has been set to measure PMTs and liquids properties such as offsets, gains, etc...
This multiwavelength LED-fiber system injects light into the ID and the IV from several points located all around the buffer vessel. The optical fibers are attached to the covers of PMTs in the inner detector (IDLI) and the inner veto (IVLI), some equipped with diffuser plates in order to homogeneously illuminate the detector. The others end of the fibers are connected to blue and UV LEDs (385, 425 and 470 nm for IDLI, and 365 and 475 nm for IVLI) whose emission properties such as rate, intensity and pulse width are controlled remotely. The various wavelengths available for light calibration help characterizing the liquid properties in terms of attenuation and absorption. For instance, while the 385 nm light should be totally absorbed by the liquid's wavelength shifters, the 475 nm light should not be impaired and should be detected by PMTs on the other side of the fiber. The intermediate 425 nm light, only partially absorbed, allows the monitoring of the absorption of the NT and GC liquid. The light injection system is independent and remotely operated and a control board provides an external trigger at each light injection.

Calibrations using the light injection system are performed on a weekly basis in each

[3]The IBD threshold of 1.806 MeV described in Section 4.1 is the energy threshold of a $\bar{\nu}_e$ below which an IBD reaction can not occur. This IBD detection threshold is simply the annihilation energy of the positron (2×0.511 keV), minimum prompt energy seen by the detector.

[4]The SF yield of ^{252}Cf is only 3.1%, the remaining fraction corresponding to α-decays, whose energy deposition is contained in the capsule.

detector in the form of sequences, combinations of calibration runs with different wavelengths, intensities and positions. Longer and more complete calibration sequences are performed on a monthly basis. Since it requires on-site work and extra manpower, calibration campaigns with radioactive sources are less frequent and are performed approximately on a yearly basis.

6.3 Event reconstruction

The data acquisition system records the waveforms provided by the PMTs upon each energy deposition that triggers the detector. The reconstruction of an event consists of using the detector calibration, explained in Section 6.2, to transform the waveform information provided by the PMTs into an energy and vertex information.
The DAQ generates binary files that are quickly converted into ROOT [162] files. One of the main role of the Double Chooz Offline Group Software (DOGS) is to perform a complete reconstruction process on each event saved in the ROOT data files. DOGS consists of several packages, each in charge of different offline tasks, such as analysis, data production or simulation. The packages related to the latter will be presented in Section 6.4. The package in charge of event reconstruction is the Common Trunk (CT) which consists of several algorithms applied on RAW data, i.e. unprocessed ROOT files.

6.3.1 Pulse reconstruction

The event reconstruction starts from the pulse reconstruction whose purpose is to extract the time and charge information recorded by each PMT. This first step is performed by the DCRecoPulse algorithm [227].
To better understand each waveform digitized by the FADCs, a trigger with a 1 Hz periodicity is taken to provide the mean ADC counts of the baseline, B_{mean}, and its fluctuation, B_{rms} for each of the 468 PMTs. The integrated charge of a given event is defined as the sum of the ADC counts in the integration window of each waveform, once the pedestal, integration of B_{mean} over the same window, has been subtracted. The time integration window duration has been set to 112 ns to optimize the charge resolution of a single photoelectron, while its start time, set as the time when the pulse reaches 20% of its maximum, maximizes the integrated charge for each channel and each event. For typical events of a few MeVs in the NT, most PMTs only detect a single photoelectron so in order to reduce noise fluctuations, each signal is required to satisfy two conditions in order to be accepted: more than 2 ADC units in the pulse's maximum bin and an integrated charge $q > B_{\text{rms}} \times \sqrt{N_S}$ where N_S is the number of integrated waveform sample, i.e. 56 for a 112 ns window.
From these corrected digitized waveforms, the charge information is extracted using a sliding window algorithm that searches for the maximum integrated charge within the whole pulse while keeping the integration window constant. Although slower than simpler methods based on fixed integration windows, it is also the most accurate. The time information is provided by a dedicated algorithm whose output includes the maximum amplitude time, where the pulse is maximum, and the start time, defined as the time the pulse reaches a fixed or maximum-dependent value. The algorithm also provides other time-related information, such as the rise time T_{start} and its spread RMS(T_{start}) over several start times, later used in the neutrino selection (*c.f.* Section 6.5).

6.3.2 Vertex reconstruction

The vertex reconstruction is performed by the RecoBAMA package [228] using an algorithm based on a time and energy likelihood.
A event, defined as a point-like source of light, can be characterized by:

$$\mathcal{X} = (x_0, y_0, z_0, \Phi) \tag{6.2}$$

where (x_0, y_0, z_0) are the Cartesian coordinates of the event position in the detector frame and Φ is the light intensity per solid angle, expressed in photons/sr. The predicted amount of light μ_i received at the i$^{\text{th}}$ PMT and its arrival time t_i can be obtained by:

$$\mu_i = \Phi \epsilon_i \Omega_i A_i \tag{6.3}$$

$$t_i^{\text{pred.}} = t_0 + \frac{r_i}{c_n}, \tag{6.4}$$

with A_i accounting for the liquid attenuation such that:

$$A_i = \exp -\frac{r_i}{\lambda}, \tag{6.5}$$

λ being the attenuation length of the liquid and c_n its associated speed of light[5], r_i the distance between the i$^{\text{th}}$ PMT and the vertex, Ω_i the solid angle of the i$^{\text{th}}$ PMT at a distance r_i and ϵ_i its quantum efficiency.

Using these information, the event likelihood is defined as:

$$\mathcal{L}(\mathcal{X}) = \prod_{q_i=0} f_q(0;\mu_i) \prod_{q_i>0} f_q(q_i;\mu_i)\, f_t\left(t_i; t_i^{pred.}; \mu_i\right), \tag{6.6}$$

the first product accounting for the PMTs that have not been hit, while the second product goes over the remaining PMTs that have recorded a charge q_i at a time t_i. The charge term $f_q(q_i;\mu_i)$ is the probability of measuring a charge q_i given an expected charge μ_i and the time term $f_t\left(t_i; t_i^{\text{pred.}}; \mu_i\right)$ represents the probability of observing photons at t_i given an expected time of $t_i^{pred.}$ and an expected charge μ_i. Both probabilities are obtained by simulations and verified by physics and calibration data.
RecoBAMA then finds the best set of parameters $\mathcal{X}_{\min}$ which maximizes $\mathcal{L}(\mathcal{X})$ or, equivalently, minimizes its negative logarithm:

$$F(\mathcal{X}) = -\ln \mathcal{L}(\mathcal{X}) = -\sum_i \ln f_q(q_i;\mathcal{X}) - \sum_{q_i>0} \ln f_t(t_i;\mathcal{X}) \tag{6.7}$$

$$= F_q(\mathcal{X}) + F_t(\mathcal{X}). \tag{6.8}$$

While the reconstruction can be performed using charge-only (F_q) or time-only (F_t) information, the combination of both components enhances the accuracy and stability of the reconstruction. The precision on the position reconstruction is of the order of 12 cm at 1 MeV using both the charge and time likelihoods.

[5]The speed of light in a liquid is defined by $c_n = c/n$ with c the speed of light in vacuum and n the refraction index of the liquid.

6.3.3 Energy reconstruction

The accurate knowledge of the neutrino energy spectrum is of crucial importance to perform a precise measurement of θ_{13}. Whether when comparing data with simulations (MC) with one detector only or by comparing the energy spectra observed in both detectors, great care needs to be taken when reconstructing the neutrino energy.

For each event, the visible energy $\mathrm{E_{vis}}$, observed in the detector, is reconstructed from the total number of photoelectrons $\mathrm{N_{pe}}$ as:

$$E_{\mathrm{vis}}^{\mathrm{data}} = N_{\mathrm{pe}} \times f_u^{\mathrm{data}}(\rho, z) \times f_{MeV}^{\mathrm{data}} \times f_s\left(E_{\mathrm{vis}}^0, t\right) \quad (6.9)$$

$$E_{\mathrm{vis}}^{\mathrm{MC}} = N_{\mathrm{pe}} \times f_u^{\mathrm{MC}}(\rho, z) \times f_{MeV}^{\mathrm{MC}} \times f_{nl}\left(E_{\mathrm{vis}}^0\right), \quad (6.10)$$

for data and MC events, respectively. The ρ and z parameters, respectively the radial distance such as $\rho = \sqrt{x^2 + y^2}$ and z the vertical Cartesian coordinate characterize the position of the reconstructed vertex in the detector frame while t is the time elapsed since the beginning of the data taking. The presence of these terms shows the non-uniformity of the detector response throughout the detection volume but also during the data taking. The correction factors account for uniformity (f_u), absolute energy scale (f_{MeV}), time stability (f_s, only for data) and non-linearity (f_{nl}, only for MC). E_{vis}^0 is the visible energy corrected for uniformity only.

The number of photoelectrons $\mathrm{N_{pe}}$ can be computed as the sum of the charges detected by each PMT i such that:

$$N_{\mathrm{pe}} = \sum_i q_i / g_i(q_i, t), \quad (6.11)$$

with q_i, the integrated charge reconstructed in the $\mathrm{i^{th}}$ PMT and g_i, its gain, being by definition a charge-to-p.e. conversion factor. The gain, charge and time-dependent, is computed using calibration data taking into account its non-linearities and time stability. These non-linearity are due to the limited sampling of the FADCs which can induce a bias of $\pm$ 1 ADC count in the baseline subtraction, thus leading to non-linearities in the low-energy regime, where only a few p.e. are detected. The PMT gains are measured, using calibration data taken with the IDLI and IVLI systems, as $g_i = \alpha \times \sigma_i^2/\mu_i$ with μ_i and σ_i the integrated charge mean and standard deviation (RMS) and α a correction factor accounting for the σ_i dispersion due to single p.e. and electronic noise. As displayed in Figure 6.11 for a typical readout channel, the data points are well fitted by a function characterized by three parameters: constant gain at high charge, non-linearity slope at low charge and a transition point.

Once the gains have been correctly computed and the number of photoelectrons have been obtained, one needs to account for the position dependence via the uniformity calibration. The center of the detector, (x=0,y=0,z=0) or (ρ=0,z=0), is supposed to be the location where the detector response is the most uniform because of the symmetries. The uniformity correction factor f_u is applied to a $\mathrm{N_{pe}}$ at a given ρ and z and converts it into an $\mathrm{N_{pe}}$ at the center of the detector. The $f_u(\rho, z)$ function is obtained using 2.2 MeV gamma rays created upon spallation neutron captures on H in the NT and the GC. This two-dimensional function, called calibration map, is shown in Figure 6.12 for both data and MC. While the uniformity correction factor reaches up to 5% in the NT, its associated systematic uncertainty has been

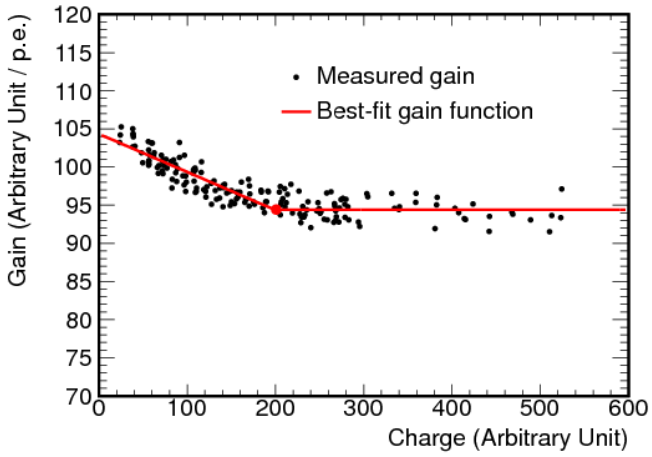

Figure 6.11: Gain as a function of the integrated charge. The black points are measurements performed for a typical PMT and the red line is the best-fit (3 parameters) gain function later used in the reconstruction [75]. The slope at low charges shows the gain non-linearity.

evaluated to be equal to 0.36% from the residual differences between data and MC.

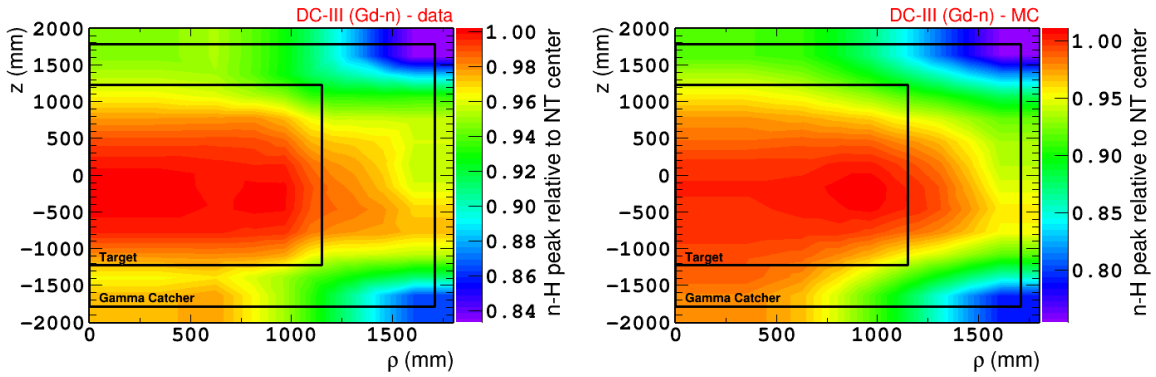

Figure 6.12: Uniformity correction function of the detector (NT+GC) using neutron capture on H in data (left) and MC (right) [75].

To obtain the absolute energy scale, later corrected for non-uniformities, a ^{252}Cf source is placed at the center of the detector. The energy peak of neutron captures on H at 2.2 MeV provides the absolute energy scale in units of p.e./MeV for data and MC as shown in Figure 6.13. The energy scale computed for the third and latest Double Chooz publication [75] is 186.2 p.e./MeV for data and 186.6 p.e./MeV for MC.

The detector response stability has been varying over time since the beginning of the data taking. By monitoring the PMT gains and the detector response using spallation neutron captures on H and Gd, as well as α-decays of ^{212}Po from Bi-Po processes, a stability factor can be computed and applied at each energy E^0_{vis} and each time t, defined as the time elapsed

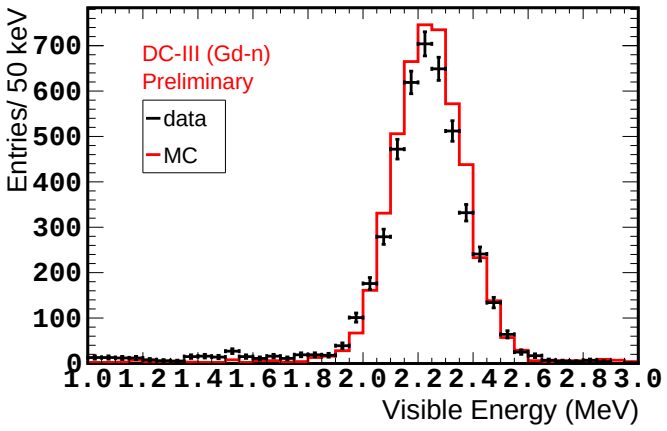

Figure 6.13: Energy peak of neutron capture on H for data (black) and normalized MC (red) taken with a ^{252}Cf source deployed at the center of the detector.

since the first deployment of a Cf source in August 2011. The effect of the stability correction is displayed in Figure 6.14. Since the MC is not affected by time instabilities, this correction is only applied to data. The systematic uncertainty associated to the detector instabilities is obtained from the remaining fluctuations and has been evaluated to be 0.50%.

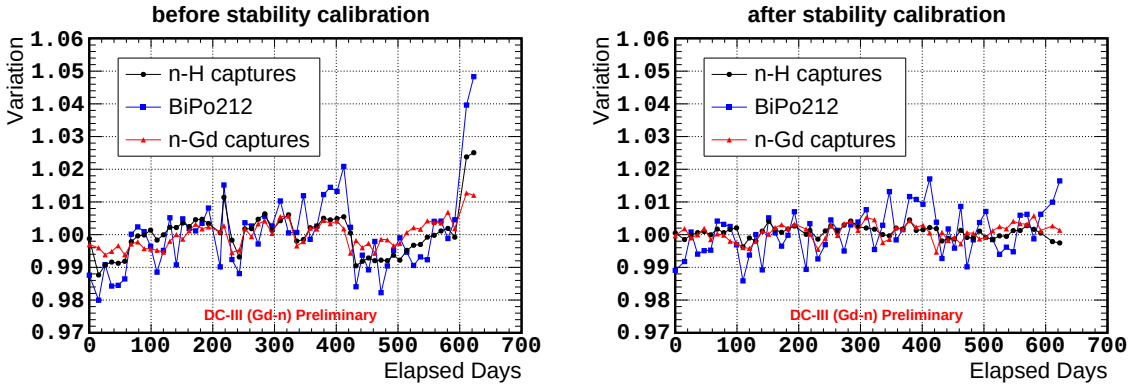

Figure 6.14: Ratio of the peak energy over its nominal value as a function of time for ^{212}Po α decays (blue) and neutron captures on Gd (black) and H (red) before (left) and after (right) application of the stability correction [75].

The last correction taken into account in the energy reconstruction is the non-linearity correction. It accounts for the MC-data discrepancies due to non-linearities arising from charge (QNL) and light (LNL). It is thus only applied to MC. The QNL correction is applied to the visible energy of all events since it is associated with the MC modeling of the electronics and the charge integration algorithm. On the other hand, the LNL correction, since it is associated with the particle-dependent scintillator modeling, is only applied to prompt event, i.e. positron energy deposition. The QNL correction function can be estimated by

comparing the ratio of the Gd/H capture peak positions using a Cf source between data and MC. The data points displayed in Figure 6.15 show the discrepancies left after the application of the QNL correction. To determine the LNL correction function, several MC simulations were performed with different combinations Birks' quenching parameter and light yield of the liquid scintillator within the uncertainties obtained during lab measurements [229, 230]. When a set of these two parameters is found in good agreement with data, it is recorded and a positron MC simulation is generated. The comparison between this simulation and one performed with the nominal set of parameters provides the LNL correction function and its associated uncertainty. The red line in Figure 6.15 shows the agreement between data and MC after application of the two non-linearity correction functions.

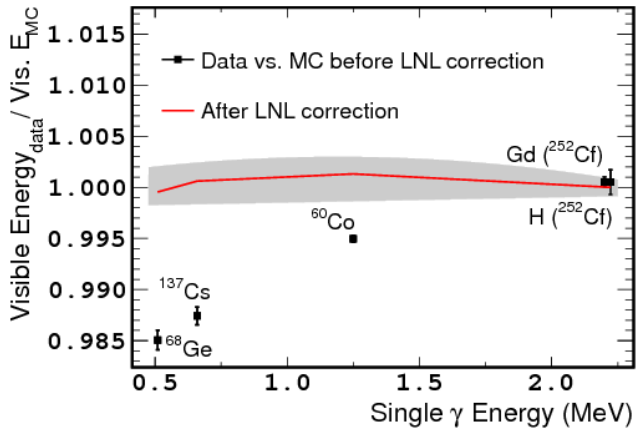

Figure 6.15: Visible energy ratio between data and MC for various single gamma energies after application of the QNL correction (black squares) and after application of the QNL+LNL correction (red line). The gray band corresponds to the systematic uncertainty of the correction. [75].

Finally, after the application of all the corrections, a good agreement between data and MC is found, as shown in Figure 6.16. The figure displays the energy resolutions for data and MC, expressed as:

$$\sigma/E_{\text{vis}} = \sqrt{a^2/E_{\text{vis}} + b^2 + c^2/E_{\text{vis}}^2}, \tag{6.12}$$

where a, b and c are respectively the statistical fluctuation, constant term and energy independent width due to electronic noise. Table 6.1 summarizes the values of these factors, obtained by fitting data and MC with the previous equation.

	a [MeV$^{1/2}$]	b	c [MeV]
Data	0.077 ± 0.002	0.018 ± 0.001	0.017 ± 0.011
MC	0.077 ± 0.002	0.018 ± 0.001	0.024 ± 0.006

Table 6.1: Parameters of the energy resolution.

The total uncertainty associated to the energy scale, combination of the non-uniformity, instability and non-linearity uncertainties, is equal to 0.74%.

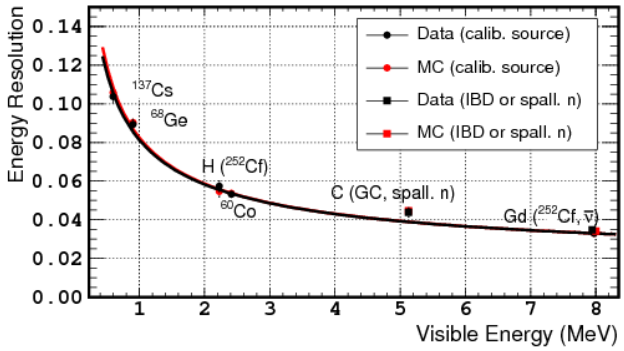

Figure 6.16: Comparison of the visible energy reconstructed in data and MC. The black (data) and red (MC) lines are fits of the energy resolution as a function of the visible peak energy showing a $1/\sqrt{E\ (MeV)}$ behavior at first order. The dots correspond to calibration sources while the squares correspond to neutron captures (spallation or IBD) [75].

6.3.4 Muon tracks reconstruction

As discussed in Section 6.5.1, muons passing through or in the vicinity of the detector induce several types of backgrounds. Dedicated algorithm, such as the Fused Inner Detector Outer veto MUon Track reconsTruction [231], or FIDO, have been developed in DOGS to efficiently detect, tag and track those muons. Using information from the ID, the IV and the OV, FIDO allows the reconstruction of muons crossing any part of the detector. While, given their energy, most muons simply travel through the detector, some stop within the detector (stopping muons), thus creating Michel electrons. The algorithm is able to distinguish between these two cases and provides track reconstruction uncertainties of the order of 10 cm in the x and y directions for through-going muons intersecting the NT, with the help of the OV. In the case of stopping muons, the detection of the subsequent Michel electrons provides reconstruction uncertainties of the order of 14 cm in the x, y and z directions. FIDO is now used by default in the Common Trunk and provides likelihoods, used to suppress and better constrain cosmogenic backgrounds. More details about the FIDO algorithm and the muon reconstruction in Double Chooz can be found in Ref. [232].

6.4 The Double Chooz simulation package

In order to study and optimize the selection cuts used in the data analysis and compare oscillated data with non-oscillated prediction, precise Monte Carlo simulations of the experiment from the $\bar{\nu}_e$ generation to the data output are mandatory. The Double Chooz Monte Carlo, embedded in the DOGS software, is composed of three main packages: the $\bar{\nu}_e$ generation, the simulation of all physical processes occurring in the detector and the readout simulation. The Double Chooz simulation chain is shown in Figure 6.17.

6.4.1 $\bar{\nu}_e$ generation

The generation of $\bar{\nu}_e$ is performed by the DCRxtrTools package [233]. For each data file recorded at a given time corresponds a simulation file, taking in consideration all the infor-

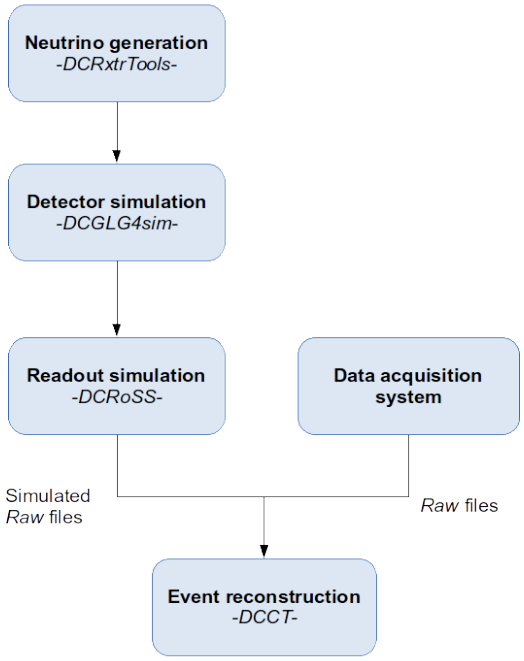

Figure 6.17: Sketch of the Double simulation chain. The goal of the complete simulation is to produce simulation files comparable to data files.

mation related to the current status of the reactors, such as power and fuel composition. This information is combined with an oscillation probability to produce an expected neutrino rate and its corresponding interactions in the detector. As do NuMC and SuperNustradamus (*c.f.* Section 4.3.1 and 4.3.2), DCRxtrTools simulates an IBD interaction by generating a (e^+,n) pair in the detector with the correct energy and momentum distributions. Note that the choice of the IBD cross section used in DCRxtrTools (Vogel and Beacom) does not yield significant discrepancies, the neutrino energy being limited to less than 10 MeV. The list containing all the pairs is then fed into the next package of the simulation chain.

6.4.2 Detector response simulation

The role of Double Chooz detector simulation package DCGLG4sim [234] is to simulate the behavior of particles in the Double Chooz detector. It is based on GLG4sim [164], the generic GEANT4 [161] simulation software derived from KLG4sim, and has been modified to fit the needs of the Double Chooz experiment. It encompasses detector properties such as geometry (Figure 6.18), liquid precise composition, optical properties and material reflectivity. DCGLG4sim runs on the 9.2.p02 version of GEANT4 [235] with custom models of neutron scattering, radiative neutron capture, scintillation and photocathode surface.

The (e^+,n) pairs generated by DCRxtrTools are simulated in DCGLG4sim and the light

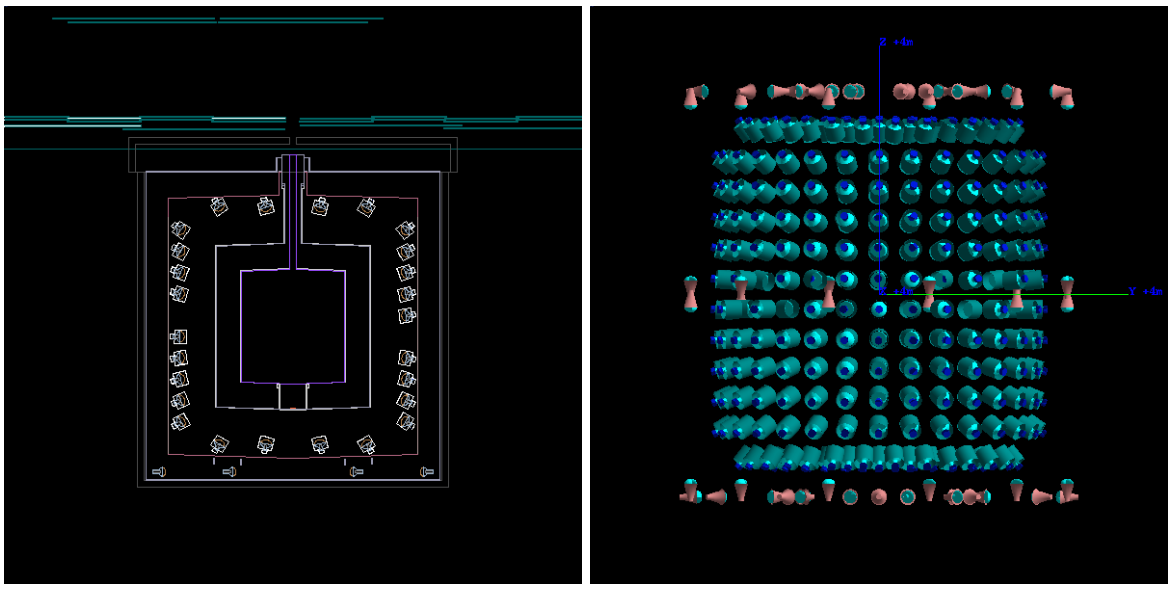

Figure 6.18: Left: Main volumes of the Double Chooz detector visualized in DCGLG4sim. Right: Visualization of the placement of the ID and IV PMTs in the simulation. Pictures generated with DCGLG4sim and extracted from [234].

emitted upon their energy deposition is propagated as far as the PMTs. Once the photons reach the photocathodes, a photoelectron might be produced, depending on the quantum efficiency of each PMT and the response homogeneity of its photocathode. Once the number of p.e. generated in each PMT has been computed, the event is recorded and the simulation goes on. At the end of a DCGLG4sim simulation, the simulation file containing all the p.e. information of each event is fed into the final step of the Monte Carlo simulation: the readout simulation.

Note that, in order to characterize the simulation and better understand backgrounds, physical interactions other than IBD events can be simulated. For instance, DCGLG4sim includes a set of generators used to simulate radioactive sources such as the ones described in Section 6.2.2. Cosmogenic isotopes, muon interactions and external radioactivity can be studied as well.

6.4.3 Readout simulation

The readout simulation package, DCRoSS [236], intends to simulate the complete electronics readout chain from the PMTs to the FADCs. The PMT response to each p.e. is simulated with respect to the PMT's gain and collection efficiency, and, based on measurements, a waveform is produced. Additional effects such as dark noise, offsets and fluctuations are taken into account in the waveform generation to predict dispersion effects. Each waveform is then amplified and digitized such that the electronics response simulated in DCRoSS agrees within 1% with the actual data. The output format of DCRoSS is identical to the format of data files provided by the DAQ. Both files can be sent to the Common Trunk, DCCT, so that the reconstruction algorithms (*c.f.* Section 6.3) can be applied similarly to data and MC.

6.5 Data analysis

In order to perform an oscillation fit as presented in Section 6.6, the detected $\bar{\nu}_e$ events have to be selected. With an average trigger rate of 300 Hz and an expected neutrino rate of about 50 $\bar{\nu}_e$ .d^{-1} and 300 $\bar{\nu}_e$ .d^{-1} in the far detector (FD) and the near detector (ND) respectively, great care is taken to reject backgrounds and select a sample of $\bar{\nu}_e$ as pure as possible (*c.f.* Section 6.5.3). Nonetheless, the selection of $\bar{\nu}_e$ candidates extracted from the data samples, described in Section 6.5.2 still contains an amount of irreducible backgrounds, indistinguishable from true $\bar{\nu}_e$ events. The study of these backgrounds is presented in Section 6.5.1.

6.5.1 Backgrounds

Several types of backgrounds have been observed in Double Chooz and are carefully studied. The main background, in terms of trigger rate, is the light noise caused by the PMTs. However, since it doesn't originate from a physical event and can be efficiently rejected, the light noise background is not accounted for in the oscillation analysis. Since a small fraction of the remaining correlated and accidental backgrounds cannot be reduced by the neutrino selection cut, their rates and spectral shapes are taken into account in the oscillation analysis.

Light noise

Upon switching on the far detector, an important rate of unexpected background events had been observed. This background, known as light noise, is caused by random spontaneous light emissions from the bases of some PMTs. The impossibility of optically shielding the PMT bases in the far detector to reduce this background led to the development of several rejection techniques. A light noise event being caused by the glowing of a single PMT, its signature is mainly localized to one PMT with some propagation to its closer neighbors. This typical distribution of detected light is spread less homogeneously across the detector than for physics events. The strategy to reject light noise events has been presented in Ref. [170] and relies on both charge and time of the PMT signals, as presented in Section 6.5.3.

Accidental background

The random coincidences caused by two valid triggers that satistfy the IBD selection cuts are referred to as accidental background. Usually the association of a prompt trigger from natural radioactivity and a delayed trigger from a spallation neutron capture, an accidental coincidence is composed of two random events and is thus considered as an uncorrelated background. Without the existence of a correlation between the two events, the accidental background can be strongly reduced by applying distance and time separation cuts. However, a small component of accidentals remains in the data set of $\bar{\nu}_e$ candidates and the rate and energy spectrum of these events has to be estimated.
To do so, an off-time window analysis is conducted, in which the delayed event is not looked for upon the prompt event but long after, typically of the order of 1 s. This method removes correlations between the two events and provides a high statistic of fake accidental events (the number of windows opened for each prompt candidate) thus allowing a precise measurement of the rate and energy spectrum of the accidental background.
The rates of accidental background measured in the n-H and n-Gd datasets are summarized in Table 6.2.

Cosmogenic background

The main background of the Double Chooz experiment, upon rejection of light noise, is the correlated cosmogenic background. The spallation of muons on ^{12}C atoms within the detector volume creates radio-isotopes such as ^{9}Li and ^{8}He[6]. Though this muon is most likely to be tagged and vetoed, these cosmogenic isotopes have lifetimes of the order of hundreds of ms and their decays therefore escape the veto applied after the incoming muon detection. Their decays lead to the emission of electrons, alphas and neutrons and can thus mimic an IBD event. For instance, the 257 ms lifetime of ^{9}Li, its Q-value at 13.6 MeV and the subsequent emission of α's and neutrons from its daughter nucleus ^{9}Be is indistinguishable from a neutrino interaction. Tremendous efforts have been dedicated to the detection and simulation of this background [237, 238]. The prompt energy spectrum of cosmogenic background, measured in the n-Gd dataset, and its simulation performed by considering additional branches of the β-decay chain, are displayed in Figure 6.19.
The rate of cosmogenic backgrounds measured in the n-H and n-Gd datasets is summarized in Table 6.2.

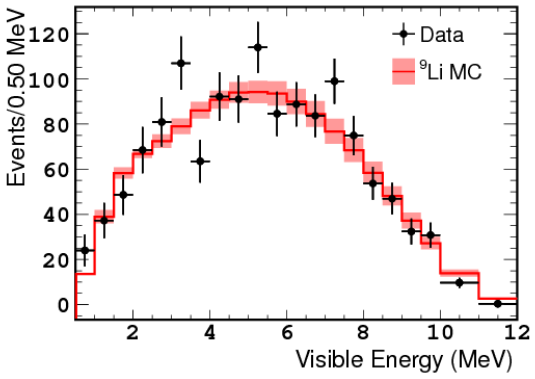

Figure 6.19: Prompt energy spectrum of cosmogenic background. Black points show the data measured. The red histogram shows the normalized MC simulation, including only ^{9}Li, and its uncertainty [75].

Fast neutrons and stopping muons

Muons passing nearby the detector can generate fast neutrons via spallation. If not discarded by the muon veto cut, these neutrons can enter the detector volume and induce proton recoils before being thermalized and finally captured. These two signals, correlated in time and space, are hardly distinguishable from IBD events. However, this background being distributed over a broad energy range, it can be estimated by searching high energy prompt events in a range where the reactor component is negligible.
In some cases, muons can enter the detector through the loosely-instrumented chimney and interact in the inner detector without being tagged. Although most of these muons will deposit a significant amount of energy and be therefore rejected, some might loose enough

[6]These two isotopes showing similar behaviors, we will now focus on ^{9}Li only since it represents the main contribution.

energy to pass the prompt event selection cut. These muons will then decay thus emitting a Michel electron and mimicking a delayed neutrino event. This correlated background events are referred to as stopping muons.
The combined energy spectrum of fast neutrons and stopping muons has been measured over the energy range of interest for the Double Chooz analyses and is respectively fitted by a linear flat function and an exponential function in the n-Gd and n-H analyses.
The rate of fast neutrons and stopping muons background measured in the n-H and n-Gd datasets is summarized in Table 6.2.

Background	n-Gd rate (d^{-1})	n-H rate (d^{-1})
Accidental	0.0701 ± 0.0054	4.334 ± 0.007 (stat) ± 0.008 (syst)
Cosmogenic	$0.98^{+0.41}_{-0.16}$	$0.95^{+0.57}_{-0.33}$
Fast-n + stop-μ	0.604 ± 0.051	1.55 ± 0.15

Table 6.2: Summary of the background rates measured in the n-Gd and n-H datasets [239, 240].

6.5.2 Data samples

The Double Chooz far detector has been continuously acquiring data since April 13$^{\text{th}}$, 2011. The first two publications [26, 241] reported measurements of θ_{13} using respectively 101.5 days and 251.3 days of data taking. The following section is dedicated to the data analysis performed for the third Double Chooz publication [75] which encompasses 467.9 days of data taking. During this period, several reactor configurations have been observed, including two periods, of respectively $\sim$1 and $\sim$6 days, during which both reactors were shut down. The analysis of the $\bar{\nu}_e$ candidates observed during this period is of crucial interest to understand intrinsic detector backgrounds and has been the subject of a dedicated publication [242].
Since Double Chooz proved its ability to select $\bar{\nu}_e$ events with neutron capture on H, the data analysis performed on a data set based on neutron captures on H will be presented as well. This dataset encloses 462.7 days of data taking.
Finally, since the commissioning of the near detector is not achieved at the moment, its data has not been officially released yet. Nonetheless, I will present the results of preliminary data analyses I performed with the limited number of physics runs that have been processed. Since the accidental background cut, discussed in Section 6.5.1, has not been implemented in the ND data yet, only $\bar{\nu}_e$ events leading to neutron captures on Gd will be analyzed.

To sum up, the three following data sets will be presented:

- n-Gd (FD): Neutrino selection based on the observation of neutron captures on Gd in the far detector target.
- n-H (FD): Neutrino selection based on the observation of neutron captures on H in the far detector target and gamma catcher.
- n-Gd (ND): Neutrino selection based on the observation of neutron captures on Gd in the near detector target.

Unlike the n-Gd analysis, restricted to the target volume, the n-H analysis extends to the boundaries of the gamma catcher. Although this enlargement of the fiducial volume

yields to an increase of the IBD rate by a factor of ∼1.8, an increase of the background rate is expected in the n-H analysis as well, the gamma catcher being less shielded from the external background than the target. The discrepancy between the fast neutrons spectral shapes in both analyses shows the effect of this reduced shielding. Similarly, given the higher interaction rate observed in the low energy region of the spectrum, an increase of the accidental background is expected in the n-H analysis, looking for a delayed event around 2.223 MeV. This increase is accentuated by the enlargement of the coincidence window applied to select IBD pairs in the n-H analysis. To palliate these issues, different selection cuts have to be applied in both analyses, as explained in Section 6.5.3. The discrepancies between the n-Gd and n-H background rates displayed in Table 6.2 is explained by the fiducial volume increase as well as the difference of selection cuts.

6.5.3 Neutrino selection

The neutrino selection is based on several cuts that have been added and improved over time. While several of these cuts are dependent on the data sample and differ for n-Gd and n-H analyses, they are all applied on pre-selected events called valid triggers.

Valid triggers selection

A valid trigger is defined as an event not tagged as a random trigger, a muon event or a light noise event. Furthermore, its visible energy is required to be above 0.4 MeV, where the trigger efficiency reaches 100%. Finally, in order to reduce the correlated and cosmogenic backgrounds due to muon spallation, a veto of 1000 μs (1250 μs for n-H) is applied after each event identified as a muon. No valid trigger can be accepted within this veto duration.
As explained in Section 6.3.1, periodic triggers are sent with a frequency of 1 Hz to measure the baseline and dispersion of the PMTs' response. Such a trigger is an unphysical event and is therefore not considered a valid trigger.
An event is considered a muon if it deposited a total charge in the IV larger than 30,000 charge units (∼16 MeV) or if its visible energy in the ID is above 20 MeV.
To be tagged as light noise, an event needs to fulfill specific charge and time criteria. The light noise emitted by a PMT, being detected at first in said PMT, will induce very inhomogeneous PMT responses. The emitting PMT and its neighbors detect a faster and much more intense signal than the rest of the PMTs, an effect one can quantify by observing the pulse of each PMT, their start time spread RMS(T_{start}) and charge spread RMS(Q). A trigger satisfying all the following criteria is not considered a light noise event and is consequently kept as a valid trigger:

- Max(Q)/Total(Q) < 0.12
- $Q_{diff} < 30000$ charge units
- RMS(T_{start}) < 36 or RMS(Q) $<$ 464 - 8×RMS(T_{start}),

with Max(Q) the highest charge received by a PMT, Total(Q) the total charge recorded by all PMTs for the event and Q_{diff} a variable built to assess the charge spread between the PMT receiving Max(Q) and its neighbors within a 1 m radius sphere. The Max(Q)/Total(Q) and the Q_{diff} cuts reject events whose charge distribution is strongly inhomogeneous, a characteristic of light noise events. The effect of the RMS(T_{start}) cut is displayed in Figure 6.20.

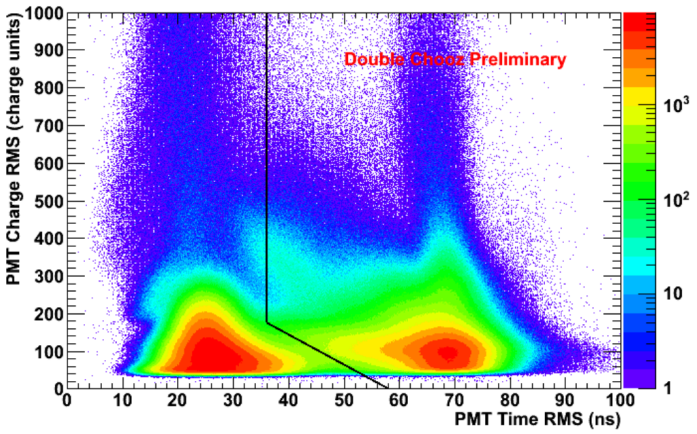

Figure 6.20: RMS(Q) as a function of RMS(T_{start}). The light noise charge cuts have already been applied. The black line represents the cut separating the physics region (left) and the light noise region (right). The respective location of these two regions is known via the use of calibration sources and MC simulations. Figure taken from [170].

After selecting valid triggers only, the IBD selection cuts can be applied.

n-Gd selection and results

The n-Gd analysis with the far detector only is based on a data sample having a live time of 460.67 days with at least one reactor in operation and 7.238 days with both reactors shut down. The observed and expected $\bar{\nu}_e$ rate during this period are displayed in Figure 6.21. The selection cuts that lead to the observation of this rate will now be described.

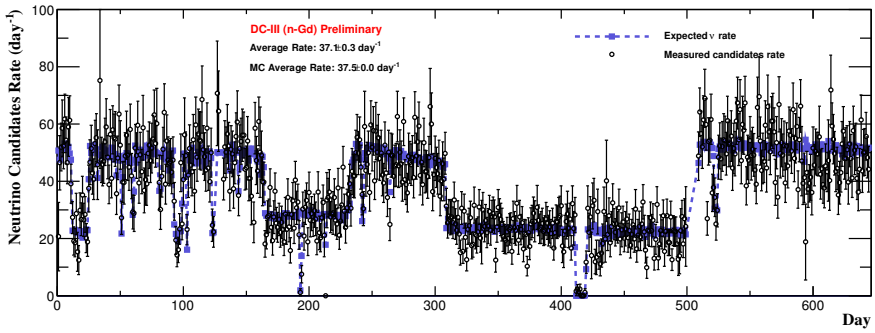

Figure 6.21: Rate of $\bar{\nu}_e$ candidates per day for the n-Gd analysis. The observed rate is shown in empty black squares and the expected rate, from MC predictions, is displayed in dashed blue lines. Several periods with only one reactor operating have been observed along with two periods with both reactors shut down (at day ∼190 and day ∼415).

Prompt event The prompt event corresponds to the energy deposition of the positron, via ionization and annihilation, in the liquid scintillator. The positron energy being closely

related to the neutrino energy as presented in Eq. 4.3, valid at reactor energies, the energy cuts to apply on the prompt event directly depend on the $\bar{\nu}_e$ energy spectrum. Although the minimum visible energy deposited by a positron is 1.022 MeV, from its annihilation, the visible prompt energy is allowed to vary within an energy range such that:

- $0.5 < E_{\text{vis}} < 20$ MeV.

The lower cut allows to record low energy background events, later used to help constrain the shape of the total background, while still in the 100% trigger efficiency range. The upper cut has a similar purpose in the high energy region, where no neutrino signal is expected but only correlated background is present. Recent studies have been performed [243] to possibly raise this upper limit to 100 MeV and further constrain the correlated background.

To reduce the muon-induced background as much as possible, one has to make sure that the prompt event is not in fact a muon-induced event such as a neutron whose capture would lead to a coincidence, hardly distinguishable from an IBD event. To do so, several veto cuts are applied on the prompt event.
First of all, a prompt event is rejected if it has occurred at the same time as a consequent energy deposition in the IV. The IV being subjected to a larger background than the ID, this energy deposition is defined by the following criteria:

- IV PMT multiplicity ≤ 2
- $Q_{IV} > 400$ charge units ($\sim$0.2 MeV)
- ID-IV space coincidence: $\Delta d < 3.7$ m
- ID-IV time coincidence: $\Delta t < 50$ ns

The IV PMT multiplicity corresponds to the number of PMTs that received a signal and Q_{IV} is the total charge received in the IV. The ID-IV time and space coincidences correspond to time and spatial difference between the prompt event, reconstructed in the ID, and the energy deposition in the IV.
The second cut aims at reducing the background induced by cosmogenic isotopes such as ^{9}Li and ^{9}He. A likelihood function taking into consideration the spatial correlation between the event and the track of the last muon that crossed the detector, as well as the multiplicity of the spallation neutrons it induced, is computed on an event-by-event basis. The value returned by the likelihood function assesses the probability of observing a cosmogenic event. Prompt events satisfying the condition:

- ^{9}Li likelihood < 0.4

are kept.
Finally, a prompt event is rejected if it occurs in coincidence with an OV trigger. Since the OV has not been active for the full duration of the data taking, this cut is only applied for prompt events detected during periods with an OV activity. In this n-Gd sample, 27.6% of the data has been recorded with a full OV, 56.7% with only the lower two layers and 15.7% without an active OV.

Delayed event Similarly to the prompt event, the delayed event is selected with respect to its energy. However, since the expected energy deposited upon a neutron capture is well known, the selection energy window is smaller. Since a neutron capture on Gd releases an ∼8 MeV gamma cascade, the visible energy of a delayed event must satisfy:

- $4 < E_{\text{vis}} < 10$ MeV.

The upper limit of the selection windows has been fixed to contain most of the delayed reconstructed energies, including energy resolution smearing. The lower limit has been set to maximize the detection efficiency and recover delayed events whose Gd cascade was not fully contained in the active volume of the detector.

The last cut to apply on the selection of delayed events is the Functional Value (or FV) cut. The FV variable is provided by RecoBAMA and corresponds to the minimum of the negative log-likelihood function shown in Eq. 6.8. While the value of FV is small when reconstructing point-like energy depositions, it increases for broader and more irregular energy depositions such as stopping muons and light noise. The condition a delayed event has to fulfill to be accepted is:

- $E_{\text{vis}} > 0.068 \times e^{FV/1.23}$.

Figure 6.22 illustrates the effect of the FV cut on delayed events. Three regions are clearly highlighted, corresponding to IBD events, stopping muons and light noise, in order of increasing functional values.

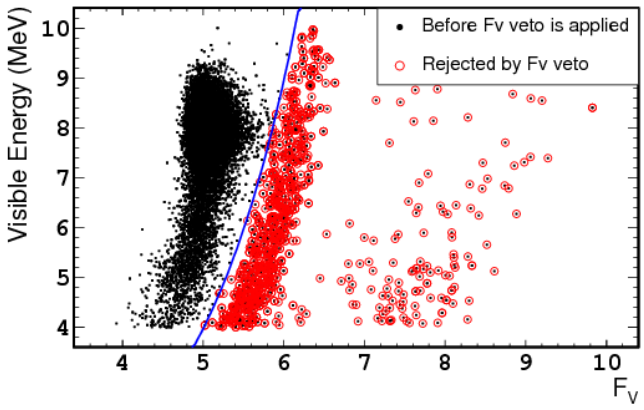

Figure 6.22: Correlation between the functional value and the visible energy for pre-selected delayed signals. Blacks points represent the data points before the application of the FV cut. The events rejected by the cut are encircled in red [75].

Coincidence The correlation between the prompt and delayed events of an IBD interaction is one of the main source of background reduction. The spatial and time distributions of the neutron thermalization and capture determine the coincidence cuts in the analysis. As previously shown in Figure 4.15 (left), a vast majority of thermal neutrons are captured within 100 cm of their thermalization point in a Gd-loaded liquid such as Double Chooz's.

The increase of the capture cross section brought by the addition of Gd also modifies the neutron capture time, equal to 30 μs in the target. From these correlations, the coincidence selection cut on the time and space separation of the prompt and delayed events has been set to:

- $0.5 < \Delta T < 150$ μs
- $\Delta R < 100$ cm

The lower ΔT cut has been lowered from 2 μs in previous analyses to its current value of 0.5 μs, due to the reduction of the stopping muons component thanks to the FV cut. The upper ΔT has been set to enclose almost 100% of the IBD signals while being optimized to reject accidental background.

Multiplicity The goal of the multiplicity cut is to isolate the pairs of prompt and delayed events from other energy depositions. The implementation of vetos before and after the prompt event allows the rejection of correlated backgrounds, such as fast neutrons, usually generated in bunches by muon spallation. The multiplicity cut conditions are as follows:

- No valid trigger allowed in the 200 μs preceding the prompt event
- Only one valid trigger (the delayed event) allowed in the 600 μs following the prompt event

Results After applying the cuts previously described, the n-Gd neutrino dataset includes 17,351 candidates detected during periods of reactor activity and 7 candidates detected during the simultaneous shutdown of the two reactors, for a total of 17,358 neutrino candidates. The prompt and delayed energy spectra of these neutrino candidates are displayed in Figure 6.23. The delayed spectrum, whose shape is not affected by the θ_{13}-driven oscillation, is compared to its MC prediction and both are found in agreement, the remaining discrepancies being caused by non-linearities (*c.f.* Section 6.3.3). The comparison between the prompt energy spectrum of the $\bar{\nu}_e$ candidates and its prediction will be developed in Section 6.6.

Figures 6.24 and 6.25 show the vertex distributions of the prompt and delayed events, respectively. The n-Gd selection being based on neutron captures on Gd, only captures occurring in the target are observed. However, in some cases, a prompt event can occur in the gamma catcher, close to the target, thus leading to the detection of its associated delayed event in the target. These events, referred to as *spill-in* events[7], have been thoroughly studied [244, 245].

n-H selection and results

The n-H analysis with the far detector only is based on a data sample similar to the n-Gd sample with a live time of 455.57 days with at least one reactor in operation and 7.15 days with both reactors shut down. The observed and expected $\bar{\nu}_e$ rate during this period is displayed in Figure 6.26. The higher neutrino rate is due to the larger number of n-H interactions, the

[7] As opposed to *spill-out* events, where a prompt event is detected in the target and its associated delayed event occurs in the gamma catcher.

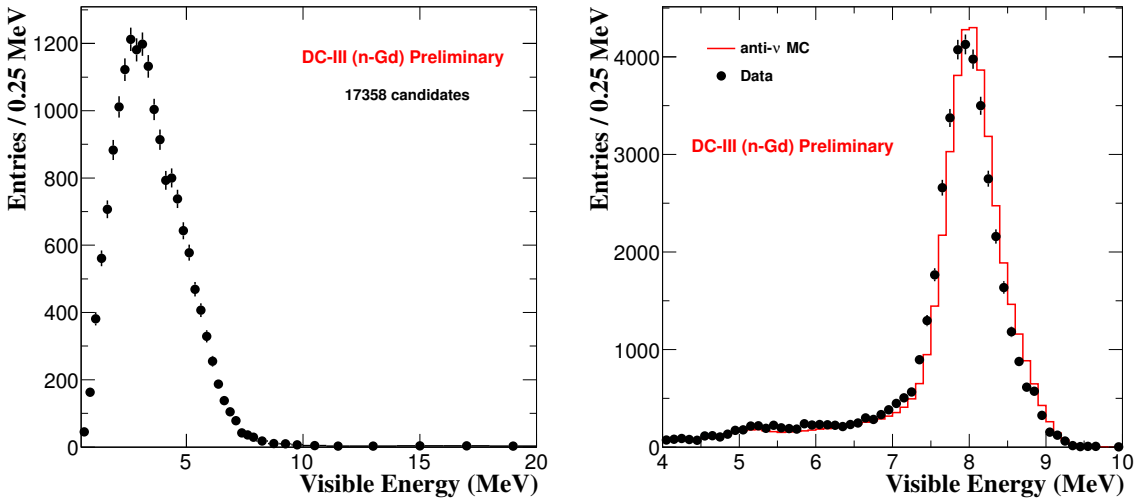

Figure 6.23: Left: Prompt energy spectrum of the n-Gd candidates. Right: Delayed energy spectrum of the n-Gd candidates for $\bar{\nu}_e$ candidates (black dots) and MC prediction (red line).

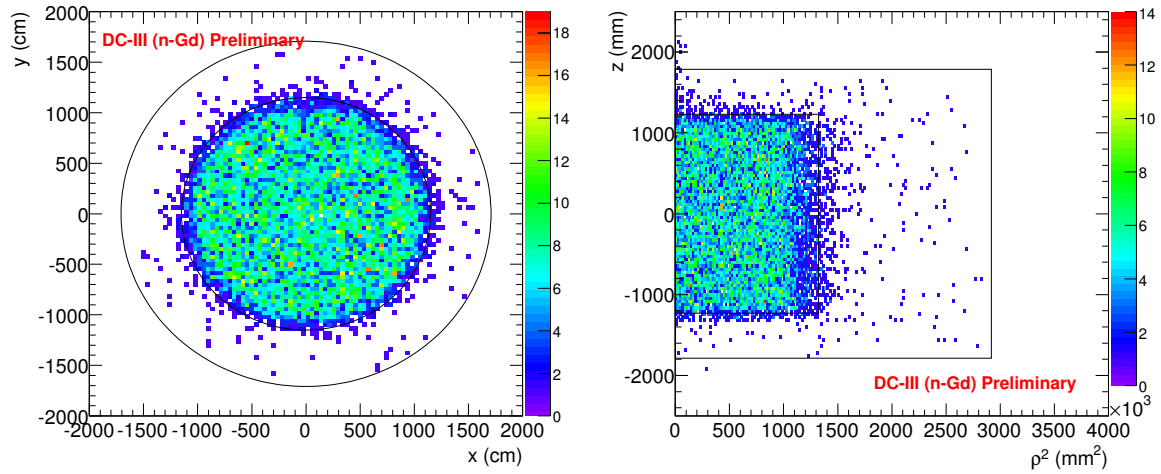

Figure 6.24: Prompt event vertex distributions of the n-Gd $\bar{\nu}_e$ candidates in the (X,Y) plane (left) and in the (ρ^2,Z) plane (right), with $\rho^2 = X^2 + Y^2$. The black solid lines delimit the target and gamma catcher vessel boundaries.

target and the gamma catcher liquids being both potential targets for the neutron capture with respective H to Gd capture ratios of 14.7:85.3 and 100:0. The selection cuts between n-Gd and n-H are very similar but additional cuts have been introduced for n-H given the large background its energy region is subjected to.

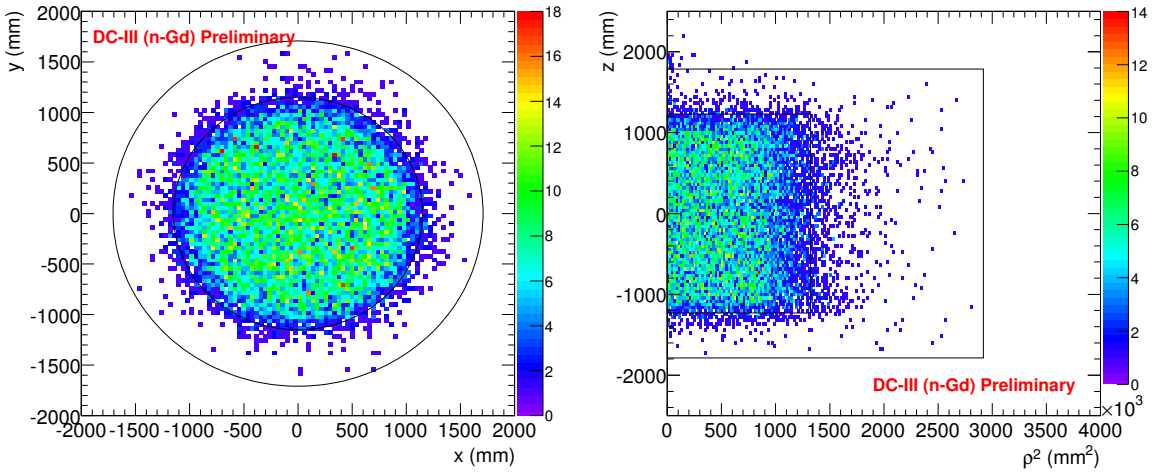

Figure 6.25: Delayed event vertex distributions of the n-Gd $\bar{\nu}_e$ candidates in the (X,Y) plane (left) and in the (ρ^2,Z) plane (right), with $\rho^2 = X^2 + Y^2$.

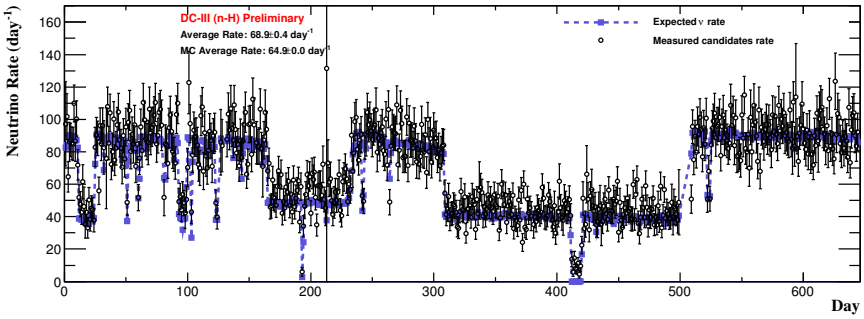

Figure 6.26: Rate of $\bar{\nu}_e$ candidates per day for the n-H analysis. The observed rate is shown in empty black squares and the expected rate, from MC predictions, is displayed in dashed blue lines. The periods are similar to the ones observed in Figure 6.21.

Prompt event The prompt energy selection cut being directly dependent on the neutrino energy, it does not differ significantly from the n-Gd analysis and a prompt event visible energy must be observed within:

- $1.0 < E_{\text{vis}} < 20$ MeV.

The lower prompt energy cut has been set to 1.0 MeV to exclude the signal peaking at 0.5 MeV created by the loss of one annihilation photon in the buffer volume.

The IV cut does not differ significantly as well and the simultaneous energy deposition in the IV leading to the rejecting of the prompt event must meet the following criteria:

- IV PMT multiplicity ≤ 2

- $Q_{IV} > 400$ charge units (∼0.2 MeV)
- ID-IV space coincidence: $\Delta d < 3.7$ m
- ID-IV time coincidence: $\Delta t < 50$ ns

While the OV and ^{9}Li-likelihood cuts are similar to the n-Gd analysis, an additional cut [246] has been introduced to further reduce the fast neutron background. This cut, called MPS cut (Multiple Pulse Shape) and applied to the prompt event, is based on the pulse shape analysis of the events. Recording the waveform of all PMT signals with a 2 ns binning allows the observation of early proton recoils in a small number of PMTs before the final interaction of the fast neutron. To do so, the start time of all pulses are measured (*c.f.* Figure 6.27), corrected for the light flight path, and plotted to form the overall pulse shape (PS) of the event.

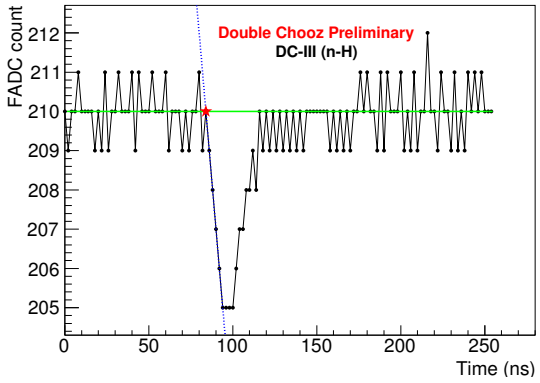

Figure 6.27: Waveform of a single PMT signal. The green line represents the pedestal, the dashed blue line represents the fit to the pulse edge and the red dot, intersection of the two latter lines, corresponds to the pulse start time.

Pulse shapes for a typical IBD event and a fast neutron are shown in Figure 6.28. In the latter, the cluster of start times is shifted from zero and the PS displays pulses arising from early proton recoils. For each PS, the highest peak is fitted with a Gaussian function of mean, m, and width, σ. The initial position of the PS, depicted by the red vertical line in Figure 6.28, is defined as $m - 1.8\sigma$. Tests performed with a γ-emitting ^{60}Co source show that all source events are contained within the first 5 ns of the distribution between the first hit and the initial position of the PS, refered to as "shift".

As explained in Ref.[247], the positron is likely to form ortho-positronium (oPs) in some IBD events. The positron energy deposition followed by the oPs decay (1.022 MeV) yields to the double peak structure in the PS of the event, depicted in Figure 6.28 (right). For low-energy events (E_{vis} <2 MeV), the first peak is smaller than the second one and the event is considered as a fast neutron, its shift being larger than the cut value fixed at 5 ns. These events are recognized as double-peaked oPs (oPs tag) and rejected from the fast neutron selection.

A prompt event satisfying one of the following criteria is considered originated from a fast neutron and subsequently rejected:

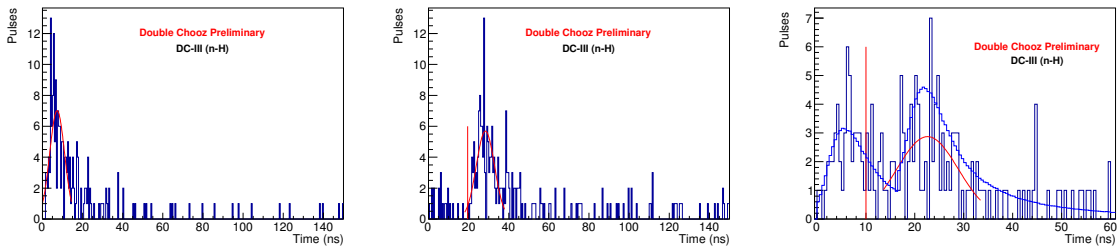

Figure 6.28: Pulse shapes as a function of start time per 2 ns for a typical IBD event (left), a fast neutron (center) and an IBD o-PS event (right). Red curves are the Gaussion functions used to determine the initial PS initial positions, represented by the red vertical lines. Blue curves on the right plot are fits using the oPs algorithm.

- $E_{vis} \leq 3$ MeV and $\Delta PS > 5$ ns
- $1.2 < E_{vis} < 3$ MeV and $\Delta PS > 5$ ns and no oPs tag

with ΔPS the MPS shift, i.e. the time interval between the first hit recorded in the waveform and the time corresponding to 1.8σ left of the highest peak in the hit time distribution.

Delayed event The neutron capture on H leads to the emission of a 2.2 MeV gamma ray. In order for an event to be a considered a delayed event, it has to fulfill:

- $1.3 < E_{vis} < 3$ MeV.

This energy range encloses most of the reconstructed energy depositions upon neutron capture on H, while rejecting some low energy radioactivity background. However, the biggest contributions to accidental background, the ^{40}K and ^{208}Tl gamma lines at 1.461 MeV and 2.615 MeV respectively, are not rejected using this cut.

For the n-H analysis, an IV cut is applied on the delayed event as well to further reduce the fast neutron background. The criteria of this cut are the same as the criteria for the prompt event.

The FV cut helps reducing the stopping muons component in the n-H analysis as well. Nonetheless, the criteria are different and only delayed events satisfying:

- $E_{vis} > 0.2755 \times e^{FV/2.0125}$,

are kept as potential candidates.

Coincidence A coincidence between a prompt and a delayed event is accepted as such if:

- $0.5 < \Delta T < 800$ μs
- $\Delta R < 120$ cm.

The increase of the values with respect to the n-Gd analysis comes from the longer mean neutron path before capture on H, as well as the longer capture time on H ($\sim$200 μs), both directly related to the neutron capture cross section on H.

Multiplicity The multiplicity cut for the n-H analysis has been extended and is now defined as follows:

- No valid trigger allowed in the 800 μs preceding the prompt event
- Only one valid trigger (the delayed event) allowed in the 900 μs following the prompt event

Accidental reduction The higher accidental background of the n-H analysis led to the implementation of more elaborated selection criteria. The ANN (Artificial Neural Network) [248] cut has been developed to reject accidental background using a multivariate analysis based on an artificial neural network, the Multi Layer Perception network with Back Propagation from ROOT's TMVA package. Using the delayed energy E_d and the time and space separation ΔT and ΔR as inputs to generate a single output parameter in the range -1.2 to 1.2, the neural network was trained using a Monte Carlo sample of IBD signal events and a background sample of accidental background events, measured using an off-time window analysis. After this training, a data sample was used to test the neural network. This sample was selected using the following pre-selection cuts: $1.3 < E_d < 3$ MeV, $\Delta R < 150$ cm and $0.5\ \mu s < \Delta T < 1000\ \mu s$. The output of the ANN is not impacted by the choice of pre-selection cuts. The output of the ANN being expressed in arbitrary units, the ANN cut rejects prompt and delayed candidates satisfying the following criteria:

- ANN output < -0.23.

For comparison, before the implementation of the ANN cut, the signal over background ratio of the n-H analysis was of the order of 1.4 while, with the ANN cut, it has reached 11.9 with looser cuts. The results of the ANN for several distributions of signal and accidental background are displayed in Figure 6.29. The difference between data and accidental background is in very good agreement with the Monte Carlo signal.

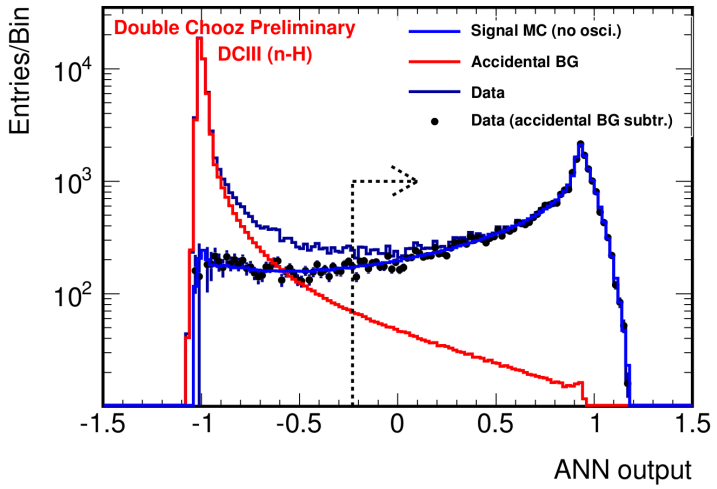

Figure 6.29: Output of the ANN classifier for several distributions: signal MC (light blue), accidental background (red), data (dark blue) and accidental subtracted data (black points). The ANN cut, set at -0.23, yields to a ratio "signal MC/accidental" of ∼15 [248].

Results After applying the cuts previously described, the n-H neutrino dataset encloses 31,835 candidates detected during periods of reactor activity and 63 candidates detected during the simultaneous shutdown of the reactor, for a total of 31,898 neutrino candidates.
The prompt and delayed energy spectra of these neutrino candidates is displayed in Figure 6.30. While, as expected, the prompt energy spectrum exhibits a shape similar to that of the n-Gd analysis, the delayed energy spectrum now shows the energy peak of neutron captures on H at 2.2 MeV.

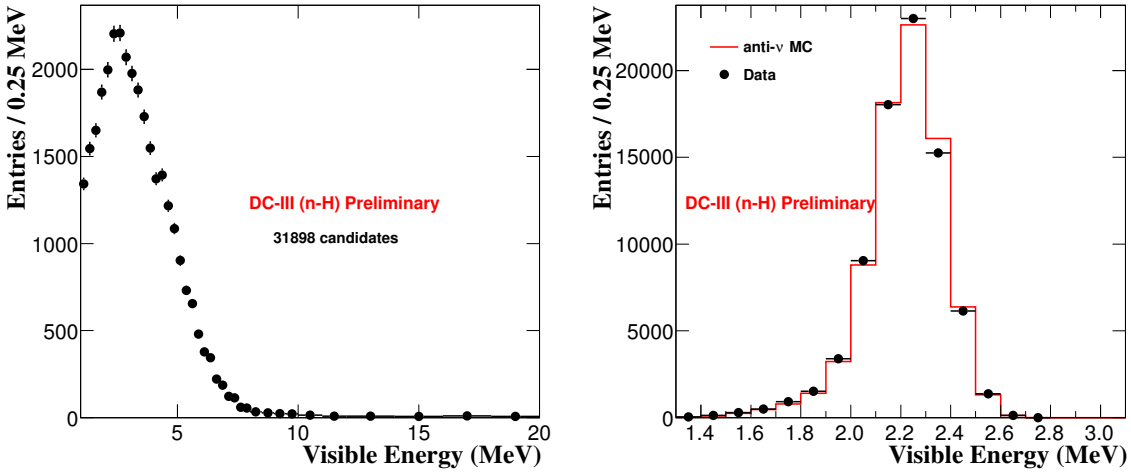

Figure 6.30: Left: Prompt energy spectrum of the n-H candidates. Right: Delayed energy spectrum of the n-H candidates for $\bar{\nu}_e$ candidates (black dots) and MC prediction (red line).

Figures 6.24 and 6.32 show the vertex distributions of the prompt and delayed events, respectively. The n-H selection being based on neutron captures on H, captures occurring in the target and gamma catcher are taken into account. However, given the high capture cross section of Gd, about 85% [184] of the neutron captures in the target occur on Gd. Combining this Gd capture yield with the fact that the gamma catcher is twice as large as the target leads to an expected fraction of n-H captures occurring in the gamma catcher equal to 95%.

Near detector selection and results

In this section, I will present the analysis I performed on the near detector data. The detector has not been calibrated yet and is still in commissioning hence, the results presented hereafter are still very preliminary and should be looked upon with great care.

Data sample The near detector started its official data taking on Tuesday 23$^{\text{rd}}$ December 2014. The processing of its data taken since then has only started in June 2015, after asserting the detector's stability and smooth operation. However, in order to check the quality of the data taking, two 1-hour long runs were processed each day to be later analyzed. The data sample used for the following analysis encloses all the events recorded during these 292 runs, for a livetime roughly corresponding to 12 days. Furthermore, most of the data sample were recorded during a maintenance of the B2 reactor.

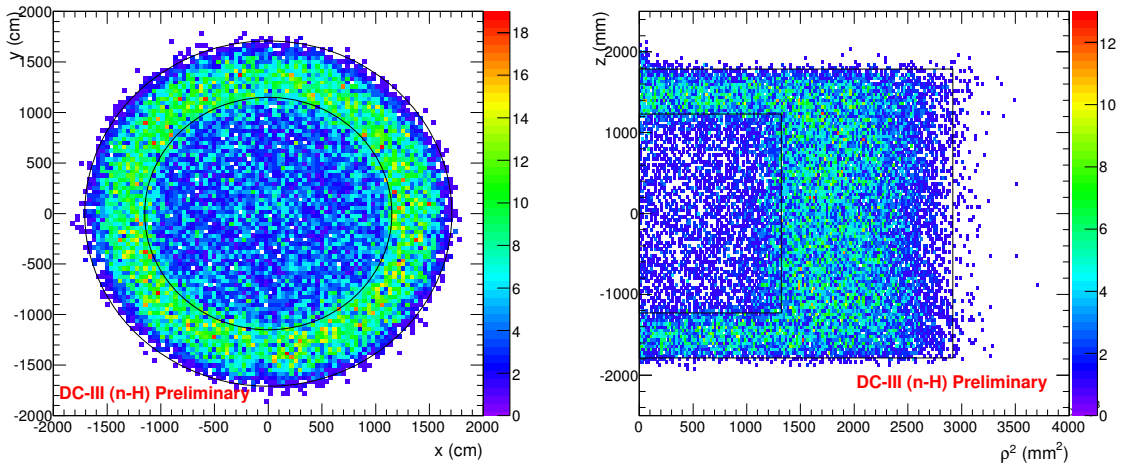

Figure 6.31: Prompt event vertex distributions of the n-H $\bar{\nu}_e$ candidates in the (X,Y) plane (left) and in the (ρ^2,Z) plane (right), with $\rho^2 = X^2 + Y^2$. The black solid lines delimit the target and gamma catcher vessel boundaries.

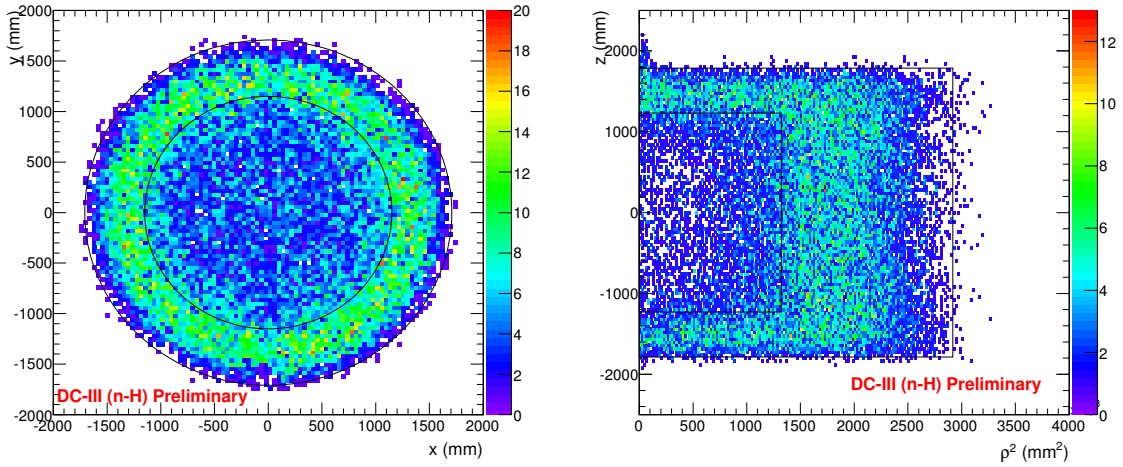

Figure 6.32: Delayed event vertex distributions of the n-H $\bar{\nu}_e$ candidates in the (X,Y) plane (left) and in the (ρ^2,Z) plane (right), with $\rho^2 = X^2 + Y^2$.

Several of the reconstruction and background rejection algorithms have not been applied yet to the near detector's data, including the ANN cut described in Section 6.5.3. This cut allows a powerful rejection of accidental events, main background of the n-H analysis, and its absence leads to a signal over background ratio close to 1. Hence, I decided not to show the results of my data analyses with n-H.

Selection cuts As stated earlier, the near detector has not been calibrated yet. There is no known equivalence between the charge observed by the ID PMTs and the deposited energy it originates from. In order to obtain a rough energy scale for the selection cuts, I isolated a known energy peak and extracted its charge. The most frequent and easy to tag source of monoenergetic gamma rays is the capture of spallation neutrons on hydrogen. By selecting only events occuring within 1000 μs after a muon and applying basic light noise selection cuts, I obtained the energy spectrum displayed in Figure 6.33. The n-H peak at 2.2 MeV is well fitted by a Gaussian function with a mean of 76,000 charge units. The conversion factor expressing visible energy as a function of the observed charge is approximately 34,000 charge units/MeV. This factor has been applied to every visible energy value in the following analysis without accounting for the position in the detector such as explained in Eq. 6.10.

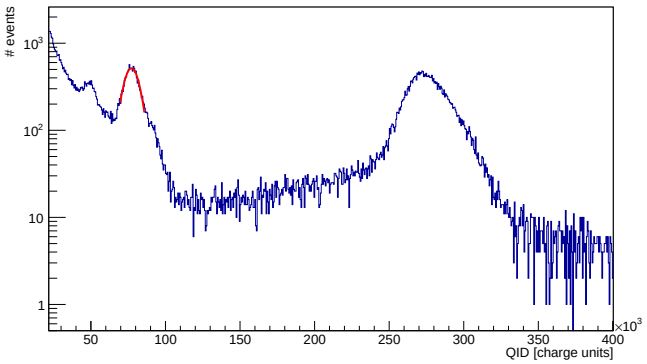

Figure 6.33: Energy spectrum of the spallation neutron capture occuring after muon events expressed in charge units. The hydrogen capture peak is fitted by a Gaussian function (red) and the peak at 275×10^3 charge units represents the captures on Gd at $\sim$8 MeV.

The selection cuts applied to the analysis of the near detector's data are looser than the far detector's cuts. The detector still being in a commissioning phase, several background analyses have not been conducted yet and the definition of light noise or muon events is not finalized yet. While the following cuts allow an efficient neutrino selection, they are not fully optimized and the results that will be presented encompass background events that can and will be rejected in forthcoming analyses.

The bases of the near detector's PMTs have been covered with black vinyl sheets to prevent the emission of light noise. Nonetheless, events having light noise characteristics have been observed in the near detector's data [249], though with a much lower frequency. A cut is thus applied to every valid trigger in order to reject a large majority of this unexpected background. An event satisfying:

- Max(Q)/Total(Q) $>$ 0.12,

is considered a light noise event and consequently rejected.

The selection cut on the prompt and delayed energies is similar to the one applied on the far detector's data:

- $0.5 < E_{\text{vis}}\,(\text{prompt}) < 20$ MeV
- $4 < E_{\text{vis}}\,(\text{delayed}) < 10$ MeV.

The coincidence cut:

- $0.5 < \Delta\text{T} < 150$ μs

and the multiplicity cut:

- No valid trigger allowed in the 200 μs preceding the prompt event
- Only one valid trigger (the delayed event) allowed in the 600 μs following the prompt event

used for the far detector's n-Gd analysis have been applied as well.

Finally, in order to discriminate stopping muons and possible high energy light noise events, a functional value cut is applied such that:

- $E_{\text{vis}} > 0.059 \times e^{FV/1.2}$

Given the average muon rate of 245 Hz observed in the near detector [250], in comparison with the 45 Hz far detector's muon rate, the FV cut is safely applied to both prompt and delayed events.

The preliminary selection cuts I applied are common to several analyses performed with the near detector's data [251, 252] and the following results are in agreement with these analyses.

Results After applying the cuts previously described, the near detector's n-Gd neutrino dataset encloses 1883 candidates during its ∼12 days duration. The average number of $\bar{\nu}_e$ detected each day is thus ∼160 $\bar{\nu}_e.\text{d}^{-1}$, in agreement with the expected rate of ∼300 $\bar{\nu}_e.\text{d}^{-1}$ after selection cuts and considering the shutdown of the B2 reactor.

The prompt and delayed energy spectra of these neutrino candidates is displayed in Figure 6.34. Their time and spatial separation is shown in Figure 6.35. Figure 6.36 shows the vertex distributions of the prompt event in the detector. No comparison with the MC is shown since it has not been generated yet.

A directionality measurement has been performed on the neutrino candidates enclosed in this dataset, as presented in Section 5.3.3.

6.6 Oscillation parameters determination

The oscillation fit performed to determine the value of θ_{13} consists of a comparison between the $\bar{\nu}_e$ candidates and a prediction, including backgrounds, computed in the absence of neutrino disappearance. The observation of a deficit of detected events can be interpreted as a θ_{13}-driven oscillation. The oscillation fit is performed with two complementary methods: the Reactor Rate Modulation (RRM) and the Rate+Shape (R+S).

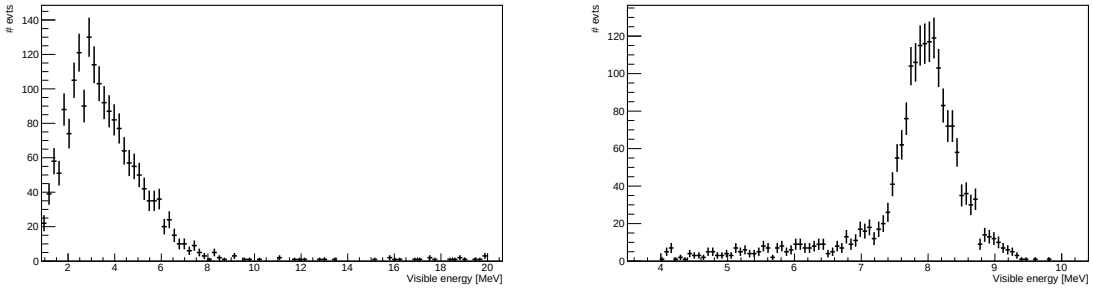

Figure 6.34: Left: Prompt energy spectrum of the ND's n-Gd candidates. Right: Delayed energy spectrum of the ND's n-Gd.

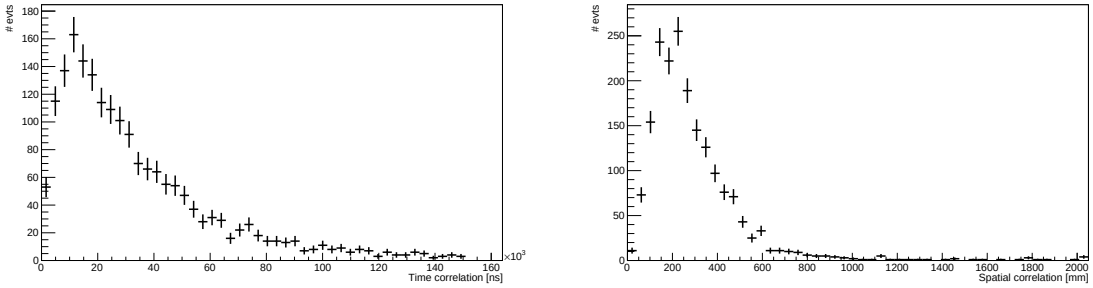

Figure 6.35: Left: Time correlation between the prompt and delayed signals. The time profile is well fitted by an exponential function with a time constant $\tau = 28.5$ μs, in agreement with the average neutron capture time on Gd in the target. Right: Spatial correlation between the prompt and delayed signals.

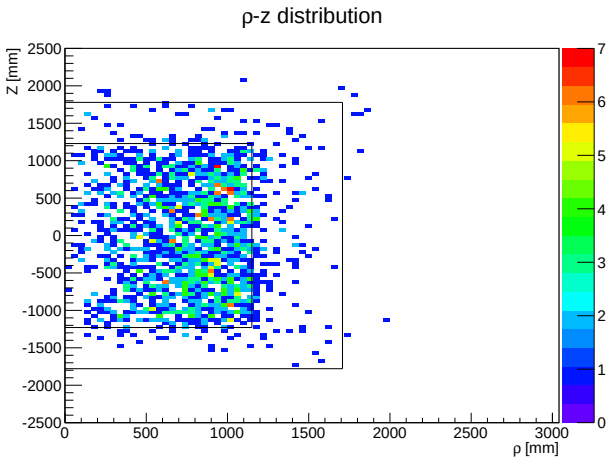

Figure 6.36: Prompt event vertex distribution of the ND's n-Gd $\bar{\nu}_e$ candidates in the (ρ,Z) plane, with $\rho = \sqrt{X^2 + Y^2}$. The black solid lines delimit the target and gamma catcher vessel boundaries.

6.6.1 Reactor Rate Modulation Analysis

The RRM analysis is based on a fit to compare the number of $\bar{\nu}_e$ candidates with the prediction, depending on the number of operating reactors and their respective thermal powers [253]. Given the simplicity of the Double Chooz layout, there are three main well known reactor configurations, as presented in Section 6.1.2. The expected neutrino rate within each of these scenarios can differ due to the baselines and possible reactor operations at low power. Consequently, the data set is divided into seven bins as a function of the reactor power: one bin for the (2-Off) period, three bins for the (1-On,1-Off) periods and three bins for the (2-On) period (*c.f.* Figure 6.37 (left)).

Three sources of systematic uncertainties are taken into account in the RRM analysis: the IBD signal detection efficiency (σ_d=0.6%), the residual $\bar{\nu}_e$ prediction (σ_ν=30%) and the reactor flux prediction (σ_r=1.73% at full power and σ_r=1.91% otherwise). These three uncertainties are then injected in the RRM's χ^2 defined as follows:

$$\begin{aligned}\chi^2 &= \sum_{i=1}^{6} \frac{\left(R_i^{obs} - R_i^{exp} - B\right)^2}{(\sigma_i^{stat})^2} + 2\left[N_{off}^{obs} \times \ln \frac{N_{off}^{obs}}{N_{off}^{exp}} + N_{off}^{exp} - N_{off}^{obs}\right] \\ &+ \frac{(B - B^{exp})^2}{\sigma_{bg}^2} + \frac{\epsilon_d^2}{\sigma_d^2} + \frac{\epsilon_r^2}{\sigma_r^2} + \frac{\epsilon_\nu^2}{\sigma_\nu^2}, \end{aligned} \tag{6.13}$$

where R_i^{obs} and R_i^{exp} are respectively the observed and expected rates per bin, B and B^{exp} are respectively the observed and expected background rate, N_{off}^{obs} and N_{off}^{exp} are respectively the observed and expected number of $\bar{\nu}_e$ candidates during the (2-Off) period. σ_i^{stat} accounts for the statistical uncertainty and the "ϵ/σ" terms constrain the systematic uncertainties to the fit parameter. The expected rate R_i^{exp} carries the θ_{13} information.
Minimizing this χ^2, the best value for $\sin^2 2\theta_{13}$ with the n-Gd data set is found at:

$$\sin^2 2\theta_{13} = 0.090^{+0.034}_{-0.035}, \tag{6.14}$$

with a background rate of $1.56^{+0.18}_{-0.16}$ d^{-1}. The allowed regions on the background rate and $\sin^2 2\theta_{13}$ plane are shown in Figure 6.37 (right).

One can perform a RRM analysis without the background constraint brought by the $\frac{(B-B^{exp})^2}{\sigma_{bg}^2}$ term on Eq. 6.13, hence providing a θ_{13} measurement independent of a background model. Doing so, the best fit value for $\sin^2 2\theta_{13}$ becomes:

$$\sin^2 2\theta_{13} = 0.060 \pm 0.039, \tag{6.15}$$

with a background rate, treated as a free parameter, of $0.93^{+0.43}_{-0.36}$ d^{-1}.

The (2-Off) period was a unique opportunity for Double Chooz to measure and constrain backgrounds as reported in Ref. [242]. To estimate the impact of the data taken during this period, one can perform a RRM analysis without taking it into account thus removing the second term of Eq. 6.13 from the χ^2 minimization as well as the first bin of Figure 6.37 (left). In this case, the best fit of $\sin^2 2\theta_{13}$ worsens and becomes:

$$\sin^2 2\theta_{13} = 0.089 \pm 0.052, \tag{6.16}$$

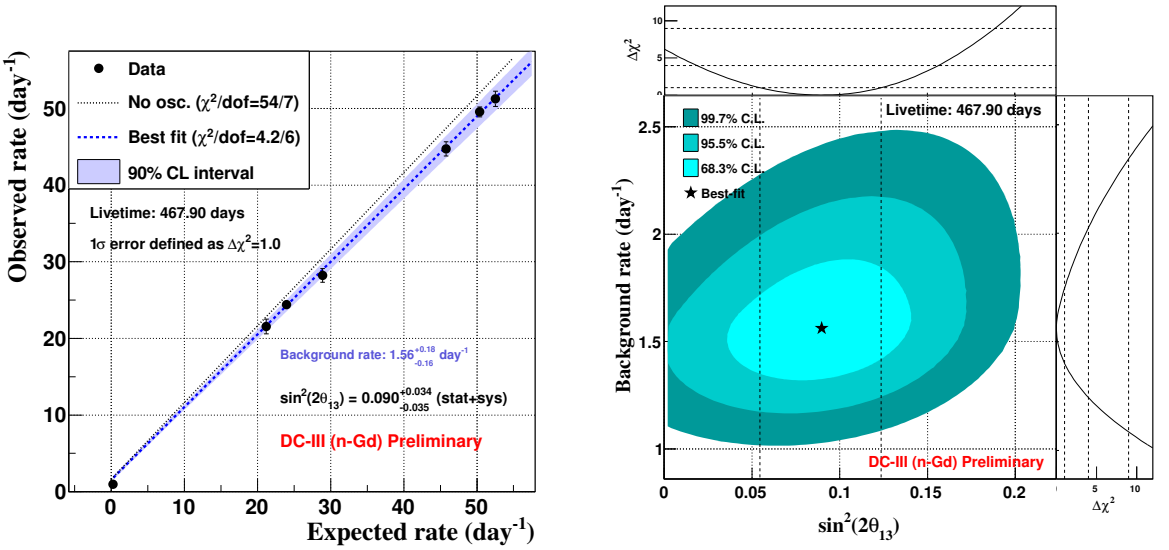

Figure 6.37: Left: Correlation between the observed and expected $\bar{\nu}_e$ rates for different reactor powers. The null hypothesis (no oscillation) is displayed with the black dashed line. The best-fit to the data points (black dots) is displayed with the blue dashed line, its 90% CL uncertainty is shown in blue. Right: Contour plot ($\sin^2 2\theta_{13}$,B) and $\Delta\chi^2$ behavior at 68.3%, 95.5% and 99.7%.

with a background rate, treated as a free parameter, of 1.56 ± 0.86 d^{-1}. While the three RRM fits lead to similar $\sin^2 2\theta_{13}$ values, within error bars, the consideration of the (2-Off) period brings a precious constraint on the backgrounds and on θ_{13}.

The RRM analysis has been applied to the n-H data set as well and yield similar results. The best fit of the background model dependent analysis is $\sin^2 2\theta_{13} = 0.098^{+0.038}_{-0.039}$ with a background rate of 7.29 ± 0.49 d^{-1}. The rate correlation and the contour plot of this analysis are shown in Figure 6.38. Treating the background rate as a free parameter leads to a similar estimation of $\sin^2 2\theta_{13} = 0.123^{+0.042}_{-0.043}$ with a free background rate of 8.28 ± 0.87 d^{-1}.

6.6.2 Rate+Shape Analysis

The R+S analysis is the default analysis performed in the Double Chooz oscillation fit. It is based on a fit to the observed energy spectrum in which both the interaction rate and the spectral shape are used to constrain θ_{13}.
The χ^2 of the R+S fit is defined as such:

$$\begin{aligned}\chi^2 &= \sum_{i=1}^{40}\sum_{j=1}^{40}\left(N_i^{obs}-N_i^{exp}\right)M_{ij}^{-1}\left(N_j^{obs}-N_j^{exp}\right)+\sum_{k=1}^{5}\frac{\epsilon_k^2}{\sigma_k^2}\\ &+ (\epsilon_a\epsilon_b\epsilon_c)\begin{pmatrix}\sigma_a^2 & \rho_{ab}\sigma_a\sigma_b & \rho_{ac}\sigma_a\sigma_c\\ \rho_{ab}\sigma_a\sigma_b & \sigma_b^2 & \rho_{bc}\sigma_b\sigma_c\\ \rho_{ac}\sigma_a\sigma_c & \rho_{bc}\sigma_b\sigma_c & \sigma_c^2\end{pmatrix}^{-1}\begin{pmatrix}\epsilon_a\\ \epsilon_b\\ \epsilon_c\end{pmatrix}\\ &+ 2\left[N_{off}^{obs}\times\ln\frac{N_{off}^{obs}}{N_{off}^{exp}}+N_{off}^{exp}-N_{off}^{obs}\right].\end{aligned} \tag{6.17}$$

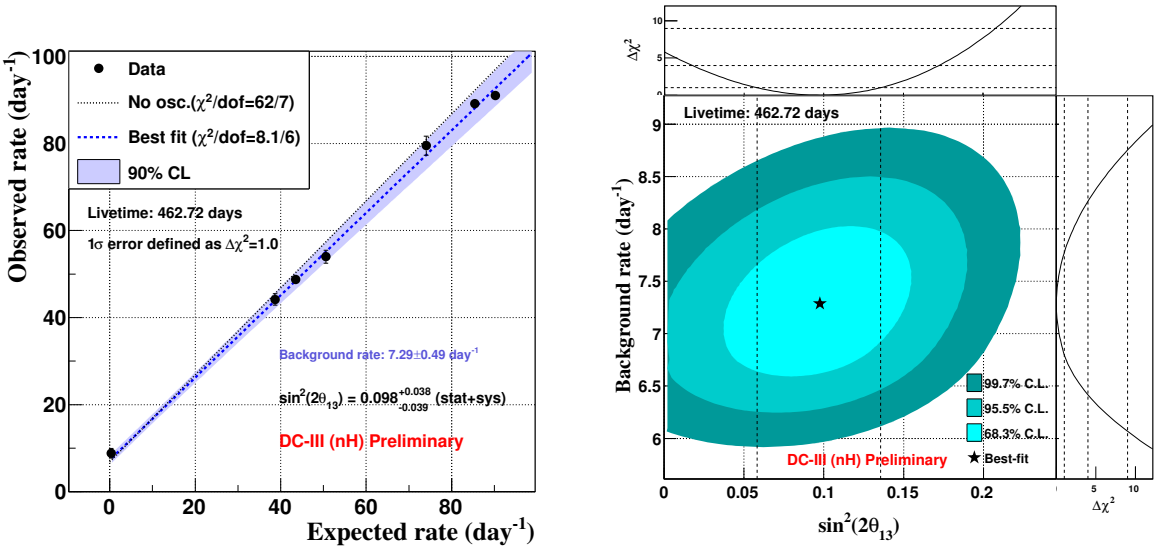

Figure 6.38: Left: Correlation between the observed and expected $\bar{\nu}_e$ rates for different reactor powers. The null hypothesis (no oscillation) is displayed with the black dashed line. The best-fit to the data points (black dots) is displayed with the blue dashed line, its 90% CL uncertainty is shown in blue. Right: Contour plot ($\sin^2 2\theta_{13}$,B) and $\Delta\chi^2$ behavior at 68.3%, 95.5% and 99.7%.

The visible energy spectra are separated in 40 bins for n-Gd and 38 bins for n-H spaced between 0.5 MeV (1.0 MeV for n-H) and 20 MeV. N_i^{obs} and N_i^{exp} are the number of $\bar{\nu}_e$ candidates in the i-th energy bin of the observed and expected spectra, respectively. M_{ij} is a covariance matrix accounting for the statistical and systematic uncertainties in each bin and for the bin-to-bin correlations. It is composed of the following matrices:

$$M_{ij} = M_{ij}^{\text{stat}} + M_{ij}^{\text{flux}} + M_{ij}^{\text{eff}} + M_{ij}^{\text{Li/He(shape)}} + M_{ij}^{\text{acc(stat)}}, \tag{6.18}$$

with M_{ij}^{stat} and $M_{ij}^{\text{acc(stat)}}$ being diagonal matrices accounting for the $\bar{\nu}_e$ and accidental rate uncertainties, M_{ij}^{flux} accounting for the reactor flux uncertainties, M_{ij}^{eff} enclosing the MC normalization uncertainty and $M_{ij}^{\text{Li/He(shape)}}$ representing the uncertainty on the Li/He sprectral shape. The second and third terms of the χ^2 account for the systematic uncertainties of the following parameters: the squared mass difference Δm^2_{13}, the number of residual $\bar{\nu}_e$ in the (2-Off) period, the rates of ^{9}Li+^{8}He, fast-n+stop-μ and accidentals backgrounds and the energy scale. The uncertainty of the energy scale is given by a second-order polynomial: $\delta\left(E_{\text{vis}}\right) = \epsilon_a + \epsilon_b E_{\text{vis}} + \epsilon_c E^2_{\text{vis}}$ with σ_a, σ_b and σ_c the systematic uncertaities on ϵ_a, ϵ_b and ϵ_c. The last term of the χ^2 accounts for the contribution of the (2,Off) period.

After performing a scan of χ^2 over a large region of $\sin^2 2\theta_{13}$, one finds a minimum value $\chi^2/d.o.f. = 52.2/40$ for $\sin^2 2\theta_{13} = 0.090^{+0.032}_{-0.029}$. The prompt energy spectrum with its backgrounds and its best fit are shown on Figure 6.39.

Note that this result can be cross-checked by summing the energy bins of the measured and expected spectra and only comparing the observed and expected rates. This analysis,

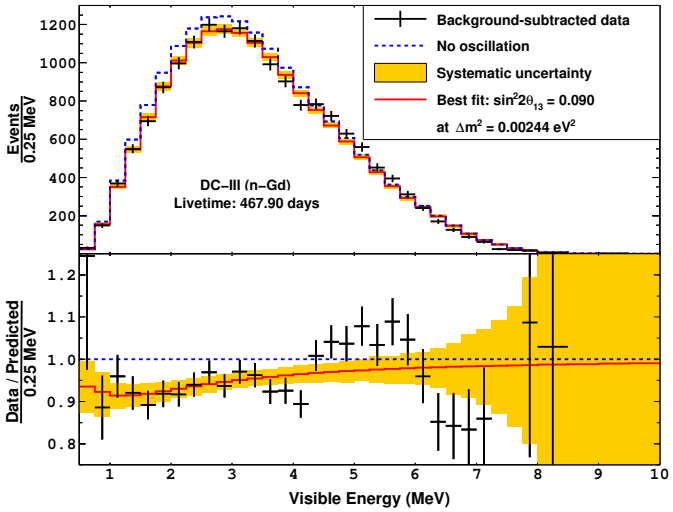

Figure 6.39: Visible energy spectrum (black points) after background subtraction. Its best fit (red) and its systematic uncertainties (yellow) are displayed together with the energy spectrum in case of no-oscillation (blue). The bottom panel represents the ratio between the observed and predicted energy spectra, clearly showing a deficit and an oscillation.

called the rate-only analysis, leads to a θ_{13} result of $\sin^2 2\theta_{13} = 0.090^{+0.036}_{-0.037}$.

Finally, performing a χ^2 minimization using the n-H dataset leads to $\sin^2 2\theta_{13} = 0.124^{+0.030}_{-0.036}$, in agreement with the n-Gd oscillation fit. Figure 6.40 shows the ratio between the observed and the predicted energy spectra for the n-H oscillation fit.

An unexpected spectrum distortion has been found between 4 and 6 MeV (*c.f.* Figures 6.39 and 6.40). A hint for a distorsion was already seen in previous Double Chooz results [26, 241], though not statistically significant, as well as in recent results from the other reactor experiments [77, 254]. A lot of effort has been put into providing an origin for this excess and explanations such as unknown backgrounds, detector effects or additional reactor $\bar{\nu}_e$ components [255] are under investigation. The observation of this distortion effect with the near detector would already show a statistically significant effect after several months of data taking.

6.6.3 Near detector sensitivity

With the incoming release of the near detector's data followed by the first Double Chooz publication with two detectors, i.e. the nominal experiment's configuration, the sensitivity of Double Chooz has been evaluated as a function of the upcoming years of data taking. This sensitivity, computed by a R+S fit with the current systematic uncertainties applied to both detectors, is displayed in Figure 6.41. The effect of the near detector and its reduction of the reactor flux systematic uncertainty is clearly seen on the sensitivity plot. The expected sensitivity, computed here for the n-Gd R+S analysis could be strongly improved by a better understanding of the remaining systematic uncertainties, illustrated by the blue shaded area, as well as by the addition of inputs from the RRM oscillation fit and the n-H data set.

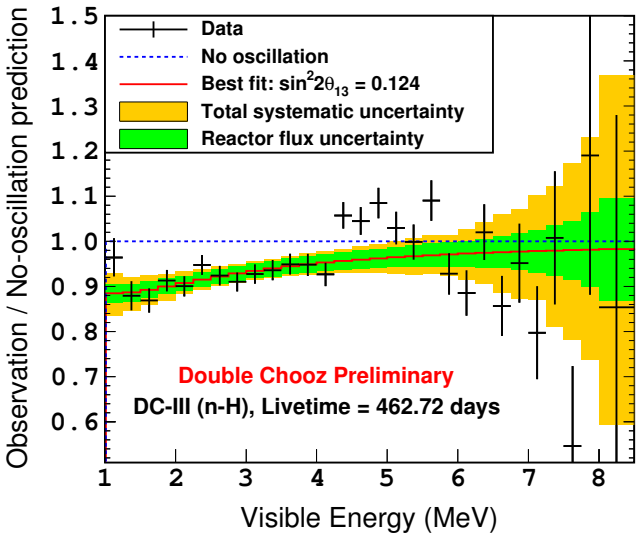

Figure 6.40: Ratio between the background-subtracted data (n-H) in black points, best fitted by the red line spectrum, and the predicted energy spectrum. Likewise the n-Gd analysis, a deficit is clearly showed.

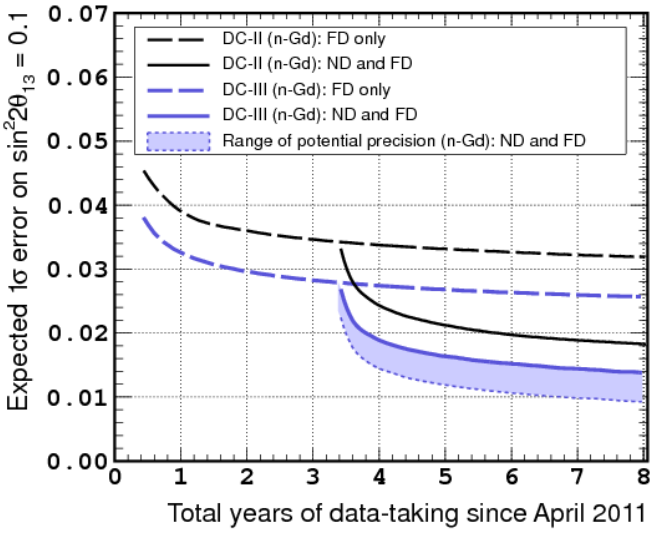

Figure 6.41: Projected sensitivity of Double Chooz with only the far detector (dashed blue line) and with both detectors (solid blue line) for the uncertainties computed in Ref [75] for the n-Gd data set. The dashed and solid black lines are the sensitivities based on the results reported in the previous publication [241]. The shaded blue area represents the sensitivity range reacheable by improving the systematic uncertainties.

Chapter 7

Study of a 4^{th} neutrino state with KamLAND/Borexino

This chapter will be dedicated to the study of a hypothetical 4^{th} oscillation with the CeLAND/CeSOX projects. When I started my internship in May 2012 and my Ph.D. in October 2012, the status of the experiment was to deploy an $\bar{\nu}_e$ generator in the KamLAND detector. However, due to technical and administrative limitations, the $\bar{\nu}_e$ generator is now expected to be deployed next to the Borexino detector. The first project CeLAND became the CeSOX experiment[1]. Since some of the simulations and analyses presented in the following have been conducted in the context of CeLAND and/or CeSOX, the distinction will be made only when necessary.

7.1 The CeSOX/CeLAND project

The idea of testing non-standard neutrino properties using radioactive sources (*c.f.* Section 3.2) in large detectors has been discussed in the late 1990's [256]. At that time, this concept was expected to probe non-standard neutrino couplings [257], neutrino magnetic moments [258] or the neutrino oscillation that is now referred to as the θ_{13} oscillation. Upon the discovery of the "reactor antineutrino anomaly", possibly explained by a fourth neutrino oscillation of electron antineutrino into sterile neutrinos, this concept has been thoroughly studied. In 2011, the "Low Energy Neutrino" group of the "Service de Physique des Particules" at CEA Saclay proposed to apply and improve this concept to test the short baseline neutrino anomalies [131]. This was the beginning of the CeLAND project.

7.1.1 Physics case

As explained in Section 2.2.2, anomalies have been reported in several neutrino oscillation experiments at L/E$\sim$1 m.MeV^{-1}. The diversity of these experiments, from their neutrino sources to their detection techniques, tends to dismiss the existence of a common experimental bias. These anomalous results could however be interpreted as the existence of sterile neutrino states, as an extension to the standard three-neutrino oscillation framework. Global fits of the neutrino disappearances observed in short-baseline neutrino experiments such as Gallex, SAGE and the reactor experiments, favor massive sterile neutrinos separated from

[1]Short distance neutrino Oscillations with BoreXino, or SOX, was first a competitor of CeLAND. The two experiments merged in 2014 and the first phase of SOX with a cerium source became CeSOX.

the active neutrinos with a squared mass difference $|\Delta m^2_{new}| > 0.1$ eV^2.
To definitely test this hypothesis with low energy neutrinos, one must observe a neutrino disappearance as well as an oscillation pattern, within the detector, depending on the energy and distance to the neutrino source. This can be achieved by two means, either by placing a detector close to an intense neutrino source, i.e. a nuclear reactor, or deploying a small-scale neutrino source, i.e. a radioactive source into or close to a large-scale neutrino detector. The latter is the concept of the CeLAND/SOX project.

In order to accumulate a significant-enough number of neutrino interactions over the duration of the experiment, typically a few mean lives of the source's isotope, one has to deploy an intense source in or next to a large detector.
Assuming a CPT invariance in neutrino oscillations, the sterile neutrino hypothesis could be tested equally using neutrinos or antineutrinos. Given the larger cross section of the IBD reaction with respect to the electron scattering reaction, source activities of the order of a few PBq in $\bar{\nu}_e$ are required while activities of the order of tens of PBq are required in ν_e. Although the deployment of $\bar{\nu}_e$ and ν_e sources have been discussed in the community and studied, I will focus on $\bar{\nu}_e$ sources in the following.
Several kiloton-scale detectors such as KamLAND, Borexino or SNO+ are or will be soon, in the case of SNO+, operating and well-suited to perform such a measurement. Even the Daya Bay experiment, though operating much smaller detectors, expressed its interest in deploying a source close to their detector modules [259]. In order to compensate for their lower detector masses, a source activity approaching 20 PBq is required. All these detectors being designed to perform precise low energy neutrino measurements, they possess good energy and vertex reconstruction capabilities in the energy range of radioactivity-emitted neutrinos. Relying on the IBD reaction with neutron captures on H (except for Daya Bay) to detect $\bar{\nu}_e$, they are subjected to a very low background rate.
The combination of such sources and detectors could allow the observation of an oscillation pattern with a L/E range between 0.1 and 10 m.MeV^{-1}.

7.1.2 The KamLAND/Borexino detectors

Although the CeSOX experiment is now planned to be conducted in the Borexino detector, most of my work has been performed in the context of CeLAND, when the experiment was planned to be conducted in KamLAND. Hence, both detectors will be described.

KamLAND

The KAMioka Liquid scintillator Antineutrino Detector (KamLAND), whose construction started in 1999, is located within the Kamioka mine at 2700 m.w.e. under the Ike mountain (Ikenoyama, 36° 25' N, 137° 18' E) in Japan. A sketch of the detector is displayed in Figure 7.1.

The inner part of the KamLAND detector consists of a 13-m-diameter spherical 135-μm thick balloon filled with 1 kton of liquid scintillator (LS). The liquid, composed by volume of 80.2% dodecane and 19.8% pseudocumene (1,2,4-Trimethylbenzene) with the addition of 1.36 ± 0.03 g/L of PPO, has a density of 0.780 g/cm^3 at 11.5°C. To shield it from external radiation, this active volume is surrounded by a 2.5-m thick buffer filled with non-scintillating oil, composed of 57% isoparaffin ($C_{12}H_{26}$) and 43% dodecane. To detect the light emitted

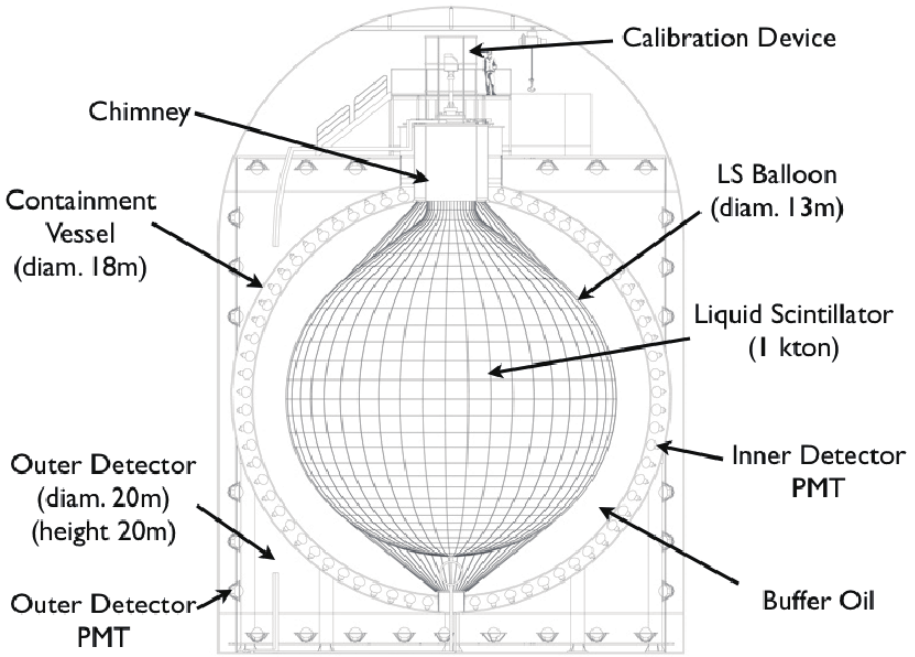

Figure 7.1: Sketch of the KamLAND detector [260].

in the active volume, 1325 17-inch PMTs and 554 20-inch PMTs, the latter reused from the Kamiokande experiment, are mounted on the inner surface of the 18-m-diameter stainless steel vessel enclosing the LS and the buffer. This vessel and its contents are considered the inner detector (ID) of KamLAND. The ID is surrounded by a 3.2-kton water Čerenkov veto instrumented with 225 20-inch PMTs whose purpose is to detect cosmic muons while shielding the ID for external radioactivity.
Most of KamLAND's $\bar{\nu}_e$ analyses are performed considering a 6-m radius fiducial volume in order to reduce the accidental background originating from the balloon. However, given the relatively large interaction rate expected in CeLAND, a fiducial volume of 6.5-m radius could be considered. The energy and vertex resolutions of KamLAND are respectively $6\%/\sqrt{\text{MeV}}$ and 14 cm$/\sqrt{\text{MeV}}$ [261].
Since September 2011, a 3.08-m-diameter balloon filled with 13 tons of xenon has been installed at the center of KamLAND to study the neutrinoless β decay in the context of the KamLAND-Zen experiment [262].

Borexino

The Borexino detector, whose construction started in 1996, is located in the Hall C of the Laboratori Nazionali del Gran Sasso (LNGS)(42° 27' 10" N, 13° 34' 30" E) in Italy. It is shielded from cosmic muons with an overburden of 3800 m.w.e. A sketch of the detector is displayed in Figure 7.2.

The active volume, or target, of Borexino consists of 278 tons of ultra-pure liquid scintillator entirely composed of pseudocumene with a 1.5 g/L PPO doping. The LS is enclosed

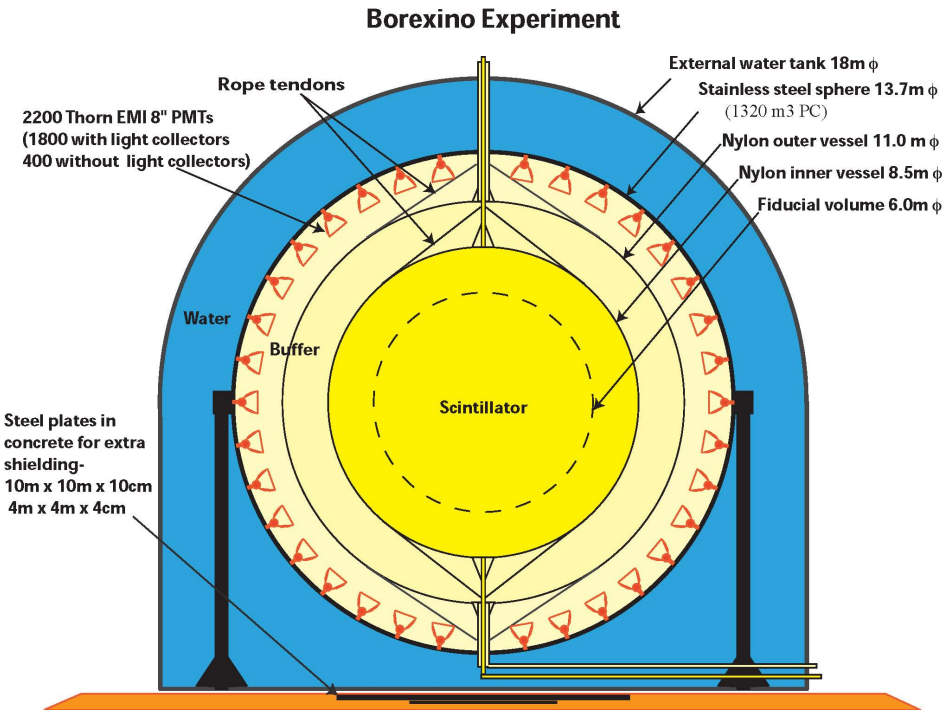

Figure 7.2: Sketch of the Borexino detector.

in a 8.5-m-diameter nylon vessel and shielded from external radiations by a 890 tons buffer. This 2.6-m thick buffer is divided in two parts, with respective thicknesses of 1.25 and 1.35-m each, separated by a second nylon vessel, preventing the diffusion of radon towards the active volume. The buffer liquid is composed of pseudocumene doped with 3-5 g/L of DMP (dimethylphthalate) to quench the scintillation light and make it passive. These three volumes are contained within a 13.7-m-diameter stainless steel spherical vessel on which 2200 8-inch PMTs are mounted, some with light collectors. This vessel and its contents are the so-called inner detector (ID) of Borexino. The ID is surrounded by a 18-m-diameter tank instrumented with 208 8-inch PMTs and filled with 2.1 kt of water acting as a Čerenkov veto for cosmic muons and a shield for external radioactivity.
Note that, by design, radioactive sources can be deployed under Borexino. A 100-cm wide pit has been expressly excavated and prepared under the detector during its construction and covered with steel plates to provide an extra shielding to gamma radiation. As in KamLAND, Borexino's fiducial volume can be increased for the sake of the experiment from a 4-m to a 4.25-m radius sphere. The addition of a fluor, such as PPO, to the inner buffer, proposed and under investigation, would increase the fiducial volume thickness to 5.5 meters thus significantly increasing the number of detected $\bar{\nu}_e$ events. The energy and vertex resolutions of Borexino are respectively $5\%/\sqrt{\text{MeV}}$ and 12 $\text{cm}/\sqrt{\text{MeV}}$ [211, 263].

7.1.3 The ^{144}Ce -^{144}Pr AntiNeutrino Generator

Given the level of precision required to perform a short-baseline oscillation measurement, one has to ensure the quality of the source, or AntiNeutrino Generator (ANG), from its production to its deployment.

Characteristics

As stated in Section 3.2.3, the ^{144}Ce - ^{144}Pr isotopic couple seems the most suitable for an ANG. This source will thus be referred to as CeANG in the following.
With a $\mathcal{Q}_\beta$ of 318.7 keV, the parent isotope ^{144}Ce emits $\bar{\nu}_e$ well below the IBD threshold at 1.806 MeV. In addition, its 284.5 days half-life is long enough to allow the production and transportation of the CeANG without a significant loss of activity. The daughter nucleus ^{144}Pr, with its $\mathcal{Q}_\beta$ of 2997.5 keV, provides $\bar{\nu}_e$ detectable via IBD over an energy range of 1.2 MeV. The ^{144}Pr half-life of 17 minutes is small enough to consider the consecutive decays of ^{144}Ce and ^{144}Pr simultaneous regarding the experiment time of more than a year. Considering the safe assumption of a secular equilibrium between the two isotopes, the CeANG activity can thus be expressed in terms of ^{144}Ce decay rate, although the isotope of interest for IBD is ^{144}Pr. A decay scheme of the ^{144}Ce - ^{144}Pr is displayed in Figure 7.3.

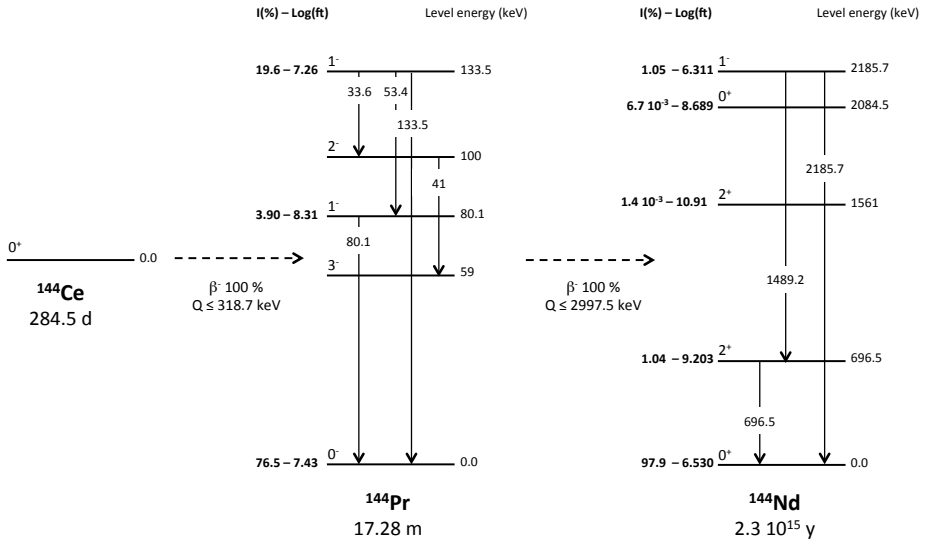

Figure 7.3: Simplified decay scheme of the ^{144}Ce -^{144}Pr couple. β branches with branching ratios greater than 0.001 % are displayed, along with the corresponding Log(ft) values, daughter nucleus level energies and spin parities. The main gamma transitions (intensity greater than 0.1 %) among the excited states of the ^{144}Pr and ^{144}Nd nuclei are also displayed together with their corresponding energies [264].

This decay scheme shows the presence of several gamma lines emitted upon the de-excitation of ^{144}Nd, daughter nucleus of the ^{144}Pr decay. With a branching ratio larger than 0.1%, these three gamma radiations of respectively 696.5, 1489.2 and 2185.7 keV could be problematic for the experiment in terms of backgrounds and radiation protection. A dedicated high density shielding, described in Section 7.1.4, is mandatory to attenuate this gamma background. The energy of the 696.5 keV line is not sufficient to be considered a background in the detector nor to escape a modest shielding (10-cm thick) and, with its

branching ratio of 0.28%, the intensity of the 1489.2 keV line is too low to be considered dangerous. Nonetheless, the most dangerous source of gamma background is the remaining 2185.7 keV line. Its relatively high penetration through matter and its high branching ratio of 0.69% make mandatory the use of a thick shielding (> 10 cm) to ensure a sufficient radiological protection. Furthermore, given its energy, its full absorption peak falls within the prompt and delayed energy ranges, thus making it a potential source of accidental background.

With an activity expected between 3.7 and 5.5 PBq (relative to the ^{144}Ce decay rate), the CeANG will generate up to 5.5 PBq of $\bar{\nu}_e$ as well as 38 TBq of 2185.7 keV gamma rays. The shielding attenuation in terms of flux and dose is developed in Section 7.1.4.

Production

As stated in Section 3.2.3, ^{144}Ce is a fission product of uranium and plutonium produced at relatively large scales in nuclear reactors and present in spent nuclear fuel (SNF). While fuel reprocessing is performed routinely in several countries with a strong nuclear program, only one facility worldwide has been identified as able to extract enough ^{144}Ce to manufacture a PBq scale CeANG: the Federal State Unitary Enterprise Mayak Production Association, hereafter referred to as "Mayak".
Mayak is a spent fuel reprocessing facility located in the Ural region of Russia. Upon its arrival at the facility, the SNF is reprocessed with the PUREX process [265] which extracts uranium and plutonium and whose steps are depicted in Figure 7.4. The unique feature of Mayak is to perform a second phase of the processing, shown in Figure 7.5 that extracts the rare-earth elements and possibly separate them from the rest of the spent fuel. The last stage of the process is the manufacturing of the cerium source, as displayed in Figure 7.6.

The spent fuel received at Mayak mostly from Russian reactors, is removed from the assemblies and dissolved in nitric acid. After a first treatment to remove the graphite and silicon impurities, this solution undergo the actual PUREX process which extracts its U, Pu and Np contents. The remaining raffinate is concentrated by evaporation. While most of this high-level waste (HLW) is vitrified and stored in dedicated long-term waste disposal facilities, some can be dissolved in water and pumped to another facility, the radioisotope plant, for further radioisotope separation upon customer requests.

Depending on the needs of the customers Mayak is conducting business with, different elements can be extracted from the raffinate. After the extraction of ^{137}Cs by sorption and ^{90}Sr by precipitation, the remaining concentrate of rare-earth and transplutonic elements (REE and TPE) is diluted in nitric acid and poured in a 500-meter long pipeline toward the chromatographic facility. The separation of the elements is then performed by displacement chromatographic separation using a series of columns, the first one being a sorption column and the others separation columns. The latter are filled with a resin containing retaining ions such as H^+ or Ni_2^+. Its purpose is to separate the REE and TPE in bands when washed with a NH_4^+ solution. The separation power of this technique is shown in Figure 7.7. While the separation and extraction of ^{147}Pm is usually the last step of the process, a dedicated cerium extraction will be performed for our needs.

The extraction of cerium leads to inevitable contamination from other REE and actinides

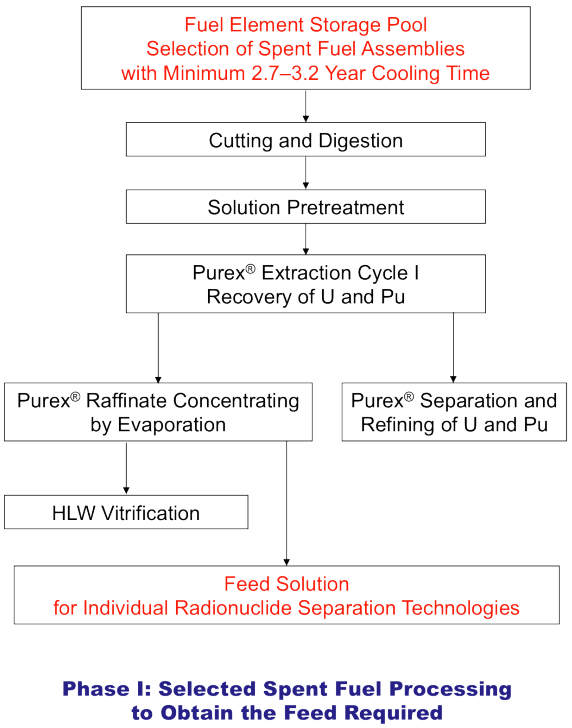

Figure 7.4: First stage of the CeANG preparation: the PUREX process.

elements. The contamination of REEs such as ^{90}Sr, β and γ emitters, is strongly reduced by the chromatographic separation and provide a negligible contribution ($< 0.1\%$) to the source activity and $\bar{\nu}_e$ emission. Actinides, produced through the successive neutron captures and β decays from ^{238}U , are α, β and γ emitters whose contribution can be considered negligible as well. However, these neutron-rich nuclei are likely to undergo spontaneous fission (SF) thus producing several gamma rays and neutrons. The latter can easily scatter out of the source and its high-Z shielding, and thus constitute a potential source of accidental and correlated background as described and studied in Section 7.2.3.

The cerium extracted from the separation column is diluted in a solution. It is precipitated and then calcined into a powder of cerium oxide CeO_2. The powder in then sintered into several pellets with densities of 4-6 g/cm^3 and inserted into a capsule. The whole operation has to be conducted in hot cells, given the amount of radiation emitted by the source. This capsule filled with cerium oxide is the final product that will be delivered by Mayak.

Between 5 and 10 tons of SNF will be processed in order to produce the CeANG. The use of fresh fuel, whose last irradiation dates back to about a year and a half instead of the usual three years, is preferable since it maximizes the ^{144}Ce /Ce ratio of radioactive over stable cerium (the ^{144}Ce activity). From this SNF batch, only about 5 kg of cerium oxide will be extracted by the chromatographic separation and enclosed in the capsule. Given its specific activity of 118 TBq/g [266] and its concentration among stable cerium isotopes between 0.1 and 1%, only about 25 g of ^{144}Ce will be providing the 3.7 PBq activity of the final CeANG.

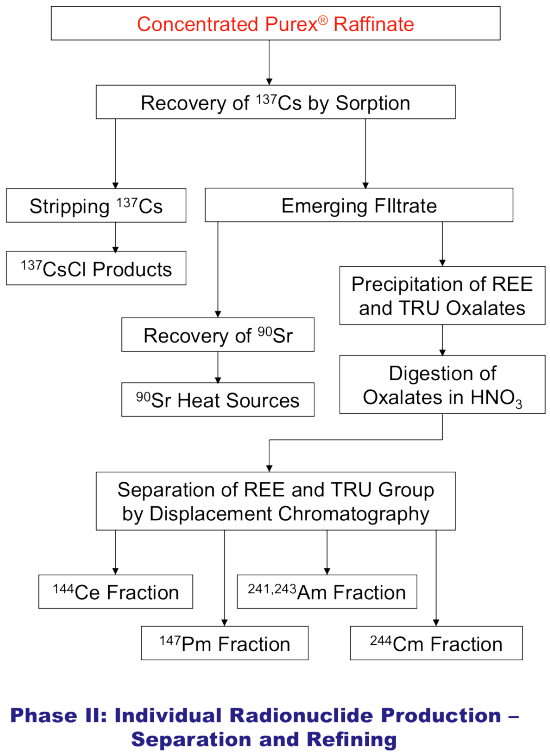

Figure 7.5: Second stage of the CEANG realization: the individual isotopic separation process.

Activity

Related to the number of expected events by a simple exponential decay law, the source activity drives the statistical precision of the experiment. While maximizing this activity, within technical limits, is an important task, the key for reaching the ultimate level of sensitivity required for the experiment is the precise measurement of the source activity. A systematic uncertainty of 1% on the source activity, the goal of the collaborators, would improve the sensitivity over the complete $\sin^2 2\theta_{\text{new}}$-$\Delta m^2_{\text{new}}$ parameter space and especially at $\Delta m^2_{\text{new}} > 0.5$ eV^2. The impact of this normalization uncertainty on the experiment's sensitivity is presented in Section 7.3.

While direct activity measurements via β or γ spectroscopy could be performed for small scale radioactive sources, they are not considered applicable techniques with the CeANG. Although the shielding prevents any real-time γ spectroscopy due to the uncertainty associated to its attenuation, its removal is out of the question for radioprotection and safety considerations. Performing such measurements on samples extracted from the source material during its production is possible, however there is no guarantee that the pellets are identical nor that they all come from the same composition of spent fuel. Decreasing the activity uncertainty to 1% with this method seems hardly achievable. Mass spectroscopy would provide an accurate measurement of the ^{144}Ce concentration in the samples, however the extrapolation of the results is limited by the heterogeneity of the source as well.

The measurement technique proposed and approved for the experiment is the calorimetry.

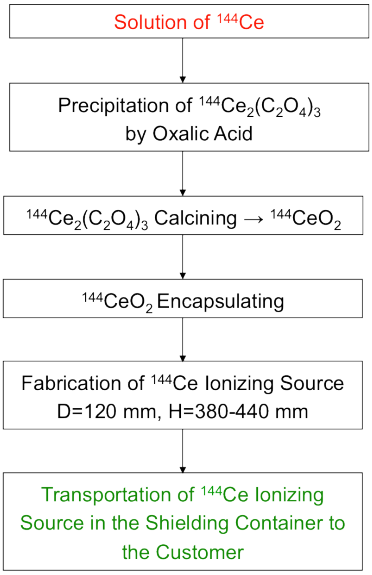

Figure 7.6: Last stage of the CeANG manufacturing: cerium extraction and delivery procedures.

Easier to calibrate and master than spectroscopy, it consists of measuring the amount of heat released by the source to extrapolate the activity knowing the average heat released per decay. From the nuclear databases [121], the average decay heat per decay, more simply expressed in W/PBq as the power-to-activity conversion constant, is equal to 216.0 ± 1.2 W/PBq. This amount of heat mainly comes from the energy deposited by the ^{144}Ce and ^{144}Pr electrons, with a small component of gamma rays. Note that ^{144}Nd originating from ^{144}Pr decay, decays into stable ^{140}Ce via α decay. However, the half-life of this decay being of the order of 2.3×10^{15} years, the heat it released is not taken into account. As presented in the next section, more recent modeling of the ^{144}Ce -^{144}Pr energy spectra provided a recalculation of the power-to-activity conversion constant which has now been estimated to 215.6 ± 1.3 W/PBq.
The design of the calorimeter relies on the measurement of the source heat via its transfer to a water volume. By monitoring the massive flow rate and temperature of the water before and after it has circulated at the contact of the source's shielding, one can estimate the amount of heat transfered to the water. The extrapolation leading to the determination of the source heat then relies on previous calibration measurements performed with known heat sources placed in the same configuration within the shielding. A sketch of the calorimeter is displayed in Figure 7.8. The design, construction, tests and operation of the calorimeter are performed at CEA Saclay by physicists and engineers from Irfu and DEN (Direction de l'Energie Nucleaire) [267]. A similar instrument is being built by a joint team from INFN[2] Genova and TUM[3] [268].

Assuming an activity of 5.5 PBq, the heat generated by the source approaches 1200 W,

[2]Istituto Nazionale di Fisica Nucleare (National Institute for Nuclear Physics), the coordinating institution for nuclear, particle and astroparticle physics in Italy.
[3]Technische Universität München, a research university in Munich, Germany.

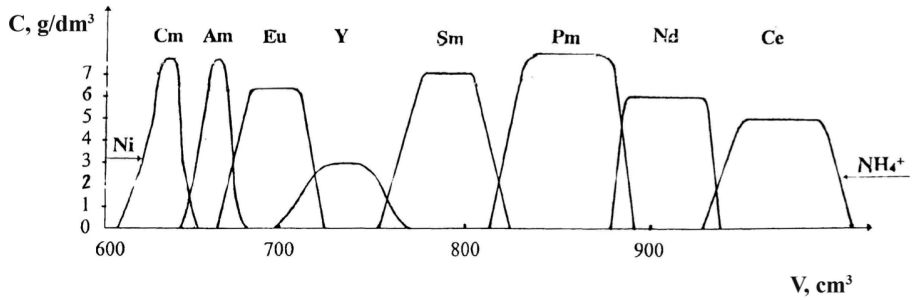

Figure 7.7: Output of the chromatography expressed in concentration as a function of column volume for the elements separated.

enough to increase the source core temperature to 500°C and the shielding up to 100°C, depending on the position of the probe.

Energy spectrum

The accurate knowledge of the ^{144}Ce and ^{144}Pr electron and $\bar{\nu}_e$ spectra has a strong impact on the whole experiment.
The computation of the power-to-activity conversion constant previously described depends on the mean energy released by each β decay, a quantity sensitive to the shape of the electron spectrum. The goal of reaching a 1% precision on the calorimetric measurement requires a precise understanding of the ^{144}Ce and ^{144}Pr electron spectra. In addition, the ^{144}Pr $\bar{\nu}_e$ spectral shape above the IBD threshold has an influence on the expected number of events, key input for the oscillation fit and the determination of the oscillation parameters.

The β and $\bar{\nu}_e$ spectra of ^{144}Ce and ^{144}Pr are combinations of several β branches. The energy conservation principle dictates that $\mathcal{Q}_\beta = E_\beta + E_{\bar{\nu}_e}$ with E_β and $E_{\bar{\nu}_e}$ the kinetic energy of the electron and the $\bar{\nu}_e$, respectively. Its application allows the computation of the $\bar{\nu}_e$ spectrum from the β spectrum, as shown in Figure 7.9. This calculation has been performed using Fermi's theory of β decay [125] corrected for several effects such as the finite size and mass of the nucleus [269], nuclear recoil [269], radiative corrections [270], screening effect [271] and weak magnetism [95]. This work have been conducted by Mathieu Durero at Saclay and detailed descriptions of these effects and the computation method can be found in Ref. [160].

Although all β branches of ^{144}Ce and ^{144}Pr must be considered to compute the power-to-activity conversion factor, only two transitions, both belonging to ^{144}Pr and accounting for 98.94% of its decays, show $\mathcal{Q}_\beta$ larger than the IBD threshold. The product of the $\bar{\nu}_e$ spectra of these branches and the IBD cross section, as well as the prompt energy spectrum it leads to, is shown in Figure 7.10.

The precise measurement of the ^{144}Ce -^{144}Pr β spectrum, combined with its modeling described above, is thus mandatory to reduce the spectral shape uncertainty. In the context of CeSOX, two teams are currently performing this measurement, one based in TUM and the other in Saclay. However, given the tight bonds between the two institutes and the expertise

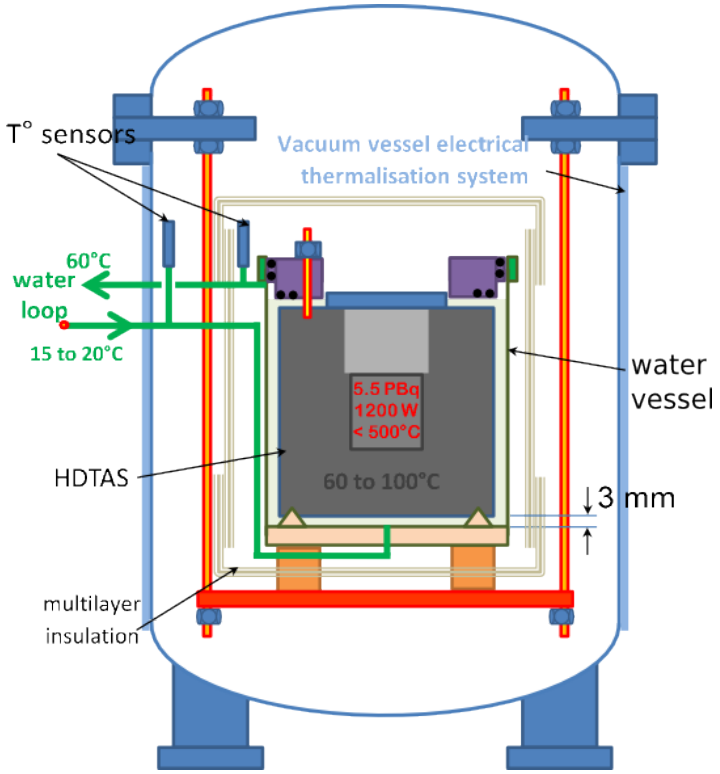

Figure 7.8: Simplified sketch of the calorimeter being built at Saclay. The shielding enclosing the source is placed in the vacuum-sealed water vessel. The heat transfered to the water raises its temperature from 20°C to 60°C in one loop.

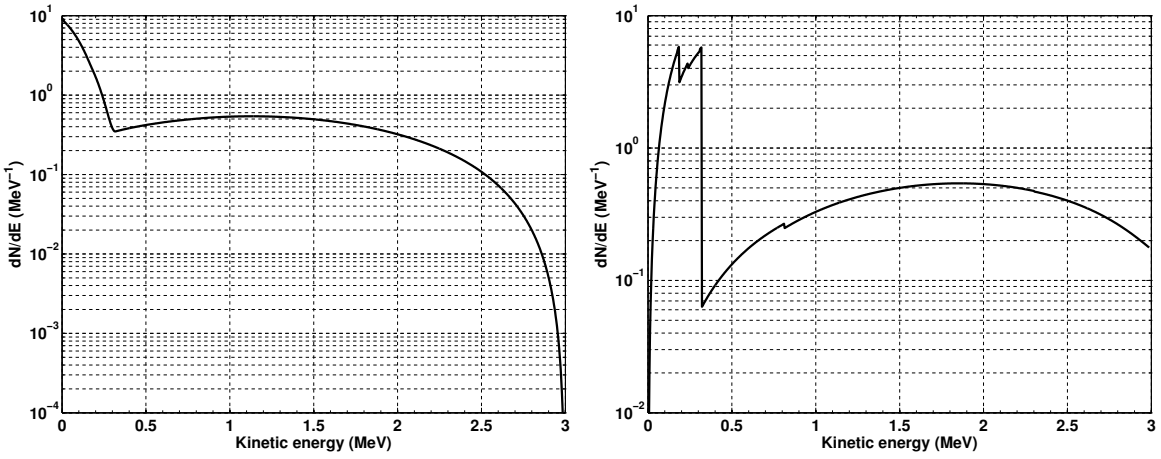

Figure 7.9: Left: Total electron (left) and $\bar{\nu}_e$ (right) energy spectrum emitted by the ^{144}Ce -^{144}Pr pair at equilibrium (equal contributions) [264]. Only β transitions of ^{144}Pr with branching ratios larger than 0.01% are considered. The apparent discontinuities in the neutrino spectrum are direct consequences of the energy conservation principle.

of CEA in terms of radioactive isotope's production and handling, both measurements are performed at Saclay using source samples provided by Mayak and calibration sources pro-

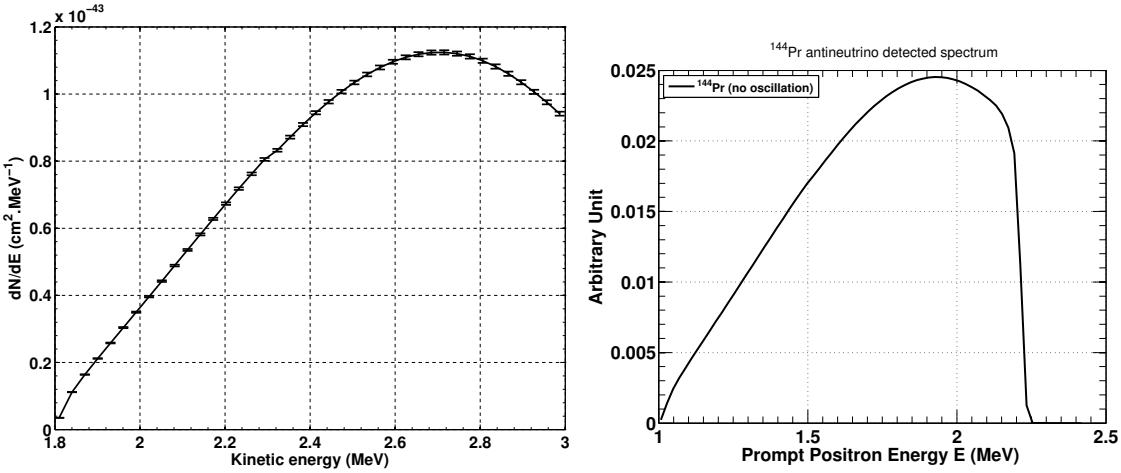

Figure 7.10: Left: Neutrino energy spectrum of ^{144}Pr multiplied by the IBD cross section. Right: Prompt energy spectrum of ^{144}Pr without oscillation.

vided by the LNHB[4].

7.1.4 Transportation and deployment

Shielding

The cylindrical capsule enclosing the cerium oxide pellets is the first shielding of the source. This 4 mm thick double stainless steel sealed container has been designed to hold the source in a leak-proof and heat resistant container. However, in order to reduce the amount of gamma radiation generated in the source, one has to enclose this capsule in an additional high-Z shielding.
With a theoretical density of 19.3 g.cm^{-3}, tungsten (element W) has been considered the most suitable material to manufacture this shielding. Since pure tungsten is fragile and hard to machine, the shielding will be made of an alloy composed of about 97% of tungsten, the remaining elements being iron and nickel. This alloy has a density of 18.0 g.cm^{-3}. For comparison, the density of lead, widely used in radiation shielding, is only 11.34 g.cm^{-3}. To choose a manufacturer and start its assembly, a call for tenders has been conducted and won by the Xiamen Tungsten company [272], whose mining and production sites are located in China.

The dimensions of the shielding have been thoroughly chosen to comply with regulations on radiation protection.
The shielding thickness is dependent on the radiation attenuation it brings. To estimate the thickness needed to ensure a radiological protection within IAEA regulations, one has to compute the dose received by a worker during the manipulation of the CeANG. The absorbed

[4]The "Laboratoire National Henri Becquerel" (LNHB), located at CEA Saclay, a member of the French national metrology office, stores and updates the national metrological records on ionising radiation.

dose, expressed in Gray/s, is given by:

$$\mathrm{D(J/g/s)} = \mathcal{A}[\mathrm{Bq}] \times \frac{4\pi}{d[\mathrm{cm}]^2} \frac{\mu_{en}}{\rho}[\mathrm{g/cm^2}] \times E[\mathrm{J}], \tag{7.1}$$

with $\mathcal{A}$ the source activity, d the distance to the source, $\frac{\mu_{en}}{\rho}$ the mass attenuation coefficient of the shielding material and E the energy of the radiation. Considering $\frac{\mu_{en}}{\rho} \simeq 25$ g/cm^2 for γ energies between 1 and 3 MeV and a weighting factor w=1, one can express the more convenient equivalent dose (in Sv) as:

$$\mathrm{D(mSv/h)} = 4.24 \times \mathcal{A}[\mathrm{Ci}] \times \mathrm{E[MeV]/d[m]^2}. \tag{7.2}$$

The activity in this equation is considered at the shielding's surface, i.e. it represents the source initial activity corrected with the shielding attenuation.
The mass attenuation coefficient of each material composing the shielding has been extracted from nuclear databases [121] in order to compute the attenuation length of the tungsten alloy. For a gamma ray energy of 2.185 MeV, the attenuation length in the shielding is equal to 1.238 cm.
Considering a 3.7 PBq source enclosed in a 16-cm thick shielding, the absorbed dose received at 1 m is equal to 20 μSv/h. For comparison, the annual dose limit fixed by IAEA for personnel authorized to work in radioactive environment is 20 mSv/y[5]. A 16-cm thick shielding could thus be considered suited to enclose a 3.7 PBq ^{144}Ce -^{144}Pr source, considering a realistic working time during the manipulation of the CeANG. However, this dose computation has been performed considering only the 2.185 MeV gamma rays escaping the tungsten while the degraded gamma rays escaping from the shielding also influence the equivalent dose. Dedicated simulations have thus to be performed to take into account the whole energy spectrum of escaping gamma rays.

I performed such simulations using GEANT4 soon after acquiring the KamLAND simulation package. For this simulation, I considered a 5-cm radius sphere of CeO_2 with a density of 5 g.cm^{-3}, enclosed in a 16-cm thick shielding with a density of 18.5 g.cm^{-3}. While the final form of the shielding will be a cylinder of radius and half-height larger than 16 cm, considering a spherical shielding is a conservative assumption. I extracted the energy deposited outside the shielding by 2.185 MeV gamma rays, generated randomly with the cerium source. The energy spectrum of these gammas is displayed in Figure 7.11.

After applying Eq. 7.1 to each bin of the energy spectrum, I found an equivalent dose of 1.24 mSv/h at the shielding's contact. The equivalent dose at 1 m is 37 μSv/h. A similar simulation can be performed for the 1.489 MeV gamma line with a 0.28% branching ratio. For this gamma ray, the equivalent dose at contact is 35 μSv/h. Note that, given the fact they account for the whole energy spectrum, these doses are substantially larger than the previous ones.

To ensure the robustness of these results, critical for the shielding's design, another dose computation has been performed by the radioprotection division (SPR) at CEA. Using the MCNP particle transport simulation code [273], they simulated the propagation of 1.489 and

[5]This dose is the limit for category A workers. Category B workers, such as CeSOX collaborators, are limited to 6 mSv/y.

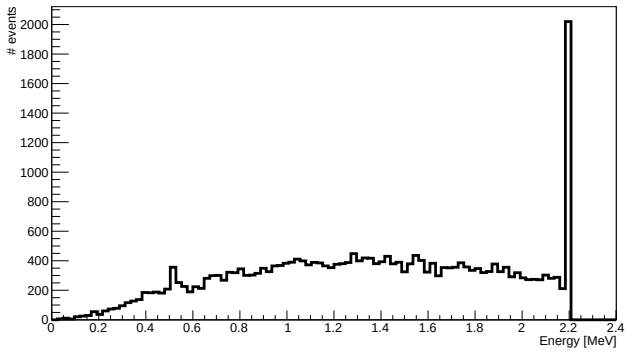

Figure 7.11: Energy deposited by 2.185 MeV gammas escaping a 16 cm tungsten alloy shielding. The peak at 511 keV corresponds to the energy deposited by a positron created by pair production.

2.185 MeV gamma rays in a source and shielding's design identical to the one previously described. For the 1.489 MeV ray, equivalent doses of 52 μSv/h at contact and <20 μSv/h at 1 meter were computed. The equivalent doses corresponding to the 2.185 MeV gamma ray were found equal to 2 mSv/h at contact and 56 μSv/h at 1 meter. Though quite similar to my GEANT4 calculations, the higher values of these doses could be explained by a better estimation of the solid angle between the shielding and the volume receiving the dose (a human body).
The SPR-CEA also studied the influence of the Bremsstrahlung radiation caused by the deceleration of the ^{144}Ce and ^{144}Pr electrons in the source. Given the mean free path of electrons and X-rays in tungsten, the dose corresponding to this radiation is thought to be quite small. With a computed equivalent dose less than 1 μSv/h at contact, the influence of Bremsstrahlung can safely be neglected in comparison with the dose induced by the 2.185 MeV gammas.

In order to conservatively respect the IAEA regulations as well as to match the LNGS requirements, the thickness of the shielding has finally been fixed to 19 cm. A sketch of the capsule inserted into it is displayed in Figure 7.12. The total weight of the shielding is 2.4 tons.

Transportation

Although encapsulated in a shielding, the CeANG is considered a highly radioactive material and its transport from Mayak to the experiment's site must follow strict regulations dictated by the IAEA [274]. These regulations establish the characteristics and type of transport container depending on the activity, mass, heat and type of radioactive material.
The production and deployment sites of the CeANG being in two separate countries, its transportation is required to be performed in a "type B(U)" container, usually employed to transport nuclear fuel worldwide[6]. In 2013, discussions have been initiated with AREVA-TNI, division responsible for radioactive material transportation, and only one container has been identified as suitable for the CeANG transportation. This container, called "TN-MTR", has been designed by AREVA and is used to transport irradiated fuel and radioisotopes. Among

[6]The "U" in B(U) stands for "Universal".

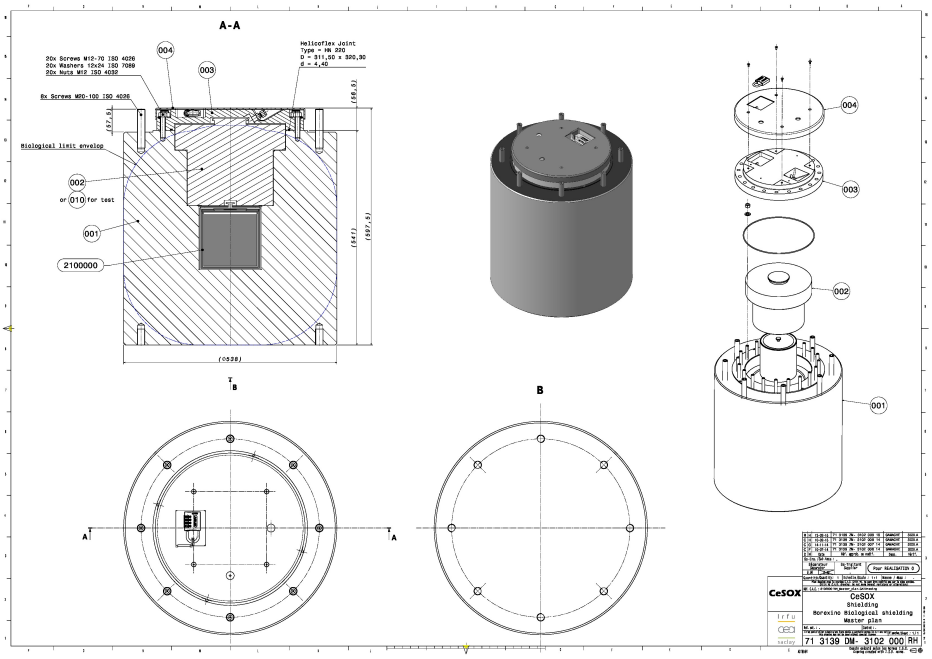

Figure 7.12: Design of the tungsten shielding made by CEA-Irfu.

the four specimens built, the DEN division of CEA owns one cask that will be used for the experiment. Its characteristics are summarized in Table 7.1 and its design is displayed in Figure 7.13.

Type	Manufacturer	Weight	External dimensions	Cavity dimensions	Max. weight
B(U)	AREVA	23,300 kg	H=2008 mm D=2080 mm	H=1080 mm D=960 mm	28,000 kg

Table 7.1: Main characteristics of the TN-MTR container.

Able to hold the source and its shielding while respecting the maximum load of 28 tons, this container is licensed to travel within Europe, Australia and USA. Only a certification to transport ^{144}Ce is required, since the source has been classified as a "Special form of radioactive material". Note that when the deployment of the CeANG was planned in KamLAND, an additional license to travel to Japan would have been necessary. The procurement of this license, if possible, would have affected significantly the experiment's schedule.

Upon performing the calibrations of the calorimeter with a heat generator at Saclay, the shielding will be shipped to Mayak. After the insertion of the capsule containing the ^{144}Ce source, it will be sealed, tested for leaks and finally cleaned to ensure the absence of contamination from its manipulation in the hot cell. The shielding will then be inserted in the TN-MTR container, already received at Mayak for preparatory purposes. The container will travel by train to the Kapitolovo station, close to St. Petersburg and by truck to the St. Petersburg harbor. After this part of the transportation, taken in charge by Mayak, the CeANG will be officially delivered and will become the property of CEA when the cask will

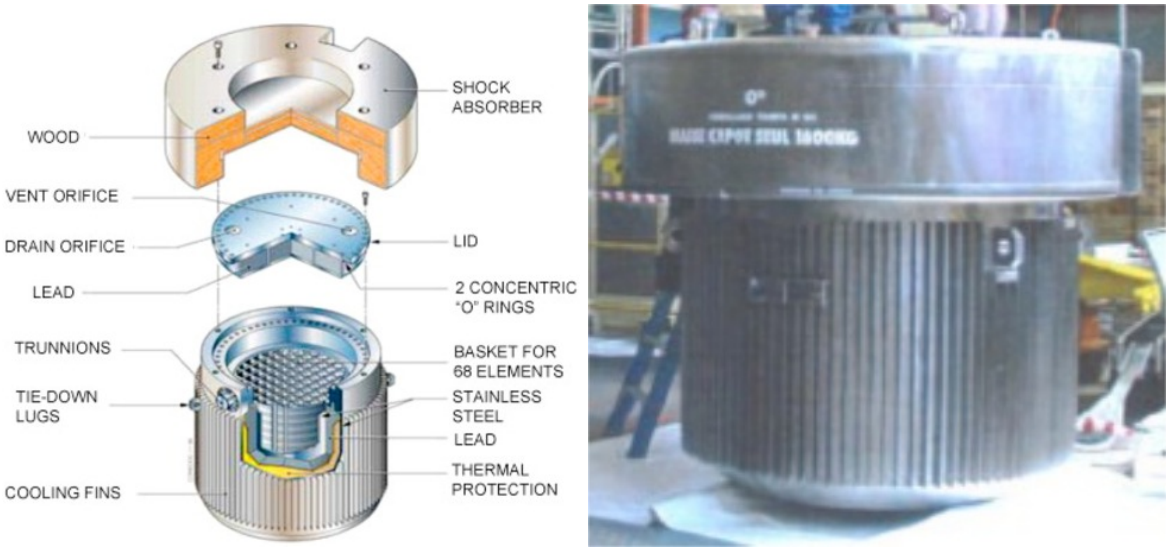

Figure 7.13: Sketch (left) and photo (right) of the TN-MTR transport container.

be loaded onto a dedicated vessel. This vessel will then sail for a journey of about 2 weeks towards the harbor of Le Havre in North-West France. Hereafter, the container will transit by truck until it arrives at the Gran Sasso laboratory (LNGS) in Italy. A possible stop at CEA Saclay is being considered. The total transit time of the CeANG from Mayak to LNGS is about 3 weeks, thus corresponding to an activity loss of 5%.

At the time the deployment was stil planned in Japan, the transit route was significantly longer since the boat could only pass around the cape of Good Hope, thus reaching the Tokyo/Yokohama harbor in about 2 months. A shorter (∼3 weeks) route departing from the Vostochniy harbor in East Siberia, near Vladivostok, was therefore investigated. An alternative route passing north of Russia in the Arctic sea was also studied but then discarded since it required the transportation to be performed in summer only.

Deployment

Upon its arrival in Kamioka/LNGS, the CeANG will be carefully extracted from the transport container in order to be deployed next to the detector. Let us now review the deployment options studied in KamLAND and Borexino.

In the first paper presenting the concept of the experiment [131], a source deployment at the center of a large liquid scintillator detector was considered. The observation of an oscillation pattern directly depending on the detector radius provided the best sensitivity to test the existence of light sterile neutrinos. It was thus chosen as the default deployment scenario of the CeLAND experiment at that time. However, given the high gamma activity, a thicker shielding of 35 cm was being considered. While the physics potential of this deployment was by far the best, it was also confronted to several physical and technical issues.

First of all, the shielding was expected to be in contact with the liquid scintillator. In addition to raising the concern of a possible contamination of the KamLAND's ultra-pure

liquid whether from radioactive material or tungsten oxidation, it implied strong constraints on the amounts of U, Th and Co impurities in the tungsten. Constraining the level of contamination of the tungsten would have been difficult to achieve given the process employed to manufacture the shielding. Some of these technical issues could have been solved by encasing the W-shielding in a 2-cm thick external layer of ultra-pure copper to achieve both radiopurity and material compatibility. Another concern raised by the contact between the shielding and the LS was related to the surface temperature of the tungsten. With pseudocumene's flashing point equal to 54°C, the installation of a dedicated heat evacuation system would have been mandatory.
The second issue was purely technical and concerned the size incompatibility between the shielding and the chimney's opening. Indeed, the neck located at the top of the KamLAND detector and used to access the ID and the inside of the LS is only 55-cm large in diameter, whereas the diameter of the complete shielding was expected to reach 80 cm. Being able to fit the shielding through this opening required the dismantling of the cage holding the balloon tightness system, a perilous operation that could have damaged the thin nylon balloon. To circumvent this issue, two options were discussed. The first was to separate the shielding into several parts. The central part, a 16-cm thick cylinder would have provided the strict minimum radioprotection as described in Section 7.1.4, it was thus referred to as the "biological shielding". This central part, thin enough to fit in the opening, would have been deployed first at the center of the ID. The other parts, providing the additional mandatory shielding, would have been fixed to the shielding after its deployment, as displayed in Figure 7.14 (left). This operation was considered too hazardous and this solution was finally discarded. The second option was to deploy the biological shielding in a pre-installed additional shielding made of a balloon filled with a high density liquid, as shown in Figure 7.14 (right). Such liquids, such as sodium polytungstate[7] (abbreviated to $NaWO_3$), are manufactured in large quantities and commercially available [275]. Non-flammable, non toxic, easy to handle and with a density[8] of 2.8 g.cm^{-3}, a 80-cm radius balloon filled with $NaWO_3$ would have provided an attenuation equivalent to the original design. However, this option faced technical issues as well and the installation of a balloon filled with 14 tons of $NaWO_3$ would have been difficult.
Finally, the deployment of the CeANG inside the LS required the removal of the KamLAND-Zen balloon, not planned before the end of the third phase of the experiment starting in 2016 [276].
Considering the significant challenges such a deployment would have faced, it was finally abandoned as the default configuration. Nonetheless the idea has not been completely discarded and, in the hypothesis of a successful observation of an oscillation pattern, it could be reconsidered as the second phase of the experiment to achieve a better sensitivity.

The default deployment location for the first phase of the CeLAND experiment was therefore located in the water Čerenkov detector, the so-called outer detector (OD). The location of the CeANG during the two phases of the experiment is displayed in Figure 7.15 (left).
Using the 2.5 meters of buffer oil as an additional shielding, the source would have been deployed within its 16-cm thick biological shielding for a total weight of 1.6 tons. In order to prevent any contamination of the detector, the shielding must have been isolated from the OD's water. For that purpose, the shielding was expected to be installed in a stainless

[7]The chemical formula of sodium polytungstate is $Na_6[H_2W_{12}O_{40}]$.
[8]Density is adjusted by dilution and can reach up to 3 g.cm^{-3}.

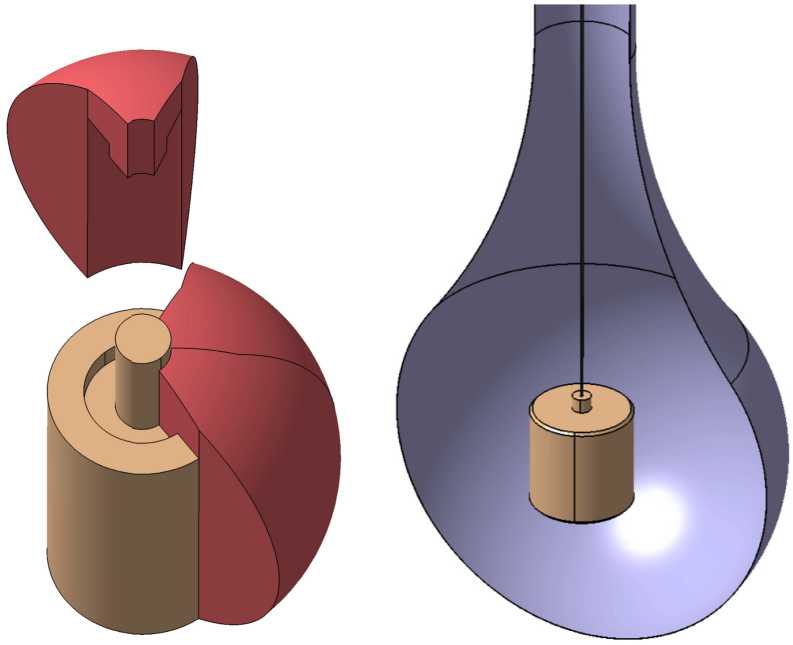

Figure 7.14: Left: Sketch of the CeLAND's biological shielding and its additional parts as first planned for its deployment in the KamLAND's ID. Right: Sketch of the CeLAND's biological shielding in the $NaWO_3$ balloon.

steel vessel, hereafter referred to as a "sock", attached to the floor of the detector's dome and accessible through a hatch. The design of this sock and its location are shown in Figure 7.15 (right). To ensure an efficient thermal regulation and provide an additional layer of shielding material, the sock was expected to be filled with water. Assuming a conservative safety margin on the distance between the sock and the vessel and a moderator thickness of 10 cm, the center of the source was located 9.6 m away from the detector's center. A source activity of 2.7 PBq was thus required to compensate for the loss of interactions due to the geometry.

This scenario consisting of a deployment of the CeANG in the OD for the first phase and the ID for the second phase was selected for the CeLAND experiment. However, due to the logistic issues previously described, the CeLAND project has been abandoned in favor of the CeSOX experiment. Let us now review the deployment of the source in Borexino in the context of CeSOX.

Due to the small diameter of the neck of the Borexino detector, a deployment in the ID at the center of the detector is not technically feasible. However, if an oscillation pattern is observed to a level significant enough but not decisive (for instance, between 3 and 5 sigmas C.L.), this possibility is not to be completely excluded but would necessitate a major detector upgrade. Likewise CeLAND, this deployment in the ID is thus considered a possible second phase of the experiment.

During the first phase of CeSOX, the CeANG will be deployed within the pit expressly built for the deployment of sources underneath Borexino, whose picture is displayed in Figure 7.16 (left). The current design of the shielding, a 19-cm thick tungsten alloy cylinder,

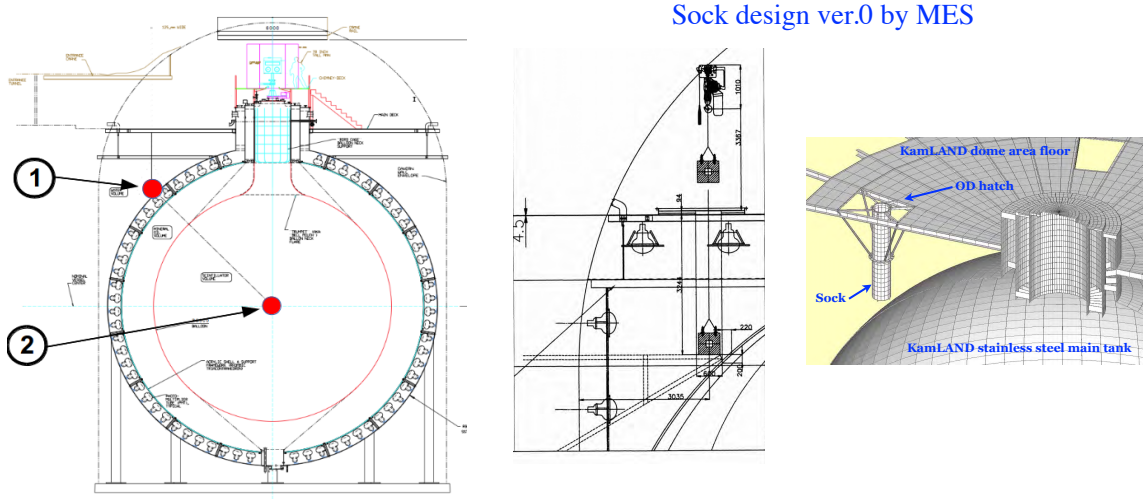

Figure 7.15: Left: Location of the CeANG during the first (OD) and second (ID) phase of CeLAND. Right: Design of the "sock" containing the CeANG in the OD.

will provide a gamma attenuation sufficient enough for radioprotection. The outer detector and the two buffer volumes will grant the additional attenuation required for accidental background reduction, as explained in Section 7.2.3. The source will be located at a distance of 8.3 m from the detector's center.
Upon its arrival at LNGS, the CeANG and its shielding will be extracted from the TN-MTR transport container and moved toward the clean room of Borexino. After an activity measurement performed with both calorimeters, it will be placed on a trolley for the whole duration of the data taking. As displayed in Figure 7.16 (right), the trolley will be placed on a rail system directed toward the pit and the deployment location. Preliminary tests with a 2.2-ton dummy lead shielding have been performed and ensure the feasibility of the operation [277].

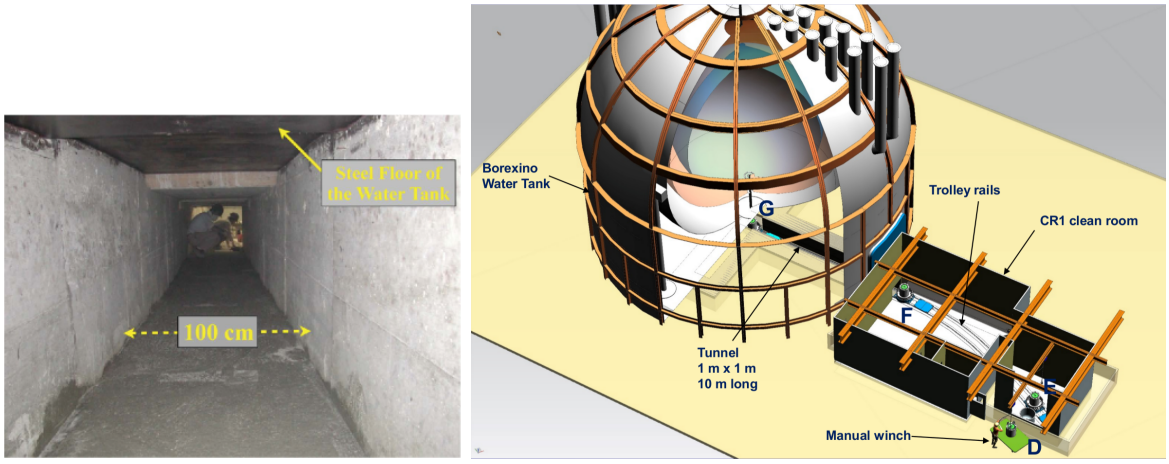

Figure 7.16: Left: Photo of Borexino's source deployment tunnel. Right: Scheme of the deployment operation planned for CeSOX [277].

7.2 Simulations

In order to assess the sensitivity of CeSOX as well as validate the design of the CeANG and its shielding, simulations of both expected signals and backgrounds were required.

7.2.1 Simulation softwares

The KamLAND and Borexino detectors have dedicated simulation softwares, respectively named KLG4sim and G4Bx.

KLG4sim, the simulation package of the KamLAND detector [278], is built off the GEANT4 toolkit [161]. Started in 1999 at Tohoku University by Glenn Horton-Smith and Haruo Ikeda, its development is still ongoing. Precursor to GLG4sim [164], the "Generic-LAND" simulation package, it includes several customized features not available by default in GEANT4. These additional routines, such as the "Torus Stack" geometry class, used to better construct the PMT's' bulged shape, or the "KLScint" physical process, providing a more accurate description of photon propagation in liquid scintillator, are used in the simulation packages of several experiments such as Double Chooz or Nucifer [156].
I started working with KLG4sim at the beginning of my Ph.D. upon a 2-month stay at RCNS in Tohoku University under the supervision of Prs. F. Suekane and K. Inoue. From the latest version of the code, Jonathan Gaffiot and I developed additional features, dedicated to the CeLAND experiment and later used for CeSOX. A non-exhaustive list of these modifications includes:

- The implementation of the CeLAND geometry including the source, shielding, sock and their respective materials;
- The development of a dedicated analysis software, based on Nucifer developments;
- The implementation of a new output dataformat, based on ROOT, containing additional event, particle and tracking information ;
- The development of several event generators: backgrounds and $\bar{\nu}_e$ signals (unoscillated and oscillated);
- The KLG4sim upgrade from GEANT4's 9.4 version to the 9.5 and 9.6 versions.

The complete access to the official source code of KLG4sim being limited to KamLAND collaborators only, we could not perform simulations using *KAT* (KLG4sim Analysis Tool) [279], the simulation's readout and reconstruction software. Likewise DCRoSS and DCCT (*c.f.* Section 6.4.3), KAT intends to simulate the detector's electronics readout chain in order to perform event reconstructions comparable between data and MC. The CeLAND simulations presented in the following are performed with the default KLG4sim energy and vertex reconstruction algorithm. Although it does not take into account fine-tuned effects, it provides a level of precision satisfactory for the preparation and design of the experiments.

Likewise KLG4sim, G4Bx, the simulation package of the Borexino detector [280], is based on GEANT4. Given the strong implication of the Borexino collaboration in CeSOX, its source code is continuously developed and upgraded. Although, as members of the SOX collaboration, an access to the official G4Bx source code has been provided to all members of the

CEA group, I did not perform simulations using G4Bx. This task is one of the thesis topics of Thibaut Houdy, Ph.D. student at CEA/APC.

The accuracy and fidelity of simulation codes based on GEANT4, provided by the complete particle tracking and the consideration of many physical processes, leads to time and resource-consuming simulations. Given the activity of the CeANG and the high attenuation of the overall experimental setup, the simulation of source-induced backgrounds is hardly achievable by *brute force*. To circumvent this issue, the TRIPOLI-4® [281] simulation code was used.
TRIPOLI-4®, developed at CEA, has been designed to study criticality and accurately transport both gammas and neutrons in nuclear reactors. The use of this simulation code, validated by numerous experiments and currently utilized by several French nuclear companies, has been motivated by its state-of-the-art neutron transport and biasing techniques. These techniques, based on variance reduction, allow the transportation of gammas and neutrons trough the highly attenuating layers of shieldings separating the source from the detector active volumes. In particular, TRIPOLI-4® includes the INIPOND module based on the exponential transform method [282]. The biasing is performed through the use of a pre-calculated importance map of the phase space, providing the probability for a particle to reach the detector. By doing so, a weight is associated to each particle traveling in a given path, thus allowing the rejection of particles reaching a given weight value, e.g. if a particle is directed towards the detector's opposite direction. With a large number of particles reaching the detector's active volumes, however with different weights, this method provides statistically significant results with respect to a brute force Monte Carlo such as GEANT4.

7.2.2 Signals

In CeLAND and CeSOX, the expected number of $\bar{\nu}_e$ events $N_{\bar{\nu}_e}$ during a time dt, in a detector volume d^3V and a dE energy bin can be expressed as:

$$\begin{aligned} \frac{d^5 N_{\bar{\nu}_e}}{dt dE d^3V} &= \mathcal{A}_0 e^{-t\lambda_{Ce}} N_p \epsilon \frac{1}{4\pi L^2} && (7.3) \\ &\times \sigma_{IBD}(E)\, \mathcal{S}_{Ce}(E)\, \mathcal{P}_{\bar{\nu}_e \to \bar{\nu}_e}(E, L), && (7.4) \end{aligned}$$

with $\mathcal{A}_0$ the initial activity of the CeANG, λ_{Ce} the ^{144}Ce decay constant, N_p the number of free protons in the detector and ϵ the detection efficiency. The IBD cross section, $\sigma_{IBD}(E)$, the ^{144}Pr $\bar{\nu}_e$ energy spectrum, $\mathcal{S}_{Ce}(E)$ and the oscillation probability, $\mathcal{P}_{\bar{\nu}_e \to \bar{\nu}_e}(E, L)$, expressed in Eq. 1.44, are dependent on the distance L and the energy E. When computing an expected event rate in case of non-oscillation, one can set $\mathcal{P}_{\bar{\nu}_e \to \bar{\nu}_e}(E, L)$ to 1.

In order to reach a level of sensitivity significant enough to detect an oscillation, the total number of events expected must be of the order of $\mathcal{O}(10^4)$ at the end of the whole data taking. Given the characteristics of each detector in terms of mass and size, different source activities are required in each experiment. Table 7.2 summarizes the number of expected events in CeLAND for two fiducial volume configurations.

A data taking time of 24 months leads to the detection of about 20,000 $\bar{\nu}_e$ interactions in KamLAND. In the original design of CeLAND with a 1.85 PBq CeANG at the center of the detector, the expected event rate reached 40,000 $\bar{\nu}_e$ interactions in 12 months. These two

	Exposure (months)			
FV radius	6	12	18	24
6 m	8380	13750	17200	19440
6.5 m	10850	17800	22280	25150

Table 7.2: Expected $\bar{\nu}_e$ interactions in KamLAND (without oscillation) as a function of the exposure time and the fiducial volume (FV) radius. The 2.7 PBq (75 kCi) CeANG is located at 9.6 m in the OD.

values will be chosen as default in the CeLAND simulations presented hereafter.
In these simulations, performed with KLG4sim, two $\bar{\nu}_e$ datasets are generated and compared. The first dataset represents the non-oscillation case while the second one takes into account a $\bar{\nu}_e \rightarrow \bar{\nu}_s$ disappearance. As an illustration, the parameters of this oscillation towards a sterile neutrino state are chosen as: $\sin^2 2\theta_{new} = 0.1$ and $|\Delta m^2_{new}| = 2$ eV^2. This set of oscillation parameters is consistent with the best-fit values predicted by previous short-baseline experiments, as presented in Section 2.3.2.
In order to smoothen the distributions and better observe the effects of the oscillation, each dataset is generated with a total of 10,000,000 $\bar{\nu}_e$ and later normalized, with corresponding statistical errors, to the actual expected interaction rate, i.e. 20,000 and 40,000 $\bar{\nu}_e$ for an CeANG in the OD and at KamLAND's center, respectively.

In the following results, the KamLAND intrinsic backgrounds, presented later in Section 7.2.3, are displayed as an illustration of the high signal over background ratio of the experiment. All background events are generated uniformly over the whole detector volume. The spatial distribution of $\bar{\nu}_e$ interactions in the detector is displayed in Figure 7.17 for an CeANG located 9.6 m away from the detector's center. Only the deficit of events caused by the $\bar{\nu}_e \rightarrow \bar{\nu}_s$ oscillation is visible. The same distribution with respect to the source's center is displayed in Figure 7.18 (right). The visible energy spectrum of $\bar{\nu}_e$ events with and without oscillation is shown in Figure 7.18 (left) along with the KamLAND intrinsic backgrounds for comparison. Note that this spectrum contains the sum of all $\bar{\nu}_e$ events in the detector. Given the energy and distance dependence of the event rate in case of oscillation, the energy spectra observed in different points of the detector is expected to differ significantly. The oscillation is clearly visible on the radial distribution displayed in Figure 7.19. This distribution has been normalized, i.e. each bin represents the number of events in a detector "slice" (with respect to the source's center) divided by the detector's volume enclosed in this slice.

Figure 7.20 (left) shows the energy spectrum observed in the case of an CeANG at KamLAND's center. The radial distribution of $\bar{\nu}_e$ events with respect to the detector's center is displayed in Figure 7.20 (right). This distribution, directly extracted from the simulation output without any kind of normalization such as Figure 7.19, allows the direct observation of the oscillation pattern. Indeed, the expected number of $\bar{\nu}_e$ interactions and the detection volume, dependent on $1/L^2$ and L^2, respectively, compensate each other thus leading to a sinusoidal radial distribution in case of oscillation and a flat distribution otherwise.

Borexino being much smaller than KamLAND, the use of a more intense CeANG is thus mandatory in CeSOX and activities as high as 5.2 PBq are anticipated. The expected

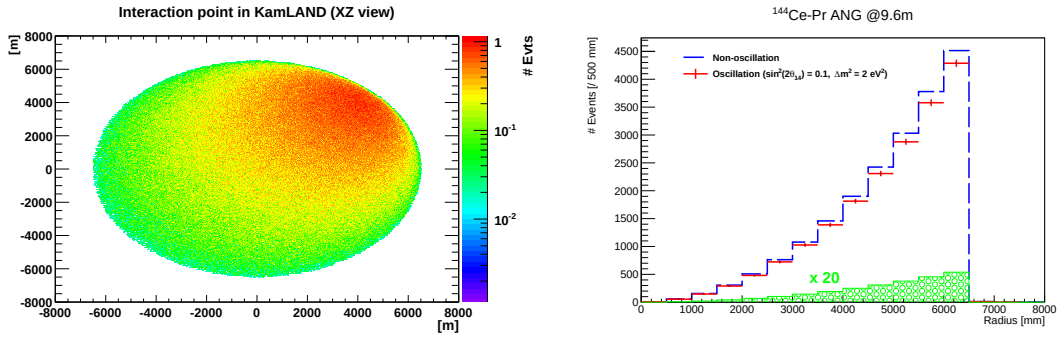

Figure 7.17: Left: Spatial distribution of $\bar{\nu}_e$ interactions in the XZ plane, for the CeANG located in the OD at 9.6 m from the detector's center (at Y=6.8 m and Z=6.8 m). Right: Radial distribution of $\bar{\nu}_e$ interactions (dashed blue without oscillation, red with oscillation) and background events (green). Backgrounds are enhanced by a factor 20 to be visible on the plot. The origin of the radius is taken at the center of the detector.

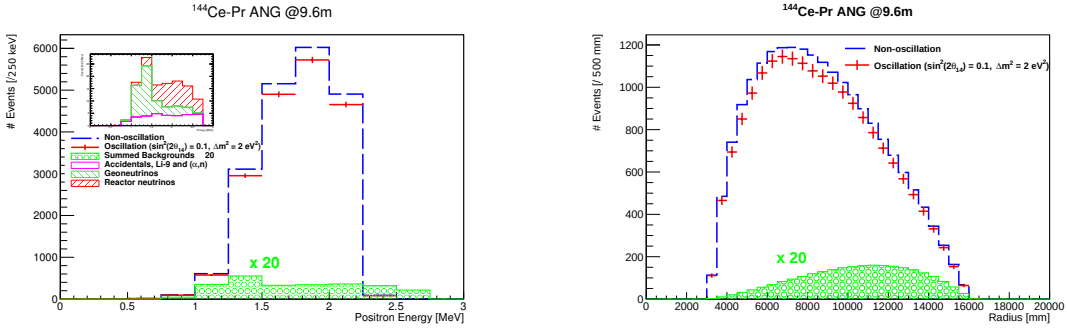

Figure 7.18: Left: Expected energy spectrum of $\bar{\nu}_e$ events (dashed blue without oscillation, red with oscillation) and background events (green). The KamLAND intrinsic background components, enhanced by a factor 20, are stacked in the inset. Right: Radial distribution of the signal and background with the same color codes. The origin of the radius is taken at the center of the source, 9.6 m away from the detector center.

number of IBD events with respect to the source activity and for two detector configuration are displayed in Table 7.3.

	Activity (PBq)		
FV radius	2.7	3.7	5.2
4.25 m	7060	9410	13180
5.5 m	16040	21370	29940

Table 7.3: Expected $\bar{\nu}_e$ interactions in Borexino (without oscillation) as a function of the source activity and the fiducial volume (FV) radius during 18 months of data taking [283]. While the 4.25 FV radius has been chosen as default for the experiment, the possibility of increasing this radius to 5.5 m is being investigated as explained in Section 7.1.2.

Unlike in the context of CeLAND, I did not perform simulations of $\bar{\nu}_e$ events in Borexino. Nonetheless, very similar results are expected. A simulation of the $\bar{\nu}_e$ propagation in Borexino with and without oscillation has been performed by Matthieu Vivier at Saclay. The results,

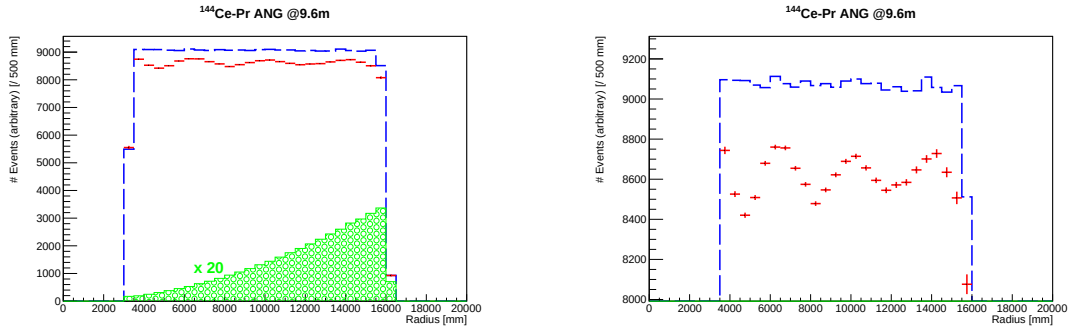

Figure 7.19: Left: Normalized radial distribution of the signal and background in case of non-oscillation (blue) and oscillation (red) and the background (green, enhanced by a factor 20). Each bin content at equidistance to the source is divided by the total scintillator volume at the corresponding distance. Right: Close-up view of the left panel.

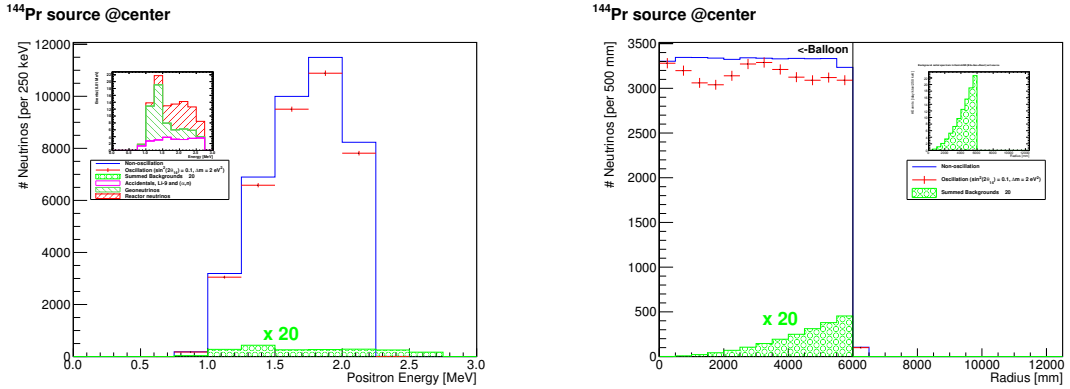

Figure 7.20: Left: Expected energy spectrum of $\bar{\nu}_e$ events (dashed blue without oscillation, red with oscillation) and background events for an 1.85 PBq CeANG at the detector's center. The KamLAND intrinsic background components, enhanced by a factor 20, are stacked in the inset. Right: Radial distribution of the signal and background with the same color codes. A 6-m radius fiducial volume is considered.

displayed in Figure 7.21, are expressed as L/E distributions for various oscillation scenarios. The nominal configuration of CeSOX, with a 3.7 PBq CeANG placed 8.25 m away from Borexino's 4.25-m radius fiducial volume's center during 18 months, is considered in this analysis.

7.2.3 Backgrounds

In order to assess the sensitivity of each experimental setup, one has to determine the backgrounds they are exposed to and estimate their impact on the sensitivity. Two types of backgrounds are presented in the following, intrinsic detector backgrounds and source-induced backgrounds.

Detector backgrounds

The main intrinsic backgrounds of large neutrino detectors are:

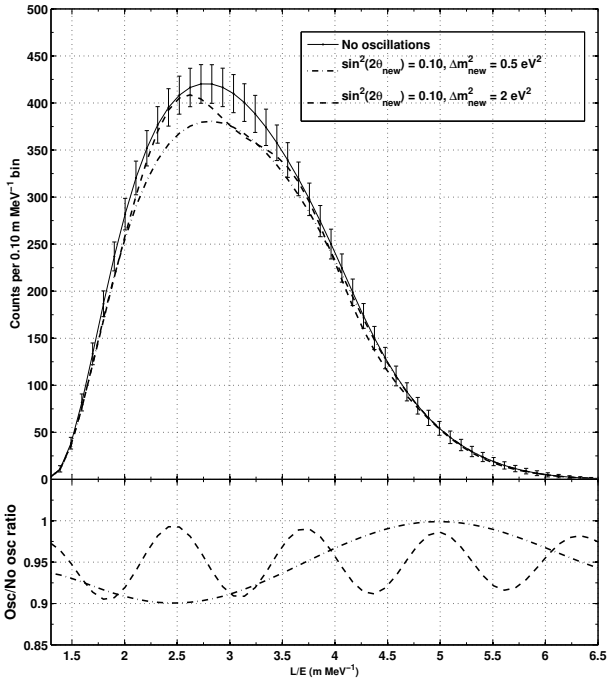

Figure 7.21: L/E distribution of the $\bar{\nu}_e$ events observed in CeSOX nominal configuration [283]. The non-oscillation case is displayed in solid line and two oscillation cases with different squared mass differences Δm^2_{new} are displayed in dashed and dash-dotted lines, respectively. The effect of Δm^2_{new} on the oscillation pattern is clearly visible on the oscillated over non-oscillated ratio (bottom panel).

- accidental events, usually originating from natural radioactivity.
- cosmogenics, i.e. muon-induced production of radioactive isotopes, such as ^{8}H and ^{9}Li.
- (α,n) events, capture of a ^{210}Po α particle (prompt event) by a carbon atom emitting a neutron upon deexcitation (delayed event)

Although very low, these backgrounds must be taken into account in $\bar{\nu}_e$ analysis such as geoneutrinos or reactor neutrinos measurement. In the context of CeLAND/CeSOX, even the latter are considered as backgrounds since they do not originate from the CeANG.
A recent KamLAND $\bar{\nu}_e$ analysis [212] provides an estimation of the total background rate. This rate, not exceeding 0.5 event per day in the [0.9-2.6] MeV energy region, of interest for the experiment, can be considered negligible[9] with respect to the IBD interaction rate brought by the CeANG.

Although exposed to similar rates of reactor neutrinos and geoneutrinos, the liquid purity and the overburden of Borexino essentially suppress the accidental, (α,n) and cosmogenic background components. The impact of Borexino's intrinsic backgrounds can thus be considered negligible as well.

[9]Note that the reactor neutrinos component has been strongly suppressed since the shutdown of a vast majority of the Japanese nuclear reactors in 2012.

Detector's intrinsic backgrounds have been proven negligible with respect to the $\bar{\nu}_e$ signal expected from the CeANG. Let us now study the possible impact of the source-induced backgrounds.

Gamma backgrounds

The CeANG itself is a potential source of gamma background for the experiment. The most serious component of this background is the 2.185 MeV gamma ray emitted upon the β decay of ^{144}Pr. Other sources of gamma rays such as Bremsstrahlung of ^{144}Ce -^{144}Pr electrons or contaminations of radioactive elements in the source have been investigated and do not represent a significant source of background. Currently under examination, the contamination of the tungsten shielding in U, Th and K chain elements is not considered problematic in case of a source deployment outside the active detector volume. However, if a deployment is planned at the center of the detector, this contamination has to be seriously taken into account and strict constraints on the shielding's radiopurity are expected.

To estimate the attenuation provided by the shielding and the passive layers of the detector in order to obtain the expected gamma background rate, the propagation of the 2.185 MeV gammas has to be simulated. I first performed such simulations with GEANT4 for the CeLAND experiment.

For these simulations, I implemented the simplified CeLAND geometry in KLG4sim: a 7-cm diameter and height cylinder of CeO_2 enclosed in a 16-cm thick tungsten shield placed 9.6 m away from KamLAND's center. The sock, expected to hold the CeANG during its deployment, was not taken into account in the simulations.
The simulation of the ^{144}Pr gammas is quite straightforward and the monoenergetic 2.185 MeV rays are simply generated isotropically and homogeneously within the source volume. Given the large attenuation brought by the shielding and the detector's layers, long and resource-consuming simulations are expected. I thus decided to use biasing techniques in order to reduce the computing time.

In GEANT4, when creating a volume, one can consider it as part of a previously defined "mother" region. In these regions, usually combinations of several volumes, customized cuts, physical processes or material properties can be applied independently from the rest of the detector's volumes. I thus defined a "shielding region", enclosing both the CeO_2 source and the tungsten shielding regions. In this region, through the "G4ProductionCuts" class, I increased the production threshold for electrons and gammas, i.e. the minimum energy required for a gamma or an electron to generate secondary particles. The effect of this cut is to prevent the creation of low-energy particles. These particles being contained within the shielding, their tracking would have pointlessly slowed down the simulation.
The second cut consists of "killing"[10] particles that reach a certain energy threshold by losing energy. By getting rid of primary particles (^{144}Pr γ rays generated in the source) that reached an energy of 700 keV, threshold energy for a KamLAND event [261], I ensure that their propagation will not waste simulation's time.

[10]In simulation terms, killing a particle is equivalent to stopping its tracking, setting its energy to zero and considering it as lost.

Although these cuts increased the processing speed, simulations were still time-consuming. An execution speed of about 10^8 $\gamma.\mathrm{h}^{-1}$ has been observed thus leading to the simulation of one second of the experiment in about 200,000 hours for a 2.7 PBq CeANG (20 TBq of 2.185 MeV γ's). Using the resources available at the IN2P3 computing center [284], I simulated a total 1.05×10^{12} gammas. Out of these particles, only 30 deposited energy in the active detector's volume, enclosed in a 6.5-m radius sphere. Among these 30 energy depositions, only 4 deposited more than 0.9 MeV, enough to be considered a prompt event in an $\bar{\nu}_e$ analysis.
Since no gammas reached the 6-m radius fiducial volume nor deposited more than 1.8 MeV, minimum delayed event energy considered for a n-H capture [261], this simulation can only provide a higher limit on accidental background. A rough but accurate enough estimation of the accidental background, not taking multiplicity cuts into account, is given by:

$$R_{\mathrm{acc}} = R_{\mathrm{p}} \times R_{\mathrm{d}} \times \Delta t, \tag{7.5}$$

with R_{p} and R_{d}, the rate (in Hz) of prompt and delayed events and Δt the coincidence time window (in s), equal to 1 ms for the KamLAND's $\bar{\nu}_e$ analyses. Considering a 2.7 PBq CeANG, the results of the simulation led to attenuations larger than 1.05×10^{12} in the prompt and delayed energy windows thus yielding to a maximum accidental rate of 0.36 Hz.
The low efficiency of these simulations motivated the use of a much faster software: TRIPOLI-4®.

Jonathan Gaffiot and I started to implement the KamLAND geometry in TRIPOLI-4® and simulate γ background in the context of CeLAND. However, the collaboration with KamLAND ended and the CeSOX experiment quickly began afterwards. All the simulations performed with TRIPOLI-4® thus concern the CeSOX experiment and have been conducted by Jonathan Gaffiot.

Prior to generating and propagating gammas from the CeANG to the detector, one has to implement the complete geometry of the experiment in TRIPOLI-4®. In this case, the geometry of the Borexino detector, as displayed in Figure 7.2, and the CeANG with its shielding has been defined, as shown in Figure 7.22. Only the PMTs, whose shape is not considered a basic volume in the simulation, have not been implemented.

Significant results can be obtained generating only 10^9 gammas, thanks to the efficient biasing techniques presented in Section 7.2.1. This relatively low number of particles allows to reach statistical errors of 2% over the whole energy range, with an increase to about 5% in the 2.1-2.2 MeV energy bin. Figure 7.23 displays the probability of interacting in each detector layer for an initial gamma generated in the CeANG. The volume referred to as "fiducial" is used in the solar analyses of Borexino [285]. It consists of a 3-m radius sphere at the center of the target volume.

The total probability of a gamma to deposit energy in the detector, expressed as the integral of the detected energy spectrum, reaches very low values. The total attenuation of gammas integrated over the whole energy spectrum is equal to $7\ 10^{-18}$ in the target volume (4.25 m radius sphere) and $4\ 10^{-20}$ in the fiducial volume (3-m radius sphere). Assuming a 3.7 PBq CeANG (25 TBq of 2.185 MeV gammas), interaction rates of 16 $\gamma.\mathrm{d}^{-1}$ and 0.1 $\gamma.\mathrm{d}^{-1}$

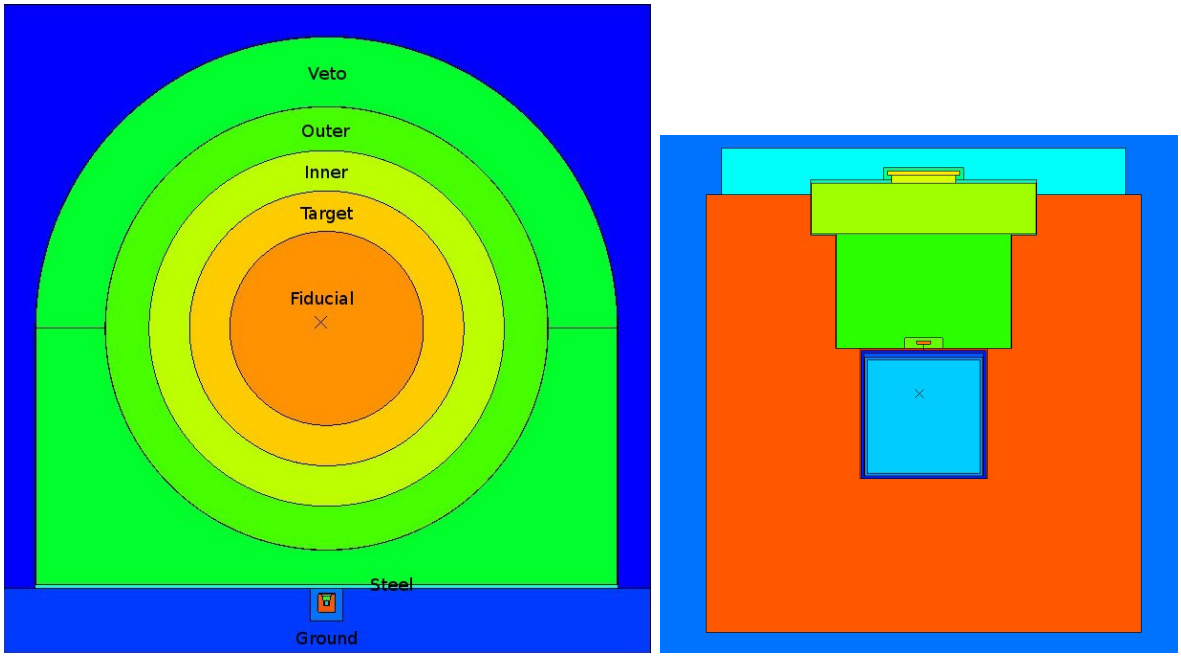

Figure 7.22: Left: View of Borexino with the ANG and its shielding placed in the source deployment tunnel. Right: Close-up view of the CeANG with its shielding. Both images are generated with the TRIPOLI-4® visualization tool.

in the target and fiducial volumes, respectively, are expected, regardless of the deposited energy.
Considering a prompt energy window of [1.0-2.4] MeV and a delayed energy window of [2.0-2.4] MeV, prompt event rates of 4.2 10^{-18} Hz and 2.8 10^{-20} Hz and delayed event rates of 2.0 10^{-19} Hz and 2.0 10^{-21} Hz are expected in the target and fiducial volumes, respectively. From Eq. 7.5, accidental rates of 5.7 10^{-15} Hz and 3.8 10^{-17} Hz are expected in the target and fiducial volumes, respectively. With no energy cuts taken into account, these respective accidental rates increase to 3 10^{-6} d^{-1} and 1.2 10^{-10} d^{-1}.
While this background can be considered negligible for CeSOX, even taking into account the full active detector volume, the solar analysis might be impacted, especially when trying to detect the CNO component of the solar neutrino flux.
Note that considering a scintillating inner buffer (referred to as "inner" in Figures 7.22 and 7.23), single gamma background rates of $\sim$2000 $\gamma.d^{-1}$ are expected, still acceptable for CeSOX.

Neutron backgrounds

Spontaneous fissions (SF) of actinides contaminants in the CeANG are a potential source of neutron background. The interaction of actinides-emitted α particles in the source's light nuclei such as oxygen is a source of fast neutrons as well. However, since this process is not dominant, it will not be covered in the following.
Fast neutrons emitted by SF lose a small fraction of their energy in the high-Z tungsten shielding and easily scatter out in the detector materials. Given the large thickness of water and organic liquids in the active and passive volumes of the detector, these neutrons are likely

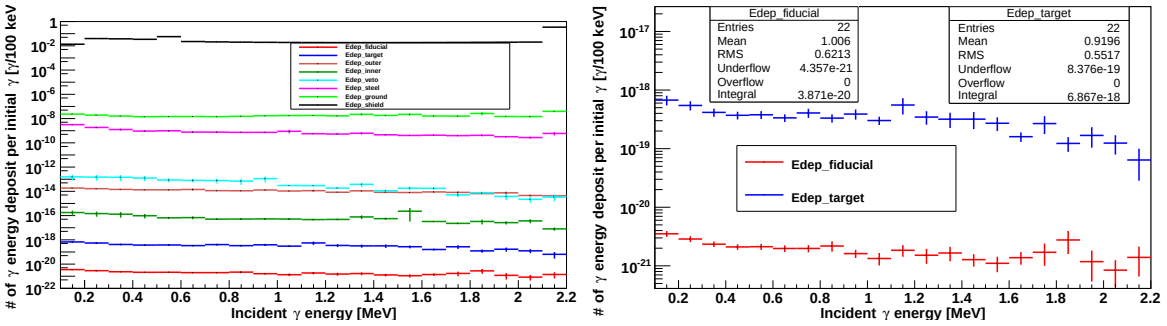

Figure 7.23: Left: Energy deposited in all detector volumes for each initial 2.185 MeV γ generated. The fiducial volume is considered a 3-m radius sphere at the center of the target volume. Right: Close-up view of the left panel centered on the two innermost volumes.

to undergo radiative capture on hydrogen, thus creating a 2.2 MeV gamma ray that could mimic an IBD prompt or delayed event. Captures on metallic structures, yielding to the production of high-energy (6-9 MeV) gammas, are expected as well. Although apparently accidental, this background might be considered weakly correlated given the neutron multiplicity of each fission. Indeed, spontaneous fission can simultaneously emit several neutrons whose moderations and captures are related in time and dependent on the capture time in water or organic liquids. As presented in Section 6.5.1 for Double Chooz, SF fast neutrons could be another potential source of correlated background. The interaction of such neutron in the active detector could lead to a proton recoil, mimicking a prompt event, and a subsequent capture on H, mimicking a delayed event.
The weak neutron attenuation provided by the shielding might cause a high neutron-induced background rate in the detector, even with relatively small actinide contamination in the source. Since fresh nuclear fuel does not contain elements heavier than ^{238}U, actinides are created during the fuel irradiation through several neutron captures and β decays, as shown in Figure 7.24. Therefore, the probability of creating a heavy actinide decreases with its mass and number of neutrons. Table 7.4 summarizes the half-life, SF yield[11], specific neutron activity and activity normalized to the ^{144}Ce activity in spent nuclear fuel for the most produced isotopes of americium (Am) and curium (Cm).

Although the increase of SF yield and specific neutron activity for heavier isotopes tends to compensate their lower relative activity, the contribution of americium isotopes and low SF yield curium isotopes to the neutron emission in the CeANG is considered weak. Furthermore, given the low SF yield of odd nucleon number isotopes, only even curium isotopes (^{244,246,248}Cm) are expected to provide a neutron activity high enough to be considered an issue. Among these isotopes, ^{244}Cm with its half-life of 18 years, high SF yield, important neutron activity and large concentration in SNF is the most problematic. Furthermore, its mean number of neutrons emitted per SF of 2.7 could potentially induce correlated backgrounds.
Although α spectroscopy measurements have been performed on ^{144}Ce samples at Saclay, the expected contamination of ^{244}Cm in the final CeANG, expressed in Bq per Bq of ^{144}Ce, is unknown. As shown in Figure 7.7, the separation of Cm is performed quite early in the chromatographic displacement process and contamination of the order of 10^{-6} Bq/Bq have been

[11]The SF yield is equivalent to the branching ratio toward spontaneous fission.

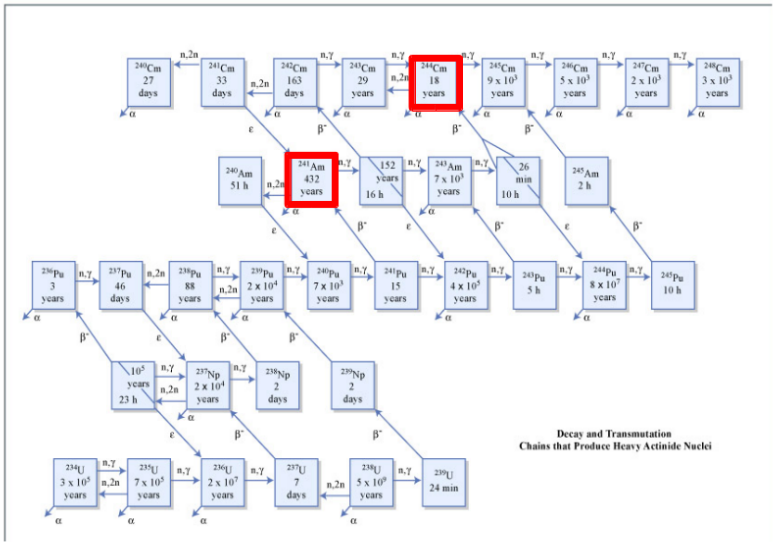

Figure 7.24: Scheme of the production chain of actinides during fuel irradiation [286]. The two most dangerous isotopes, ^{241}Am and ^{244}Cm have been highlighted in red.

Isotope	Half-life	I_{SF}	Specific neutron activity (n/g)	$\mathcal{A}/\mathcal{A}(^{144}Ce)$ (Bq/Bq)
^{241}Am	432.2 y	4.0 10^{-10}	1.2	5 10^{-3}
^{242m}Am	141 y	4.7 10^{-9}	46	1 10^{-4}
^{243}Am	7370 y	3.7 10^{-9}	0.72	2 10^{-4}
^{240}Cm	27 d	3.9 10^{-6}	6.7 10^{7}	
^{242}Cm	162.8 d	6.2 10^{-6}	1.9 10^{7}	
^{243}Cm	29.1 y	5.3 10^{-9}	2.6 10^{2}	2 10^{-4}
^{244}Cm	18.10 y	1.4 10^{-4}	1.6 10^{7}	2 10^{-2}
^{245}Cm	8.5 10^{3} y	6.1 10^{-7}	1.1 10^{2}	3 10^{-6}
^{246}Cm	4.73 10^{3} y	3.0 10^{-2}	1.0 10^{7}	5 10^{-7}
^{248}Cm	3.40 10^{5} y	8.39	4.2 10^{7}	<1 10^{-7}

Table 7.4: Characteristics of the most abundant Am and Cm isotopes present in spent nuclear fuel [264]. The activity $\mathcal{A}$ is given in Bq/Bq in 2-year old SNF and normalized to the ^{144}Ce activity. Only isotopes with a half-life larger than 180 days are depicted, the contribution of the others being strongly suppressed in the CeANG at delivery.

observed [287] in promethium[12] (Pm). Since the concentration of cerium is located further down the chromatography chain than Pm, lower contamination of Cm are expected. However, in the following simulations, a contamination of 10^{-5} Bq(^{244}Cm)/Bq(^{144}Ce) is assumed, in agreement with the results of the α spectroscopy. This level of contamination leads to a neutron flux of 1.4 10^{5} n/s emitted by the CeANG [264].

[12]Pm is used as fuel for radioisotope thermoelectric generators.

Although the first simulations of the SF-induced neutron background I performed for CeLAND have been made using GEANT4, the need for accurate neutron transport and fast execution time drove our choice toward the use of TRIPOLI-4®, as for the gamma background simulations. The following simulations have been performed in the context of CeSOX, using routines developed for CeLAND.
Neutrons are generated on an event-by-event basis and distributed homogeneously in the source. Their energy is chosen randomly in a Watt spectrum peaked at 1 MeV, accurately describing the energy spectrum of fission-induced neutrons. About 60% of neutrons are captured in the shielding, mostly on W atoms. The remaining 40% travel toward the detector. The so-called "neutron current", representing the number of neutrons that crossed the interface between two adjacent volumes, is displayed in Figure 7.25 (left). On this plot, the neutron currents at the "shield-tunnel", "tunnel-steel plates", "steel plates-veto" and "veto-outer buffer" interfaces are displayed. Given the large attenuation of steel, water and oil, only a few neutrons reached the outer buffer, leading to an upper limit on the neutron attenuation of 10^{-12} between the source and the buffer. No neutrons reached the detector's active volume thus setting strict constraints on the fast neutron background, considered negligible hereafter.

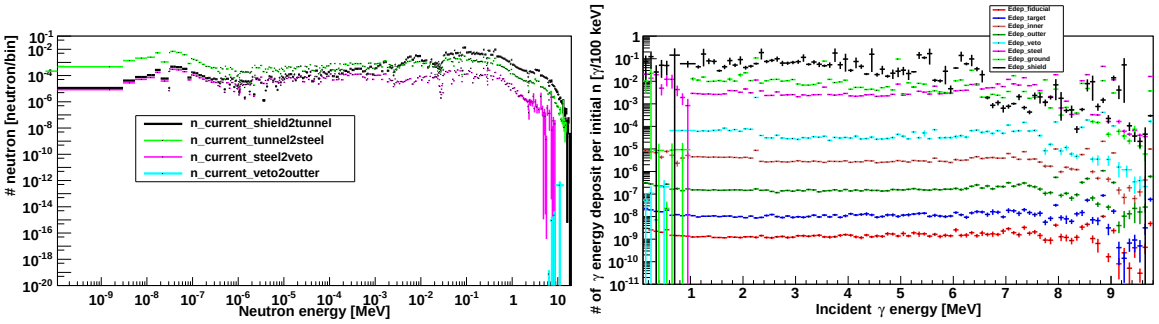

Figure 7.25: Left: Neutron current observed at the interfaces between several detector's volumes: shielding, tunnel, steel plates, veto and outer buffer. Right: Energy deposited in all detector volumes for each SF neutron generated.

Neutrons traveling in the detector get quickly thermalized and captured in the ground, the water veto or the metal surrounding the detector. While captures on hydrogen in the veto produce 2.2 MeV gammas, captures on metals produce high-energy gammas. The spectrum of neutron-induced gamma energy depositions thus extends up to 10 MeV, as shown in Figure 7.25 (right). This plot displays the number of energy depositions per initial neutron, i.e. the probability of a neutron to generate an energy deposition, in each detector's volume. Integrated over the whole energy spectrum, the attenuation of neutron-induced energy deposition reaches 1.0 10^{-6} in the target volume and 1.5 10^{-7} in the fiducial volume. Assuming a 3.7 PBq CeANG and a ^{244}Cm contamination of 10^{-5} Bq/Bq, this induces interaction rates of 140 mHz and 21 mHz in the target and fiducial volumes, respectively. Considering a prompt energy window of [1.0-2.4] MeV and a delayed energy window of [2.0-2.4] MeV, prompt event rates of 19.6 mHz and 2.9 mHz and delayed event rates of 5.6 mHz and 0.8 mHz are expected in the target and fiducial volumes, respectively. From Eq. 7.5, accidental rates of 9.5 10^{-3} d^{-1} and 2.0 10^{-4} d^{-1} are expected in the target and fiducial volumes, respectively.
Although several orders of magnitude larger than the gamma-induced accidental background, this background can be considered negligible. Note that, given the relatively weak neutron

multiplicity of ^{244}Cm (2.7 neutrons/SF in average) and the back-to-back emission of SF neutrons (neutrons are emitted by the two fission fragments and therefore acquire a strong boost), this background is considered not to be correlated.

7.3 Expected sensitivity

The sensitivity to short baseline oscillation is estimated by comparing the observed and expected IBD rates, both binned in energy and distance to the source. To test the oscillation hypothesis and constrain the $\sin^2 2\theta_{\text{new}}$-$\Delta m^2_{\text{new}}$ parameter space, the following χ^2 is used:

$$\chi^2 = \sum_{i,j} \frac{\left(N^{\text{obs}}_{i,j} - (1+\alpha)N^{\text{exp}}_{i,j}\right)^2}{N^{\text{exp}}_{i,j}} + \left(\frac{\alpha}{\sigma_{\text{N}}}\right)^2, \tag{7.6}$$

with $N^{\text{obs}}_{i,j}$ and $N^{\text{exp}}_{i,j}$,the observed and expected number of IBD events in the i^{th} energy bin and j^{th} distance bin, respectively. α is a nuisance parameter accounting for the normalization uncertainty, related to the uncertainty on the CeANG activity, and is allowed to vary within σ_{N}. The precision on the calorimetric measurement of the source activity will set σ_{N} for the final oscillation fit. By doing so, both the spectral shape and the rate will bring information to the fit. This is the "rate+shape" analysis, similar to the default oscillation fit of Double Chooz (*c.f.* Section 6.6.2). On the other hand, if the source activity is unknown, σ_{N} is set to infinity and only spectral shape distortions bring information to the final fit. This is the "free rate" or "shape only" analysis.
The minimization of the χ^2 function expressed in Eq. 7.6 over the α nuisance parameter provides the exclusion contours for different confidence levels (C.L.) through the formula: $\Delta\chi^2 = \chi^2\left(\theta_{new}, \Delta m^2_{\text{new}}\right) - \chi^2_{\text{min}}$. The 90%, 95% and 99.73% (3σ) C.L. exclusion contours are computed such that $\Delta\chi^2 < 4.6$, 6.0 and 11.8, respectively.
These three contours are displayed in Figure 7.26 for the CeLAND experiment for a rate+shape (left) and a shape only (right) oscillation fit.
The 95% C.L. contour is shown in Figure 7.27 for CeSOX in its "nominal" (left) and "upgraded" configurations.

To compare the potential of both rate+shape and shape only analyses, one has to understand the shape of their sensitivity contours.
At low $\Delta m^2_{\text{new}} \lesssim 10^{-1}$ eV^2, the oscillation length, proportional to E/Δm^2_{new}, is larger than the detector's size and the $\bar{\nu}_e$ survival probability is approximated to: $\mathcal{P}\left(E, L\right) \simeq 1 - \alpha \sin^2 2\theta_{\text{new}} \left(\Delta m^2_{\text{new}}\right)^2$ with α, a constant. In this region, a linear correlation in logarithmic scale is expected between $\sin^2 2\theta_{\text{new}}$ and Δm^2_{new} to provide a constant $\Delta\chi^2$ contour.
In the $\Delta m^2_{\text{new}} \sim 0.1 - 10$ eV^2 region, oscillation lengths slightly smaller than the detector's size are expected. The energy and vertex resolutions of the detector allow the observation of a well-developed oscillation pattern. This region is the most sensitive to an oscillation.
At high $\Delta m^2_{\text{new}} \gtrsim 10$ eV^2, the oscillation length is smaller than the detector's vertex resolution and an oscillation pattern can barely be observed. In this region, the spectral shape brings no information on the $\sin^2 2\theta_{\text{new}}$ and Δm^2_{new} parameters. The rate information however allows the determination of $\sin^2 2\theta_{\text{new}}$ since the $\bar{\nu}_e$ survival probability can be approximated to $\mathcal{P}\left(E, L\right) \simeq 1 - \frac{1}{2}\sin^2 2\theta_{\text{new}}$. Although more sensitive over the whole parameter space, the

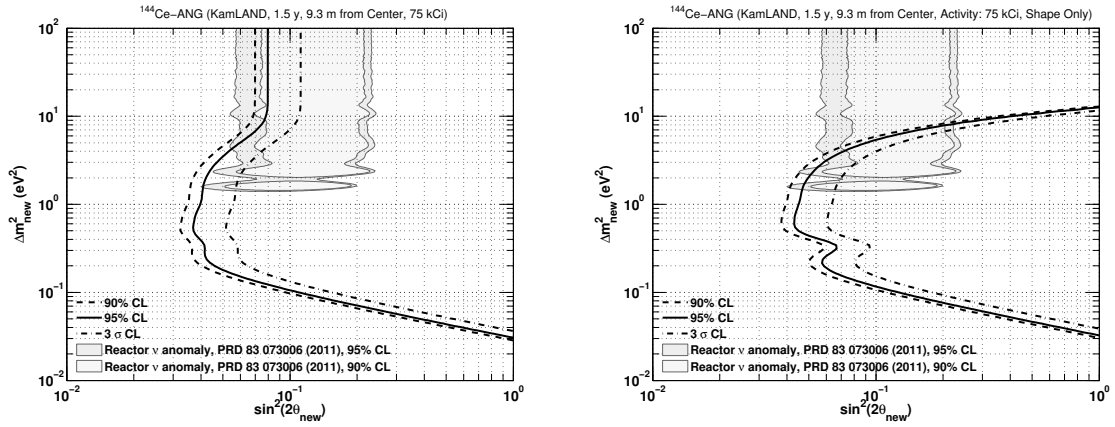

Figure 7.26: Sensitivity contours to exclude the non-oscillation hypothesis at 90%, 95% and 3σ C.L. [286]. A data taking period of 18 months with a 2.7 PBq (75 kCi) CeANG located 9.3 m away from KamLAND's center is considered. A 1.5% normalization uncertainty is taken into account. Results are expressed for a rate+shape (left) and a shape only (right) analysis. The reactor anomaly favored contours are displayed in gray shaded areas for comparison.

strength of the rate+shape analysis over the shape only analysis is best displayed at high Δm^2_{new}.
Note that the sensitivity to lower $\sin^2 2\theta_{\text{new}}$ values is mostly driven by statistics and can be significantly improved with an higher ^{144}Ce activity, a longer data taking time and a shorter distance between the source and the detector's center.

Several experimental parameters such as the activity uncertainty, the energy and vertex resolutions or the source spatial extension are likely to affect the sensitivity of the experiment as well. Detailed studies of the impact of these parameters have been performed and their results can be found in Ref. [286] for CeLAND and Ref. [283] for CeSOX.

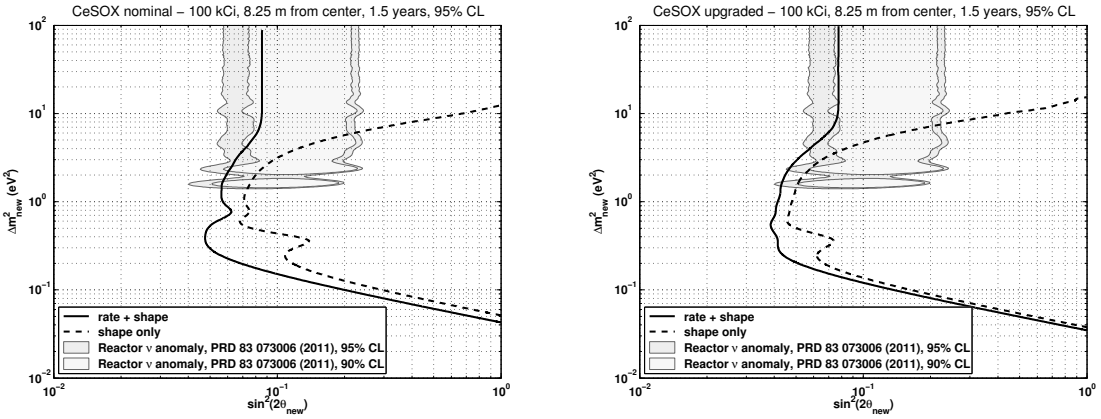

Figure 7.27: Sensitivity contours to exclude the non-oscillation hypothesis at 95% C.L. [283] in CeSOX. The "nominal" (left) and "upgraded" (right) configurations correspond to a fiducial volume of 4.25 and 5.5-m radius, respectively. A data taking period of 18 months with a 3.7 PBq (100 kCi) CeANG located 8.25 m away from Borexino's center is considered. A 1.5% normalization uncertainty is taken into account. Results are expressed for a rate+shape (solid line) and a shape only (dashed line) analysis. The reactor anomaly favored contours are displayed in gray shaded areas for comparison.

Conclusion

"I have done a terrible thing, I have postulated a particle that cannot be detected": here are the immortal words pronounced by Wolfgang Pauli in 1930 upon postulating the existence of the neutrino. It took about a quarter century to prove him wrong and finally detect the first neutrino, or rather antineutrino, with a liquid scintillator detector located next to a nuclear reactor, an apparatus still being widely used nowadays. Since then, the development of the detection technologies led to an acceleration of discoveries in the field of neutrino physics. Over the last decades, it has been understood that the phenomenon leading to an apparent loss of neutrinos when observing a certain flavor was due to oscillations, a well-explained quantum mechanics artifact. Although not strictly compatible with the Standard Model of particle physics, the framework of neutrino oscillations seems now well understood. The measurement of the last mixing angle θ_{13}, anticipated in 2011 by Double Chooz and confirmed in 2012 by Daya Bay and RENO, was one of the last milestone leading to the complete parametrization of the PMNS matrix. However, tensions remain between several experimental results and there is still some room for an additional oscillation. The observation of this disappearance of $\bar{\nu}_e$ toward sterile neutrinos is the goal of the CeSOX experiment.
While studied for its fundamental properties, the supposedly undetectable neutrino is now considered to provide several real world applications. From the monitoring of nuclear reactors for non-proliferation purposes to the determination of the Earth's composition through U, Th and K decays, its impact is not limited to neutrino physics only. Among these applications, directionality is of interest since it could allow the localization of a neutrino source such as a supernova or a nuclear reactor.

Although small in terms of manpower, the "Low Energy Neutrinos" group of CEA Saclay is involved in many experiments. Each member of the group is thus in charge of several tasks and often works on various subjects, as I was.
When I began my "pre-Ph.D." internship in May 2012, the Nucifer detector was just deployed in the vicinity of the Osiris reactor at Saclay. The detection of $\bar{\nu}_e$ emitted in the reactor core was one of the last validation test of Nucifer's design, proving the detector's capabilities to perform non-proliferation studies. Since the global effort of the group was focused on Nucifer, I thus started to analyze its data along with other Ph.D. students and interns. These analyses put in evidence the most important challenge the experiment has to cope with: the accidental background (*c.f.* App. A). The installation of the two additional lead wall helped reduce this background and, since then, Nucifer is able to detect neutrinos from Osiris' core, although with a large and irreducible statistical uncertainty.
At the same time, the CeLAND experiment was still in its early stages and simulations of the CeANG in KamLAND were required. Designed to test the existence of an hypothetical fourth neutrino state using an antineutrino source in or next to the KamLAND detector, the

CeLAND experiment relies on both a good understanding of the detector and of the CeANG. I acquired the KamLAND simulation from the people developing it at Tohoku University and brought it back to Saclay where we enhanced it for CeLAND. The studies of the source-induced gamma and neutron backgrounds performed with it (*c.f.* Section 7.2) motivated us to use another simulation tool in order to properly estimate the impact of these backgrounds on the experiment. The results obtained with TRIPOLI-4® led us to consider the CeLAND, or CeSOX since the deployment of the CeANG is now planned next to the Borexino detector, experiment as almost background-free. Nonetheless, these studies indicated the extreme care that needs to be taken is a deployment at the center of the detector is planned.
Meanwhile, I started working on the Double Chooz experiment, the initial topic of my thesis. Although smaller in size than the other two experiments and with only one detector operating, Double Chooz has provided several measurements of θ_{13}. The latest value of $\sin^2 2\theta_{13} = 0.090^{+0.032}_{-0.029}$ is the most precise performed by Double Chooz to this day. The recent start of the near detector opens the second phase of the experiment with two detectors and, due to an important reduction of systematic and statistical errors, ensures the improvement of the measurement. Although it was still in its commissioning phase, I performed data analyses (*c.f.* Section 6.5.3) with the near detector and isolated, with rudimentary cuts, a total of 1883 neutrino candidates with neutron capture on Gd (n-Gd). With the calibration campaign planned starting August 2015 and the ongoing data production, the Double Chooz's near detector will be fully operational quickly.
The strength of Double Chooz also comes from its ability to conduct parallel analyses such as neutrino directionality studies. In order to replicate the results presented by the CHOOZ experiment, the "Directionality group", myself included, performed directionality analyses on the most recent datasets of neutrino events. The 17,358 n-Gd neutrino candidates led to a reconstruction uncertainty of 5.16° and 5.30° in azimuthal and zenith angle, respectively. A similar analysis on the 31,898 neutrino candidates with neutron capture on H (n-H) provided uncertainties of 5.03° and 5.17° in azimuthal and zenith angle, respectively (*c.f.* Section 5.3). This measurement is a conclusive proof that neutrino directionality with IBD can be applied, not only to Gd-loaded detectors, but to large undoped liquid scintillator detectors as well.
This result motivated us to apply IBD directionality to the field of astrophysics (*c.f.* Section 5.4). By releasing 99% of its energy in the form of neutrinos several hours before emitting visible light, a core-collapse supernova can be detected through its neutrinos before an optical observation. The inter-experiment SNEWS network aims at providing a global alert in case of the detection of a burst of neutrinos in several large neutrino detectors scattered over the globe. The addition of a combined directional information to this alert would increase the probability of observing a complete supernova process, including it early phases. Considering a supernova occurring 10 kpc away from Earth, the combination of all large liquid scintillator detectors currently operating could provide a localization within a 45°(68% C.L.) cone. With the addition of JUNO, this uncertainty could decrease to 14°(68% C.L.) by 2020.

Appendix A

Study of accidental background in the Nucifer experiment

In this appendix, I will present the studies I performed on the Nucifer experiment in order to help reduce its accidental background. Detailed descriptions of the Nucifer experiment and its results can be found in Jonathan Gaffiot's and Maxime Pequignot's theses [156, 288] as well as in Ref. [289].

A.1 Nuclear non-proliferation

With the increasing worldwide need for energy, the expansion of nuclear energy is certain. In order to guarantee that this technology is being used for peaceful and civilian purposes only, one of the duties of the United Nations International Atomic Energy Agency (IAEA) is to control the complete nuclear fuel cycle from the extraction to the reprocessing. By doing so, the IAEA ensures that no fissile material, in quantities large enough to manufacture a nuclear weapon, has been diverted during the operation of the nuclear reactors scattered over the globe. To perform this constant watch, the Agency has been evaluating the potential of new technologies for future safeguard purposes.
Neutrino detectors have the unique ability to monitor a nuclear reactor's operational status, power and fissile content in real-time, from outside the reactor containment. Able to detect an unrecorded production of fissile material in declared reactors and to estimate the total burn-up of a reactor core, they could have a considerable value for safeguard purposes. The detection of electron antineutrinos emitted in the decay chains of the fission products in nuclear reactors associated with accurate simulations provides an efficient method to assess both the thermal power and the evolution of the fuel composition. As presented in Section 3.1.3 and displayed in Figure 3.4, the $\bar{\nu}_e$ emission rate of a nuclear reactor core decreases over time at constant thermal power, due to the burning of ^{235}U into ^{239}Pu and ^{241}Pu. The observation of this effect with a neutrino detector could provide a real time measurement of the amount of plutonium in the reactor, thus ensuring the match between the quantity of plutonium declared by the operator and the quantity actually produced during the reactor cycle.

A.2 The Nucifer experiment

The Nucifer experiment aims to demonstrate the concept of neutrinometry at the pre-industrialized stage. Its detector has been specifically designed to match the criteria set by IAEA: easy deployment, non-intrusive, remote monitoring, low maintenance rate and relatively low price.

Nucifer is installed on the lowest floor of the Osiris reactor in Saclay, 11 meters below the surface of the reactor's water pool as displayed in Figure A.1 (left). Such an overburden is equivalent to ∼15 m.w.e and leads to a reduction of the muon flux, especially the hadronic component, of a factor ∼2.7. Located only 7.2 m away from Osiris' core, Nucifer is shielded from the radiations by 3.5 m of water and 2.5 m of concrete, as shown in Figure A.1 (right).

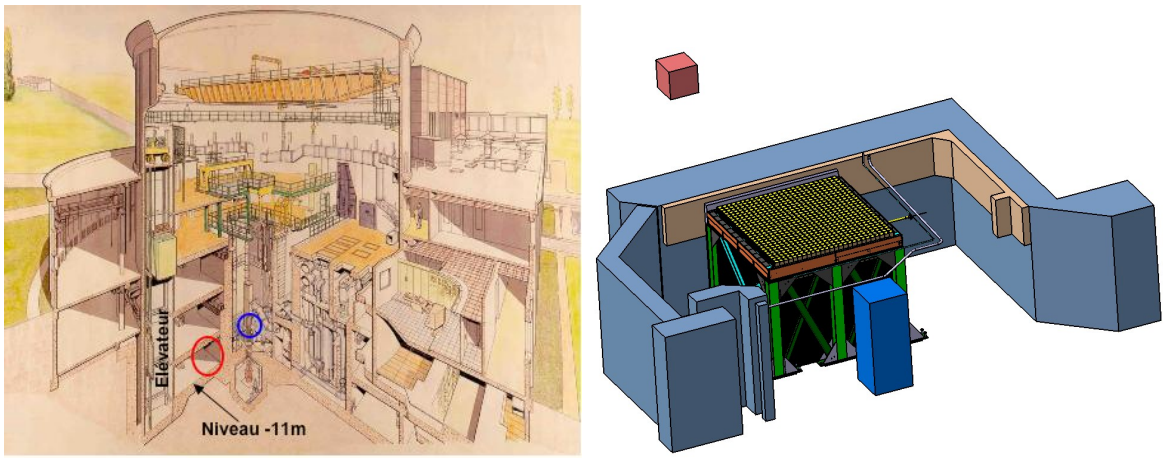

Figure A.1: Left: View of the Osiris building with the reactor (blue) and Nucifer (red). Right: Nucifer in its shieldings with respect to the core of Osiris (red box).

Osiris is an open-pool type light water experimental reactor located in CEA Saclay, designed for material irradiation and radioisotope production [290]. Delivering a maximal thermal power of 70 MW in operation, its compact core of 80 cm × 70 cm × 70 cm is loaded with 38 standard fuel elements (U_3Si_2Al plates enriched at 19.75 % in ^{235}U). Osiris operates on a 4-week cycle basis. Each cycle consists of three weeks with the reactor at full power (ON) followed by a week of shutdown (OFF) for the refueling of the core (by $1/7^{th}$).

The Nucifer detector, as depicted in Figure A.2, consists of a neutrino target detector, an active veto to tag muon-induced backgrounds, 14 cm of polyethylene to shield the target against neutrons and a 10-cm lead layer to stop gamma rays. An extra 10-cm lead wall has been erected on the reactor side to further shield reactor-induced gamma rays.
The neutrino target is contained inside a cylindrical double-vessel made of stainless steel (height 1.8 m, diameter 1.2 m) with a diffusive internal surface to increase light collection. The tank is filled with 0.85 m^3 of Gd-loaded liquid scintillator.
The chemistry of the Nucifer scintillator is based on a development for the target liquid of the Double Chooz reactor neutrino experiment. The Gd is dissolved in the organic liquid in the form of a Gd-beta-diketonate complex. The focus in the scintillator design was on long-

term stability over several years and chemical purity. In order to better reject backgrounds, the Gd-concentration was increased to about 0.2% and the o-PXE (ortho-Phenylxylylethane) concentration was raised to about 50% with respect to the n-dodecane concentration.
Sixteen 8-inch (20 cm) photomultipliers tubes (PMTs) located at the top of the detector vessel ensure an efficient light collection. A 25 cm thick acrylic disk optically couples the PMTs with the liquid surface while shielding the intrinsic PMT radioactivity from the scintillator and ensuring a more uniform response in the whole target volume. A LED based light injection system allows the monitoring of the PMT gains and possible instrumental drifts. In addition small encapsulated radioactive sources can be deployed along the target central axis inside a vertical tube.
The veto design is based on a novel concept: 32 modular detectors, each one containing a 5 cm thick plastic scintillator of 150 to 170 cm length and 25 cm large observed by one PMT decoupled from its surface. The scintillator thickness was chosen in order to discriminate cosmic muons from gamma rays and the selected threshold allows a muon detection efficiency greater than 95%.

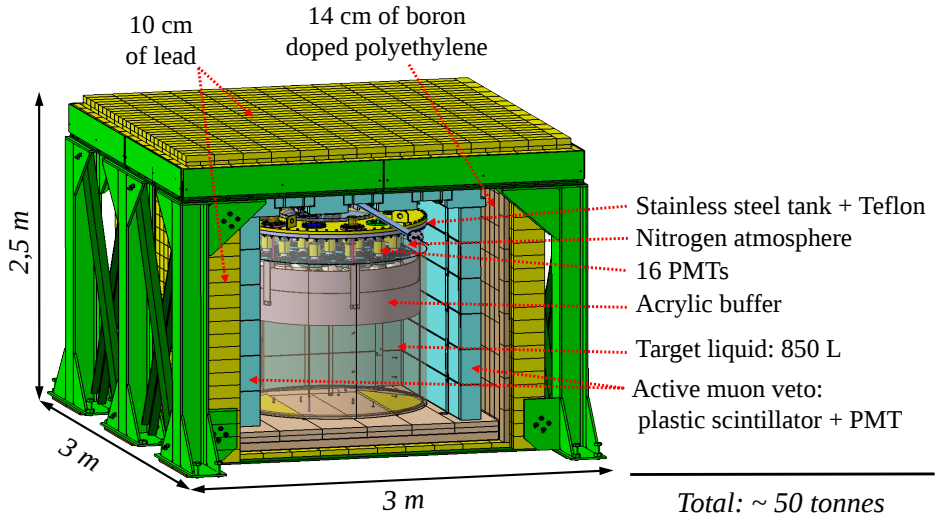

Figure A.2: Drawing of the Nucifer detector and its components.

The IBD interaction rate expected in Nucifer during a reactor ON period is ∼960 $\bar{\nu}_e$.d^{-1}. Considering the detector's mean detection efficiency of 30.3%, about 280 neutrinos per day are expected to be detected.
Nucifer has been installed in the building of Osiris in Spring 2012 and is acquiring data ever since, until the shutdown of Osiris planned at the end of 2015.

A.3 Accidental background reduction

Upon switching the detector with Osiris at nominal power in Spring 2012, an unexpectedly high trigger rate of more than 6 kHz was observed, leading to an acquisition dead time of more than 60%. Considering basic energy cuts and a coincidence window of 30 μs, the accidental rate, obtained from Eq. 7.5, easily reached 1,000,000 events per day [291]. This unexpected

feature originated from the South direction (the reactor is located in the East direction) and, after investigation, was found to be due to the presence of a primary water loop of the main reactor cooling circuit. This circuit, located 1 m behind the concrete wall, contains water highly activated by the tremendous fast neutrons flux in the reactor, hence its designation as "deactivation tank", as displayed in Figure A.3.

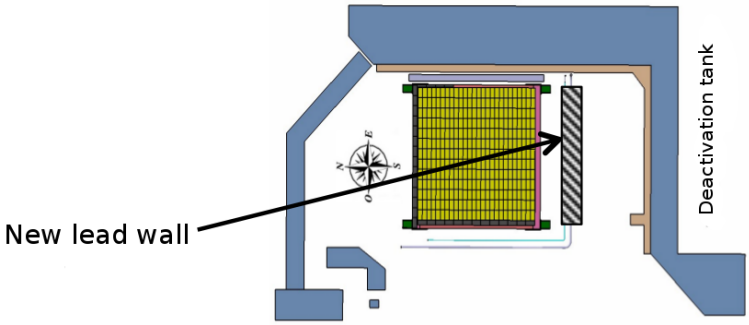

Figure A.3: Above view of the Nucifer layout with the deactivation tank on the South side.

The neutron activation produces ^{16}N from ^{16}O, which subsequently decays with a 7.13 s half-life emitting a 6.1 MeV gamma ray, easily detectable in Nucifer. This background being too high to allow the experiment to continue taking data, an additional 10 cm lead wall has been erected on the South side in March 2013. The installation of this additional shielding reduced the trigger rate by a factor 9 and allowed the acquisition dead time to reach a value of 1.5% [292]. With the cuts and efficiencies valid at that time, an accidental rate of 8908 events per day was computed, still largely above the expected neutrino rate of 227 $\pm$ 16 $\bar{\nu}_e$.d^{-1} [293].

The radiation coming from the deactivation tank has been strongly reduced, however it did put in evidence the background coming from the reactor itself. Although attenuated by two 10-cm thick lead walls, this background is now dominant. Neutron propagation studies carried out by Eric Dumonteil at CEA/DEN/CERMA and confirmed by Pulse Shape Discrimination (PSD) studies [294] rejected the contribution of a fast neutron component to this background. Exclusively due to gamma radiations, either directly from Osiris' core or from neutron captures in the pool or the structures surrounding Nucifer, this background can be further reduced by the addition of an additional shielding. However, given the promiscuity of Nucifer's layout and the constraint on the total mass allowed on Osiris' ground, this shielding has to be carefully designed in terms of size, mass and material.
In May 2013, Maxime Pequignot and myself performed tests using steel plates placed over the reactor wall. By moving the plates over the wall, we were able to find the optimal position covering the maximum solid angle shielding the detector to the reactor-induced radiation [295]. The choice of thickness and material, however, needs to be driven by simulations in order to assess the effect of the background attenuation on the accidental rate. Given the rather complicated GEANT4 geometry of Nucifer and its high amount of shielding, I chose to simulate the attenuation using a very simplified geometry based on the CeLAND geometry. This is the so-called NuCemLAND simulation [296].

The NuCemLAND simulation aims at roughly simulating the impact of Nucifer's shieldings. Based on the CeLAND simulation, it consists of concentric spherical layers of shielding materials placed at the center of the KamLAND detector, as displayed in Figure A.4 (left). Starting from the reactor concrete wall, the gammas will travel through successive layers of air, additional shielding material (lead or stainless steel) and lead before finally entering the detector. Thus, in the simulation, the gammas are emitted isotropically from the center of the source at (0,0,0), travel through the central volume made of air, then through the first shielding layer made of steel or lead and finally through the second layer of the shielding made of 20 cm of lead before reaching the detection medium (the whole KamLAND scintillator balloon).
Since we assume that the gammas originate from the concrete, we are shooting them using a similar energy spectrum measured at the ILL reactor, as displayed in Figure A.4 (right). By changing the first shielding layer material and thickness, one can try different configurations of additional shielding. Results of the NuCemLAND simulations performed for these various configurations can be found in Ref. [296].

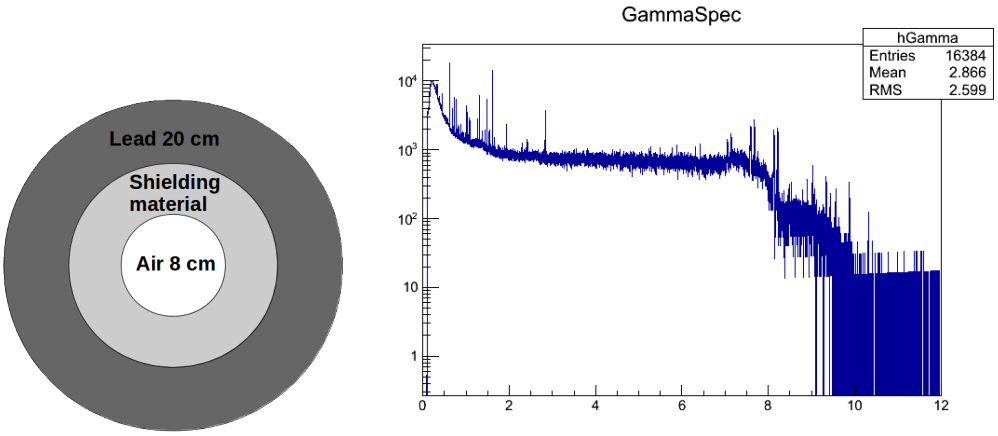

Figure A.4: Left: Geometry of the NuCemLAND simulation. The thickness and material of the different layers is changed in the simulation code. Right: Energy spectrum of gamma rays measured at the ILL reactor [297].

To ensure the highest attenuation while still respecting the size and mass constraints of the Nucifer layout, a 4-cm thick lead screen has been installed in April 2014 between the pre-existing 10-cm thick lead wall and the reactor concrete wall.
From the NuCemLAND simulations, the addition of this shielding was expected to reduce the total gamma radiation flux by a factor of 5.2. Considering prompt and delayed energy windows of respectively [2;6] and [6;10] MeV, the accidental rate was expected to be reduced by a factor 40.
However, upon analyzing the first data recorded with the new lead screen, an accidental background reduction of a factor 3 only has been unraveled. The discrepancy of one order of magnitude between the expected and measured attenuation can be due to a combination of several factors. In NuCemLAND simulations, the geometry of the shieldings covers the total solid angle of the gamma radiation emission, inconsistent with the experimental configuration of Nucifer. In addition, gammas originating from radiative neutron captures on concrete or

metallic structures might not travel trough the lead screen and could enter the detector unattenuated.

Appendix B

Characterization of ^{144}Ce samples

Given the high sensitivity expected from the CeSOX experiment, one has to perform a thorough characterization of the CeANG source in order to lower its associated systematic uncertainties. Since direct measurements are hazardous and hardly achievable on the unshielded source itself, these characterizations are performed on cerium samples provided by Mayak. Due to the variety of spent fuel reprocessed at Mayak, in terms of age, type and activity, each production of radioactive material is considered unique and these samples might not accurately represent the final CeANG.
In the context of the gamma spectroscopy studies presented in Section B.1, this discrepancy is problematic since it does not allow the measurement of impurities in the CeANG. Yet, the samples being produced during a pilot production phase, it provides limits on the amount of undesired contaminations generated during the official production. On the other hand, the beta spectroscopy studies presented in Section B.2 aim at measuring the shape of the ^{144}Pr electron spectrum, as explained in Section 7.1.3. This measurement is seldom impacted by the discrepancies between the samples and the CeANG since only ^{144}Pr is of interest.

Mayak delivered the samples to CEA Saclay in September 2014 in the form of three vials containing 10 cm^3 of cerium nitrate $Ce(NO_3)_3$ each.

B.1 Gamma spectroscopy

The gamma spectroscopy of the cerium samples aims at determining the amount of impurities present in the ^{144}Ce extracted during the production at Mayak. By observing additional energy lines in the ^{144}Ce energy spectrum, one can can detect the presence of gamma emitters such as ^{244}Cm, potential generators of backgrounds.

The instrument used to conduct the gamma spectroscopy is a high purity germanium counter (HPGe). The high sensitivity and excellent energy resolution of this detector make it the ideal device for radiopurity measurements. In order to replace the HPGe formerly operated at Saclay [298] and dedicated to the measurement of samples for Double Chooz and Nucifer, the group acquired another HPGe build, as its predecessor, by the ORTEC company [299]. To host the detector, a dedicated underground laboratory, the Dario Motta laboratory, has been build in Saclay, in the basement of the building n° 538, previously accommodating the Saclay synchrotron. The overburden of the laboratory helps reducing the

incoming muon flux, especially its hadronic component, by a factor of 2.
Installed and mounted since March 2014, the HPGe is protected from external backgrounds by an airtight acrylic box enclosed in a 10-cm thick lead chamber (*c.f.* Figure B.1). While the lead attenuates the ambient gamma background, mostly originating from U and Th decays in the surrounding concrete but from material activation due to the former synchrotron operation as well, the inner acrylic ensures a protection against the ambient radon background. Radioactive gas present in the ^{238}U and ^{232}Th decay chains, radon can easily accumulate and decay in the lead chamber. In addition, the ^{222}Rn half life of 3.8 days often induces bias when subtracting background samples from data samples. Indeed, with typical measurement durations of one or two weeks, instabilities arise in the background rate due to the initial concentration of radon. To solve this issue, a nitrogen circulation system has been installed in order to flush the acrylic box and purify its air prior to any measurement. With a flux of 200 mL/min, the 22.4 liters box can be considered radon-free in less than a day.
Since its installation, I participated in many aspects of the operation of the HPGe detector. Besides performing regular maintenance tasks such as liquid nitrogen refurbishment, I installed the nitrogen circulation system to prevent radon contamination. In addition, I carried out data analyses and simulations of samples along with Thibaut Houdy, whose thesis tasks include the operation of the HPGe.

Figure B.1: Picture of the germanium counter in its airtight acrylic box.

One of the three cerium samples has been measured in the HPGe for a week. With an activity at delivery of 60 kBq, it provides an interaction rate of about 120 Hz in the germanium crystal, well above the typical background rate of about 1 Hz. Nonetheless, in order to isolate the ^{144}Ce-^{144}Pr component of the spectrum, we subtracted it with a background energy spectrum measured during the same amount of time. The energy spectrum obtained after subtraction is displayed in Figure B.2.

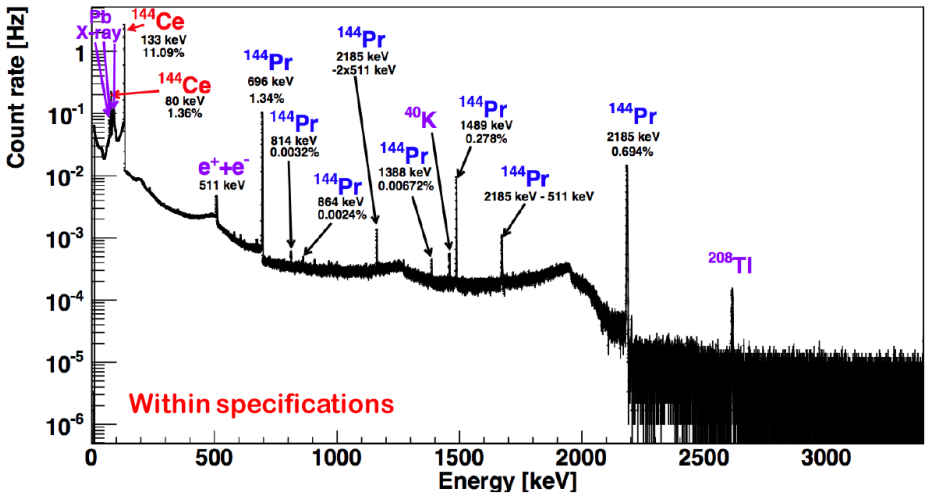

Figure B.2: Energy spectrum of the cerium sample. The ^{144}Ce and ^{144}Pr components are observed through the 133.5 and 2185 keV lines, respectively.

On this spectrum, one can identify several peaks, all originating from the cerium sample. Since background has been subtracted, the 1460.8 and 2614.5 keV peaks are emitted respectively by K and Th contaminations in the sample. Th and K components with a smaller branching ratio, as well as U components, have been detected as well, although they are not visible on this spectrum. The other peaks corresponds to gamma radiations emitted upon ^{144}Ce and ^{144}Pr decays. Table B.1 summarizes the main radiations observed in the spectrum. The last two entries of this table corresponds to the single (SEP) and double escape peaks (DEP) of the ^{144}Pr 2185.7 keV gamma.

Energy (keV)	BR (%)	Isotope
133.5	11.09	^{144}Ce
511.0		Annihilation
696.5	1.342	^{144}Pr
1460.8		^{40}K
1489.2	0.278	^{144}Pr
2185.7	0.694	^{144}Pr
2614.5		^{232}Th
1674.7		^{144}Pr 2185.7 keV SEP
1163.7		^{144}Pr 2185.7 keV DEP

Table B.1: Energy, branching ratios and origin of the main peaks observed in the ^{144}Ce sample.

Discrepancies remain at low energies (E<100 keV) between the data and the simulation. These differences come from the lack of knowledge of the germanium crystal's exact geometry. Indeed, the active region of the crystal is surrounded by a so-called "dead layer", inactive and of unknown thickness. The evaluation of this layer's thickness is possible using a radioactive source emitting a low energy energy gamma ray, such as ^{241}Am and its 59.54 keV radiation.

Described in Ref. [298] for the previous HPGe operating at Saclay, this protocol has yet to be applied to our current detector.
Nonetheless, the absence of unexpected gamma lines in the energy spectrum, and especially at low energy (E<300 keV), set upper limits on the amount of gamma-emitting impurities in the sample:

- $< 10^{-3}$ Bq/Bq of ^{144}Ce in the E<500 keV energy range
- $< 10^{-4}$ Bq/Bq of ^{144}Ce in the E>500 keV energy range

Additional cerium samples are expected to be delivered from Mayak prior to the ANG production.

B.2 Beta spectroscopy

As stated in Section 7.1.3, the electron and $\bar{\nu}_e$ spectra of the ^{144}Ce-^{144}Pr pair need to be accurately known with a percent-level precision. Although theoretical models allow the computation of the contribution of the allowed branches to the energy spectrum at the percent-level, the determination of the forbidden branches contribution is only accessible through experiment. The accurate measurement of the electron spectrum at the percent-level is thus mandatory.
To perform such a measurement, two groups belonging to the CeSOX collaboration have deployed experimental setups. However, I will focus on the apparatus installed and operating by the CEA group in the following.

The SAclay Beta Spectrometer, informally called "SABS"[1] has been installed in the LNHB laboratory at Saclay. It consists of two identical pieces of plastic scintillator surrounded by two photomultiplier tubes, as depicted in Figure B.3. By depositing a radioactive source in the form of a droplet at the center between the two plastic cylinders, one can collect the light emitted by electrons traveling through the plastic without significant losses.

Special care has been taken when designing the SABS experimental setup. First of all, in order to observe the full electron spectrum of ^{144}Pr up to 3 MeV, the dimensions of the plastic scintillator cylinders have been set to 4 cm in diameter and height. The plastic scintillator material finally chose is the EJ204, manufactured by the Eljen company [300]. Its high light yield and good match to the PMTs sensitivity in terms of light emission spectrum drove the choice towards this material. The two PMTs are Hamamatsu R6231-100, equipped with a flat and circular 2-inch photocathode, thus minimizing light loss at the edge of the plastic scintillator cylinders. Their quantum efficiencies of 35% further increase the light collection. The signal recorded by the PMTs is then sent to a charge integrator (QDC) and saved in binary files.

The main advantage of this simple setup lies in its ability to be quickly operated, thus allowing a repeatability of the measurement. Indeed, given its impact on the final sensitivity of the experiment, the main goal of SABS is the measurement of the ^{144}Pr beta spectrum. In this context, the low energy ^{144}Ce component acts as a background for the determination

[1] As opposed to the TUM beta spectrometer informally called "TUBS".

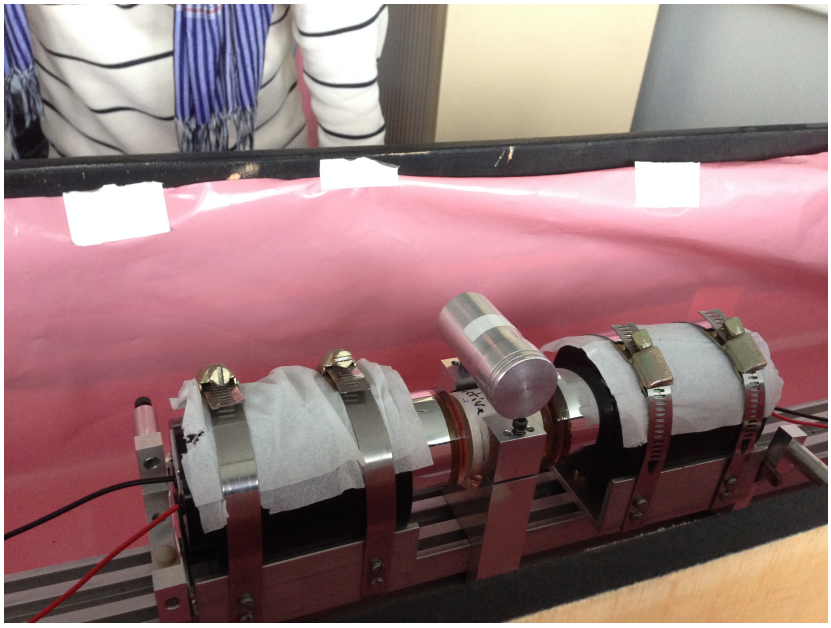

Figure B.3: Picture of the SABS setup.

of the ^{144}Pr $\bar{\nu}_e$ spectrum at high energy. In order to isolate the ^{144}Pr component, it is thus planned to chemically separate the two isotopes to only extract ^{144}Pr. Given the ^{144}Pr relatively short half-life of 17 minutes, the separation, source deposition and setup preparation have to be performed quite fast in order to reduce the loss of activity. After a typical data taking time of 1 hour, the plastic is expected to be removed and rinsed. The operation is then repeated until a satisfying energy spectrum has been recorded.

Presently, the main effort is directed towards the characterization of the setup. The gains of the PMTs are obtained by observing the pedestals and single photoelectrons with the use of a photodiode. This measurement allows to express the charge recorded by the QDC as a number of photoelectrons (n.p.e.), more suitable for the rest of the analysis. To convert an energy deposition expressed in n.p.e. into a proper energy unit such as keV or MeV, the use of radioactive calibration sources is mandatory. A preliminary calibration has been conducted with a ^{207}Bi source deposited at the center of the two scintillators. The decay of ^{207}Bi toward ^{207}Pb through electron capture is followed by the emission of several conversion electrons as well as gamma rays. The latter are often not fully contained and escape the plastic scintillator without depositing their total energy. The energy spectrum obtained after analysis is displayed in Figure B.4. The main structures observed in this spectrum correspond to the main β and γ radiations of ^{207}Bi and ^{207}Pb.

Additional calibrations are planned with other isotopes emitting low energy electrons such as ^{133}Ba and ^{109}Cd. First measurement of ^{144}Pr are expected by November 2015.

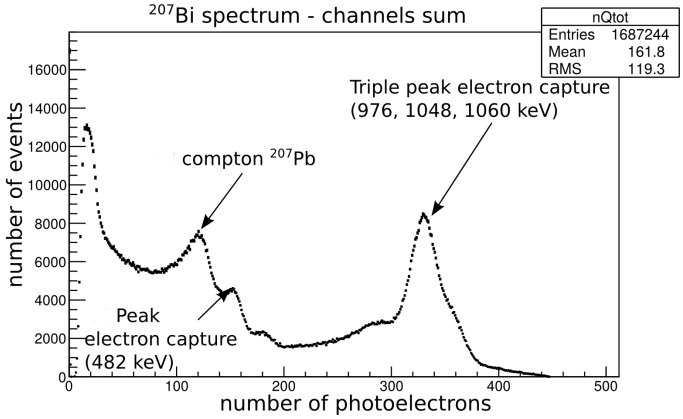

Figure B.4: Energy spectrum of ^{207}Bi observed in SABS [301]. The signals from the two PMTs are summed. The three highlighted peaks respectively correspond to the sum of the Compton edge of the 570 keV gamma ray from ^{207}Pb, the 482 keV conversion electron line and the 975.7, 1047.8 and 1059.8 keV conversion electron lines, indistinguishable due to the detector's resolution.

Bibliography

[1] W. Pauli. Dear radioactive ladies and gentlemen. *Phys. Today*, 31N9:27, 1978.

[2] E. Fermi. An attempt of a theory of beta radiation. *Z. Phys.*, 88:161–177, 1934.

[3] C. L. Cowan et al. Detection of the free neutrino: A Confirmation. *Science*, 124:103–104, 1956.

[4] A. H. Becquerel. On the rays emitted by phosphorescence. *Comptes Rendus*, 122:420–421, 1896.

[5] J. Chadwick. The intensity distribution in the magnetic spectrum of β particles from radium (B + C). *Verh. Phys. Gesell.*, 16:383–391, 1914.

[6] J. Chadwick. Possible Existence of a Neutron. *Nature*, 129:312, 1932.

[7] F. Reines. The early days of experimental neutrino physics. In K. Sakurai, editor, *Neutrinos in Cosmic Ray Physics and Astrophysics*, pages 71–84. Terra Scientific Publishing Company, 1990.

[8] P. Vogel and J. F. Beacom. The angular distribution of the neutron inverse beta decay, $\bar{\nu}_e + p \to e^+ + n$. *Phys. Rev.*, D60, 1999.

[9] T.D. Lee and Chen-Ning Yang. Question of Parity Conservation in Weak Interactions. *Phys.Rev.*, 104:254–258, 1956.

[10] C.S. Wu, E. Ambler, R.W. Hayward, D.D. Hoppes, and R.P. Hudson. Experimental Test of Parity Conservation in Beta Decay. *Phys.Rev.*, 105:1413–1414, 1957.

[11] M. Goldhaber, L. Grodzins, and A.W. Sunyar. Helicity of Neutrinos. *Phys.Rev.*, 109:1015–1017, 1958.

[12] Sheldon L. Glashow. Partial-symmetries of weak interactions. *Nuclear Physics*, 22(4):579 – 588, 1961.

[13] Steven Weinberg. A Model of Leptons. *Phys.Rev.Lett.*, 19:1264–1266, 1967.

[14] Abdus Salam. Weak and Electromagnetic Interactions. *Conf.Proc.*, C680519:367–377, 1968.

[15] K.A. Olive et al. Review of Particle Physics. *Chin.Phys.*, C38:090001, 2014.

[16] G. Danby et al. Observation of High-Energy Neutrino Reactions and the Existence of Two Kinds of Neutrinos. *Phys. Rev. Lett.*, 9:36–44, 1962.

[17] K. Kodama et al. Observation of tau-neutrino interactions. *Phys. Lett.*, B504:218–224, 2001.

[18] R. Davis Jr., D. S. Harmer, and K. C. Hoffman. Search for neutrinos from the sun. *Phys. Rev. Lett.*, 20:1205–1209, 1968.

[19] K. S. Hirata et al. Observation of a small atmospheric ν_μ/ν_e ratio in kamiokande. *Phys. Lett.*, B280:146–152, 1992.

[20] Tommy Ohlsson. A brief status of non-standard neutrino interactions. *Nucl.Phys.Proc.Suppl.*, 237-238:301–307, 2013.

[21] B. Pontecorvo. Mesonium and anti-mesonium. *Sov. Phys. JETP*, 6:429, 1957.

[22] B. Pontecorvo. Inverse beta processes and nonconservation of lepton charge. *Sov. Phys. JETP*, 7:172–173, 1958.

[23] Z. Maki, M. Nakagawa, and S. Sakata. Remarks on the unified model of elementary particles. *Prog. Theor. Phys.*, 28:870–880, 1962.

[24] Y. Fukuda et al. Evidence for oscillation of atmospheric neutrinos. *Phys. Rev. Lett.*, 81:1562–1567, 1998.

[25] Q. R. Ahmad et al. Direct evidence for neutrino flavor transformation from neutral-current interactions in the Sudbury Neutrino Observatory. *Phys. Rev. Lett.*, 89, 2002.

[26] Y. Abe et al. Indication for the disappearance of reactor electron antineutrinos in the Double Chooz experiment. *Phys. Rev. Lett.*, 108:131801, 2012.

[27] J. K. Ahn et al. Observation of Reactor Electron Antineutrino Disappearance in the RENO Experiment. *Phys. Rev. Lett.*, 108:191802, 2012.

[28] F. P. An et al. Observation of electron-antineutrino disappearance at Daya Bay. *Phys. Rev. Lett.*, 108:171803, 2012.

[29] K. Zuber. *Neutrino Physics*. Institute of Physics Publishing, 2003. Series in High Energy Physics.

[30] E. Majorana. Theory of the Symmetry of Electrons and Positrons. *Nuovo Cim.*, 14:171–184, 1937.

[31] M. Fukugita and T. Yanagida. Baryogenesis Without Grand Unification. *Phys. Lett.*, B174:45, 1986.

[32] C. Giuntu and C. W. Kim. *Fundamentals of Neutrino Physics and Astrophysics*. Oxford University Press, 2007.

[33] Fabrice Fleurot. Neutrino oscillations. `http://nu.phys.laurentian.ca/~fleurot/oscillations/`.

[34] Carlo Giunti. Theory of neutrino oscillations. pages 427–438, 2004.

[35] Thomas J. Weiler. Big Bang Cosmology, Relic Neutrinos, and Absorption of Neutrino Cosmic Rays. *Astrophys. J.*, 285:495, 1984.

[36] L. Wolfenstein. Neutrino oscillations in matter. *Phys. Rev.*, D17:2369–2374, 1978.

[37] S.P. Mikheev and A. Yu. Smirnov. Resonance Amplification of Oscillations in Matter and Spectroscopy of Solar Neutrinos. *Sov.J.Nucl.Phys.*, 42:913–917, 1985.

[38] S.P. Mikheev and A. Yu. Smirnov. Resonant amplification of neutrino oscillations in matter and solar neutrino spectroscopy. *Nuovo Cim.*, C9:17–26, 1986.

[39] G. B. Gelmini and J. W. F. Valle. Fast Invisible Neutrino Decays. *Phys. Lett.*, B142:181, 1984.

[40] Christian Weinheimer. Neutrino mass from triton decay. *Progress in Particle and Nuclear Physics*, 57(1):22 – 37, 2006. International Workshop of Nuclear Physics 27th course Neutrinos in Cosmology, in Astro, Particle and Nuclear Physics Ettore Majorana Center for Scientific Culture.

[41] Ch. Weinheimer. Direct neutrino mass experiments - present and future. *Nuclear Physics B - Proceedings Supplements*, 118(0):279 – 286, 2003. Proceedings of the {XXth} International Conference on Neutrino Physics and Astrophysics.

[42] Ch. Kraus et al. Final results from phase II of the Mainz neutrino mass search in tritium beta decay. *Eur. Phys. J.*, C40:447–468, 2005.

[43] V. N. Aseev et al. An upper limit on electron antineutrino mass from Troitsk experiment. *Phys. Rev.*, D84:112003, 2011.

[44] S. Fischer. Status of the KATRIN experiment. *PoS*, EPS-HEP2011:097, 2011.

[45] K. Assamagan, Ch. Brönnimann, M. Daum, H. Forrer, R. Frosch, P. Gheno, R. Horisberger, M. Janousch, P. R. Kettle, Th. Spirig, and C. Wigger. Upper limit of the muon-neutrino mass and charged-pion mass from momentum analysis of a surface muon beam. *Phys. Rev. D*, 53:6065–6077, 1996.

[46] R. Barate et al. An Upper limit on the tau-neutrino mass from three-prong and five-prong tau decays. *Eur.Phys.J.*, C2:395–406, 1998.

[47] Nathalie Palanque-Delabrouille et al. Constraint on neutrino masses from SDSS-III/BOSS Lyα forest and other cosmological probes. *JCAP*, 1502(02):045, 2015.

[48] Stephen F. King and Christoph Luhn. Neutrino Mass and Mixing with Discrete Symmetry. *Rept.Prog.Phys.*, 76:056201, 2013.

[49] M. Goeppert-Mayer. Double beta-disintegration. *Phys.Rev.*, 48:512–516, 1935.

[50] W.H. Furry. On transition probabilities in double beta-disintegration. *Phys.Rev.*, 56:1184–1193, 1939.

[51] Nasim Fatemi-Ghomi. Measurement of the double beta decay half-life of Nd-150 and search for neutrinoless decay modes with NEMO-3 detector. 2009.

[52] H.V. Klapdor-Kleingrothaus and I.V. Krivosheina. The evidence for the observation of 0nu beta beta decay: The identification of 0nu beta beta events from the full spectra. *Mod.Phys.Lett.*, A21:1547–1566, 2006.

[53] I.V. Kirpichnikov. Klapdor's claim for the observation of the neutrinoless double beta-decay of Ge-76. Analysis and corrections. 2010.

[54] M. Agostini et al. Results on Neutrinoless Double-β Decay of ^{76}Ge from Phase I of the GERDA Experiment. *Phys.Rev.Lett.*, 111(12):122503, 2013.

[55] John N. Bahcall, Aldo M. Serenelli, and Sarbani Basu. New solar opacities, abundances, helioseismology, and neutrino fluxes. *The Astrophysical Journal Letters*, 621(1):L85, 2005.

[56] B. T. Cleveland et al. Measurement of the solar electron neutrino flux with the Homestake chlorine detector. *Astrophys. J.*, 496:505–526, 1998.

[57] W. Hampel et al. GALLEX solar neutrino observations: Results for GALLEX IV. *Phys. Lett.*, B447:127–133, 1999.

[58] M. Altmann et al. GNO solar neutrino observations: Results for GNO I. *Phys. Lett.*, B490:16–26, 2000.

[59] J. N. Abdurashitov et al. Measurement of the solar neutrino capture rate with gallium metal. *Phys. Rev.*, C60, 1999.

[60] S. Abe et al. Precision Measurement of Neutrino Oscillation Parameters with KamLAND. *Phys. Rev. Lett.*, 100, 2008.

[61] A. Gando et al. Constraints on θ_{13} from A Three-Flavor Oscillation Analysis of Reactor Antineutrinos at KamLAND. *Phys.Rev.*, D83:052002, 2011.

[62] Y. Ashie et al. A Measurement of Atmospheric Neutrino Oscillation Parameters by Super-Kamiokande I. *Phys. Rev.*, D71, 2005.

[63] P. Adamson et al. Improved search for muon-neutrino to electron-neutrino oscillations in MINOS. *Phys.Rev.Lett.*, 107:181802, 2011.

[64] Ulrich F. Katz. The ORCA Option for KM3NeT. In *Proceedings of the 15th International Workshop on Neutrino Telescopes (Neutel 2013)*, 2014.

[65] M.G. Aartsen et al. Letter of Intent: The Precision IceCube Next Generation Upgrade (PINGU). 2014.

[66] Yu-Feng Li. Overview of the Jiangmen Underground Neutrino Observatory (JUNO). *Int.J.Mod.Phys.Conf.Ser.*, 31:1460300, 2014.

[67] D.S. Ayres et al. NOvA: Proposal to build a 30 kiloton off-axis detector to study nu(mu) to nu(e) oscillations in the NuMI beamline. 2004.

[68] C. Adams et al. The Long-Baseline Neutrino Experiment: Exploring Fundamental Symmetries of the Universe. 2013.

[69] M. Apollonio et al. Search for neutrino oscillations on a long baseline at the CHOOZ nuclear power station. *Eur. Phys. J.*, C27:331–374, 2003.

[70] F. Boehm, J. Busenitz, B. Cook, G. Gratta, H. Henrikson, et al. Final results from the Palo Verde neutrino oscillation experiment. *Phys.Rev.*, D64:112001, 2001.

[71] F. Ardellier et al. Double Chooz: A Search for the neutrino mixing angle theta(13). 2006.

[72] Xinheng Guo et al. A Precision measurement of the neutrino mixing angle θ_13 using reactor antineutrinos at Daya-Bay. 2007.

[73] J.K. Ahn et al. RENO: An Experiment for Neutrino Oscillation Parameter θ_{13} Using Reactor Neutrinos at Yonggwang. 2010.

[74] F. Ardellier et al. Letter of intent for Double-CHOOZ: A Search for the mixing angle theta(13). 2004.

[75] Y. Abe et al. Improved measurements of the neutrino mixing angle θ_{13} with the Double Chooz detector. *JHEP*, 1410:086, 2014.

[76] K. Abe et al. Indication of Electron Neutrino Appearance from an Accelerator-produced Off-axis Muon Neutrino Beam. *Phys. Rev. Lett.*, 107:041801, 2011.

[77] F.P. An et al. A new measurement of antineutrino oscillation with the full detector configuration at Daya Bay. 2015.

[78] K. Nakajima. θ_{13} and directionality measurements: Talk for neutrino geoscience 2013, 2013. Double Chooz internal document, DocDB ♯4652.

[79] M.H. Ahn et al. Measurement of Neutrino Oscillation by the K2K Experiment. *Phys.Rev.*, D74:072003, 2006.

[80] K. Abe et al. Observation of Electron Neutrino Appearance in a Muon Neutrino Beam. *Phys.Rev.Lett.*, 112:061802, 2014.

[81] P. Adamson et al. Electron neutrino and antineutrino appearance in the full MINOS data sample. *Phys.Rev.Lett.*, 110(17):171801, 2013.

[82] W. Hampel et al. Final results of the Cr-51 neutrino source experiments in GALLEX. *Phys.Lett.*, B420:114–126, 1998.

[83] J.N. Abdurashitov et al. Measurement of the response of the Russian-American gallium experiment to neutrinos from a Cr-51 source. *Phys.Rev.*, C59:2246–2263, 1999.

[84] F. Kaether, W. Hampel, G. Heusser, J. Kiko, and T. Kirsten. Reanalysis of the GALLEX solar neutrino flux and source experiments. *Phys.Lett.*, B685:47–54, 2010.

[85] C. Athanassopoulos et al. The Liquid scintillator neutrino detector and LAMPF neutrino source. *Nucl.Instrum.Meth.*, A388:149–172, 1997.

[86] E. Church et al. A proposal for an experiment to measure $\nu_\mu \to \nu_e$ oscillations and muon-neutrino disappearance at the fermilab booster: Boone. 1997.

[87] A.A. Aguilar-Arevalo et al. Unexplained Excess of Electron-Like Events From a 1-GeV Neutrino Beam. *Phys.Rev.Lett.*, 102:101802, 2009.

[88] A.A. Aguilar-Arevalo et al. Event Excess in the MiniBooNE Search for $\bar{\nu}_\mu \to \bar{\nu}_e$ Oscillations. *Phys.Rev.Lett.*, 105:181801, 2010.

[89] A.A. Aguilar-Arevalo et al. Improved Search for $\bar{\nu}_\mu \to \bar{\nu}_e$ Oscillations in the MiniBooNE Experiment. *Phys.Rev.Lett.*, 110:161801, 2013.

[90] H. Chen et al. A proposal for a new experiment using the booster and numi neutrino beamlines: Microboone. 2007.

[91] A (Director) Harrison. ILL :: Neutrons for science. `https://www.ill.eu/`.

[92] K. Schreckenbach et al. Determination of the antineutrino spectrum from U-235 thermal neutron fission products up to 9.5 MeV. *Phys. Lett.*, B160:325–330, 1985.

[93] A. A. Hahn et al. Antineutrino spectra from Pu-241 and Pu-239 thermal neutron fission products. *Phys. Lett.*, B218:365–368, 1989.

[94] Th. A. Mueller et al. Improved Predictions of Reactor Antineutrino Spectra. *Phys. Rev.*, C83:054615, 2011.

[95] P. Huber. On the determination of anti-neutrino spectra from nuclear reactors. *Phys. Rev.*, C84:024617, 2011.

[96] G. Mention et al. The Reactor Antineutrino Anomaly. *Phys. Rev.*, D83:073006, 2011.

[97] Raymond R. Volkas. Introduction to sterile neutrinos. *Prog. Part. Nucl. Phys.*, 48:161–174, 2002.

[98] K. N. Abazajian et al. *Light Sterile Neutrinos: A White Paper*. Virginia Tech, 2012.

[99] Alexander Kusenko, Fuminobu Takahashi, and Tsutomu T. Yanagida. Dark Matter from Split Seesaw. *Phys.Lett.*, B693:144–148, 2010.

[100] C.D. Froggatt and Holger Bech Nielsen. Hierarchy of Quark Masses, Cabibbo Angles and CP Violation. *Nucl.Phys.*, B147:277, 1979.

[101] James Barry, Werner Rodejohann, and He Zhang. Sterile Neutrinos for Warm Dark Matter and the Reactor Anomaly in Flavor Symmetry Models. *JCAP*, 1201:052, 2012.

[102] Takehiko Asaka, Steve Blanchet, and Mikhail Shaposhnikov. The nuMSM, dark matter and neutrino masses. *Phys.Lett.*, B631:151–156, 2005.

[103] Zurab G. Berezhiani and Rabindra N. Mohapatra. Reconciling present neutrino puzzles: Sterile neutrinos as mirror neutrinos. *Phys.Rev.*, D52:6607–6611, 1995.

[104] Adrian Signer. ABC of SUSY. *J.Phys.*, G36:073002, 2009.

[105] K. Hiraide et al. Search for Charged Current Coherent Pion Production on Carbon in a Few-GeV Neutrino Beam. *Phys. Rev.*, D78:112004, 2008.

[106] G. Cheng et al. Dual baseline search for muon antineutrino disappearance at $0.1\text{eV}^2 < \Delta m^2 < 100\text{eV}^2$. *Phys. Rev.*, D86:052009, 2012.

[107] A.A. Aguilar-Arevalo et al. A Search for electron neutrino appearance at the $\Delta m^2 \sim 1\text{eV}^2$ scale. *Phys.Rev.Lett.*, 98:231801, 2007.

[108] F.P. An et al. Improved Measurement of Electron Antineutrino Disappearance at Daya Bay. *Chin.Phys.*, C37:011001, 2013.

[109] C. Giunti, M. Laveder, Y.F. Li, Q.Y. Liu, and H.W. Long. Update of Short-Baseline Electron Neutrino and Antineutrino Disappearance. *Phys.Rev.*, D86:113014, 2012.

[110] Gianpiero Mangano, Gennaro Miele, Sergio Pastor, Teguayco Pinto, Ofelia Pisanti, and Pasquale D. Serpico. Relic neutrino decoupling including flavor oscillations. *Nucl. Phys.*, B729:221–234, 2005.

[111] Jan Hamann, Steen Hannestad, Georg G. Raffelt, Irene Tamborra, and Yvonne Y.Y. Wong. Cosmology seeking friendship with sterile neutrinos. *Phys.Rev.Lett.*, 105:181301, 2010.

[112] Marc Davis, George Efstathiou, Carlos S. Frenk, and Simon D.M. White. The Evolution of Large Scale Structure in a Universe Dominated by Cold Dark Matter. *Astrophys.J.*, 292:371–394, 1985.

[113] Alexey Boyarsky, Oleg Ruchayskiy, and Dmytro Iakubovskyi. A Lower bound on the mass of Dark Matter particles. *JCAP*, 0903:005, 2009.

[114] Alexey Boyarsky, Dmytro Iakubovskyi, Oleg Ruchayskiy, and Vladimir Savchenko. Constraints on decaying Dark Matter from XMM-Newton observations of M31. *Mon.Not.Roy.Astron.Soc.*, 387:1361, 2008.

[115] Esra Bulbul, Maxim Markevitch, Adam Foster, Randall K. Smith, Michael Loewenstein, and Scott W. Randall. Detection of An Unidentified Emission Line in the Stacked X-ray spectrum of Galaxy Clusters. *Astrophys. J.*, 789:13, 2014.

[116] Alexey Boyarsky, Oleg Ruchayskiy, Dmytro Iakubovskyi, and Jeroen Franse. Unidentified Line in X-Ray Spectra of the Andromeda Galaxy and Perseus Galaxy Cluster. *Phys. Rev. Lett.*, 113:251301, 2014.

[117] Hiroyuki Ishida, Kwang Sik Jeong, and Fuminobu Takahashi. 7 keV sterile neutrino dark matter from split flavor mechanism. *Phys. Lett.*, B732:196–200, 2014.

[118] Anatoly Klypin, Andrey V. Kravtsov, Octavio Valenzuela, and Francisco Prada. Where are the missing galactic satellites? *The Astrophysical Journal*, 522(1):82, 1999.

[119] J.M. Conrad, C.M. Ignarra, G. Karagiorgi, M.H. Shaevitz, and J. Spitz. Sterile Neutrino Fits to Short Baseline Neutrino Oscillation Measurements. *Adv.High Energy Phys.*, 2013:163897, 2013.

[120] Tarik Akhal Lylia Hamidatou, Hocine Slamene and Boussaad Zouranen. Concepts, Instrumentation and Techniques of Neutron Activation Analysis, 2013.

[121] Brookhaven National Laboratory. National nuclear data center. `http://www.nndc.bnl.gov/`.

[122] Wikimedia Foundation. Wikipedia. `http://www.en.wikipedia.org`.

[123] P. Huber and T. Schwetz. Precision spectroscopy with reactor anti-neutrinos. *Phys. Rev.*, D70:053011, 2004.

[124] Th. A. Mueller. *Expérience Double Chooz : simulation des spectres antineutrinos issus de réacteurs*. PhD thesis, Université Paris Sud, 2010.

[125] D.H. Wilkinson. Evaluation of beta-decay: I. the traditional phase space factors. *Nuclear Instruments and Methods in Physics Research Section A: Accelerators, Spectrometers, Detectors and Associated Equipment*, 275(2):378 – 386, 1989.

[126] J.C. Hardy, B. Jonson, and P.G. Hansen. A COMMENT ON PANDEMONIUM. *Phys.Lett.*, B136:331, 1984.

[127] F. Von Feilitzsch, A. A. Hahn, and K. Schreckenbach. Experimental beta spectra from Pu-239 and U-235 thermal neutron fission products and their correlated antineutrinos spectra. *Phys. Lett.*, B118:162–166, 1982.

[128] W. Mampe et al. The double focusing iron-core electron-spectrometer BILL for high resolution (n,e^-) measurements at the high flux reactor in Grenoble. *Nuclear Instruments and Methods*, 154(1):127–149, 1978.

[129] N. Haag, A. Gütlein, M. Hofmann, L. Oberauer, W. Potzel, et al. Experimental Determination of the Antineutrino Spectrum of the Fission Products of ^{238}U. *Phys.Rev.Lett.*, 112(12):122501, 2014.

[130] D. Lhuillier. Reactor flux calculations. In *Proccedings of Neutrino-2012*. To be published in Nucl. Phys. B-PS., 2012. Available at `http://neu2012.kek.jp/`.

[131] Michel Cribier, Maximilien Fechner, Thierry Lasserre, Alain Letourneau, David Lhuillier, et al. A proposed search for a fourth neutrino with a PBq antineutrino source. *Phys.Rev.Lett.*, 107:201801, 2011.

[132] L. B. et al. Auerbach. Measurement of electron-neutrino electron elastic scattering. *Phys. Rev. D*, 63:112001, May 2001.

[133] Th. Lasserre. Testing the Reactor and Gallium Anomalies with Intense (Anti)Neutrino Emitters. *Nucl.Phys.Proc.Suppl.*, 235-236:214–219, 2013.

[134] David A. Green and F. Richard Stephenson. The Historical supernovae. *Lect.Notes Phys.*, 598:7, 2003.

[135] M. Betoule et al. Improved cosmological constraints from a joint analysis of the SDSS-II and SNLS supernova samples. *Astron.Astrophys.*, 568:A22, 2014.

[136] Enrico Cappellaro and Massimo Turatto. Supernova types and rates. *Astrophys.Space Sci.Libr.*, 264:199, 2001.

[137] E.G. Adelberger, A.B. Balantekin, D. Bemmerer, C.A. Bertulani, J.-W. Chen, et al. Solar fusion cross sections II: the pp chain and CNO cycles. *Rev.Mod.Phys.*, 83:195, 2011.

[138] Hans-Thomas Janka. Explosion Mechanisms of Core-Collapse Supernovae. *Ann.Rev.Nucl.Part.Sci.*, 62:407–451, 2012.

[139] H.-Thomas Janka, Florian Hanke, Lorenz Huedepohl, Andreas Marek, Bernhard Mueller, et al. Core-Collapse Supernovae: Reflections and Directions. *PTEP*, 2012:01A309, 2012.

[140] Cristina Volpe. Open issues in neutrino astrophysics. *Annalen Phys.*, 525(8-9):588–599, 2013.

[141] Irene Tamborra et al. Self-sustained asymmetry of lepton-number emission: A new phenomenon during the supernova shock-accretion phase in three dimensions. *Astrophys.J.*, 792:96, 2014.

[142] Australian Astronomical Observatory David Malin. Photograph of SN1987A.

[143] C. Inserra, A. Pastorello, M. Turatto, M.L. Pumo, S. Benetti, et al. Luminous type II Supernovae. *Astron.Astrophys.*, 555:A142, 2013.

[144] T. Totani, K. Sato, H.E. Dalhed, and J.R. Wilson. Future detection of supernova neutrino burst and explosion mechanism. *Astrophys.J.*, 496:216–225, 1998.

[145] Jerome Gava, James Kneller, Cristina Volpe, and G.C. McLaughlin. A Dynamical collective calculation of supernova neutrino signals. *Phys.Rev.Lett.*, 103:071101, 2009.

[146] George Sonneborn, Bruce Altner, and Robert P. Kirshner. The progenitor of sn 1987a - spatially resolved ultraviolet spectroscopy of the supernova field. *Astrophys. J.*, 323:L35–L39, 1987.

[147] K. Hirata et al. Observation of a Neutrino Burst from the Supernova SN 1987a. *Phys.Rev.Lett.*, 58:1490–1493, 1987.

[148] R.M. Bionta, G. Blewitt, C.B. Bratton, D. Casper, A. Ciocio, et al. Observation of a Neutrino Burst in Coincidence with Supernova SN 1987a in the Large Magellanic Cloud. *Phys.Rev.Lett.*, 58:1494, 1987.

[149] E.N. Alekseev, L.N. Alekseeva, I.V. Krivosheina, and V.I. Volchenko. Detection of the Neutrino Signal From SN1987A in the LMC Using the Inr Baksan Underground Scintillation Telescope. *Phys.Lett.*, B205:209–214, 1988.

[150] M. Aglietta, G. Badino, G. Bologna, C. Castagnoli, A. Castellina, et al. On the event observed in the Mont Blanc Underground Neutrino observatory during the occurrence of Supernova 1987a. *Europhys.Lett.*, 3:1315–1320, 1987.

[151] Francesco Vissani. Comparative analysis of SN1987A antineutrino fluence. *J.Phys.*, G42:013001, 2015.

[152] R.N. Mohapatra and P.B. Pal. Massive neutrinos in physics and astrophysics. *World Sci.Lect.Notes Phys.*, 41:1–318, 1991.

[153] Thomas J. Loredo and Don Q. Lamb. Bayesian analysis of neutrinos observed from supernova SN-1987A. *Phys.Rev.*, D65:063002, 2002.

[154] Pietro Antonioli, Richard Tresch Fienberg, Fabrice Fleurot, Yoshiyuki Fukuda, Walter Fulgione, et al. SNEWS: The Supernova Early Warning System. *New J.Phys.*, 6:114, 2004.

[155] K. Scholberg. The SuperNova Early Warning System. *Astron.Nachr.*, 329:337–339, 2008.

[156] J. Gaffiot. *Étude des neutrinos de réacteur : mise en place et caractérisation du détecteur Nucifer*. PhD thesis, Université Paris Sud, 2012.

[157] Alessandro Strumia and Francesco Vissani. Precise quasielastic neutrino/nucleon cross-section. *Phys.Lett.*, B564:42–54, 2003.

[158] V. Fischer, T. Chirac, T. Lasserre, C. Volpe, M. Cribier, et al. Prompt directional detection of galactic supernova by combining large liquid scintillator neutrino detectors. 2015.

[159] A.N. Ivanov, R. Hollwieser, N.I. Troitskaya, M. Wellenzohn, O.M. Zherebtsov, et al. Deficit of reactor antineutrinos at distances smaller than 100 m and inverse beta-decay. *Phys.Rev.*, C88:055501, 2013.

[160] M. Durero. Modeling of beta spectrum for CeLAND experiment. Rapport de stage, Royal Institute of Technology - KTH, Stockholm, 2013.

[161] A. Afanaciev et al. Geant4: A toolkit for the simulation of the passage of particles through matter. `http://geant4.cern.ch/`.

[162] R. Brun, F. Rademakers, et al. ROOT | A Data Analysis Framework. `http://root.cern.ch/drupal/`.

[163] Glenn Horton-Smith. Information on generators for the KamLAND simulation, 2001. `http://neutrino.phys.ksu.edu/~GLG4sim/`.

[164] Glenn Horton-Smith. An introduction to GLG4sim features, 2006. `http://neutrino.phys.ksu.edu/~GLG4sim/`.

[165] T. Chirac. Etude de la reconstruction de la position d'explosions d'étoiles dans le ciel par la détection de neutrinos dans les grands détecteurs à liquide scintillant. Rapport de stage, Ecole Centrale de Lyon, 2014.

[166] Inc. The MathWorks. Matlab, 2013.

[167] *SNOwGLoBES : SuperNova Observatories with GLoBES : DRAFT http://www.phy.duke.edu/ schol/snowglobes/*, version 1.1 edition, March 11th 2013.

[168] The GEANT4 collaboration. Geant4 9.5 release notes. `http://www.geant4.org/geant4/support/ReleaseNotes4.9.5.html`.

[169] John F. Beacom and P. Vogel. Can a supernova be located by its neutrinos? *Phys.Rev.*, D60:033007, 1999.

[170] R. Roncin. *From the measurement of the θ_{13} mixing angle to the search for geo-neutrinos: studying $\bar{\nu}_e$ with Double Chooz and Borexino.* PhD thesis, Université Paris 7, 2014.

[171] Glenn R. Jocher, Daniel A. Bondy, Brian M. Dobbs, Stephen T. Dye, James A. Georges, et al. Theoretical antineutrino detection, direction and ranging at long distances. *Phys.Rept.*, 527:131–204, 2013.

[172] Thierry Lasserre, Maximilien Fechner, Guillaume Mention, Romain Reboulleau, Michel Cribier, et al. SNIF: A Futuristic Neutrino Probe for Undeclared Nuclear Fission Reactors. 2010.

[173] N.N. Das Gupta and S.K. Ghosh. A Report on the Wilson Cloud Chamber and its Applications in Physics. *Rev.Mod.Phys.*, 18:225–290, 1946.

[174] Kamioka Observatory. ICRR (Institute for Cosmic Ray Research), The University of Tokyo. `http://www-sk.icrr.u-tokyo.ac.jp/sk/index-e.html`.

[175] C Backhouse. Results from MINOS and NOνA. *J.Phys.Conf.Ser.*, 598(1):012004, 2015.

[176] M. Apollonio et al. Determination of neutrino incoming direction in the CHOOZ experiment and supernova explosion location by scintillator detectors. *Phys.Rev.*, D61:012001, 2000.

[177] F. Boehm, J. Busenitz, B. Cook, G. Gratta, H. Henrikson, et al. Results from the Palo Verde neutrino oscillation experiment. *Phys.Rev.*, D62:072002, 2000.

[178] J. Ashenfelter et al. PROSPECT - A Precision Reactor Oscillation and Spectrum Experiment at Short Baselines. 2013.

[179] Th. Langford. ^{6}Li-Loaded Liquid Scintillator for the PROSPECT Short-Baseline Neutrino Experiment, 2014.

[180] G. Zacek et al. Neutrino Oscillation Experiments at the Gosgen Nuclear Power Reactor. *Phys.Rev.*, D34:2621–2636, 1986.

[181] M. Vivier. Double chooz geodetic survey, 2013. Double Chooz internal document, DocDB ♯4753.

[182] V. Fischer. Survey's results, 2013. Double Chooz internal document, DocDB ♯4934.

[183] M. Vivier. Status of dc geodetic survey, 2015. Double Chooz internal document, DocDB ♯6061.

[184] Y. Abe et al. First Measurement of θ_{13} from Delayed Neutron Capture on Hydrogen in the Double Chooz Experiment. *Phys.Lett.*, B723:66–70, 2013.

[185] Kathrin A. Hochmuth, Manfred Lindner, and Georg G. Raffelt. Exploiting the directional sensitivity of the Double Chooz near detector. *Phys.Rev.*, D76:073001, 2007.

[186] Michael Wurm et al. The next-generation liquid-scintillator neutrino observatory LENA. *Astropart.Phys.*, 35:685–732, 2012.

[187] Alessandro Mirizzi, G.G. Raffelt, and P.D. Serpico. Earth matter effects in supernova neutrinos: Optimal detector locations. *JCAP*, 0605:012, 2006.

[188] Kate Scholberg. Supernova Neutrino Detection. *J.Phys.Conf.Ser.*, 375:042036, 2012.

[189] C. Alberini et al. The Large Volume Detector (Lvd) of the Gran Sasso Laboratory. *Nuovo Cim.*, C9:237–261, 1986.

[190] K. Eguchi et al. First results from KamLAND: Evidence for reactor anti-neutrino disappearance. *Phys.Rev.Lett.*, 90:021802, 2003.

[191] Mark C. Chen. The SNO+ Experiment. 2008.

[192] G. Alimonti et al. The Borexino detector at the Laboratori Nazionali del Gran Sasso. *Nucl.Instrum.Meth.*, A600:568–593, 2009.

[193] Andrew O. Bazarko. MiniBooNE: The Booster neutrino experiment. 1999.

[194] R. Dharmapalan et al. A new investigation of electron neutrino appearance oscillations with improved sensitivity in the MiniBooNE+ experiment. 2013.

[195] K. Abe, T. Abe, H. Aihara, Y. Fukuda, Y. Hayato, et al. Letter of Intent: The Hyper-Kamiokande Experiment — Detector Design and Physics Potential —. 2011.

[196] Hanyu Wei. Supernova Early Warning in Daya Bay Reactor Neutrino Experiment. 2013.

[197] Eric C. Bellm. The Zwicky Transient Facility. 2014.

[198] Scott M. Adams, C.S. Kochanek, John F. Beacom, Mark R. Vagins, and K.Z. Stanek. Observing the Next Galactic Supernova. *Astrophys.J.*, 778:164, 2013.

[199] Kate Scholberg, Armin Burgmeier, and Roger Wendell. Obtaining supernova directional information using the neutrino matter oscillation pattern. *Phys.Rev.*, D81:043007, 2010.

[200] J.R. Alonso, N. Barros, M. Bergevin, A. Bernstein, L. Bignell, et al. Advanced Scintillator Detector Concept (ASDC): A Concept Paper on the Physics Potential of Water-Based Liquid Scintillator. 2014.

[201] Jaime V. Dawson and D. Kryn. Organic Liquid TPCs for Neutrino Physics. *JINST*, 9:P07002, 2014.

[202] Leslie Camilleri. Private discussion.

[203] Katsuhiko Sato and Hideyuki Suzuki. Total Energy of Neutrino Burst From the Supernova Sn1987a and the Mass of Neutron Star Just Born. *Phys.Lett.*, B196:267, 1987.

[204] James M. Lattimer and Madappa Prakash. The Ultimate energy density of observable cold matter. *Phys.Rev.Lett.*, 94:111101, 2005.

[205] Sebastien Guillot, Mathieu Servillat, Natalie A. Webb, and Robert E. Rutledge. Measurement of the Radius of Neutron Stars with High S/N Quiescent Low-mass X-ray Binaries in Globular Clusters. *Astrophys.J.*, 772:7, 2013.

[206] Brian P. Schmidt, R.P. Kirshnerm, and R.G. Eastman. Expanding photospheres of type II supernovae and the extragalactic distance scale. *Astrophys.J.*, 395:366–386, 1992.

[207] V. Fischer. Neutrino directionality with large liquid scintillator detectors - application to geoneutrinos detection. Neutrino Geoscience 2015 Conference, `http://www.ipgp.jussieu.fr/fr/evenements/neutrino-geoscience-2015-conference`.

[208] L. Ludhova and S. Zavatarelli. Studying the Earth with Geoneutrinos. page 425693, 2013.

[209] Ondrej Sramek, William F. McDonough, Edwin S. Kite, Vedran Lekic, Steve Dye, et al. Geophysical and geochemical constraints on geoneutrino fluxes from Earth's mantle. *Earth Planet.Sci.Lett.*, 361:356–366, 2013.

[210] J. H. Davies and D. R. Davies. Earth's surface heat flux. *Solid Earth*, 1(1):5–24, 2010.

[211] M. Agostini et al. Spectroscopy of geo-neutrinos from 2056 days of Borexino data. 2015.

[212] A. Gando et al. Reactor On-Off Antineutrino Measurement with KamLAND. *Phys.Rev.*, D88(3):033001, 2013.

[213] G. Bellini et al. Measurement of geo-neutrinos from 1353 days of Borexino. *Phys.Lett.*, B722:295–300, 2013.

[214] S.T. Dye, Y. Huang, V. Lekic, W.F. McDonough, and O. Sramek. Geo-neutrinos and Earth Models. *Phys.Procedia*, 61:310–318, 2015.

[215] John G. Learned, Stephen T. Dye, and Sandip Pakvasa. Hanohano: A Deep ocean anti-neutrino detector for unique neutrino physics and geophysics studies. pages 235–269, 2007.

[216] Framatome/AREVA.

[217] C. de la Vaissière. laradioactivite.com. IN2P3 / EDP Sciences. `http://www.laradioactivite.com`.

[218] C. Pauquet. La médiathèque EDF.

[219] Nuclear Energy Agency. MURE, MCNP Utility for Reactor Evolution: couples Monte-Carlo transport with fuel burnup calculations, 2009. `http://www.oecd-nea.org/tools/abstract/detail/nea-1845`.

[220] O. Meplan et al. MURE: MCNP Utility for Reactor Evolution - Description of the methods, first applications and results. In *European Nuclear Conference 2005*, 2005. Nuclear Power for the XXIst Century : From basic research to high-tech industry.

[221] Y. Declais, H. de Kerret, B. Lefievre, M. Obolensky, A. Etenko, et al. Study of reactor anti-neutrino interaction with proton at Bugey nuclear power plant. *Phys.Lett.*, B338:383–389, 1994.

[222] C. Aberle, C. Buck, B. Gramlich, F. X. Hartmann, M. Lindner, S. Schonert, U. Schwan, S. Wagner, and H. Watanabe. Large scale Gd-beta-diketonate based organic liquid scintillator production for antineutrino detection. *JINST*, 7:P06008, 2012.

[223] C. Bauer, E. Borger, R. Hofacker, K. Janner, F. Kaether, et al. Qualification Tests of 474 Photomultiplier Tubes for the Inner Detector of the Double Chooz Experiment. *JINST*, 6:P06008, 2011.

[224] T. Matsubara, T. Haruna, T. Konno, Y. Endo, M. Bongrand, et al. Evaluation of 400 low background 10-in. photo-multiplier tubes for the Double Chooz experiment. *Nucl.Instrum.Meth.*, A661:16–25, 2012.

[225] CAEN S.p.A. Tools for discovery - electronic instrumentation. `http://www.caen.it/csite/HomePage.jsp`.

[226] Y. Abe, T. Akiri, A. Cabrera, B. Courty, J.V. Dawson, et al. The Waveform Digitiser of the Double Chooz Experiment: Performance and Quantisation Effects on PhotoMultiplier Tube Signals. *JINST*, 8:P08015, 2013.

[227] P. Novella. Recopulse: Software and algorithms for pulse reconstruction, 2009. Double Chooz internal document, DocDB ♯649.

[228] H. Shahnoor. Reconstruction of events in recobama, 2012. Double Chooz internal document, DocDB ♯4331.

[229] C. Aberle, C. Buck, F.X. Hartmann, S. Schonert, and S. Wagner. Light output of Double Chooz scintillators for low energy electrons. *JINST*, 6:P11006, 2011.

[230] C. Aberle, C. Buck, F.X. Hartmann, and S. Schonert. Light yield and energy transfer in a new Gd-loaded liquid scintillator. *Chem.Phys.Lett.*, 516:257–262, 2011.

[231] M. Strait. Fido: The fused inner detector outer veto muon track reconstruction, 2012. Double Chooz internal document, DocDB ♯3603.

[232] Y. Abe et al. Precision Muon Reconstruction in Double Chooz. *Nucl.Instrum.Meth.*, A764:330–339, 2014.

[233] A. Franke. Event generation & uncertainty propagation in dcrxtrtools using the bugey4 anchor point, 2011. Double Chooz internal document, DocDB ♯3221.

[234] G. Horton-Smith. Double chooz geant4 summary talk for march 2012 dc paris analysis live meeting, 2012. Double Chooz internal document, DocDB ♯3805.

[235] The GEANT4 collaboration. Geant4 9.2 release notes. `http://geant4.cern.ch/support/ReleaseNotes4.9.2.html`.

[236] A. Cabrera. Ross: status report, 2012. Double Chooz internal document, DocDB ♯3773.

[237] V. Sibille. Cosmogenic spectra generation, 2014. Double Chooz internal document, DocDB ♯5916.

[238] M. Ishitsuka. Internal note of li and he spectrum and fraction measurement using dc-iii dataset, 2015. Double Chooz internal document, DocDB ♯5957.

[239] M. Ishitsuka. Internal note of dc-iii neutrino oscillation analyses using energy spectrum, 2014. Double Chooz internal document, DocDB ♯5162.

[240] M. Ishitsuka. H-iii analysis tech-note, 2015. Double Chooz internal document, DocDB ♯5918.

[241] Y. Abe et al. Reactor electron antineutrino disappearance in the Double Chooz experiment. *Phys.Rev.*, D86:052008, 2012.

[242] Y. Abe et al. Direct Measurement of Backgrounds using Reactor-Off Data in Double Chooz. *Phys.Rev.*, D87:011102, 2013.

[243] E. Chauveau. Investigation of bsm contamination above 20 mev prompt, 2015. Double Chooz internal document, DocDB ♯6169.

[244] A. Collin. *Étude des antineutrinos de réacteurs : mesure de l'angle de mélange leptonique θ_{13} et recherche d'éventuels neutrinos stériles*. PhD thesis, Université Paris 11, 2014.

[245] J. Haser. Spill-in/-out technical note (1st and 2ndpub), 2013. Double Chooz internal document, DocDB ♯4127.

[246] A. Meregaglia. Fast neutron reduction by mps, 2015. Double Chooz internal document, DocDB ♯6033.

[247] Y. Abe, J.C. dos Anjos, J.C. Barriere, E. Baussan, I. Bekman, et al. Ortho-positronium observation in the Double Chooz Experiment. *JHEP*, 1410:32, 2014.

[248] R. Sharankova. Hiii: accidental bg reduction using ann, 2015. Double Chooz internal document, DocDB ♯6037.

[249] T. J.C. Bezerra. Impact of fd light noise cut at the nd ibd candidates, 2015. Double Chooz internal document, DocDB ♯6161.

[250] E. Chauveau. Preliminary selection cut of singles for fd+nd, 2015. Double Chooz internal document, DocDB ♯6160.

[251] T. J.C. Bezerra. Nd singles and ibd candidates, 2015. Double Chooz internal document, DocDB ♯6071.

[252] T. J.C. Bezerra. Nd ibd and buffer ibd candidates, 2015. Double Chooz internal document, DocDB ♯6086.

[253] Y. Abe et al. Background-independent measurement of θ_{13} in Double Chooz. *Phys.Lett.*, B735:51–56, 2014.

[254] Seon-Hee Seo. New Results from RENO and The 5 MeV Excess. 2014.

[255] D.A. Dwyer and T.J. Langford. Spectral Structure of Electron Antineutrinos from Nuclear Reactors. *Phys.Rev.Lett.*, 114(1):012502, 2015.

[256] A. Ianni, D. Montanino, and G. Scioscia. Test of nonstandard neutrino properties with the BOREXINO source experiments. *Eur. Phys. J.*, C8:609–617, 1999.

[257] O. G. Miranda, V. B. Semikoz, and J. W. F. Valle. Neutrino electron scattering and electroweak gauge structure: Probing the masses of a new Z boson. In *Lepton and baryon number violation in particle physics, astrophysics and cosmology. Proceedings, 1st International Symposium, Lepton-baryon'98, Trento, Italy, April 20-25, 1998*, 1998.

[258] N. Ferrari, G. Fiorentini, and B. Ricci. The Cr-51 neutrino source and borexino: A Desirable marriage. *Phys. Lett.*, B387:427–431, 1996.

[259] D. A. Dwyer, K. M. Heeger, B. R. Littlejohn, and P. Vogel. Search for Sterile Neutrinos with a Radioactive Source at Daya Bay. *Phys. Rev.*, D87(9):093002, 2013.

[260] S. Abe et al. Production of Radioactive Isotopes through Cosmic Muon Spallation in KamLAND. *Phys. Rev.*, C81:025807, 2010.

[261] H. Watanabe. *Comprehensive study of antineutrino signals at KamLAND*. PhD thesis, Tohoku University, 2012.

[262] A. Gando et al. Measurement of the double-β decay half-life of ^{136}Xe with the KamLAND-Zen experiment. *Phys. Rev.*, C85:045504, 2012.

[263] H. Back et al. Borexino calibrations: Hardware, Methods, and Results. *JINST*, 7:P10018, 2012.

[264] J. Gaffiot, T. Lasserre, G. Mention, M. Vivier, M. Cribier, et al. Experimental Parameters for a Cerium 144 Based Intense Electron Antineutrino Generator Experiment at Very Short Baselines. *Phys.Rev.*, D91(7):072005, 2015.

[265] World Nuclear Association. Processing of used nuclear fuel. `http://www.world-nuclear.org/info/Nuclear-Fuel-Cycle/Fuel-Recycling/Processing-of-Used-Nuclear-Fuel/`.

[266] A. S. Gerasimov, V. N. Kornoukhov, I. S. Sal'dikov, and G. V. Tikhomirov. Production of high specific activity 144ce for artificial sources of antineutrinos. *Atomic Energy*, 116(1):54–59, 2014. Translated from Atomnaya Énergiya, Vol. 116, No. 1, pp. 40–44, January, 2014.

[267] N. Jonqueres. Cerium calorimeter and thermal studies, 2014. SOX internal document, DocDB ♯33.

[268] L. Di Noto. Status of the genoa-munich calorimeter, 2014. SOX internal document, DocDB ♯42.

[269] D.H. Wilkinson. Evaluation of beta-decay: Ii. finite mass and size effects. *Nuclear Instruments and Methods in Physics Research Section A: Accelerators, Spectrometers, Detectors and Associated Equipment*, 290(2–3):509 – 515, 1990.

[270] A. Sirlin. Radiative correction to the $\overline{\nu}_e(\nu_e)$ spectrum in β decay. *Phys. Rev. D*, 84:014021, Jul 2011.

[271] H. Behrens and W. Bühring. *Electron Radial Wave Functions and Nuclear Beta-Decay*. The International Series of Monographs on Physics Series. Clarendon Press, 1982.

[272] Xiamen Tungsten Co. China tungsten. http://www.xiamentungsten.com/.

[273] (Ed.) Briesmeister, Judith F. MCNP: A General Monte Carlo N-Particle Transport Code. 1993.

[274] IAEA. Regulations for the safe transport of radioactive material - 2012 edition. http://www-pub.iaea.org/books/IAEABooks/10449/Regulations-for-the-Safe-Transport-of-Radioactive-Material-2012-Edition-Specific-Safety

[275] TC-Tungsten Compounds. Sodium polytungstate information datasheet. http://www.heavy-liquid.com/en/productinformation/informationdatasheet/.

[276] P. Decowski. Status of kamland-zen. GDR 2015 workshop, https://indico.in2p3.fr/event/11500/.

[277] P. Lombardi. Cr1 installation, 2015. SOX internal document, DocDB ♯128.

[278] Lauren Hsu. KLG4sim: A Full Monte Carlo Simulation for KamLAND, 2005. MAND Workshop June 2005.

[279] Shimizu Itaru. Private communication.

[280] A. Caminata. Status of g4bx2 for sox, 2014. SOX internal document, DocDB ♯61.

[281] Brun E. et al. Tripoli-4®, cea, edf and areva reference monte-carlo code. *Annals of Nuclear Energy*, to be published.

[282] F.H. Clark. The exponential transform as an importance sampling device: A review. Technical Report ORNL-RSIC-14, Oak Ridge National Laboratory, Jan 1966.

[283] M. Vivier. Spectra, background and sensitivity with cerium generator, 2014. SOX internal document, DocDB ♯31.

[284] Centre de Calcul de l'Institut National de Physique Nucléaire et de Physique des Particules. Ccin2p3 website. http://cc.in2p3.fr/.

[285] O. Yu. Smirnov et al. Measurement of neutrino flux from the primary proton–proton fusion process in the Sun with Borexino detector. 2015.

[286] A. Gando et al. CeLAND: search for a 4th light neutrino state with a 3 PBq 144Ce-144Pr electron antineutrino generator in KamLAND. 2013.

[287] Mayak PA. Private communication.

[288] M. Pequignot. *Les expériences Nucifer et Stéréo: Etudes des antineutrinos de reacteurs a courte distance*. PhD thesis, Université Paris Sud, 2015.

[289] G. Boireau et al. Online Monitoring of the Osiris Reactor with the Nucifer Neutrino Detector. 2015.

[290] Direction de l'Énergie Nucléaire (DEN), Direction Déléguée aux Affaires Nucléaires de Saclay (DANS), Département des Réacteurs et Services Nucléaires (DRSN). Le réacteur osiris. Les éditions stratégiques. http://nucleaire.cea.fr/fr/publications/pdf/osiris_plaquette_FR.pdf.

[291] J. Pelzer. Taux d'accidentels avec des coupure en barycentre et en énergie, 2012. Nucifer internal document, eLog ♯81.

[292] M. Vivier. Nucifer: un détecteur d'anti-neutrinos comme outil de contrôle des réacteurs nucléaires, 2013. Talk presented at COPHYNU-GANIL 2013.

[293] T. Nguyen. Neutrino and accidental amounts from new cuts, 2014. Nucifer internal document, eLog ♯178.

[294] D. Lhuillier. Neutrinos or fast neutrons?, 2013. Nucifer internal document, eLog ♯142.

[295] M. Pequignot. Scan of steel screen position, 2013. Nucifer internal document, eLog ♯160.

[296] V. Fischer. New nucemland results with 1.8 cm of steel, 2013. Nucifer internal document, eLog ♯155.

[297] D. Lhuillier. Background model from ill data, 2012. Nucifer internal document, eLog ♯12.

[298] M. Fechner, C. Henson, J. Gaffiot, et al. A large HPGe detector for the non-destructive radioassay of an ultra-low-background counting facility. *Applied Radiation and Isotopes*, 69(7):1033 – 1038, Jul 2011.

[299] AMETEK, Inc. Ortec. `http://www.ortec-online.com/`.

[300] Eljen Technology. `http://www.eljentechnology.com/`.

[301] M. Durero. Status of saclay beta spectrometer (sabs), 2015. Borexino collaboration meeting, July 2015.

Abstract : The framework of neutrino oscillations is quite well-understood and now requires precision rather than exploration. The Double Chooz experiment aims at measuring the θ_{13} mixing angle through the oscillations of electronic antineutrinos produced by the reactors of the Chooz nuclear power plant, in the French Ardennes. The comparison of the interaction rates and spectral shapes in the two Double Chooz's detectors allows the observation of a disappearance and a spectral distortion, both driven by θ_{13}. In this thesis, a preliminary neutrino selection with the near detector, whose data taking started in December 2014, has been performed. The most recent results of Double Chooz, providing the most precise measurement of the experiment of $\sin^2 2\theta_{13} = 0.090^{+0.032}_{-0.029}$, are presented as well. The simple layout of Double Chooz is a strong advantage to conduct directionality studies. Results of these studies using the most recent neutrino candidates with neutron captures on Gd and H are showed. Neutrino directionality can be applied to astrophysics and astronomy, with the localization of core-collapse supernovae. To this purpose, the development of SuperNustradamus, dedicated to the simulation of a supernova process detected in a liquid scintillator detector, is presented, along with results of directionality measurements performed with combinations of large neutrino detectors over the globe. Finally, recent anomalies observed in short baseline experiments provided hints of the hypothetical existence of additional sterile neutrino states. The goal of the CeLAND/CeSOX experiment is to test this hypothesis by deploying a $\bar{\nu}_e$ -generating radioactive source next to a large liquid scintillator detector such as KamLAND or Borexino. In this thesis, are presented results of signal and background simulations performed to validate the design and assess the sensitivity of such an experiment.

Keywords : Neutrino directionality, Inverse Beta Decay, core-collapse supernova, sterile neutrino, neutrino oscillations, θ_{13} mixing angle

Résumé : Le cadre global des oscillations de neutrinos est maintenant bien compris et nous quittons une ère d'exploration pour une ère de précision. L'expérience Double Chooz a pour but de mesurer l'angle de mélange θ_{13} par l'étude des oscillations des antineutrinos électroniques produits par les réacteurs de la centrale nucléaire de Chooz dans les Ardennes. La comparaison des taux d'interactions et des formes de spectres en énergie dans les deux détecteurs de l'expérience permet l'observation d'une disparition et d'une distorsion spectrale, toutes deux régies par θ_{13}. Dans cette thèse, une sélection préliminaire des neutrinos détectés dans le détecteur proche, dont la prise de données a commencée en Décembre 2014, est présentée. Les résultats les plus récents de Double Chooz, desquels sont extraits la mesure de θ_{13} la plus précise que l'expérience peut fournir à ce jour $\sin^2 2\theta_{13} = 0.090^{+0.032}_{-0.029}$, seront également discutés. La disposition géométrique des réacteurs et détecteurs de l'expérience, relativement simple, représente un avantage considérable afin d'effecteur des études de directionalité des neutrinos. Les résultats de ces études, effectuées en analysant les jeux de données les plus récents avec captures sur Gd et H, sont présentés. Ce concept de directionalité peut être appliqué à l'astronomie/astrophysique en offrant la possibilité de détecter des supernovas après détection de leurs neutrinos. Le développement de SuperNustradamus, dédié à la simulation d'un processus de supernova détecté dans un détecteur à liquide scintillant, ainsi que les résultats de simulations de directionalité effectuées avec différentes combinaisons de plusieurs détecteurs de neutrinos. Enfin, plusieurs anomalies récemment observées par des expériences de détection de neutrinos à courtes distances pourraient s'expliquer par l'existence de nouveaux états, stériles, de neutrinos. Le but de l'expérience CeLAND/CeSOX est de confirmer ou réfuter cette hypothèse en déployant une source radioactive émettant des $\bar{\nu}_e$ à coté d'un grand détecteur à liquide scintillant comme KamLAND ou Borexino. Dans cette thèse seront présentés les résultats des simulations de signaux et de bruits de fond effectuées afin de valider le principe de l'expérience et de s'assurer de sa sensibilité à l'observation d'une nouvelle oscillation vers un hypothétique neutrino stérile.

Mots-clés : Directionalité des neutrinos, désintégration beta inverse, supernova avec effondrement de coeur, neutrino stérile, oscillations de neutrinos, angle de mélange θ_{13}